To the Graduate Council:

I am submitting herewith a dissertation written by Sandip Pundlikrao Harimkar entitled "Laser Surface Structuring of Alumina". I have examined the final electronic copy of this dissertation for form and content and recommend that it be accepted in partial fulfillment of the requirements for the degree of Doctor of Philosophy, with a major in Materials Science and Engineering.

_____

Narendra B. Dahotre, Major Professor

We have read this thesis

and recommend its acceptance:

Carl J. McHargue

_____

Easo P. George

_____

Dayakar Penumadu

_____

Acceptance for the Council:

Carolyn R. Hodges

_____

Vice Provost and Dean of the Graduate School

(Original signatures are on file with official student records)

LASER SURFACE STRUCTURING OF ALUMINA

A Dissertation

Presented for the

Doctor of Philosophy

Degree

The University of Tennessee, Knoxville

Sandip Pundlikrao Harimkar

December 2007

Dedicated to

My Parents

And

Teachers

Acknowledgment

I would like to take this opportunity to thank all those who directly or indirectly made this dissertation possible. First, thanks to my research advisor Dr. Narendra B. Dahotre for his excellent guidance and support throughout the course of this project. I would also like to extend my sincere appreciation to Dr. Carl J. McHargue, Dr. Easo P. George and Dr. Dayakar Penumadu for serving on my doctoral committee. I am grateful to Dr. Claus Daniel, Dr. Ed Kenik, Dr. Craig Blue and Dr. Gene Ice of Oak Ridge National Laboratory; Dr. Arvind Agarwal of Florida International University; and Dr. Indranil Manna of Indian Institute of Technology-Kharagpur for their assistance on various technical aspects of the project. Thanks to Dr. Dunlap and Mr. Greg Jones for helping me with electron microscopy. Also, I would also like to thank my friends and colleagues Dr. Subhadarshi Nayak, Mr. Greg Engleman, Dr. Ravi Shankar Aggarwal and Dr. Yan Cui for their encouragement and fruitful discussions. Finally, I acknowledge the academic and financial support from the University of Tennessee Space Institute.

Abstract

Alumina ceramic is an important abrasive material for grinding wheels used for rough grinding/machining of materials in manufacturing industry. Purpose of this work is to explore laser surface structuring of alumina grinding wheels for precision machining/grinding of materials by modifying surface microstructure of wheels. Major objective of this work is to study the evolution of surface microstructure and depth of modification such that microstructures/properties of modified wheels can be efficiently tailored based on fundamental understanding of physical processes taking place during laser surface structuring.

Surface structuring of alumina using a continuous wave Nd:YAG laser resulted in significant surface melting and subsequent rapid solidification. The surface modified alumina consisted of microstructure characterized by regular polygonal and faceted surface grains with well defined edges and vertices. Such multifaceted grains act as micro-cutting tools on the surface of grinding wheels facilitating micro-scale material removal during precision machining. The formation of faceted morphology is explained on the basis of evolution of crystallographic texture in laser modified alumina. Furthermore, complete crystallographic description of multifaceted morphology of surface grains is provided based on detailed analysis of surface micro-texture. Due to complexity of microstructure formed during laser surface structuring, a fractal analysis-based approach is suggested to characterize surface microstructures. Detailed analysis of the effects of laser interaction with porous alumina ceramic indicated that melt surface

undergoes rapid evaporation resulting in generation of high (>10^5 Pa) evaporation-induced recoil pressures. These pressures drive the flow of melt through underlying porous alumina during modification extending the depth of modification. An integrative modeling approach combining thermal analysis and fluid flow analysis resulted in better agreements between predicted and experimental values of depths of melting. Finally, improvements in microindentation fracture toughness of alumina ceramic are reported with increasing laser fluence. Such improvements in the fracture toughness seem to be derived from better surface densification and coarsening of grain structure.

The understanding of the evolution of faceted morphology, depth of surface modifications and improvements in fracture properties in laser surface microstructured alumina ceramic reached in this work provides the foundation for tailoring of surface microstructures/properties of alumina grinding wheels for precision machining applications.

Table of Contents

Chapter 1: Laser Surface Structuring of Ceramics-An overview ……...1

1.1 Introduction …… 1

1.2 Laser-material Interactions ……3

1.2.1 Thermal Effects ……..7

1.2.2 Vapor Expansion and Recoil Pressures ……....16

1.2.3 Plasma Formation ……19

1.2.4 Ablation ……....21

1.3 Microstructure Evolution ……..23

1.4 Laser Surface Structuring Applications ……....25

1.4.1 Laser Dressing of Alumina Grinding Wheels ……..25

1.4.2 Tribological Applications ……28

1.4.3 Biomedical Applications ……..30

1.4.4 Surface Densification ……...31

Chapter 2: Experimental Procedure ……....32

2.1 Selection of Materials ……...32

2.2 Optimization of Laser Processing Parameters ……..33

2.3 Modified Surface Characterization ……...34

2.3.1 Microstructural Attributes (Scanning Electron Microscopy) ……...34

2.3.2 Phase and Micro Texture Evolution (Orientation Imaging Microscopy) ……...35

2.3.3 Surface Morphology (Stylus Profilometry and Atomic Force Microscopy) ……38

2.3.4 Fracture Behavior (Micro-indentation) ……39

Chapter 3: Laser Process Parameter Dependent Transitions in Rapidly Solidified Alumina ……..40

3.1 Evolution of Morphological Texture ……40

3.2 Evolution of Phase and Crystallographic Texture ……50

3.3 Processing Parameter-microstructure Correlations based on Fractal Analysis ….....61

3.4 Summary ……...69

Chapter 4: Laser Process Thermal Effects on Physical Attributes of Surface Modified Region ……...70

4.1 Integrative Modeling Approach ……70

4.2 Temporal Distribution of Temperature ……72

4.3 Temporal Evolution of Recoil Pressure ……81

4.4 Melt Infiltration and Effective Depth of Melting ……84

4.5 Influence of Thermal Effects on Evolution of Grain Structure ……89

4.6 Summary ……...92

Chapter 5: Fracture Properties of Laser Surface Modified Alumina ...93

5.1 Influence of Microstructure on Fracture Toughness ……94

5.2 Summary ……...98

Chapter 6: Conclusions and Suggested Future Work ……99

6.1 Conclusions ……...99

6.2 Suggested Future Work ……...100

References ……102

Appendices ……...113

Appendix A: List of Publications …….....114

Appendix B: Reprints of Published Works ……....119

Vita ……181

List of Tables

Tables		Pages
Table 3.1	Texture coefficients (TC) of various (*h k l*) planes for alumina substrate and laser surface modified alumina at various laser fluences.	54
Table 4.1	Properties of alumina used in mathematical calculations.	77
Table 4.2	Summary of the values of temperature gradient (*G*) at solid/liquid interface, solidification rate (*R*) and cooling rate calculated from one-dimensional thermal model for laser surface modified alumina at various laser fluences	90

List of Figures

Figures		Pages
Figure 1.1	Possible interactions of laser light with material.	4
Figure 1.2	Various effects of laser-material interaction: (a) heating, (b) surface melting, (c) surface vaporization, (d) plasma formation, and (e) ablation.	6
Figure 1.3	Schematic of the laser irradiation geometry and surface temperatures at various times: (a) initial condition with uniform temperature, T_0, throughout the material, (b) laser heating with surface temperature, $T_s > T_0$, and (c) cooling stage (laser off) with surface temperature $T'_s < T_s$ (surface temperatures are less than melting point at all times).	9
Figure 1.4	Schematic of the (a) heating model geometry with a moving point source of heat, and (b) typical temperature distribution (isotherms) in the x-z plane through the point source.	13
Figure 1.5	Schematic of the dressing set up and surface morphology obtained in two different approaches of wheel dressing. (a) Used grinding wheel surface before dressing showing blunt surface grains with the metal particles loaded in the interconnected porosity; (b) surface features of diamond dressed grinding wheel showing newly exposed irregular, sharp grains obtained by	

removing the blunt surface layer and (c) Surface features of laser dressed grinding wheel obtained by rapid solidification of alumina grinding wheel surface showing highly refined multi-faceted grains with well defined edges and vertices. 26

Figure 1.6 Micrographs of laser structured surfaces: (a) micro-channels in 100Cr6 generated using Q-switch laser mode, (b) micro-channels in 100Cr6 generated using continuous wave laser mode, (c) micro-pits in 100Cr6, and (d) crossed micro-channels in alumina [39]. 29

Figure 1.7 Multi-scale nature of laser textured zirconia coated titanium-based substrates [40]. 30

Figure 1.8 Micrographs of 85 % alumina samples surface densified by the CO_2 laser and the flame: (a) plan view showing boundary between treated and untreated region, (b), (c) high magnification views of a region on a laser track, and (d) cross-section of laser surface densified region [41]. 31

Figure 2.1 Experimental set-up for laser surface structuring of alumina ceramic. 33

Figure 2.2 Schematic of the diffractometer geometry for texture analysis. 36

Figure 3.1 Low magnification picture showing alumina ceramic before (upper portion) and after (lower portion) surface modification. 42

Figure 3.2 Schematic of laser surface modification process for alumina

ceramic and corresponding SEM image of cross-sectional view indicating distinct interface between laser melted region and substrate. 42

Figure 3.3 SEM micrographs of surface of (a) untreated alumina substrate and laser surface modified alumina at laser fluence of (b) 458 J/cm^2, (c) 496 J/cm^2, (d) 535 J/cm^2, (e) 573 J/cm^2, (f) 611 J/cm^2, (g) 649 J/cm^2 and (h) 687 J/cm^2 43

Figure 3.4 SEM micrographs and corresponding 3D topographical maps showing the evolution of surface morphology in laser surface modified alumina ceramics. (a) Alumina ceramic substrate before surface modification and (b–d) after surface modification with laser fluence of 496 J/cm^2, 573 J/cm^2 and 649 J/cm^2 respectively. 45

Figure 3.5 Schematic representation of the polygonal surface grains used for curvature factor calculation. Curvature factor is given by ratio R_1 / R_2. 46

Figure 3.6 Grain size, curvature factor, and corresponding SEM micrographs of the surface grains in laser surface modified alumina at various laser fluences [(♦) grain size and (■) curvature factor]. 47

Figure 3.7 Faceted morphology of polygonal surface grains associated with laser surface modification of an alumina ceramic. 49

Figure 3.8 X-ray diffraction patterns of (a) untreated alumina substrate and laser surface modified alumina at laser fluence of (b) 458 J/cm^2, (c) 496 J/cm^2, (d) 535 J/cm^2, (e) 573 J/cm^2, (f) 611 J/cm^2, (g) 649 J/cm^2 and (h) 687 J/cm^2. 51

Figure 3.9 Relative intensity of (1 1 0) reflection ($2\theta = 37.785°$) of α-Al_2O_3 substrate and laser surface modified alumina with various laser fluences. 53

Figure 3.10 Average texture coefficient for various (*h k l*) planes of α-alumina calculated over a range of laser fluences used for surface modifications. 57

Figure 3.11 Texture coefficients (TC) of (1 1 0), (2 2 0) and (2 1 1) planes of α-alumina as a function of laser fluence. (Note the data point corresponding to the texture coefficients of substrate). 57

Figure 3.12 van der Drift model illustrating the evolution of idiomorphic crystal shapes with the ratio of relative velocities (α_{3D}) of the {1 1 0} and {1 1 1} facets for 3-dimensional case [55]. 58

Figure 3.13 Schematic of the development of faceted morphology from crystallographic texture in laser surface modified alumina. 59

Figure 3.14 Example of Kikuchi pattern used for the calculation of the EBSD orientation map from the surface of laser surface modified alumina ceramic. Inset shows the unindexed Kikuchi pattern. 60

Figure 3.15 Calculated pole figures showing the distribution of $\{0001\}$, $\{1\bar{2}10\}$, $\{2\bar{3}10\}$ poles with respect to surface normal. Maximum intensities are circled and show the $(2\bar{3}10)$ texture as discussed in the text. 62

Figure 3.16 Calculation of fractal dimension from SEM micrograph using image processing and box counting algorithm. The slope of the log-log plot shown in the figure corresponds to the fractal dimension. 65

Figure 3.17 Variation of Fractal Dimension with laser processing fluence used for surface modification of alumina ceramic. 66

Figure 3.18 Variation of surface porosity of the laser surface modified alumina with fractal dimensions (Correlation parameter of data fitting, R^2=0.9735). 67

Figure 3.19 Variation of polygonal surface grain size of the laser surface modified alumina with fractal dimensions (Correlation parameter of data fitting, R^2=0.9385) 68

Figure 3.20 Variation of surface roughness of the laser surface modified alumina with fractal dimensions (Correlation parameter of data fitting, R^2=0.9456). 68

Figure 4.1 Typical polished cross section of laser surface modified alumina ceramic mounted in epoxy mould. Surface modification was carried out at a laser fluence of 535 J/cm^2. 71

Figure 4.2 Physical model showing the interaction of laser beam with porous ceramic substrate during the laser surface modification. Various effects such as surface melting, evaporation, generation of evaporation recoil pressure, and melt infiltration are shown. 73

Figure 4.3 Schematic of an integrative modeling method for predicting the overall depth of melting in laser surface modified alumina ceramic. 74

Figure 4.4 Computed temporal evolution of surface temperature during laser surface modifications of alumina ceramic processed with a range of laser fluence from 458 J/cm^2 to 764 J /cm^2. 78

Figure 4.5 Computed variation of maximum surface temperature with laser processing fluence during the surface modifications of alumina ceramic. 79

Figure 4.6 Computed temperature distribution below the surface of alumina ceramic surface modified with a range of laser processing fluence from 458 J/cm^2 to 764 J /cm^2. 80

Figure 4.7 Computed temporal evolution of evaporation-induced recoil pressure during the laser surface modification of alumina ceramic processed with a laser processing fluence of 458 J /cm^2. 83

Figure 4.8 Computed evaporation-induced maximum recoil pressure as a function of laser processing fluence employed during the laser surface modifications of alumina ceramic. 83

Figure 4.9 High magnification SEM micrograph of the interfacial region of the laser surface modified alumina illustrating the infiltration of molten material into the underlying porous material assisted by evaporation-induced recoil pressures. 85

Figure 4.10 Comparison of computed depth of melting from thermal and fluid flow model with experimental depth of melting (♦, Experimental; ■, thermal model; and ▲, integrative thermal and fluid flow model). 88

Figure 4.11 Grain size, cooling rate, and corresponding SEM micrographs of the surface grains in laser surface modified alumina at various laser fluences [(♦) grain size and (■) curvature factor]. 91

Figure 5.1 Typical Vickers hardness indentation in laser surface modified alumina ceramic. 95

Figure 5.2 Variation of fracture toughness (K_{IC}) of laser surface modified alumina ceramic with laser fluence. 96

Figure 5.3 Variation of secondary dendrite arms spacing, SDAS (♦) and calculated cooling rate (■) with laser fluence employed for surface modification of alumina ceramic. 96

Figure 5.4 High magnification scanning electron micrographs of laser surface modified alumina ceramic after indentation fracture: (a) 535 J/cm^2 and (b) 649 J/cm^2. 97

Chapter 1

Laser Surface Structuring of Ceramics-An Overview

1.1 Introduction

Ceramic is an important class of material which is finding increased applications as biomaterials and advanced structural and engineering materials. Industrially important ceramics include various oxides, carbides, nitrides, and borides [1, 2]. Various properties exhibited by these materials include high hardness and wear resistance, oxidation resistance, chemical stability, creep resistance, and thermal shock resistance. In spite of the attractive properties, actual utilization of ceramics in applications is often limited primarily due to their inherent brittleness, low flaw tolerance and low reliability [3, 4]. These limiting properties of ceramics are partly derived from bonding characteristics of the ceramics and from limited number of independent operating slip systems. Often, roots of ceramic component failure can be traced to the surface defects introduced during powder processing.

Surface engineering presents novel approaches of improving properties of advanced ceramics by locally modifying the surface microstructure. Furthermore, surface modification techniques can be directed to produce functional surfaces for advanced applications [5, 6]. The properties of these engineered ceramics are then greatly influenced by surface microstructure in the modified ceramics. The surface microstructure of engineered ceramics may be defined by various parameters such as phase, composition, grain morphology and texture at the surface. These microstructural

features in the modified material are primarily inherited from the nature of surface modification processes. Laser Surface Modifications (LSM) has emerged as a flexible and convenient technique for improving surface properties of ceramics [5, 6]. Laser surface modifications of porous alumina ceramic have recently attracted significant research interest for improving surface properties for various applications. For example, laser surface modifications of alumina ceramic linings (used in furnaces, incinerators, heat exchangers etc.) are expected to extend the life of linings by minimizing localized thermal and environmental attack due to sealing of the surface pores during surface modification [7]. Also, laser surface modifications of alumina abrasives wheels have potential to re-generate the surface topography suitable for precision machining of materials [8]. Thus, laser surface modifications of porous alumina ceramic exhibit a great potential in a wide range of applications, with each application requiring the characteristic microstructure at surface. Hence, optimizing laser processing parameters to control the microstructural features evolved during surface modifications plays a key role in tailoring the surface properties for various applications. Despite great potential of laser surface modified ceramics in various advanced applications, detailed investigations of microstructure development during laser surface modifications are limited. Keeping this in view, major efforts of present study are directed towards understanding laser interaction with an industrially important alumina ceramic and consequent surface microstructure development during laser surface modifications.

1.2 Laser-material Interactions

Understanding the capabilities laser surface modification of ceramics requires the knowledge of physical processes occurring during laser beam interactions with material. When the electromagnetic radiation is incident on a surface of material, various phenomena that occurs includes reflection, refraction, absorption, scattering and transmission (Fig. 1.1). One of the most desirable and important phenomena in laser processing of materials is the absorption of radiation. Absorption of radiation in the materials results in various effects such as heating, melting, vaporization, plasma formation, etc. which forms the basis of several laser materials processing techniques [9]. The extent of these effects primarily depends on the characteristic of electromagnetic radiation and the thermo-physical properties of material. The laser parameters include intensity, wavelength, spatial and temporal coherence, angle of incidence, polarization, illumination time, etc.; whereas, the materials parameters include absorptivity, thermal conductivity, specific heat, density, latent heats, etc. The interaction of laser with material is a complex interdisciplinary subject and requires knowledge from several branches of physics. This section briefly explains the important laser material interactions and their effects which are relevant in the laser surface modification of ceramic materials [10].

The absorption of laser radiation in a material is generally expressed by Beer-Lambert law [9]:

$$I(z) = I_0 e^{-\mu z}, \tag{1.1}$$

where I_0 is the incident intensity, $I(z)$ is the intensity at depth z and μ is the absorption coefficient. Thus, the intensity of laser radiation gets attenuated inside the material.

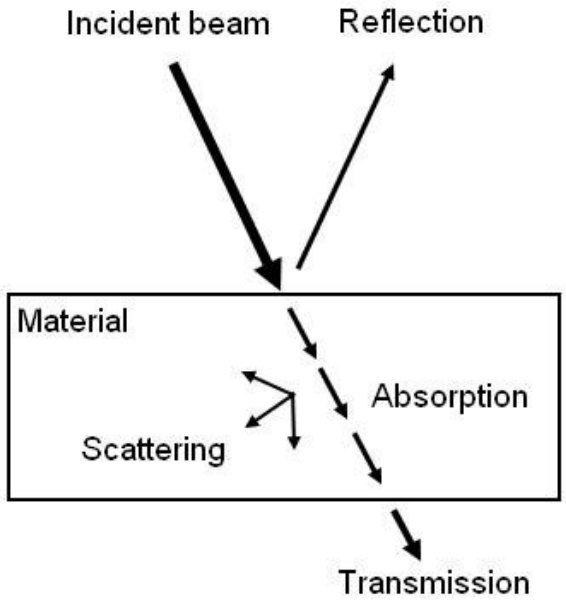


Fig. 1.1 Possible interactions of laser light with material.

The length over which significant attenuation of laser radiation takes place is often referred as attenuation length and is given by the reciprocal of absorption coefficient [11]:

$$L = \frac{1}{\mu}. \tag{1.2}$$

For strongly absorbing material, the absorption coefficients are in the range of 10^5-10^6 cm^{-1} such that the attenuation lengths are in the range of 10^{-5}-10^{-6} cm [12].

One of the important parameters influencing the effects of laser-material interactions is the absorptivity of material for laser radiation. It can be defined as a fraction of incident radiation that is absorbed at normal incidence. For opaque materials, the absorptivity (A) can be expressed as [12]:

$$A = 1 - R, \tag{1.3}$$

where R is the reflectivity of material. The reflectivity and the absorptivity of material can be calculated from the measurements of optical constants or the complex refractive index. The complex refractive index (n_c) is defined as:

$$n_c = n - ik \tag{1.4}$$

where n and k are the refractive index and the extinction coefficient respectively. These parameters are strong function of wavelength and temperature. The reflectivity at normal incidence is then defined as:

$$R = \frac{(n-1)^2 + k^2}{(n+1)^2 + k^2}. \tag{1.5}$$

Since parameters n and k are strong function of wavelength and temperature, the reflectivity (and hence the absorptivity) of material is greatly influenced by wavelength and temperature [12].

The laser energy absorbed by material during laser-material interaction is converted into heat by degradation of ordered and localized primary excitation energy. The typical overall energy relaxation times are of the order of 10^{-13} s for metals (10^{-12}-10^{-6} s for nonmetals). The conversion of light energy into heat and subsequent conduction of heat into the material establishes temperature distributions in the material. Depending on the magnitude of temperature rise, various physical effects in the material include heating, melting, and vaporization of material. Furthermore, the ionization of vapor during laser irradiation may lead to generation of plasma. In addition to the thermal effects, the laser-material interactions may be associated with photochemical processes such as photoablation of material. These effects of laser-material interactions are schematically presented in Fig. 1.2. All of these effects play important roles during laser

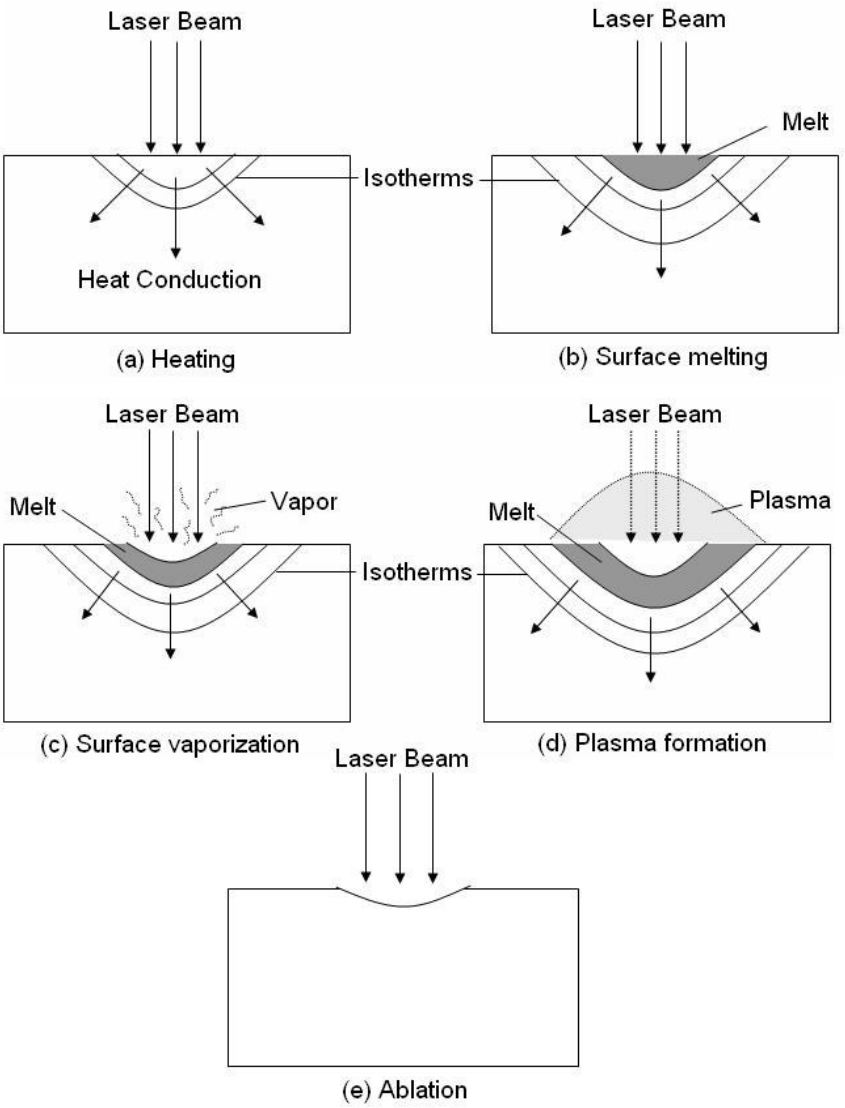


Fig. 1.2 Various effects of laser-material interaction: (a) heating, (b) surface melting, (c) surface vaporization, (d) plasma formation, and (e) ablation.

materials processing. There exist distinct combinations of laser intensities and interaction times where specific effect of laser-material interaction dominates [10].

1.2.1 Thermal Effects

When a laser beam of intensity, I_0, is irradiated on the surface of material, it results in the excitation of free electrons (in metals), vibrations (in insulators) or both (in semiconductors). As mentioned in the previous section, this excitation energy is rapidly converted into heat (time duration in the range of 10^{-13} s for metals, 10^{-12}-10^{-6} s for non metals). This is followed by various heat transfer processes such as conduction into the materials, and convection and radiation from the surface. The most significant heat transfer process being the heat conduction into the material. The generation of heat at the surface and its conduction into the material establishes the temperature distributions in the material depending on the optical and thermal properties of the material and laser parameters. If the incident laser intensity is sufficiently high, the absorption of laser energy can result in the physical phase transformations such as surface melting and evaporation. Generally, these phase transformations are associated with threshold (minimum) laser intensities referred as melting and evaporation thresholds (I_m and I_v). Melting and evaporation are the efficient material removal mechanisms during many machining processes. In this section, simplified analysis of laser heating, melting and evaporation of materials is presented [10].

To understand the thermal effects of laser irradiation on the material, it is necessary to evaluate the temporal and spatial variation of temperature distribution. Significant progress has been made in the modeling of thermal effects during laser-

material interaction effects. This includes the consideration to three-dimensionality, phase transformations and temperature dependent properties. For the clarity of concepts, most simplified thermal analysis based on the solution of one-dimensional heat conduction equation is presented here. The simplified assumptions for such analysis are [13]:

1. Material is homogeneous. The thermo-physical properties are independent of temperature.
2. The initial temperature of the material is constant.
3. Heat input is uniform during the irradiation time.
4. The convection and radiation losses from the surface are negligible.

The schematic geometry of laser irradiation and corresponding surface temperature during laser heating are presented in Fig. 1.3. The governing equation for the one-dimensional heat transfer can be written as:

$$\frac{\partial T(z,t)}{\partial t} = \alpha \frac{\partial^2 T(z,t)}{\partial z^2}, \tag{1.6}$$

where T is the temperature at location, z, after time, t; and α is the thermal diffusivity.

The initial condition can be written as:

$$T(z,0) = T_0, \quad \text{for } 0 \le z \le \infty,\ t = 0 \tag{1.7}$$

where T_0 is the initial constant temperature of the material.

The simple boundary condition at the surface ($z = 0$) assuming that laser energy absorbed at the surface equals the energy conducted can be written as:

$$-k \frac{\partial T(0,t)}{\partial z} = \delta H, \tag{1.8}$$

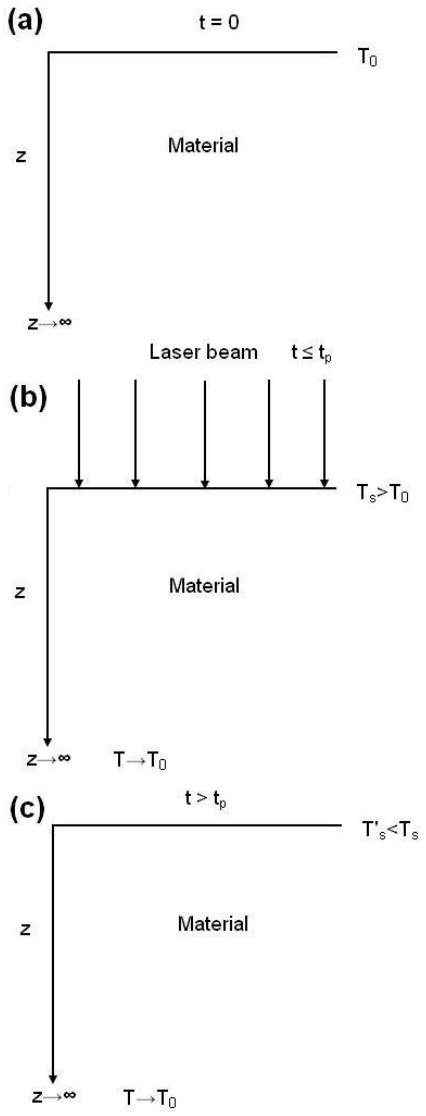


Fig. 1.3 Schematic of the laser irradiation geometry and surface temperatures at various times: (a) initial condition with uniform temperature, T_0, throughout the material, (b) laser heating with surface temperature, $T_s > T_0$, and (c) cooling stage (laser off) with surface temperature $T'_s < T_s$ (surface temperatures are less than melting point at all times) .

where k is the thermal conductivity, and H is the absorbed laser energy. The absorbed laser energy H can be given by the product of absorptivity, A, and incident laser power density, I_0 (i.e. $H = AI_0$). If t_p is the irradiation time (beam residence time) then the parameter δ equals unity when the laser is on i.e. $0 \le t \le t_p$. It can be taken as zero when the laser is off i.e. $t > t_p$.

The solutions of these equations can be obtained as:

During heating ($0 < t < t_p$):

$$\Delta T(z,t)_{t<t_p} = \frac{H}{k}(4\alpha t)^{1/2}\,\mathrm{ierfc}\left(\frac{z}{(4\alpha t)^{1/2}}\right). \tag{1.9}$$

During cooling ($t > t_p$):

$$\Delta T(z,t)_{t>t_p} = \frac{2H\alpha^{1/2}}{k}\left[t^{1/2}\,\mathrm{ierfc}\left(\frac{z}{(4\alpha t)^{1/2}}\right) - (t-t_p)^{1/2}\,\mathrm{ierfc}\left(\frac{z}{(4\alpha(t-t_p))^{1/2}}\right)\right] \tag{1.10}$$

The function ierfc(x) is defined as:

$$\mathrm{ierfc}(x) = \frac{1}{\sqrt{\pi}}\left\{\exp(-x^2) - x(1-erf(x))\right\},$$

where $erf(x) = \frac{2}{\sqrt{\pi}}\int_0^x e^{-\xi^2}d\xi$. (1.11)

The temperature at the surface during heating and cooling can be obtained by substituting $z = 0$ in Eqs. (1.9)-(1.10). Thus

$$\Delta T(0,t)_{t<t_p} = \frac{H}{k}\left(\frac{4\alpha t}{\pi}\right)^{1/2}, \tag{1.12}$$

$$\Delta T(0,t)_{t>t_p} = \frac{H}{k}\left[\left(\frac{4\alpha t}{\pi}\right)^{1/2} - \left(\frac{4\alpha(t-t_p)}{\pi}\right)^{1/2}\right]. \tag{1.13}$$

In the preceding discussion, it was considered that the incident laser power density was sufficient to heat the material without any melting or evaporation. However, the surface temperature may reach the melting point or the boiling point at sufficiently higher laser power densities ($I_0 > 10^5$ W/cm^2). The corresponding laser power densities are often referred as melting and boiling thresholds. The depth of melting can not increase to infinitely large value with increasing laser power density and residence time (irradiation time) because the location of melting point inside the sample is limited by the maximum achievable surface temperature. Once the surface temperature reaches the boiling point, the depth of melting reaches the maximum value z_{MAX}. Further increase in the laser power density or the pulse time causes the evaporative material removal from the surface without further increase in the depth of melting.

When the temperature reaches melting point (T_m) at some depth z_{MAX}, the equation (1.9) becomes:

$$T_m = \frac{H}{k}(4\alpha t)^{1/2}\,\mathrm{ierfc}\left(\frac{z_{MAX}}{(4\alpha t)^{1/2}}\right). \tag{1.14}$$

When the surface temperature reaches boiling point (T_b), the equation (1.12) becomes:

$$T_b = \frac{H}{k}\left(\frac{4\alpha t}{\pi}\right)^{1/2}. \tag{1.15}$$

Taking the ratio of above equations:

$$\frac{T_m}{T_b} = \sqrt{\pi}\; ierfc\left(\frac{z_{MAX}}{(4\alpha t)^{1/2}}\right). \tag{1.16}$$

From equation (1.15), we get:

$$(\alpha t)^{1/2} = \frac{T_b k\sqrt{\pi}}{2H}. \tag{1.17}$$

Substituting in equation (1.16):

$$\text{ierfc}\left(\frac{Hz_{MAX}}{kT_b\sqrt{\pi}}\right) = \frac{T_m}{T_b\sqrt{\pi}}. \tag{1.18}$$

Such equations facilitate the calculation of maximum depth of melting (z_{MAX}) at which the surface reaches boiling point during laser irradiation.

Once the vaporization is initiated at the surface of the material, the continued laser irradiation will cause the liquid-vapor interface to move inside the material. This is accompanied with the evaporative removal of material from the surface above the liquid-vapor interface. If V_s is the velocity of the liquid-vapor interface into the material during the laser irradiation, then the mass of material removed per unit area per unit time ($\dot{m}$) and the depth of vaporization (d) will be $V_s\rho$ (where ρ is the density) and $V_s t_p$ respectively. The velocity of the liquid-vapor interface and the depth of vaporization can be calculated by simple energy balance [9]:

$$V_s = \frac{H}{\rho(cT_b + L_v)}, \tag{1.19}$$

where c is specific heat capacity and L_v is the latent heat of vaporization.

Solving,

$$d = \frac{Ht_p}{\rho(cT_b + L_v)}. \tag{1.20}$$

The thermal model explained in the preceding section considers the irradiation of material where both the laser beam and the material are stationary. Most of the practical

laser applications such as welding, cutting, shaping etc. require the laser beam to move relative to the workpiece. Hence calculation of temperature distributions around moving source of heat (laser) becomes important. The theory of moving sources of heat was first advanced by Rosenthal in 1946 [14]. The schematic of the model geometry for heating with moving point source is presented in Fig. 1.4.

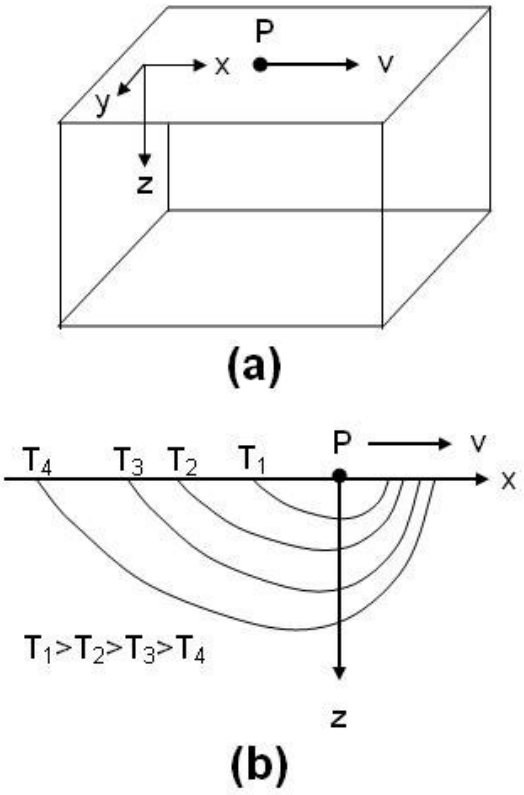


Fig. 1.4 Schematic of the (a) heating model geometry with a moving point source of heat, and (b) typical temperature distribution (isotherms) in the x-z plane through the point source.

For a point heating source moving with constant velocity, v, in the x-direction, the three-dimensional heat transfer equation can be written with point source as origin as [14]:

$$-v\frac{\partial T(\xi,y,z,t)}{\partial \xi}+\frac{\partial T(\xi,y,z,t)}{\partial t}=\alpha\left[\frac{\partial^2 T(\xi,y,z,t)}{\partial \xi^2}+\frac{\partial^2 T(\xi,y,z,t)}{\partial y^2}+\frac{\partial^2 T(\xi,y,z,t)}{\partial z^2}\right] \tag{1.21}$$

where ξ is the distance of a considered point from the point source. This distance can be expressed as:

$$\xi = x - vt\,. \tag{1.22}$$

For a solid much longer than the extent of heat dissipation, the temperature distribution around the point heat source becomes constant such that an observer located at the moving point source fails to notice the temperature changes around the point source as it moves on. This type of heat flow is generally referred as quasi-stationary heat flow. This state of heat flow is defined as:

$$\frac{\partial T(\xi,y,z,t)}{\partial t}=0 \tag{1.23}$$

Substituting in equation (1.21) yields:

$$-v\frac{\partial T(\xi,y,z,t)}{\partial \xi}=\alpha\left[\frac{\partial^2 T(\xi,y,z,t)}{\partial \xi^2}+\frac{\partial^2 T(\xi,y,z,t)}{\partial y^2}+\frac{\partial^2 T(\xi,y,z,t)}{\partial z^2}\right]. \tag{1.24}$$

The equation (1.24) can be further simplified by using

$$T = T_0 + e^{-\lambda v \xi}\varphi(\xi,y,z)\,, \tag{1.25}$$

where T_0 is the initial temperature and φ is the function which needs to be determined to calculate the temperature distributions.

The equation (1.24) becomes:

$$-\left(\frac{v}{2\alpha}\right)^2 \varphi(\xi, y, z) = \left[\frac{\partial^2 \varphi(\xi, y, z)}{\partial \xi^2} + \frac{\partial^2 \varphi(\xi, y, z)}{\partial y^2} + \frac{\partial^2 \varphi(\xi, y, z)}{\partial z^2}\right]. \tag{1.26}$$

For linear flow of heat where $\frac{\partial^2 \varphi(\xi, y, z)}{\partial y^2} = \frac{\partial^2 \varphi(\xi, y, z)}{\partial z^2} = 0$, the equation (1.26) reduces to:

$$-\left(\frac{v}{2\alpha}\right)^2 \varphi(\xi, y, z) = \frac{d^2 \varphi(\xi, y, z)}{\partial \xi^2}. \tag{1.27}$$

These equations can be solved with appropriate boundary conditions to obtain the temperature profiles around the moving point source of heat [14]. An important consideration for accurate determination of temperature distribution during laser irradiation is the temperature dependence of the thermo-physical and other properties. Properties such as thermal conductivity, thermal diffusivity, absorptivity, etc. are strongly temperature dependent and expected to influence the temporal and spatial evolution of temperature during laser irradiation.

The two important parameters in the analysis of thermal effects during laser-material interactions are the cooling rate and the temperature gradient. These factors have strong influence on the development of microstructure (such as those formed by dendritic, cellular, or planar growth) during solidification of molten material. From the above thermal analysis, the temperature gradient, *G*, and the cooling rate, $\dot{T}$, can be calculated as:

$$G(z,t) = \frac{\partial T}{\partial z}, \tag{1.28}$$

$$\dot{T}(z,t) = \frac{\partial T}{\partial t}. \tag{1.29}$$

An important relationship in the solidification theory which relates these parameters is [15]:

$$\dot{T} = GR, \tag{1.30}$$

where R is the solidification rate.

1.2.2 Vapor Expansion and Recoil Pressures

As explained in the previous section, surface vaporization is initiated when the laser intensity becomes sufficiently high ($I_0 > 10^5$-10^8 W/cm^2). The vapor plume consists of clusters, molecules, atoms, ions, and electrons. In the steady-state evaporation, the vapor particles escape from the surface (solid or liquid) at temperature T_s. Initially, the vapor particles escaping from the surface have a Maxwellian velocity distribution corresponding to the surface temperature, T_s with their velocity vectors all pointing away from the surface. Due to collisions among the vapor particles, the velocity distribution in the vicinity of the vaporizing surface (layer of the order of several mean free paths) approaches equilibrium. This region is known as Knudsen layer and often treated as discontinuity in the hydrodynamic treatment. The detailed analysis of evaporation problem was conducted by Anisimov in 1968 to determine the structure of this region and the values of hydrodynamic variables beyond the discontinuity [16]. It was assumed that the laser power density is not excessively large so that there is no significant absorption of laser light by the vapor. Further, Anisimov assumed that the distribution function

within discontinuity region can be approximated by the sum of distribution functions before and after the discontinuity with coordinate-dependent coefficients [16, 17]:

$$f(x,\mathbf{v}) = \alpha(x) f_1(\mathbf{v}) + [1-\alpha(x)] f_2(\mathbf{v}), \tag{1.31}$$

where

$$f_1 = n_0 \left(\frac{m}{2\pi k_B T_s} \right)^{3/2} \exp\left(-\frac{m v^2}{2 k_B T_s} \right), \qquad v_x > 0 \tag{1.32}$$

$$f_2 = \beta\, n_1 \left(\frac{m}{2\pi k_B T_1} \right)^{3/2} \exp\left(-\frac{m\left({v_y}^2 + {v_z}^2 + (v_x - u_1)^2 \right)}{2 k_B T_1} \right). \qquad v_x < 0 \tag{1.33}$$

Here, $\alpha(x)$ is a unknown function satisfying $\alpha(0) = 1$ and $\alpha(\infty) = 0$; k_B is the Boltzmann constant; m is the mass of the vapor molecule; T_s and n_0 are the surface temperature and the molecule number density at the evaporating surface respectively; and T_1 and n_1 are temperature and the molecule number density at the outer boundary of the kinetic layer formed near evaporating surface respectively. u_1 is the velocity at the outer boundary of the kinetic layer; β is the coefficient; and v_x, v_y, and v_z are the velocity components on the evaporating surface of the material. Assuming that u_1 is equal to the velocity of sound within the vapor (Jouguet condition), we get:

$$u_1 = \sqrt{\frac{\gamma k_B T_1}{m}}, \tag{1.34}$$

where γ is the adiabatic index of the vapor.

The conservation laws of mass, energy, momentum hold within the discontinuity region. Thus,

$$\int d\mathbf{v} v_x f(x,\mathbf{v}) = C_1$$

$$\int d\mathbf{v} v_x{}^2 f(x,\mathbf{v}) = C_2$$

$$\int d\mathbf{v} v_x v^2 f(x,\mathbf{v}) = C_3 . \qquad (1.35)$$

Solving the above equations for the monoatomic gas with γ = 5/3, Anisimov obtained:

$$\beta = 6.29 ,$$

$$T_1 = 0.67 T_s ,$$

$$n_1 = 0.31 n_0 . \qquad (1.36)$$

Thus the vapor is significantly cooler and less dense than the vapor in equilibrium with the surface. Further analysis by Anisimov indicated that approximately 18% of the vapor particles condensed back to the surface. The velocity of the vaporization front is given by:

$$V = \frac{I_a}{\rho\left(L_v + 2.2 k_B T_s / m\right)}, \qquad (1.37)$$

where I_a is the absorbed laser power density and L_v is the latent heat of vaporization. The above derivation on the expansion of vapor in the vacuum can also be extended for the case of vapor expansion into ambient gaseous atmosphere by considering the Mach number of the external flow. All the quantities T_1, and n_1 are dependent on the Mach number of the external flow [16].

The evolving vapor from the surface exerts the recoil pressure on the surface. Based on the above relationships, an equation for calculation of evaporation-induced recoil pressure, p_s, at the evaporating surface is given by [16]:

$$\frac{p_s}{Q_0 / S} = \frac{1.69}{\sqrt{L_v}}\left(\frac{b}{1+2.2b^2}\right), \tag{1.38}$$

where Q_0 is the incident laser power; S is the area of laser spot; and $b^2 = k_B T_s / m_v L_v$. For the surface temperatures equal to boiling point, the evaporation induced recoil pressure according to Anisimov becomes 0.55 p_s, where p_s is the saturated vapor pressure. Under typical materials processing (drilling, cutting, welding, etc.) conditions, this evaporation induced recoil pressure exceeds the highest possible value of surface tension pressure. Thus evaporation-induced recoil pressure plays an important role in the removal of material in molten state during materials processing.

1.2.3 Plasma Formation

When the material is irradiated with sufficiently larger laser intensity (I_v), significant surface evaporation takes place as explained in the previous sections. Once the vaporization is initiated, the interactions between the resulting vapor and the incident laser beam become important in determining the overall effect of the laser irradiation on the material. One of the most important interactions is the ionization of the vapor. The highly ionized vapor is termed as plasma. In dynamic equilibrium, the degree of ionization ξ, in a gas is often expressed by the Saha equation [18]:

$$\frac{\xi^2}{1-\xi} = \frac{2g_i}{g_a N_g}\left(\frac{2\pi m\ k_B T}{h^2}\right)^{3/2} \exp\left(-\frac{E_i}{k_B T}\right), \tag{1.39}$$

with $\xi = N_e/N_g$ and $N_g = N_e + N_a$. Here, N_e and N_a are the number densities of electrons and atoms/molecules respectively; g_i and g_a are the degeneracy of states for ions and atoms/molecules; and E_i is the ionization energy.

The generation of plasma can greatly influence (or interfere with) the interaction of laser radiation with the material. It is convenient to define the laser power density I_p, at which the significant ionization of the vapor resulting in the formation of plasma takes place. The plasma is generally considered to form near the evaporating surface of the target and remain confined to this region during laser irradiation with intensities just above I_p. This confinement of the stationary plasma near the evaporating surface is generally referred to as plasma coupling. Plasma coupling plays an important role in transferring the energy to the dense phase. The energy transfer may be due to normal electron heat conduction, short-wavelength thermal plasma radiation or condensation of vapor back to the surface [19]. The plasma coupling is particularly important in the conditions where normal laser irradiation is not strongly absorbed by the target material. Such conditions exist during irradiation of highly reflecting materials with infrared (longer wavelength) laser radiation. Plasma coupling results in the significant increase in the absorptivity of laser radiation by the material. When the laser power density is increased significantly beyond I_p, the dynamic interaction of the plasma with the laser radiation causes the rapid expansion and propagation of the plasma away from the evaporating surface (i.e. towards the laser beam). Eventually the plasma gets decoupled from the surface and transfer of energy to the dense phase ceases. The laser radiation is

then essentially absorbed in the plasma. This condition is referred as plasma shielding where the decoupling of the plasma ceases the interaction of the laser radiation with the target material via plasma. The propagating plasma is often referred to as laser supported absorption wave (LSAW). The LSAW's are generally classified into laser supported combustion waves (LSCW) and laser supported detonation waves (LSDW) depending on the speed at which they propagate with respect to gas. The LSAW propagating at the subsonic speed is termed as LSCW, while, it is termed as LSDW when propagating at supersonic speed [18].

1.2.4 Ablation

The term ablation is generally used for the material removal processes by photo-thermal or photo-chemical interactions. In photo-thermal process, the absorbed laser energy gets converted into thermal energy in the material. The subsequent temperature rise at the surface may facilitate the material removal due to generation of thermal stresses. This is more pronounced in the inhomogeneous targets such as coated materials where the thermal stresses cause the explosive ablation of thin films. When the incident laser energy is sufficiently large, the temperature at the surface exceeds the boiling point causing rapid vaporization. These processes of material removal by thermal stresses and surface vaporization are generally referred as thermal ablation [18]. In photoablation, the energy of the incident photon causes the direct bond breaking of the molecular chains in the organic materials resulting in material removal by molecular fragmentation without significant thermal damage. This suggests that for the ablation process, the photon energy must be greater than the bond energy. The ultraviolet radiation with wavelengths in the

range of 193-355 nm corresponds to the photon energies in the range of 6.4-3.5 eV. This range of photon energies exceeds the dissociation energies (3.0-6.4 eV) of many molecular bonds (C-N, C-O, C=C etc) resulting in efficient ablation with UV radiation [20]. However, it has been observed that ablation also takes place when the photon energy is less than dissociation of energy of molecular bond. This is the case for far ultraviolet radiation with longer wavelengths (and hence correspondingly smaller photon energies). Such an observation is due to multi-photon mechanism for laser absorption. In multi-photon mechanism, even though the energy associated with each photon is less than dissociation energy of bond, the bond breaking is achieved by simultaneous absorption of two or more photons.

The laser-material interaction during ablation is complex and involves interplay between the photo-thermal (vibrational heating) and photo-chemical (bond breaking) processes. One of the important considerations during the laser-material interaction studies is the thermal relaxation time (τ). Thermal relaxation time is related with the dissipation of heat during laser pulse irradiation and is expressed as [21]:

$$\tau = \frac{d^2}{4\alpha}, \tag{1.40}$$

where d is absorption depth and α is the thermal diffusivity. For longer pulses (with pulse time longer than thermal relaxation time), the absorbed energy will be dissipated in the surrounding material by thermal processes. To facilitate the photo-ablation of material with minimum thermal damage, the pulse time must shorter than thermal relaxation times. For such short pulses (pulse times in the range of microseconds), the laser energy is confined to a very thin depth with minimum thermal dissipation. Thus, efficient

ablation of the material during laser-material interactions necessitate the laser operating at shorter wavelengths with microsecond pulses. Pulsed laser ablation is extensively used in the materials processing and the medical applications. In materials processing, it can be used for micromachining, marking, grooving, cutting, drilling, and patterning of wide range of materials; while, in medical applications, it can be used for precision ablation of tissues such as human corneal tissues.

1.3 Microstructure Evolution

Laser surface processing presents convenient means of microstructure modification for material surfaces. Such microstructural modifications at the surfaces are expected to provide ways to control and achieve desired surface properties for wide range of applications. The evolution of surface microstructure and morphology depends on the regime of laser-material interactions. Extensive investigations have been done to understand the development of microstructure and topography during material heating [22-24], material melting [25-27] and material removal (evaporation/ablation) regimes [28-30]. In the heating regime (laser heat treatment), the microstructure evolution is primary due to solid-state phase transformations. In the melting regime, the laser melted material rapidly solidifies resulting in the formation of recast layer. The microstructures at the surface and within the recast laser are primarily influenced by the nature of material and thermal effects during laser processing. Ablation regime is particularly associated with microstructuring due to localized material removal resulting in the formation of physical surface features.

One of the important fundamental studies on phase and microstructure evolution during rapid solidification of ceramics is conducted by Levi et al [31]. They used electrohydrodynamic atomization technique to produce micro-droplets of alumina ceramic which subsequently solidified into collection chamber. Detailed investigation of phase selection and microstructure evolution in the rapidly cooled alumina droplets of 10 nm to 300 μm diameter have shown that amorphous phase forms in droplets below 100 nm, γ phase forms between 100 nm and 2 μm, partially transformed δ forms between 2 μm and 10 μm, and stable corundum structure forms above 20 μm. Also, the surface of the coarse droplets exhibited three distinct morphologies: faceted, dendritic, and cellular. The formation of metastable γ phase is also observed during rapid solidification of alumina particles in plasma spraying [31].

In spite of the wide applicability of the laser surface processing for alumina ceramics, the detailed studies on evolution of phase and morphology during laser surface processing are limited. Also, the rapid solidification of ceramics during laser surface melting is far from the containerless solidification in that the melt undercooling is very small because the substrate acts as a catalytic site that can lower the nucleation barrier. Hence, major part of the present study is directed towards understanding microstructure evolution during rapid solidification associated with laser surface processing of alumina ceramic compacts. The microstructure evolution is studied in terms of the development of crystallographic texture and morphology of the surface grains. The microstructural results are correlated with the cooling rates derived from heat flow model.

1.4 Laser Surface Structuring Applications

Laser surface structuring of ceramics presents the potential of modifying/improving the surface properties for broad applications in structural, engineering, electronics and biomedical industries. Some of these specific potential applications are briefly explained here.

1.4.1 Laser Dressing of Alumina Grinding Wheels

Alumina ceramic is an important conventional abrasive material used in machining (grinding) applications. Abrasive grinding wheels consist of irregular alumina particles (grains) compacted and bonded together with bonding ingredients (typically vitrified glassy compositions) and contain a certain level of controlled porosity. Each particle on the surface of the grinding wheel acts as a cutting tool and contributes to the total material removed during machining. Among various wheel and workpiece parameters, the performance of grinding wheels is highly influenced by the particle (grain) size and the sharpness of the abrasive grains. However, the properties of these surface grains progressively deteriorate as the number of grinding passes increases. During grinding, due to sliding forces, the surface grains becomes blunt and lose their ability to efficiently remove the material from the workpiece (Figure 1.5a). The most common practice in industry is called diamond dressing (mechanical dressing) which uses a single point diamond tool to fracture and remove the blunt surface grains and expose new sharp grains thus re-generating the new surface for efficient grinding (Figure 1.5b). However, the process has many quality and economic disadvantages such as increase in consumable

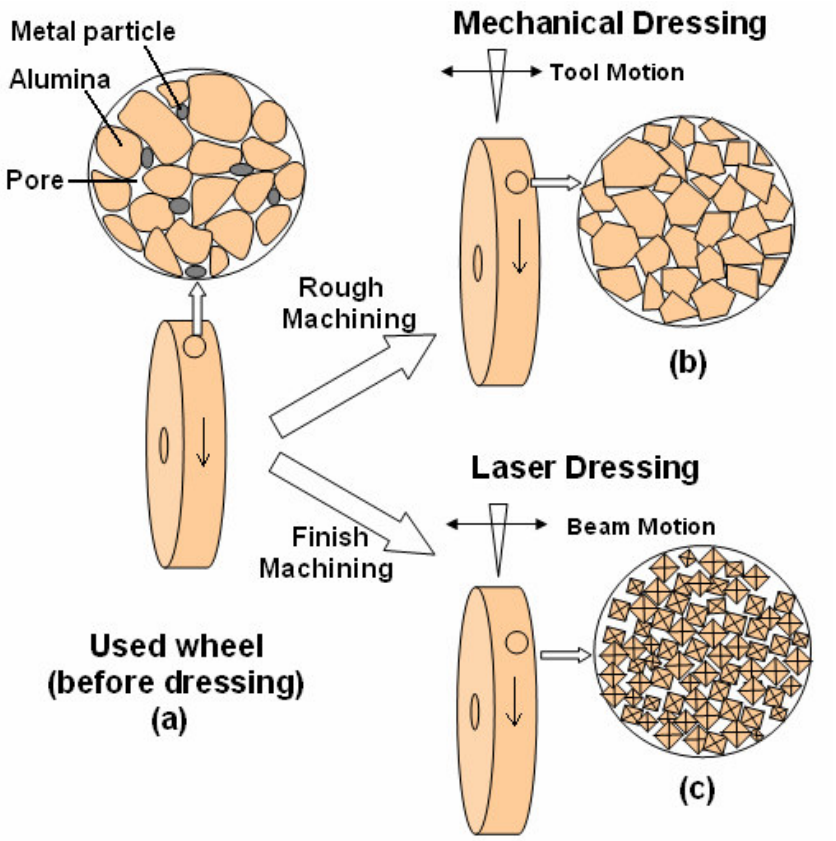


Fig. 1.5 Schematic of the dressing set up and surface morphology generated during two different approaches of wheel dressing. (a) Used grinding wheel surface before dressing showing blunt surface grains with the metal particles loaded in the interconnected porosity; (b) surface features of diamond dressed grinding wheel showing newly exposed irregular, sharp grains obtained by fracturing the surface layer of blunt grains and (c) surface features of laser dressed grinding wheel obtained by rapid solidification of alumina grinding wheel surface showing highly refined multi-faceted grains with well defined edges and vertices.

cost due to wear of diamond tool and wheel and decrease of production rate due to frequent dressing. It has been reported that up to 90% of the wheel material is consumed in dressing operation compared to the actual grinding of the workpiece [32]. Also, the diamond dressing imparts various surface and sub-surface defects such as cracks which may lead to premature fracture of the grinding wheel during machining operation.

Attempts have been made to use lasers as dressing tools for grinding wheels due to inherent advantages of the laser processing such as non-contact dressing and ease of automation. The primary motivation for such studies came from the ability of lasers to selectively ablate the low melting point bonding ingredients and/or blunt surface alumina grains of the grinding wheels so as to expose the new sharper grains on the surface of wheel for cutting action. Hence, to carry such an ablation of material, the laser dressing at high laser intensities such as 4×10^{10} W/m^2 was suggested [33, 34]. In one of the other studies, lasers are used in combination with the conventional diamond dressing [35]. Here, a laser selectively heats the grinding wheel surface, which is subsequently dressed by the diamond tool. The primary purpose in such studies is to reduce the wear of the diamond dressing tools by preheating the wheel surface by laser ahead of the diamond tool. Most of these approaches have had limited successes in realizing the full potential of non-contact laser dressing such as in-process dressing, improved productivity, low cost of production and consistency in workpiece finish.

Recently, considerable efforts have been made by our research group to develop the laser dressing method for alumina grinding wheels [36-28]. A novel approach is proposed for laser dressing technique using laser intensities lower than that is required for ablation of grinding wheel surface ingredients. The approach is based on the surface

melting and solidification rather than direct ablation of material. A laser beam is directed normal to the grinding surface of wheel with laser intensities high enough to cause melting of the blunt grains on the grinding wheel surface. Also, under these regimes of laser intensities the low melting point bonding ingredients evaporates thus facilitating the melting and solidification of high melting point alumina (melting point~2300 K). The rapid solidification associated with laser melting of alumina results in a wheel surface morphology characterized by multifaceted grains with micropores between the faceted grains. Each multifaceted grain exhibit well defined edges and vertex which can act a single micro-cutting tool on the grinding wheel surface (Figure 1.5c). Additionally, since these surface features are on the micron scale, such a laser dressed grinding wheel with these surface microstructural features is well suited for the microscale grinding application. The solidification microstructures on a surface of grinding wheel can be efficiently controlled by changing the laser dressing parameters making the lasers reliable and efficient dressing tools for grinding wheels for precision machining applications.

1.4.2 Tribological Applications

For many tribological applications, it is critically important to maintain the lubricant film between sliding components that are subjected to high load. Friction behavior and wear resistance of the sliding components is greatly influenced by topography of the surfaces. Laser structuring of the sliding surfaces is attracting significant interests for improving tribological properties of variety of materials such as metals, ceramics and glass [39]. Lasers can produce selective and periodic topographic feature on the flat surfaces by localized ablation or evaporation mechanism. Such microstructures acts as reservoirs for

the lubricating fluid and hampers the drain of it. These reservoirs also collect the abrasive particles during sliding. Some of the possible structures (channels, pits, etc.) produced by laser surface structuring of 100Cr6 and alumina are presented in Fig. 1.6. The depth of channels can be controlled by controlling the laser processing parameters. It has been observed that laser structuring results in the significant reduction of friction coefficient primarily due to creation of lubricant reservoirs on the sliding surfaces.

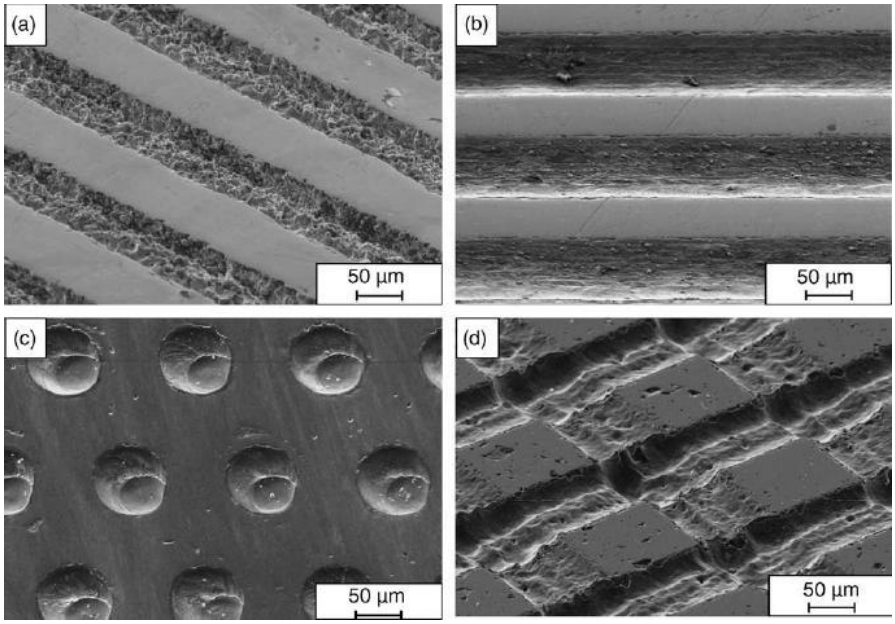


Fig. 1.6 Micrographs of laser structured surfaces: (a) micro-channels in 100Cr6 generated using Q-switch laser mode, (b) micro-channels in 100Cr6 generated using continuous wave laser mode, (c) micro-pits in 100Cr6, and (d) crossed micro-channels in alumina [39].

1.4.3 Biomedical Applications

The surfaces of biomedical implants are often coated with bioceramics like zirconia. Zirconia offers good fracture toughness and bending strength in addition to the excellent biocompatibility. However, actual utilization of such coated implants is still not realized primarily due to lack of understanding about the complexity of interactions taking place at the implant surfaces in the biological environment. It is, however, realized that surfaces of artificial implants should have hierarchical structure similar to natural bone material. Laser surface structuring of biomaterials is attracting significant interests to generate hierarchical textured bioactive material. Fig. 1.7 presents micrographs of laser textured zirconia coated titanium-based substrates showing multi-scale nature of the surface [40].

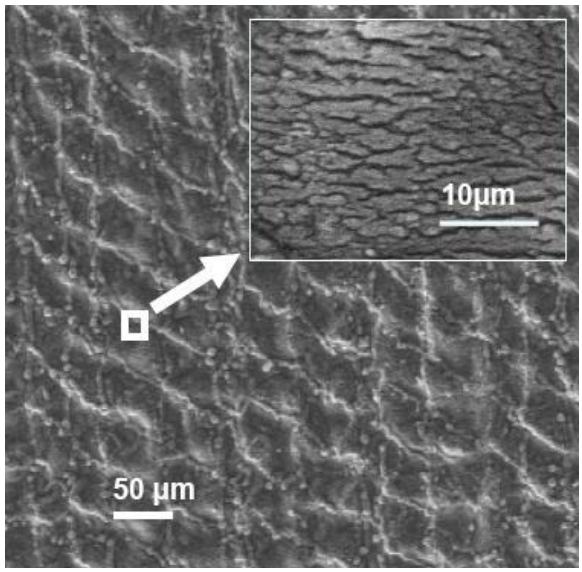


Fig. 1.7 Multi-scale nature of laser textured zirconia coated titanium-based substrates [40].

1.4.4 Surface Densification

Refractories are extensively used in crucibles and linings of furnaces and incinerators. The important properties of refractories for high temperature applications include excellent thermal shock resistance, chemical inertness and structural stability. Refractories also exhibit low thermal conductivity and coefficient of expansion. However, life of the refractories is often limited by ingression of molten slag and consequent accelerated chemical degradation. Laser surface processing can be effectively used for crack-free sealing the surface porosity of the ceramic refractories causing reduction in the penetration of molten slag and chemical degradation. This crack-free densification of the refractories is based on the surface melting of the ceramics and subsequent sealing of the pores by the molten material (Fig. 1.8) [41].

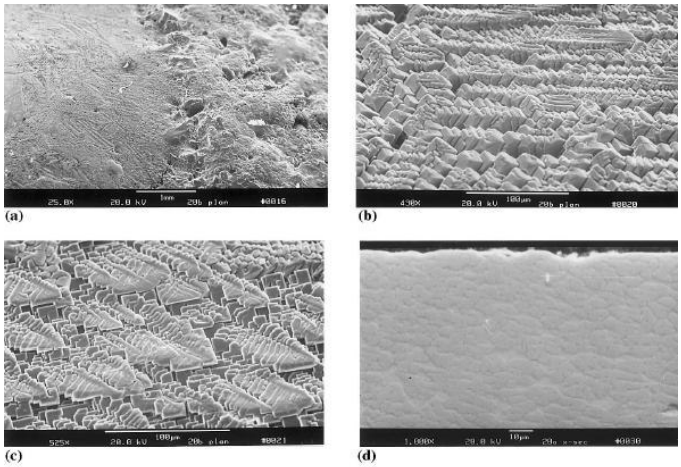


Fig. 1.8 Micrographs of 85 % alumina samples surface densified by the CO_2 laser and the flame: (a) plan view showing boundary between treated and untreated region, (b), (c) high magnification views of a region on a laser track, and (d) cross-section of laser surface densified region [41].

Chapter 2

Experimental Procedure

2.1 Selection of Materials

Rapid solidification of metallic material is extensively reported in the literature. However, there are very limited studies devoted to the rapid solidification of ceramics. This may be partly due to assumption that low thermal conductivity of these materials makes the rapid solidification less feasible. On the other hand, higher structural complexity of the ceramics is expected to result in sluggish kinetics thus enhancing undercoolability. Hence this study is primarily directed towards understanding the rapid solidification behavior of industrially important alumina ceramics subjected to laser surface processing.

Alumina-based ceramic compacts (5 cm × 5 cm × 2.5 cm) used for the laser surface modification experiments were cut from commercially available vitrified grinding wheels (purchased from MSC Industrial Supply Co.) using a carbide grit rod saw (Make: STANLEY^{TM}) in dry condition. The grinding wheels are commercially made from artificial aluminum oxide produced by melting bauxite at high temperature in an arc type electric furnace [42]. The compacts consisted of irregular abrasive grains of average size around 220 μm with average porosity of around 40% by volume. The abrasive grains were primarily composed of Al_2O_3 (~99.52 wt%) with traces of Cr_2O_3 (~0.25 wt%), Fe_2O_3 (0.05 wt%), and Na_2O (0.18 wt%).

2.2 Optimization of Laser Processing Parameters

A 4 kW HASS continuous wave Nd:YAG laser was used for the laser-assisted rapid surface microstructuring of alumina ceramic. The laser processing was carried out with laser fluence in the increment of around 38 J/cm^2 above 458 J/cm^2 up to 726 J/cm^2. This range of laser processing parameters corresponds to significant melting of the ceramic surface. The schematic of the processing set-up is presented in Fig. 2.1. The laser beam was fiber optically delivered and focused on the flat surface of the ceramic sample which was mounted on the translation stage allowing the movements along X-, Y-, and Z-axes. Entire surface of the alumina ceramic was modified by laying the parallel tracks with linear translational speed of 100 cm/min. The movements of the translation stage can be directly controlled through CNC programs such that different 2D geometric data can be used for microstructuring of surface.

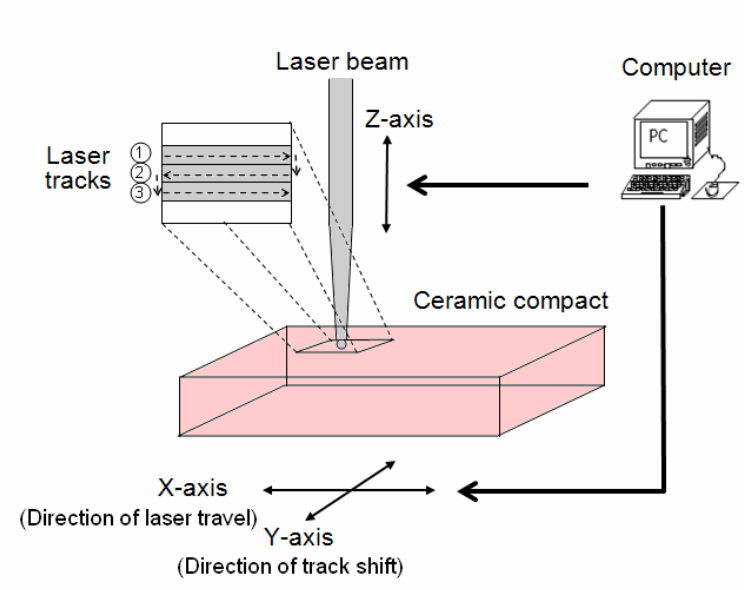


Fig. 2.1 Experimental set-up for laser surface structuring of alumina ceramic

2.3 Modified Surface Characterization

For characterization, the specimens were prepared by cutting small coupons (1.5 cm × 1.5 cm × 1.0 cm) from laser surface modified specimens with a ISOMET^{TM} low speed saw (Make: BUEHLER^{TM}) using a diamond blade (Make: BUEHLER^{TM}) in dry condition. The surfaces before and after laser surface modifications were preserved during specimen cutting to ensure that microstructure, surface condition, roughness is unaffected by the sample preparation methods. The dry condition during cutting is used to prevent the impregnation of cutting media into porous alumina samples and eliminate the possibility of undesirable affects during subsequent microstructural characterization. Additional surface preparation is carried out relevant to each characterization technique.

2.3.1 Microstructural Attributes (Scanning Electron Microscopy)

The characterization of surface morphology of alumina grains before and after laser surface modifications is conducted using a HITACHI^{TM} S3500 SEM. The SEM was operated in high vacuum mode at an accelerating voltage of 15 kV and filament current of 78 μA. Also, qualitative elemental analysis was conducted using Energy Dispersive Spectrometer (EDS) system attached to SEM. Due to low conductivity of alumina ceramic, sample preparation for SEM included an additional step of coating the specimen with gold to minimize build up of electric charge. The gold coatings on samples of alumina ceramic were deposited using SPI MODULE^{TM} sputter coater operated at pressure of 10^{-1} Torr and sputtering current of 20 mA for deposition time of 20 s. The grain size of the surface grains is given as the average diagonal distance of the polygonal

grain. The surface grain size and the porosity were determined by the image analysis of several (more than five) SEM micrographs and the average value along with the positive and negative error bars is reported.

2.3.2 Phase and Micro Texture Evolution (X-ray Diffraction and Orientation Imaging Microscopy)

Detailed characterization of the phase and micro-texture before and after laser surface modifications of alumina ceramic compacts was conducted using x-ray diffraction technique. The preliminary X-ray diffraction analysis of the laser surface modified alumina coupons was carried out using Philips Norelco x-ray diffractometer operating with Cu K_α (λ=1.54178 Å) radiation at 20 kV and 10 mA. The diffraction angle was varied between 20 and 100 degree 2-theta at a step increment of 0.02 degree 2-theta with a count time of 1 s. The surfaces of alumina ceramic before and after laser surface modification (without any pulverizing into powder) were directly examined by x-ray diffraction to facilitate the study of development of preferred orientation.

For detailed texture analysis, Philips X'Pert Analytical Diffractometer with Cu K_α radiation as a point source operating at 45 kV and 40 mA was used. Reflection method was used to obtain the pole figures by varying rotation angle, φ, between 0 and 360 degrees and varying tilt angle, ψ, between 0 and 85 degrees. Schematic of the typical diffraction geometry along with various rotation and tilt axes for texture analysis is presented in Fig. 2.2 [43, 44]. For texture measurement, each coupon of un-modified and laser surface modified alumina ceramic was mounted directly on the specimen holder using adhesive binder such that surface of the sample is as flat as possible. During texture

analysis, the counter is fixed in the 2-theta position corresponding to the planes which are expected to exhibit the preferred orientation. In the present study, texture analysis is conducted for determining preferred orientation of various planes corresponding to respective diffraction angles (2-theta). Once the counter is fixed at diffraction angle (2-theta), the sample holder is slowly rotated about the diffraction axis such that surface of the sample is equally inclined to the incident and diffracted beam directions. This corresponds to initial position of the sample. The sample is then slowly rotated about the rotation and tilt axes to obtain a series of φ-scans at different tilt angles. The step size for the rotation and tilt axes was 5 degree and the time per step was 1 s. The diffraction data obtained from these experiments was used to generate the pole figures presented as contour plots with zero angle at the center using the method described in reference [43].

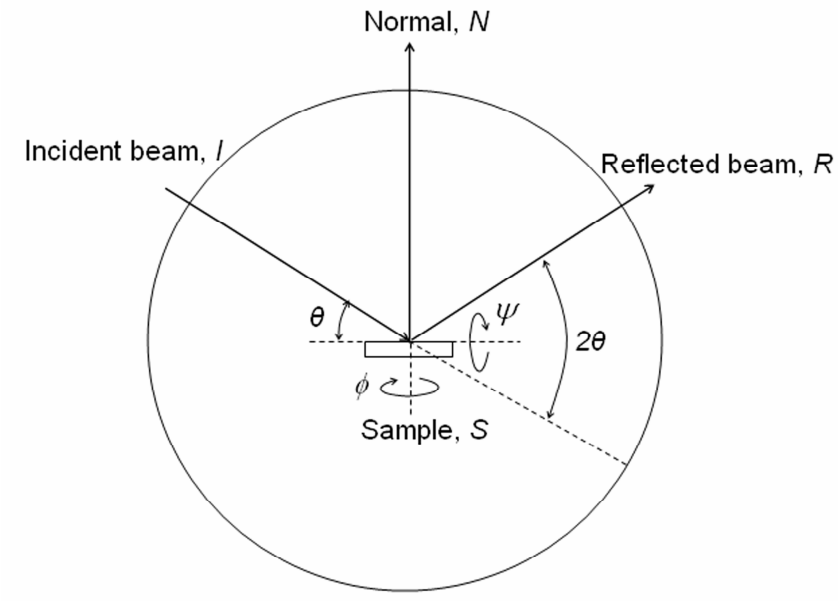


Fig. 2.2 Schematic of the diffractometer geometry for texture analysis.

The pole figure analysis explained in the previous section provides useful information about the overall texture evolution as function of laser processing parameters in the laser surface modified alumina ceramic. In order to evaluate the micro-texture evolution during directional rapid solidification of alumina ceramic during laser processing, localized crystallographic information is needed. Orientation Imaging Microscopy (OIM) gives local crystallographic information using Kikuchi patterns. This information can be used to obtain crystallographic orientation maps from the larger area of the sample thus giving more global information regarding micro-texture at the surface.

For successful characterization of micro-texture in laser surface modified alumina using OIM, the sample preparation is critically important. The surfaces for the OIM analysis must be flat in the nanometer levels to generate good quality Kikuchi patterns. In the present studies, sample surfaces were wet polished using a series of SiC grinding papers (600, 800, 1200 mesh) followed by polishing on micro-cloth with colloidal silica slurry (0.05 micron abrasive size). Since, alumina is non-conductive, the samples were carbon coated to uniform thickness of 3 nm and grounded with copper tape to the sample stage in the SEM. Kikuchi patterns and subsequent orientation maps were generated using a commercial Philips XL30 FEG SEM equipped with a TSL orientation imaging microscopy system using a special CCD camera. During OIM experiment, SEM was operated at 20 kV accelerating voltage and the sample was tilted to about 70° from the horizontal. Kikuchi pattern quality is strongly influenced by tilt angle, accelerating voltage and sample surface quality. OIM patterns are produced by a very small fraction of total scattered electrons signal. OIM procedure involves obtaining background image

which is subsequently subtracted from each acquired pattern prior to indexing. To obtain the crystallographic orientation information from a larger surface area of the sample, the electron beam is scanned over a selected area of laser modified surface with a step size of 3.75 μm. The quality and sharpness of the individual Kikuchi pattern is judged by Confidence Index (CI). Since the initial x-ray analysis suggested the formation of equilibrium α-alumina phase, indexing of the kikuchi patterns is carried out using hexagonal crystal structure.

2.3.3 Surface Morphology (Stylus Profilometry and Atomic Force Microscopy)

Surface morphology of the laser modified alumina ceramic was characterized using stylus profilometry and Atomic Force Microscopy (AFM) to get the microscopic behavior of the

A stylus-based Mahr Federal Perthometer M1 with stylus tip radius of 2 μm was used for the measurement of surface roughness parameter, R_a (arithmetic mean deviation of the roughness profile). The measurement was conducted for a tracing length of 1.75 mm on the surface of five laser surface modified specimens and the average value along with positive and negative error bars is reported. During the measurements, the sample was firmly mounted on the horizontal stage with adhesive binder to prevent the movement of specimen during traversing of stylus tip. Autoprobe M5 (Park Scientific Instruments, Sunnyvale, CA) Atomic Force Microscope (AFM) was used in contact mode to determine the topography of surface micro-features of the laser structured alumina. The maximum lateral and vertical resolutions of the instrument were 0.5 and

0.025 Å respectively. AFM measurements were conducted to profile the individual faceted polygonal grains within modified surface region.

2.3.4 Fracture Behavior (Micro-indentation)

To evaluate the influence of laser surface modification on the fracture properties of alumina ceramic, micro-indentation experiments were conducted. A microhardness tester (BUEHLER™, Lake Bluff, IL) was used for measuring hardness by performing indentations at a load of 19.6 N and holding time of 15 s. Fracture toughness (K_{IC}) was obtained using direct crack measurement method. The fracture toughness, K_{IC} (MPa.m$^{1/2}$), is given by:

$$K_{IC} = 0.016\left(\frac{E}{H}\right)^{1/2}\frac{P}{c^{3/2}}, \qquad (2.1)$$

where E is the Young's Modulus (380 GPa), H is the Vickers hardness (GPa), P is the applied load (N), and c is the diagonal crack length (m) [45]. The fracture toughness was obtained for five indentations on each sample and the average value is reported along with positive and negative error bars.

Chapter 3

Laser Process Parameter Dependent Transitions in Rapidly Solidified Alumina

This chapter present the results of laser surface modification of porous alumina ceramic carried out with a range of laser fluences. Major focus of this chapter is on the study of evolution of surface microstructure (phase, faceted surface grain morphology, and crystallographic texture) following laser surface modifications. Most importantly, this chapter discusses the formation of faceted morphology of surface grains and its correlation with the crystallographic texture, and effect of laser fluence on variation in extent of faceted morphology in terms of curvature factor. Finally, a fractal analysis based approach is introduced to characterize the complexity of surface microstructures in laser surface modified alumina.

3.1 Evolution of Morphological Texture

When the porous alumina ceramics are irradiated with a high power laser beam, the energy is absorbed into the material. The interaction of the laser beam with porous ceramic is a complex phenomenon due to effects of surface porosity. The surface porosity can cause the multiple reflections of the incident beam from the pore walls resulting in enhanced overall absorption of the laser energy. Depending on the incident laser fluence, the absorbed energy causes the heating, melting and vaporization at the surface of

ceramic. For densification of surface porosity of the alumina ceramic, the regimes of laser processing which cause the surface melting are desirable. The molten material formed at the surface flows in the surface pores and subsequently undergoes rapid solidification forming a dense resolidified surface layer. A low magnification photograph of alumina ceramic before and after laser processing is presented in Fig. 3.1. The figure indicated the parallel tracks of resolidified material over a large area of alumina specimen resulting in crack free sealing of porosity on the surface of alumina.

A typical microstructure in the cross section of the laser surface modified alumina ceramic (with laser fluence of 535 J/cm^2) in half laser track is presented in Fig. 3.2 along with corresponding schematic of the surface modification process. The figure clearly shows the highly dense semi-elliptical resolidified area and a highly porous underlying substrate separated by a well defined interface between them. The semi-elliptical shape of the resolified layer is a direct consequence of near Gaussian energy distribution of energy in the laser beam. The maximum melting depth corresponded to the energy maxima at the center of laser beam.

The effects of laser irradiation on the surface microstructure of the alumina ceramic are illustrated in Fig. 3.3. The figure presents a set of SEM surface micrographs corresponding to the untreated alumina substrate (Fig.3.3a) and laser surface modified alumina at laser fluence in the range of 458-687 J/cm^2. (Fig.3.3b-h). The untreated substrate consisted of irregular alumina grains with a high degree of interconnected porosity. The surface modification of such highly porous alumina substrate with high power laser resulted in highly dense surface microstructure characterized by systematic development of surface morphologies as a function of laser fluence. It is evident that the

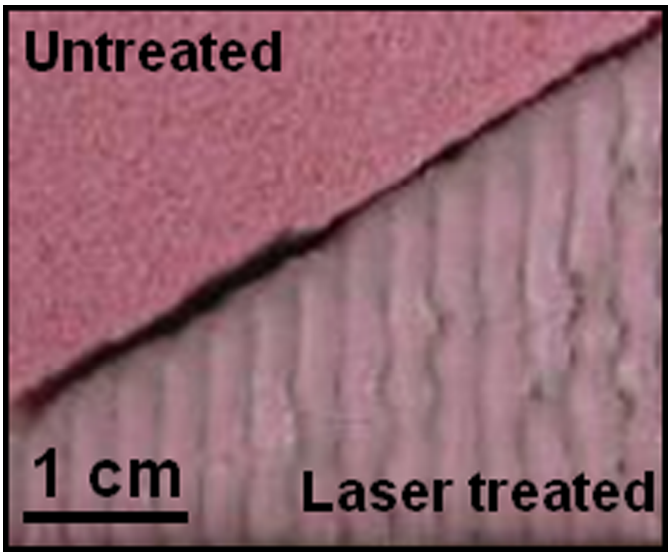


Fig. 3.1 Low magnification picture showing alumina ceramic before (upper portion) and after (lower portion) laser surface modification.

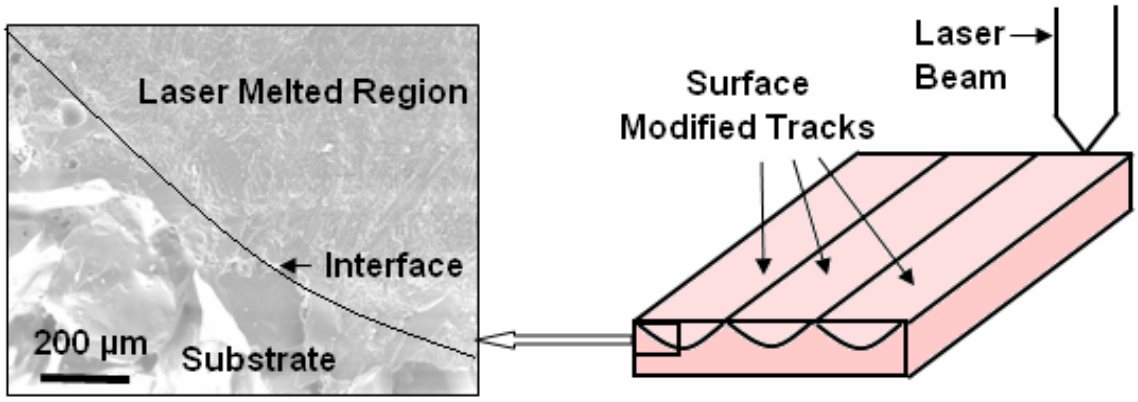


Fig. 3.2 Schematic of laser surface modification process for alumina ceramic and corresponding SEM image of cross-sectional view indicating distinct interface between laser melted region and substrate.

surface microstructure of laser modified alumina ceramic is characterised by faceted polygonal surface grains with varying sizes and extent of surface faceting depending on laser fluence. Based on these microscopic observations, two distinct regimes of explored laser processing conditions can be identified: one corresponding to the laser fluence less that 573 J/cm^2 and the other corresponding to laser fluence greater than 573 J/cm^2. Below 573 J/cm^2 (Fig.3.3b-c), the laser surface modified alumina underwent progressive development of faceting on polygonal surface grains. The surface grain morphology corresponding to laser fluence of 573 J/cm^2 is characterized by highest extent of faceting with well defined multi-faceted microstructure of each polygonal surface grain. Interestingly, above 573 J/cm^2, the surface grains tend to deviate from polygonal shapes transitioning from irregular to near circular shapes.

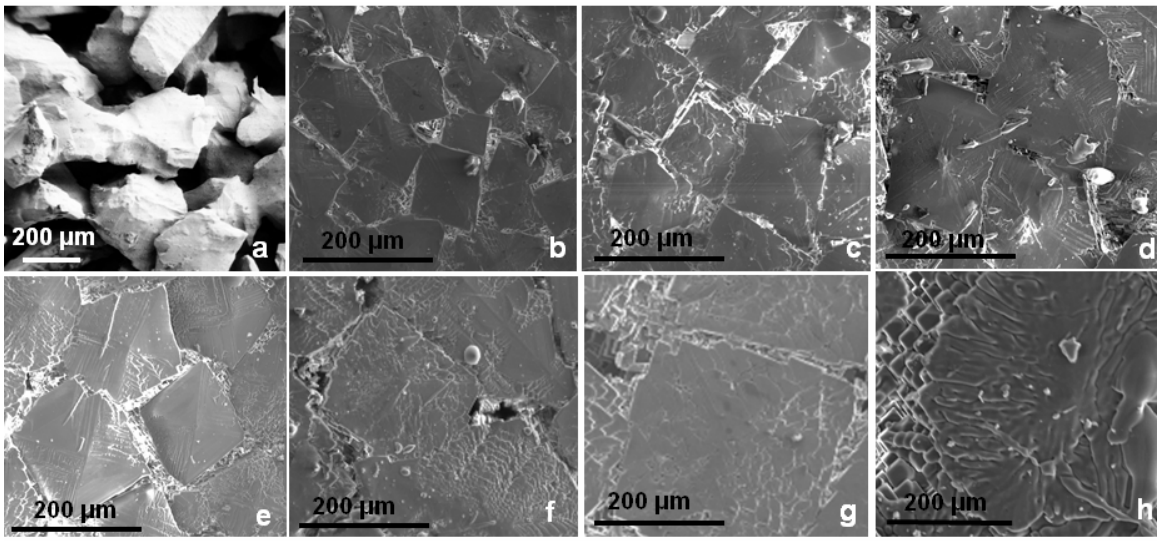


Fig. 3.3 SEM micrographs of surface of (a) untreated alumina substrate and laser surface modified alumina at laser fluence of (b) 458 J/cm^2, (c) 496 J/cm^2, (d) 535 J/cm^2, (e) 573 J/cm^2, (f) 611 J/cm^2, (g) 649 J/cm^2 and (h) 687 J/cm^2

The surface of the laser surface modified alumina ceramics was characterized by the formation of faceted surface grains by the virtue of development of texture as will be discussed in next section. In addition to faceting, these surface grains were also characterized for size and shape. Furthermore, the SEM micrographs and the corresponding 3-D topographical maps presented in Fig. 3.4 indicate that the surface morphology of the laser modified surfaces is greatly influenced by the laser processing fluence. As the laser fluence increases, the size of the polygonal surface grains increases as indicated by the progressive increase in the flat crater like areas in the topographical maps. The variation in grain size with laser fluence is in direct accordance with the established relationships between the grain size and the cooling rates [46]. As the laser fluence increases for the same traverse speed, the cooling rate decreases resulting in larger grains at higher laser fluences. Also, the surface porosity in the laser treated alumina decreases with laser fluence as indicated by the progressive flattening of the topographical map and the disappearance of contrast peaks corresponding to the surface porosity.

The evolution of shape of the surface grains can be expressed in terms of a curvature factor. The curvature factor of the faceted surface grain is defined as:

$$Curvature\ Factor\ (CF) = \frac{K_2}{K_1} = \frac{R_1}{R_2}, \tag{3.1}$$

where K and R are the curvature and radius of curvature respectively measured at corner (subscript 1) and side (subscript 2) of the polygonal faceted surface grains (Fig. 3.5). For a nearly perfect polygon, with a very small value of R_1 (radius of curvature at the corner of the polygonal grain) and a very large value of R_2 (radius of curvature at the side of the

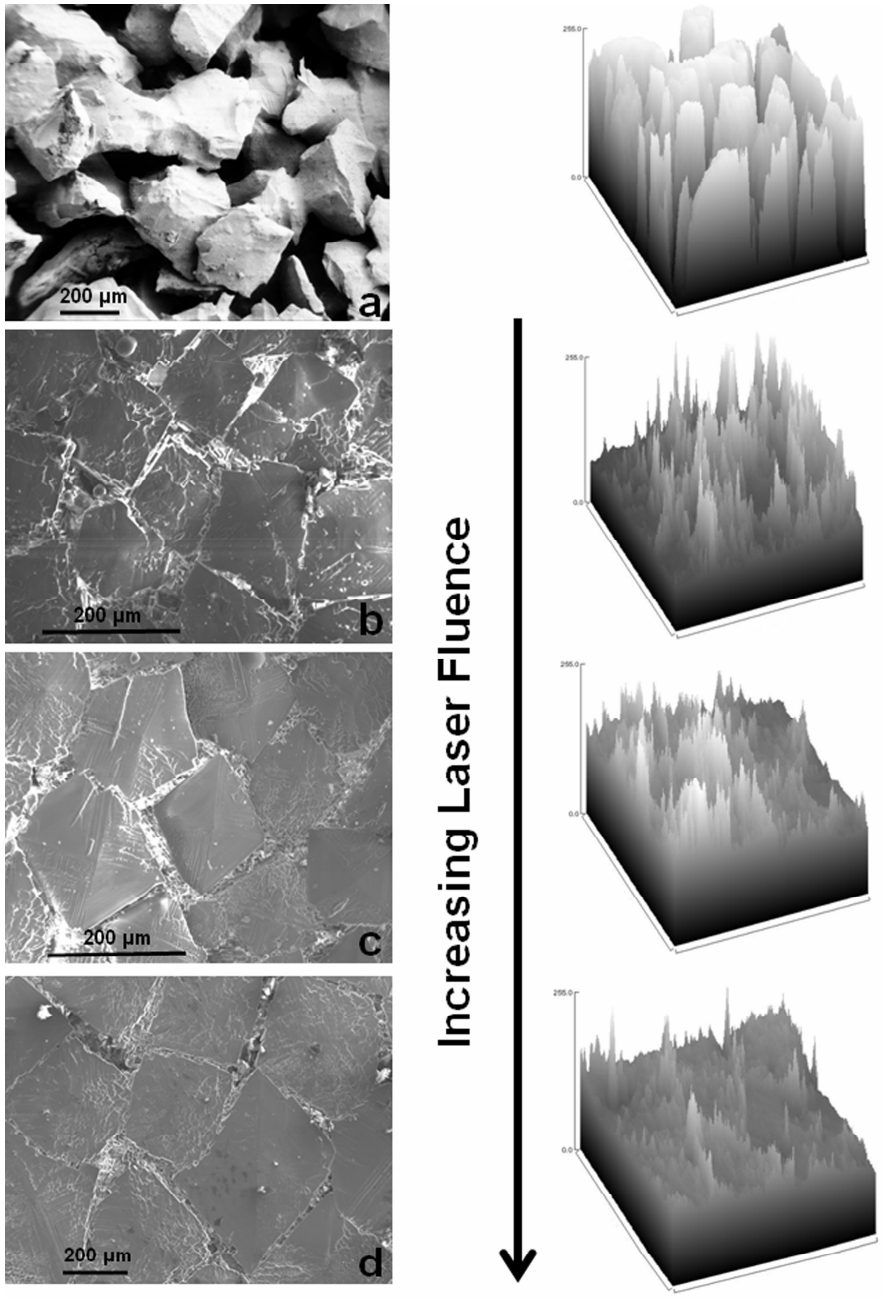


Fig. 3.4 SEM micrographs and corresponding 3D topographical maps showing the evolution of surface morphology in laser surface modified alumina ceramics. (a) Alumina ceramic substrate before laser surface modification and (b-d) after surface modification with laser fluence of 496 J/cm^2, 573 J/cm^2 and 649 J/cm^2 respectively.

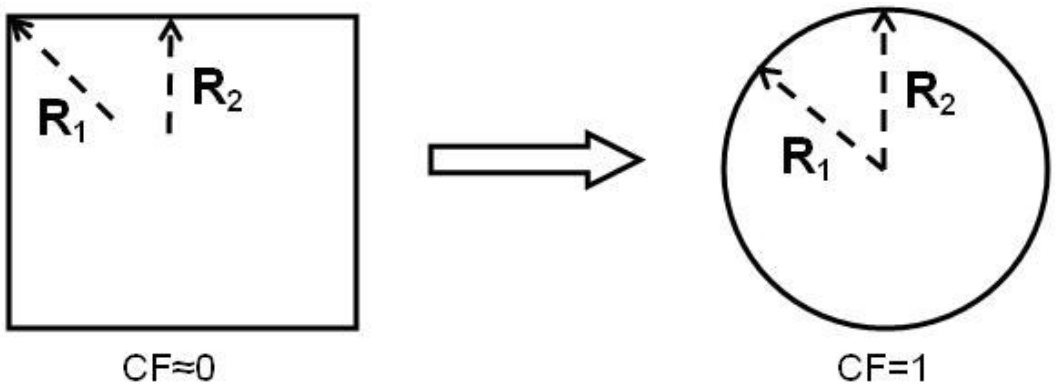


Fig. 3.5 Schematic representation of the polygonal surface grains used for curvature factor calculation. Curvature factor is given by ratio R_1 /R_2.

polygonal grain), the curvature factor yields the value close to zero, whereas, for a perfectly circular grain with equal R_1 and R_2, the curvature factor equals unity (Eq. 3.1). Hence, evolution of shape of surface grains from polygonal to nearly circular grains can be characterized by considering the variation of curvature factor from zero to unity. Curvatures of each individual grain are calculated using ImageJ software by fitting circles of varying sizes at the corner and side of grain.

The effect of laser processing parameters on the evolution of morphology of the surface grains can be visualized in the relationship between the curvature factor and the grain size of the faceted surface grains presented in Fig. 3.6 along with the corresponding SEM micrographs of surface morphology of the laser surface modified alumina. The increase in laser fluence increased the grain size of the faceted surface grains (Fig. 3.6). Also, the curvature factor showed a consistent low value (~ 0.1) up to the laser fluence of 611 J/cm^2 indicating polygonal faceted surface morphology of the surface grains. Above,

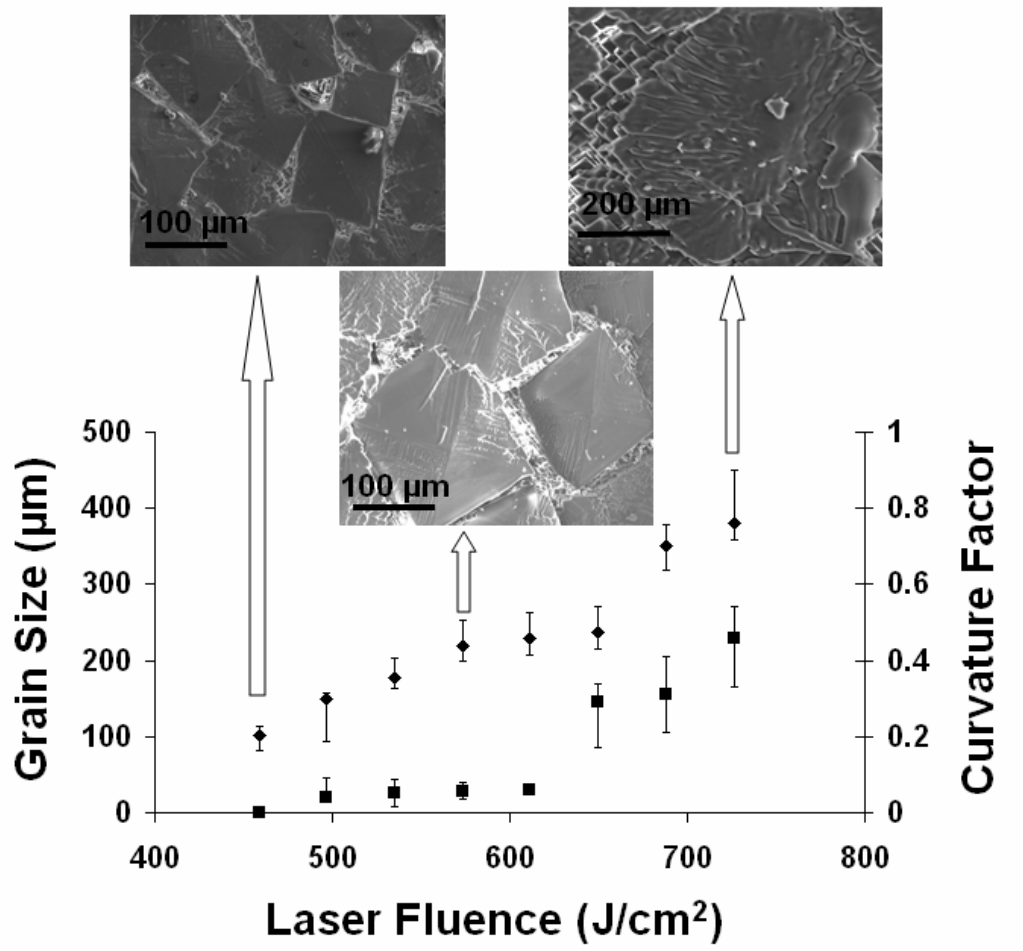


Fig. 3.6. Grain size, curvature factor, and corresponding SEM micrographs of the surface grains in laser surface modified alumina at various laser fluences [(♦) grain size and (■) curvature factor].

611 J/cm^2, the curvature factor deviated towards larger values suggesting the initiation of the change in morphology of grains from polygonal towards nearly circular grains. The observation of the SEM micrographs in Fig. 3.6 indicates that well developed faceted surface grains form at the laser fluence of 573 J/cm^2.

The faceted surface grains are also characterized by the presence of underlying cuboidal crystallites (Fig. 3.7), which are the basic building blocks for the formation of faceted polygonal surface grains. There are various theories of faceted crystal growth during solidification [47-49]. The first model is related to the formation of metastable phases at large undercooling. This is based on a theory of faceted growth during solidification proposed by Cahn [47], which takes into account the undercooling as a driving force. It was proposed that there exists a critical undercooling, ΔT_{crit}, below which the driving force is not sufficient to move the interface normal to itself resulting in non-faceted grain morphology. In the context of our specimens, it seems at first that the faceted morphology of polygonal surface grains with underlying cuboidal crystallites is the direct consequence of the phase transformation of α-Al_2O_3 to γ-Al_2O_3 at large undercooling rates. However, during laser surface modifications, the underlying substrate is expected to provide the catalytic nucleation sites for the growth of stable α-Al_2O_3 and accompanying low undercooling in constrained solidification. This is confirmed by the observation of stable α-Al_2O_3 phase in the laser surface modified alumina ceramic. The above discussion rules out the faceted growth model based on metastable phase formation at large undercooling [47, 48] for the present experimental conditions.

The faceting behavior of the α-Al_2O_3 phase in the present investigations is in accordance with the solid-liquid interface model of Jackson [49]. According to this model, a faceted interface is formed when the dimensionless parameter, *J*, is greater than 2. This dimensionless parameter is given by

$$J = \left(\frac{\Delta S}{R}\right)\xi = \left(\frac{\Delta H}{T_m R}\right)\xi, \tag{3.2}$$

where ΔS, ΔH, T_m, and R are the entropy of fusion, the heat of fusion, the melting point, and the gas constant respectively; ξ is a parameter close to unity [13, 14]. For α-Al_2O_3, the heat of fusion (ΔH) is 26 kcal/mol and the melting point (T_m) is 2323 K such that $\Delta S/R$ and hence J are equal to 5.63, suggesting the faceted growth in alumina [50]. The formation of morphological texture marked by faceted grains at the surface can be the consequence of crystallographic texture evolved at the surface of laser modified alumina under the rapid solidification conditions.

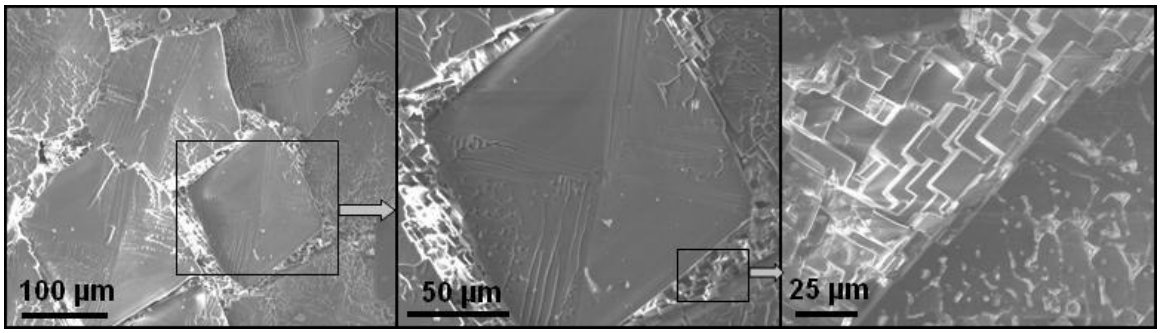


Fig. 3.7. Faceted morphology of polygonal surface grains associated with laser surface modification of an alumina ceramic.

3.2 Evolution of Phase and Crystallographic Texture

Previous section discussed the formation of faceted surface grains in laser surface modified alumina ceramic in view of general theories of faceting. Ruling out the formation of metastable phase, development of crystallographic texture seems to be the highly possible mechanism for the formation of faceted surface grains. To get insight into the development of characteristic faceted surface microstructure, detailed x-ray diffraction analysis was conducted. X-ray diffraction technique is a powerful technique for determining the development of crystallographic texture from the surface of ceramic. The x-ray analysis indicated the formation of stable α-alumina phase at all the laser fluences employed in the present study. During laser surface melting (rapid processing) of ceramics the solidification can proceed by direct growth of the crystalline phases from the solid liquid interface into the melt without nucleation within the melt pool. Hence the substrate below the melted region can act as catalytic sites for the growth of stable α-alumina. The observation of α-alumina in the present study is supported by the previous observations which indicated that the formation of metastable phases require the elimination of the catalytic sites for nucleation of α-alumina [51] which is not likely to happen during the surface melting of alumina ceramic such as in the present case. Also, studies have indicated that laser surface processing can transform the metastable γ-alumina in plasma sprayed coatings into more stable α-alumina [52]. Hence the laser processing regimes employed in the present work for surface modification of alumina ceramic resulted in formation of α-alumina due to availability of the catalytic sites at the melt-substrate interface for growth of stable phases and consequent low undercoolings in the constrained solidification.

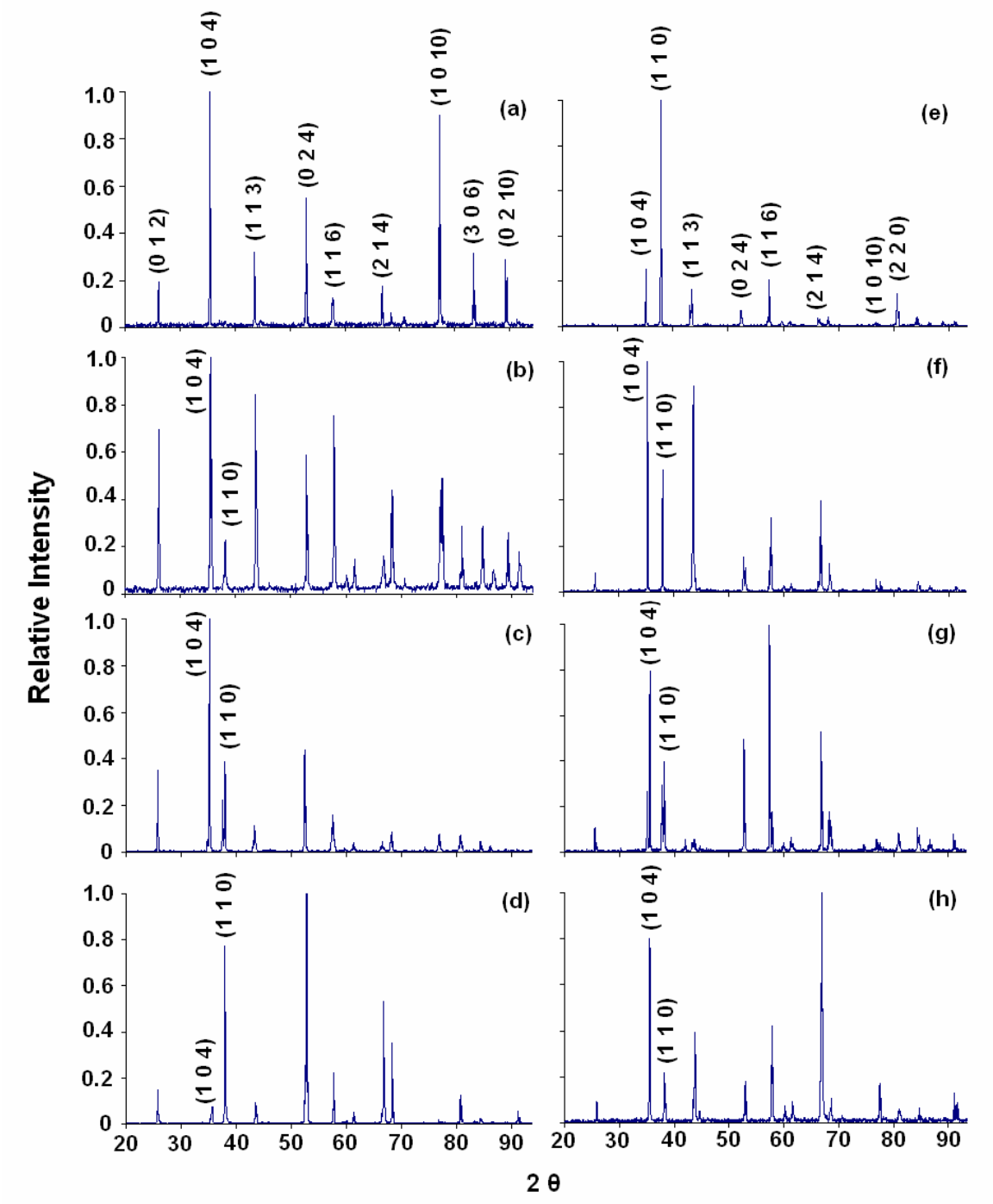


Fig. 3.8 X-ray diffraction patterns of (a) untreated alumina substrate and laser surface modified alumina at laser fluence of (b) 458 J/cm^2, (c) 496 J/cm^2, (d) 535 J/cm^2, (e) 573 J/cm^2, (f) 611 J/cm^2, (g) 649 J/cm^2 and (h) 687 J/cm^2.

The development of characteristic surface microstructures in α-alumina (Fig. 3.3) can be explained on the basis of development of crystallographic texture in the laser surface modified alumina ceramic. The x-ray diffraction spectra of the surface of alumina substrate (Fig.3.8a) and the laser surface modified alumina at laser fluence varying from 458 to 687 J/cm^2 (Fig.3.8b-h) can assist in evaluation of crystallographic texture. In order for the relative comparison among x-ray spectra of surface modified alumina using various laser fluences, the raw intensity counts data was normalized to obtain relative intensities of peaks in each spectrum. Both the substrate and laser surface modified specimens indicated the presence of highly stable α-Al_2O_3 phase (ICDD PDF#: 46-1212). The reformation of such a stable phase even under the rapid solidification rates prevailing during laser surface processing was due to the presence of underlying substrate that provided heterogeneous nucleation sites for the formation of stable α-Al_2O_3 phase.

Further analysis of the x-ray spectra revealed a systematic variation of relative intensities of (1 1 0) and (1 0 4) planes with laser fluence. The details of intensity variation corresponding to (1 1 0) peaks in representative x-ray diffraction patterns is presented in Fig. 3.9. The substrate showed a strongest peak corresponding to (1 0 4) reflection in agreement with the standard randomly oriented reference pattern (ICDD PDF#: 46-1212) and the absence of peak corresponding to (1 1 0) reflection. Earlier described two regimes of laser fluence (less and greater than 573 J/cm^2) also indicated the systematic variation of relative intensity of (1 1 0) plane. The relative intensity of (1 1 0) reflection increased progressively with laser fluence up to 573 J/cm^2 followed by a gradual decrease above the fluence of 573 J/cm^2 (Fig. 3.9). This is accompanied by the

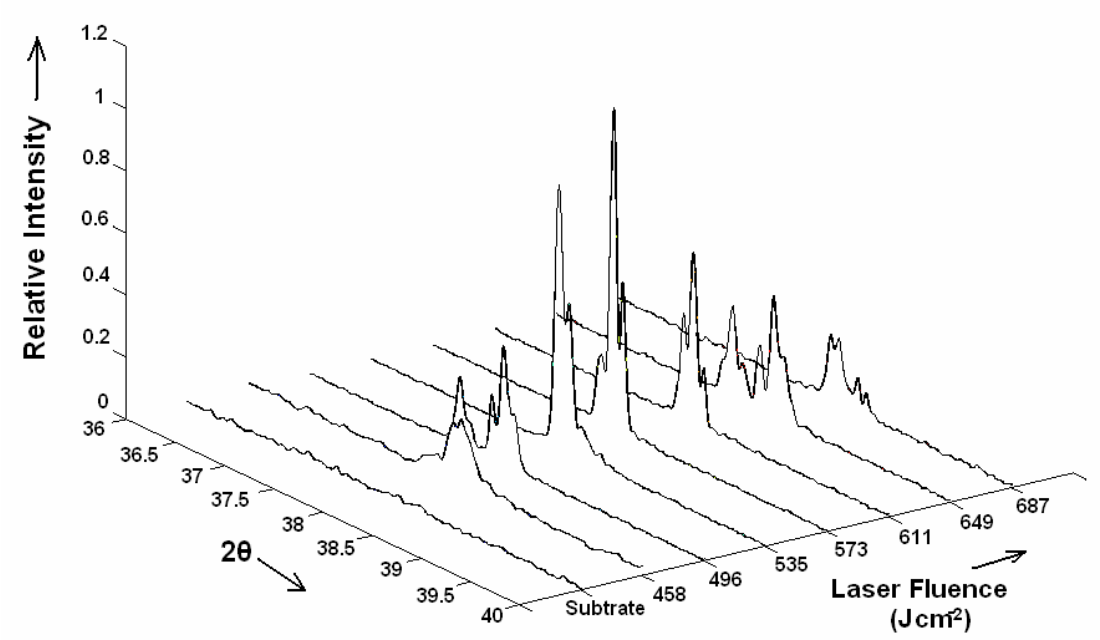


Fig. 3.9 Relative intensity of (1 1 0) reflection ($2\theta = 37.785°$) of α-Al_2O_3 substrate and laser surface modified alumina with various laser fluences.

general reverse trend of variation of the relative intensity of (1 0 4) plane compared with the trend of variation of the relative intensity of (1 1 0) plane with laser fluence. Intensities corresponding to other planes did not indicate any specific trend in variation of peak intensity as a function of laser fluence. Thus, there existed an intermediate value of laser fluence (573 J/cm^2) which showed strongest (1 1 0) peak and weak (1 0 4) peak (This (1 0 4) peak is the strongest peak in pattern of substrate and also in the reference pattern of randomly oriented sample corresponding to ICDD PDF#: 46-1212).

The development of texture with the laser fluence can be quantified in terms of the texture coefficient (TC) given by [53]:

$$Texture\ Coefficient\ (TC)\ (hkl) = \frac{I(hkl)}{I_0(hkl)}\left\{\frac{1}{n}\sum\frac{I(hkl)}{I_0(hkl)}\right\}^{-1}, \qquad (3.3)$$

where $I(h\ k\ l)$ are measured intensities of ($h\ k\ l$) reflection; $I_0(h\ k\ l)$ are powder diffraction intensities of α-alumina according to the JCPDS (card no. 46-1212); and n is the number of reflections used in the calculations. Following ($h\ k\ l$) reflections corresponding to α-alumina were used in the texture coefficient calculations: (0 1 2), (1 0 4), (1 1 0), (1 1 3), (0 2 4), (1 1 6), (2 1 1), (2 1 4), (1 0 10), (2 2 0) and (2 2 3). Table 3.1 summarizes the results of texture coefficient calculations for the observed ($h\ k\ l$) reflections in α-alumina at various laser fluences. In order to select the dominant reflections which show the strong texture in the laser surface modified alumina, an average texture coefficient is defined:

$$TC_{avg}(h\,k\,l) = \frac{\sum TC(h\,k\,l)}{N}, \qquad (3.4)$$

Table 3.1 Texture coefficients (TC) of various (*h k l*) planes for alumina substrate and laser surface modified alumina at various laser fluences.

Plane	Texture Coefficient					Average Texture
(h k l)	Substrate	496 J/cm^2	573 J/cm^2	649 J/cm^2	726 J/cm^2	Coefficient
(012)	0.14	0.74	0.02	0.13	0.00	0.22
(104)	0.35	1.13	0.17	0.49	0.02	0.42
(110)	0.00	1.73	3.52	1.16	0.30	1.39
(113)	0.17	0.16	0.17	0.06	0.91	0.36
(024)	0.56	1.36	0.13	0.90	0.22	0.74
(116)	0.04	0.17	0.16	0.72	0.08	0.23
(211)	0.00	1.13	2.22	2.26	0.00	1.53
(214)	0.22	0.16	0.09	1.42	0.05	0.83
(1 0 10)	0.92	0.25	0.04	0.10	0.00	0.22
(220)	0.00	3.45	4.84	2.55	1.58	2.54
(223)	0.22	1.24	0.81	2.15	0.28	1.05

where *N* is the number of laser fluences used in the study. The results of these calculations are also presented in Fig. 3.10, which indicate that the (1 1 0), (2 2 0) and (2 1 1) are the strongest reflections which corresponded to higher values of average texture coefficients. Hence these reflections were selected for further analysis of texture evolution during laser surface modification of alumina ceramic with various laser fluences. The variations of texture coefficients (TC) for (1 1 0), (2 2 0) and (2 1 1) reflections of α-alumina with laser fluence are presented in Fig. 3.11. The figure clearly indicates the systematic variation of the texture coefficients of these planes with laser fluence. The texture coefficient of the (1 1 0), (2 2 0) and (2 1 1) reflections increased with laser fluence, reached maximum around 573 J/cm^2 and then decreased at high laser fluences. This can also be observed from the x-ray diffraction spectra (Fig. 3.8) which show the absence of (1 1 0) and (2 2 0) reflections in the substrate (corresponding to TC(1 1 0) and TC(2 2 0) = 0) and very low intensity at high laser fluence (corresponding to small values of TC(1 1 0) and TC(2 2 0)). The intensities of (1 1 0) and (2 2 0) reflections reached maximum around the laser fluence of 573 J/cm^2 resulting in correspondingly maximum texture coefficient. The (2 1 1) reflection also exhibited the nearly similar trend of variation of texture coefficient with the laser fluence. The development of strong texture at 573 J/cm^2 can be related with the formation of highly faceted morphology of the surface grains as discussed in next sections.

The evolution of crystallographic texture during solidification or film growth has strong effect on evolution of resultant surface features such as faceted morphology of the surface grains. Early model of faceted growth was proposed by van der Drift [54]. The model considers that each crystallite or grain grows with each crystallographic facet

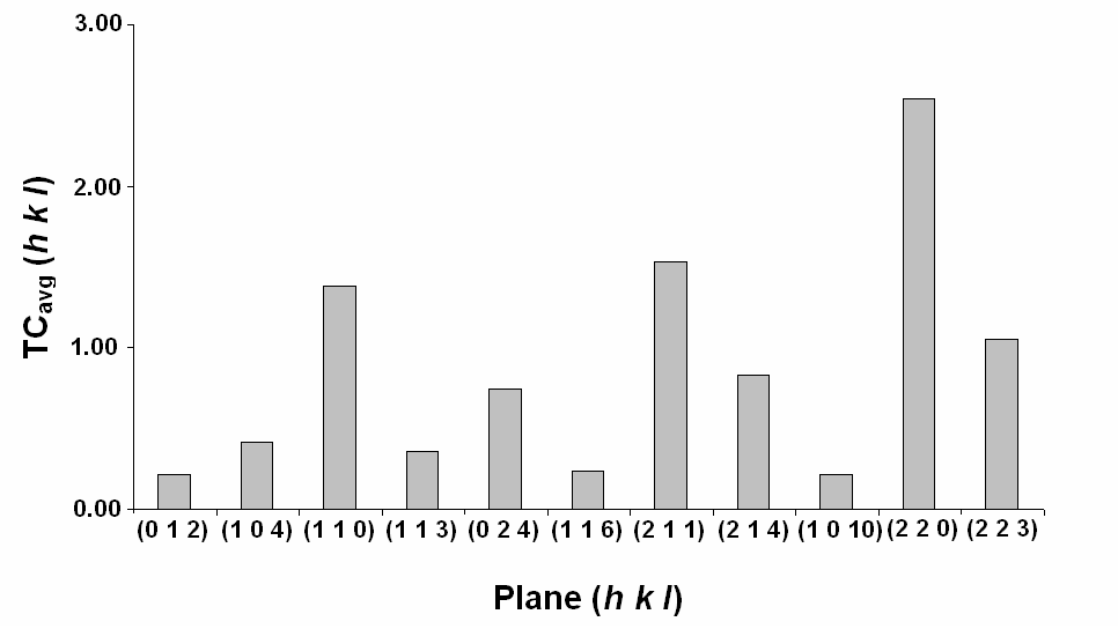


Fig. 3.10 A bar chart for average texture coefficient for various (*h k l*) planes of α-alumina calculated over a range of laser fluences used for surface modifications.

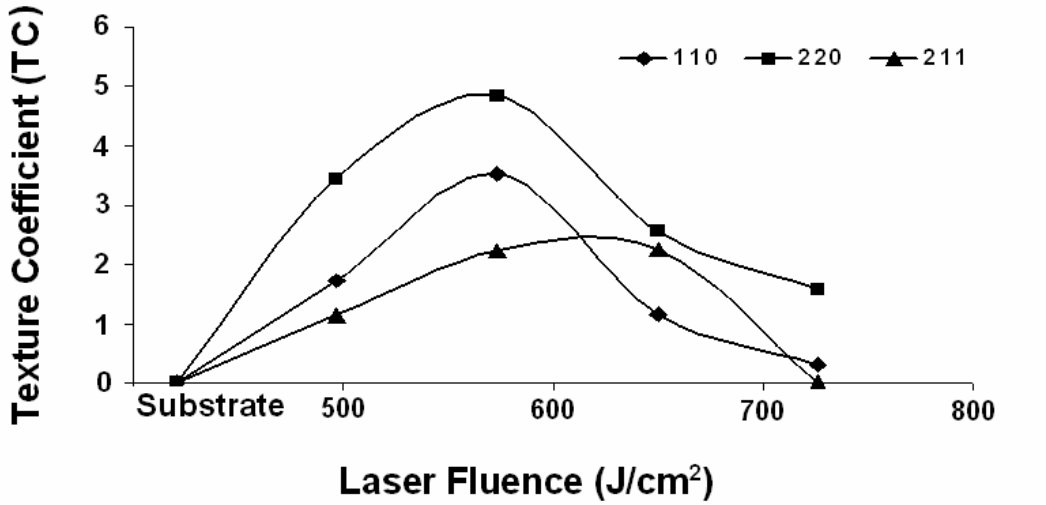


Fig.3.11 Texture coefficients (TC) of (1 1 0), (2 2 0) and (2 1 1) planes of α-alumina as a function of laser fluence. (Note the data point corresponding to the texture coefficients of substrate).

moving with a known normal velocity until a facet meets the surface of another growing crystallite. The grain boundaries are thus formed when surfaces of different grains impinge upon each other. The evolution of the faceted morphology then depends on the relative growth velocities of the various facets. This is schematically illustrated for the 3-dimensional case with (1 0 0) and (1 1 1) as growing facets (Fig. 3.12). The figure indicates that the surface morphology is determined by the ratio of velocities (α_{3D}) of (1 0 0) and (1 1 1) facets (v_{100} and v_{111} respectively). The ratio is given by:

$$\alpha_{3D} = \sqrt{3}\frac{v_{100}}{v_{111}}, \tag{3.5}$$

where $\sqrt{3}$ is numerical factor chosen such that simple, highly symmetric morphologies occur at integer values of α_{3D}. Hence, if a crystal with facets (1 0 0) and (1 1 1) and velocity ratio described by α_{3D} is allowed to grow without impingement, it will asymptotically approach a characteristic, idiomorphic crystal shapes [55].

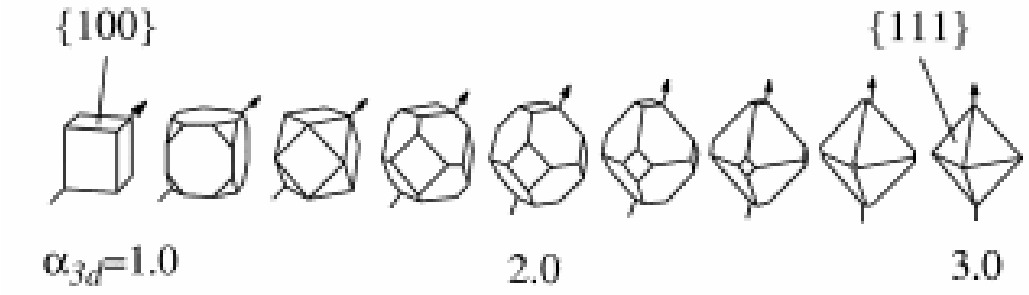


Fig. 3.12 van der Drift model illustrating the evolution of idiomorphic crystal shapes with the ratio of relative velocities (α_{3D}) of the {1 1 0} and {1 1 1} facets for 3-dimensional case [55].

For intermediate velocity ratios (α_{3D} between 1.0 and 3.0) multiple planes will grow dominantly until they impinge upon each other thereby providing a multi-plane faceted grain. From this discussion, in the context of laser surface modification of alumina ceramic the evolution of (1 1 0) or (2 2 0) and (2 1 1) texture may be related with the relative growth of (1 1 0) or (2 2 0) and (2 1 1) planes in hexagonal lattice. A schematic of the formation of faceted crystal from the intersection of {1 1 0} and {2 1 1} planes in hexagonal lattice is presented in Fig. 3.13. The corresponding shape is compared with the SEM micrograph of the faceted morphology of the surface grains in laser surface modified alumina ceramic.

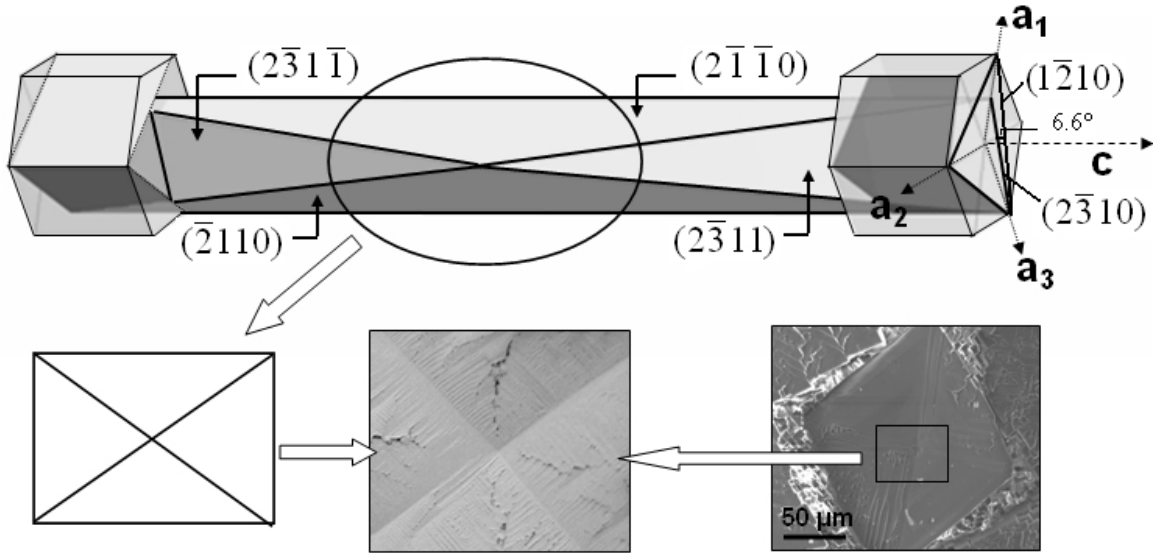


Fig. 3.13 Schematic of the development of faceted morphology from crystallographic texture in laser surface modified alumina.

From the previous discussion, it is clear that the faceted morphology of the surface grains is associated with the evolution of crystallographic texture as determined by preliminary x-ray diffraction analysis. To get local crystallographic information from faceted grains, advanced EBSD analysis based on generation of Kikuchi patterns have been performed. One representative example of a Kikuchi pattern obtained from the surface of laser surface modified alumina is presented in Fig. 3.14. The Kikuchi patterns obtained at different positions on the sample confirmed the presence of α-Al_2O_3 and were indexed according to the corresponding hexagonal crystal structure. The EBSD orientation maps based on a number of such Kikuchi patterns from the surface revealed the crystallographic orientations of the large surface grains formed during laser surface modification of alumina ceramic.

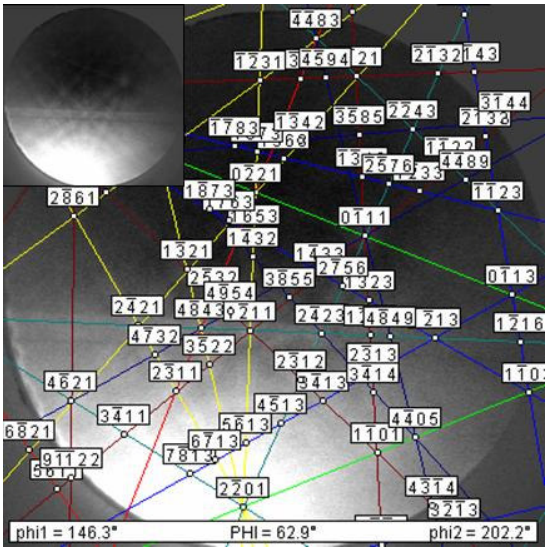


Fig. 3.14 Example of Kikuchi pattern used for the calculation of the EBSD orientation map from the surface of laser surface modified alumina ceramic. Inset shows the unindexed Kikuchi pattern.

Pole figures corresponding to planes $\{0001\}$, $\{1\bar{2}10\}$, and $\{2\bar{3}10\}$ calculated from EBSD orientation maps are presented in Fig. 3.15. The figure indicates a high density of $\{0001\}$ poles perpendicular to the surface normal which are concentrated in two opposite directions following the hexagonal representation of the unit cell. It also shows 6 to 7° tilt between the surface normal and the $(1\bar{2}10)$ pole and a non-tilted $(2\bar{3}10)$ pole. Based on the calculations from the crystallographic model (Fig. 3.13), the tilt angle between $\{1\bar{2}10\}$ and $\{2\bar{3}10\}$ is found to be 6.6°. All these observations are in close agreement with the proposed correlations for faceting based on the evolution of crystallographic texture. Thus, complete crystallographic description of faceted morphology of surface grains by assigning specific planes to the individual facets is reached based on detailed x-ray diffraction and OIM analysis. In addition to the faceted grain morphology, the surface microstructure presents additional complexity due to multi levels of microstructural features such as microporosity, grain shapes, and sizes (Figs. 3.3 and 3.4). It is important to characterize such microstructural complexity to understand the overall development of microstructure during laser surface microstructuring. This is discussed in detail in next section.

3.3 Processing Parameter-microstructure Correlations based on Fractal Analysis

As discussed in the previous section, the laser surface microstructured alumina ceramics presents substantial variation in microstructural features such as grain size, shape, texture, etc. even within a limited range of laser fluences explored in the present study. Hence to provide early handle over such variation within and possibly beyond the set of parameters

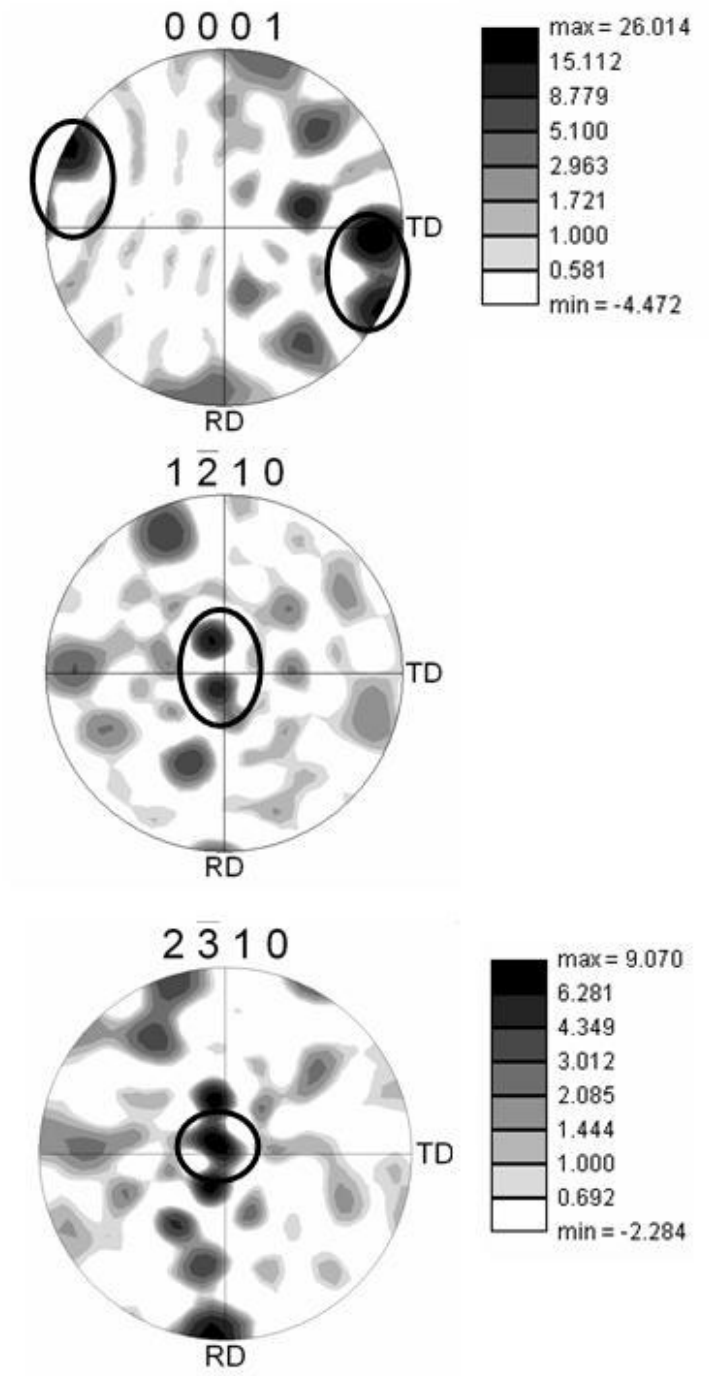


Fig. 3.15 Calculated pole figures showing the distribution of $\{0001\}$, $\{1\bar{2}10\}$, $\{2\bar{3}10\}$ poles with respect to surface normal. Maximum intensities are circled and show the $(2\bar{3}10)$ texture as discussed in the text.

use, a concept of fractal analysis is used. The concept of fractal geometry which was originally developed for analysis of irregular features in nature, is finding increased applications in the fields of materials science for the characterization of microstructures [56-61]. Fractal dimensions effectively describe the complex and geometrically irregular microstructure and have been successfully applied in the characterization of grain boundaries [57], fracture surfaces [58], dendritic microstructures [59], and precipitates, [60] etc. The effectiveness of this approach for characterization of microstructures is derived from the ability to establish the useful numerical correlations between the fractal dimensions and the various properties of the material such as fracture toughness, creep strength, etc [61]. In view of present study, the concept of fractal dimension is adopted to develop correlations between few key microstructural parameters and laser fluence. However, the concept can also be extended to estimate the behavior of several other parameters as a function of laser fluence.

Fractal dimensions can be calculated using image processing of SEM micrographs in combination with the implementation of box counting algorithm using a public-domain software, ImageJ (available from National Institute of Health, USA). In box counting technique, the fractal dimension (D_b) is measured from the number of square boxes, N (r) required to completely cover the surface profile and size of the boxes, r [62]. The basic fractal equations using Haudorff measure can be written as:

$$N(r) = Cr^{D_b}, \tag{3.6}$$

$$\log N = \log C - D_b \log r, \tag{3.7}$$

where, C is constant. The process is repeated for calculating the number of boxes N(r) required to cover the surface features with different sizes of the boxes (r). The slope of the straight line obtained by plotting the number of boxes (N(r)) against its size (r) for various box sizes on a double logarithmic scale yields the fractal dimension of the surface features in the microstructure.

In this study, the concept of fractal geometry is applied to characterize the surface microstructure and derive the useful correlations between fractal dimensions and the surface microstructural features. Fig. 3.16 represents the important steps in the calculation of fractal dimension using a SEM micrograph from laser surface modified alumina ceramic with a laser fluence of 458 J/cm^2. Fractal dimension of 1.4611 was determined for this case. Similarly, fractal dimensions for all other laser fluences were computed and correlated with various physical attributes such as roughness, porosity, grain size of laser modified region.

The variation of fractal dimension with the laser processing fluence used for surface modification of alumina is presented in Fig. 3.17. For all laser processing fluence, corresponding SEM images with same magnification were given as input to avoid any magnification related errors. Fractal dimensions of the surface microstructures of the laser surface modified alumina ranges between 1.46 and 1.71. The figure indicates that the fractal dimensions increased with laser processing fluence suggesting the increased complexity of the surface microstructural features at higher laser fluences. This complexity of microstructure arises from the combination of surface microstructural features such as porosity, roughness, and grain and subgrain dendritic structures. Similar studies on characterization of surface morphologies of thin films have demonstrated

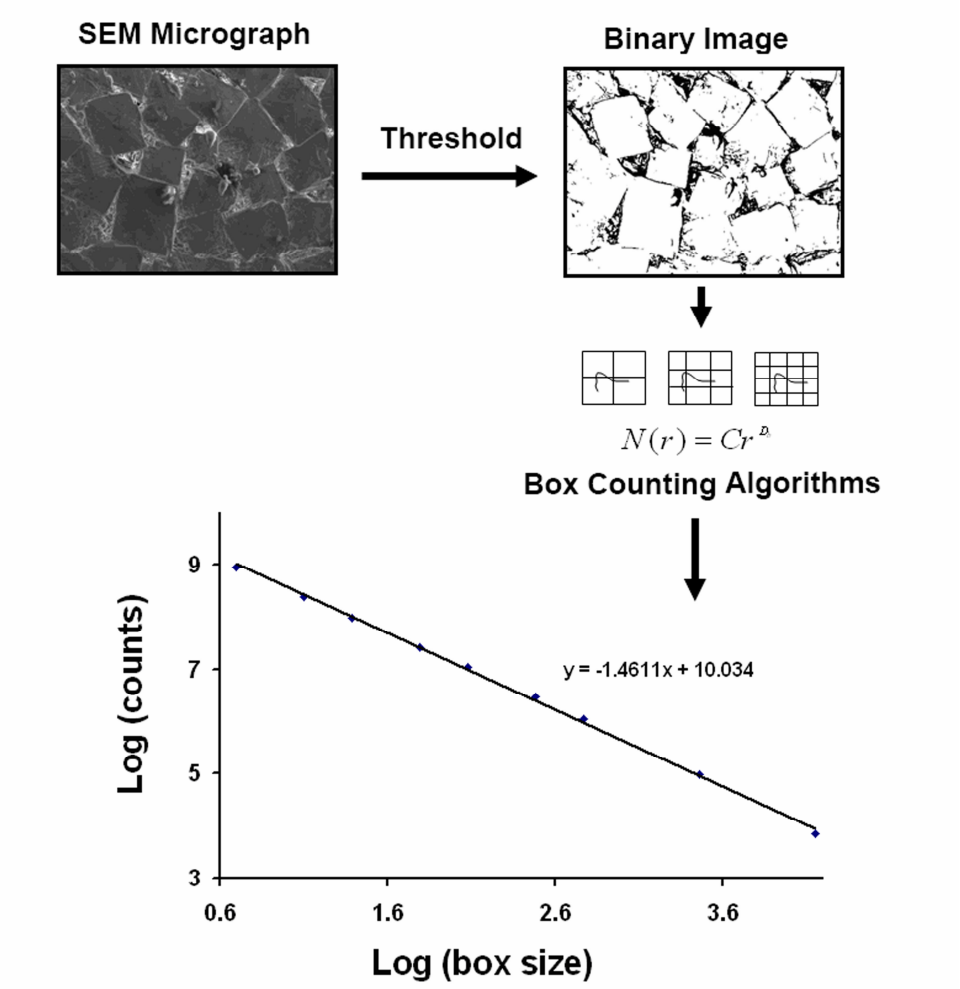


Fig. 3.16 Calculation of fractal dimension from SEM micrograph using image processing and box counting algorithm. The slope of the log-log plot shown in the figure corresponds to the fractal dimension.

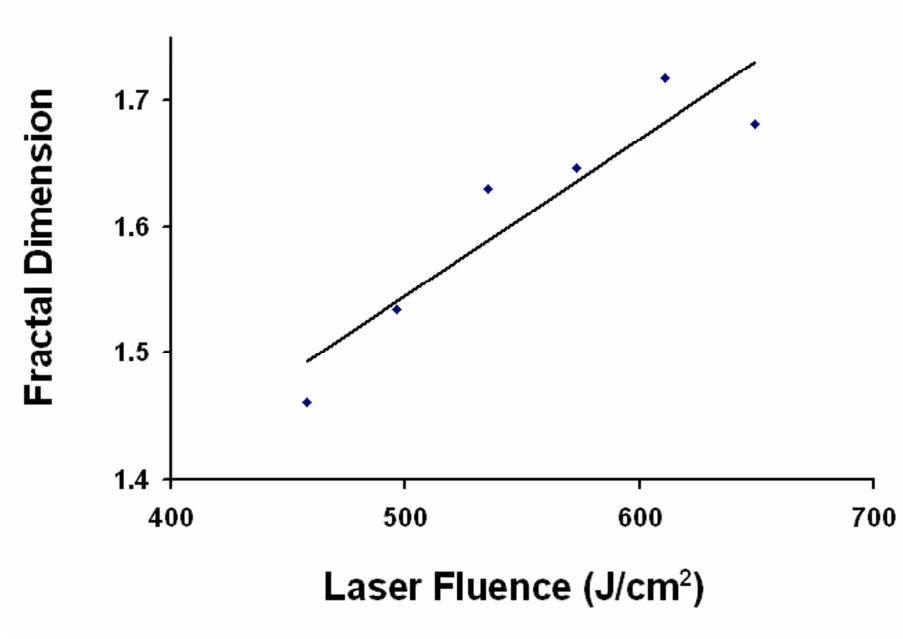


Fig. 3.17 Variation of Fractal Dimension with laser processing fluence used for surface modification of alumina ceramic.

that the complexity of thin film morphology were fractal in nature and can be better characterized quantitatively using fractal dimensions than the conventional approaches [63].

Various correlations between the fractal dimension and the microstructural features such as porosity, polygonal grain size and surface roughness are presented in Figs. 3.18-3.20. As indicated in the Fig. 3.18, the fractal dimension of the laser surface modified alumina is negatively and linearly related to the amount of porosity with a correlation parameter of data fitting (R^2) of 0.9735. Such a relationship between the fractal dimension and the porosity is in agreement with the previous studies on the fractal analysis of porosity in polished samples of plasma-sprayed yttria-stabilized zirconia

coatings [64]. Fig. 3.19 shows the variation of polygonal surface grain size with the fractal dimension. The following power relationship with a correlation parameter of data fitting (R^2) of 0.9385 can be drawn from Figure 3.19:

$$d = kD^{5.188}, \tag{3.8}$$

where, d is size of polygonal surface grains and D is fractal dimension. The relationship between the fractal dimension and the surface roughness of the laser surface modified alumina followed the negative and linear relationship with correlation parameter of data fitting (R^2) of 0.9456 (Fig. 3.20).

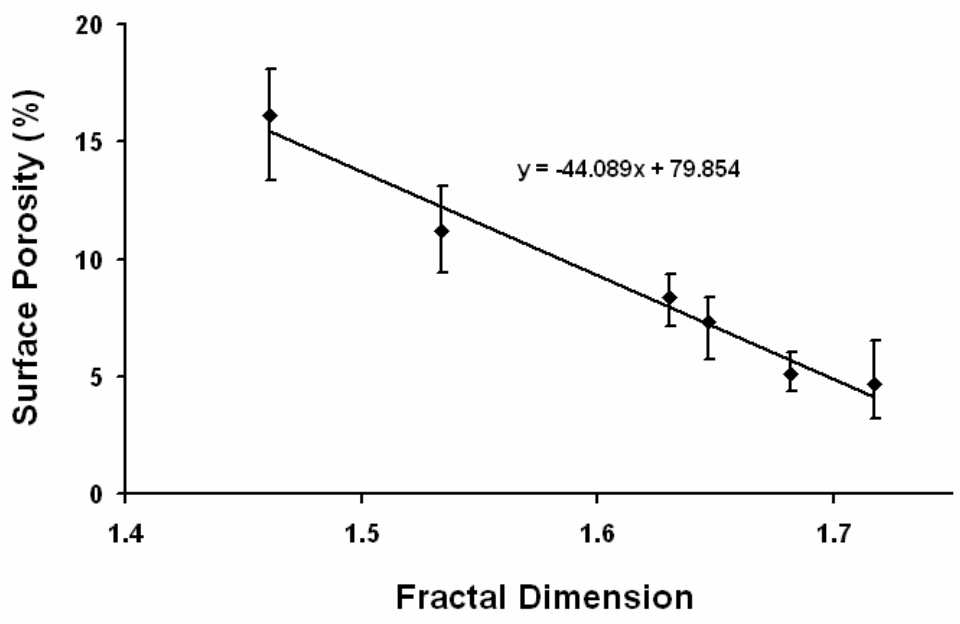


Fig. 3.18 Variation of surface porosity of the laser surface modified alumina with fractal dimensions (Correlation parameter of data fitting, R^2=0.9735).

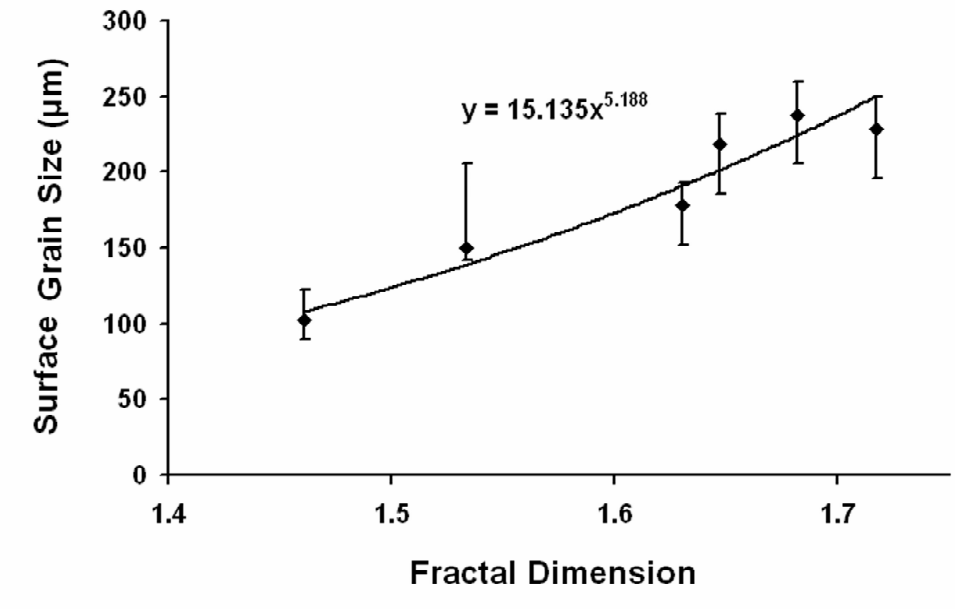


Fig. 3.19 Variation of polygonal surface grain size of the laser surface modified alumina with fractal dimensions (Correlation parameter of data fitting, R^2=0.9385).

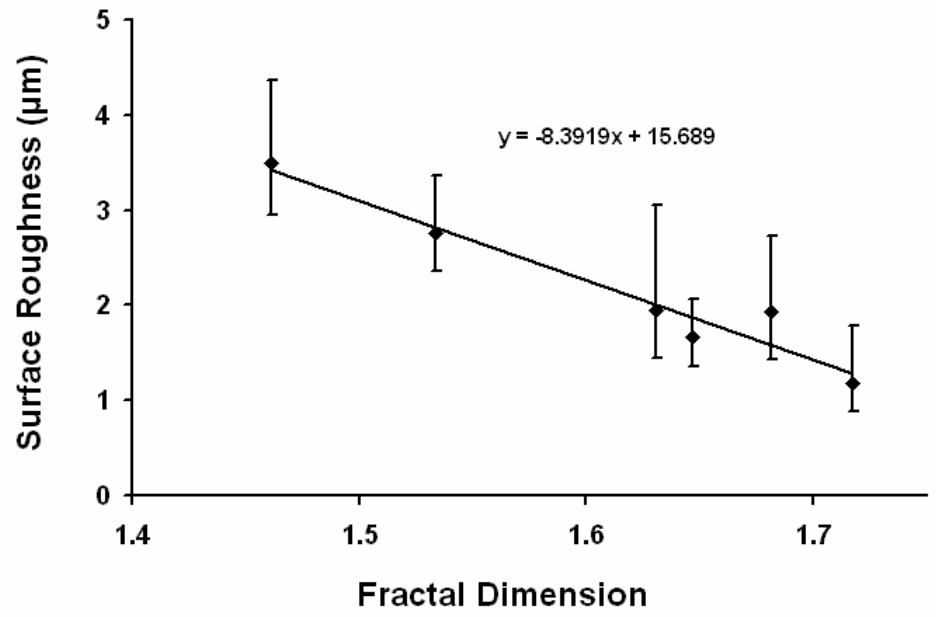


Fig. 3.20 Variation of surface roughness of the laser surface modified alumina with fractal dimensions (Correlation parameter of data fitting, R^2=0.9456).

Such relationships can be effectively utilized in predicting the porosity, surface roughness and grain sizes of the surface microstructure from the fractal dimension obtained by direct image analysis of the SEM micrographs. Thus fractal-geometry based approach for characterization of complex irregular microstructures serve as an tool for establishing the structure-property correlations in the various materials processing techniques.

3.4 Summary

Laser surface modification of porous alumina ceramics caused significant melting and rapid resolidification resulting in formation of highly densified surface layer. Most important observation of this work is related with the formation of polygonal faceted surface grains through development of crystallographic texture in laser modified alumina. The degree of faceting and associated strength of (1 1 0) crystallographic texture was found to be highest at intermediate laser fluence (573 J/cm^2) of the range used in present work. Complete description of faceted morphology is provided by assigning specific crystallographic planes to individual facets. The morphology and associated crystallographic texture of the surface grains were found to be influenced by the laser processing fluence. Finally, the concept of fractal analysis was implemented to characterize the complexity of surface microstructures. Useful correlations were found between fractal dimensions and surface microstructural features. Most of this chapter dealt with evolution of surface microstructure and its correlation with the development of crystallographic texture. It is important to understand the evolution of depth of these surface modifications during laser surface structuring of alumina. This forms the subject of next chapter.

Chapter 4

Laser Process Thermal Effects on Physical Attributes of Surface Modified Region

Most of the discussion in the previous chapter dealt with the evolution of microstructure through development of micro-texture at the surface of the laser modified alumina. To tailor the microstructure for useful applications, it is important to understand the evolution of depth of modification in addition to the surface microstructure. Due to thermal nature of the process, surface microstructure and depth of modification in the surface modified alumina are expected to be influenced by thermal aspects of the process. This chapter models the thermal and consequent hydrodynamic effects, and discusses its influence on the evolution of microstructure (primarily depth of modification and surface grain structure) during laser interaction with porous alumina ceramic.

4.1 Integrative Modeling Approach

During laser surface modification of alumina ceramic, a part of the laser energy is absorbed into the material. The amount of absorbed energy depends on several factors such as laser wavelength, temperature, surface roughness, and surface chemistry. In case of highly porous substrates such as alumina ceramics, absorptivity of the surface for 1.06 μm wavelength is expected to be as high as 0.8 due to multiple reflections from the walls of pores [50]. The absorption of the laser radiation causes the rapid heating, melting and

evaporation of the material depending on the incident laser energy. The molten material rapidly solidifies forming surface recast layer. One of the important microstructural parameters in the cross-section of the laser modified alumina is the depth of melting. A typical cross sectional microstructure of the laser surface modified alumina at laser fluence of 535 J/cm^2 is presented in Fig. 4.1. The semi-elliptical shape of the recast layer is a consequence of distribution of energy in the laser beam such that maximum depth of melting at the center of melt pool corresponds to the energy maxima along the axis of the laser beam.

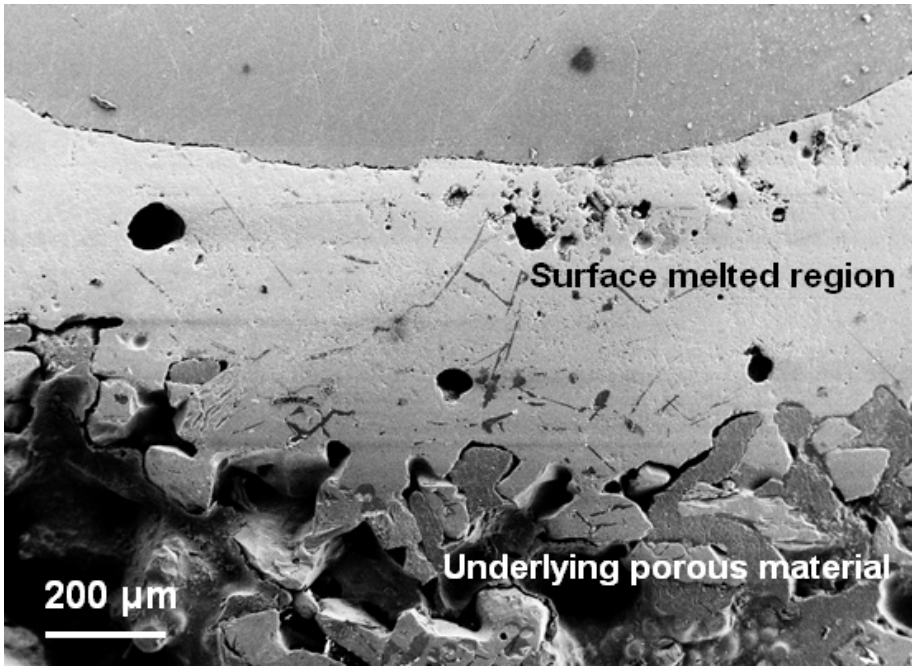


Fig. 4.1 Typical polished cross section of laser surface modified alumina ceramic mounted in epoxy mould. Surface modification was carried out at a laser fluence of 535 J/cm^2.

Accurate prediction of depth of melting (depth of laser modified layer) is important for many applications for implementing the intelligent manufacturing. This requires the understanding of physical processes during laser-material interaction. Schematic of the physical processes taking place during laser interaction with the porous alumina substrates is illustrated in Fig. 4.2. The processes are operative for the laser fluences above the threshold value of laser fluence required for evaporation to be initiated at the melt surface. Also, the rapid evaporation at the surface of the melt generates the recoil pressure which drives the flow of molten material into the porous substrate, thus further extending the depth of melting. The overall depth of melting is then given by the sum of maximum depth of melting calculated from temperature distribution within the material and the depth of melt infiltration in the porous substrate induced by recoil pressure due to rapid evaporation at the melt surface. Thus, an integrative modeling approach is proposed to calculate the overall depth of melting from heat transfer equations given by Fourier's law and fluid flow equations derived from Darcy's law (Fig. 4.3).

4.2 Temporal Distribution of Temperature

First step in the prediction of depth of melting is the determination of temperature distribution in the materials during laser irradiation. For this purpose, a three-dimensional thermal analysis is presented in this section. A control volume of $1 \times 1 \times 1$ cm^3 was considered for thermal analysis with the laser being irradiated on the top surface for irradiation time of 90 ms. Based on the experimental observations, selected control

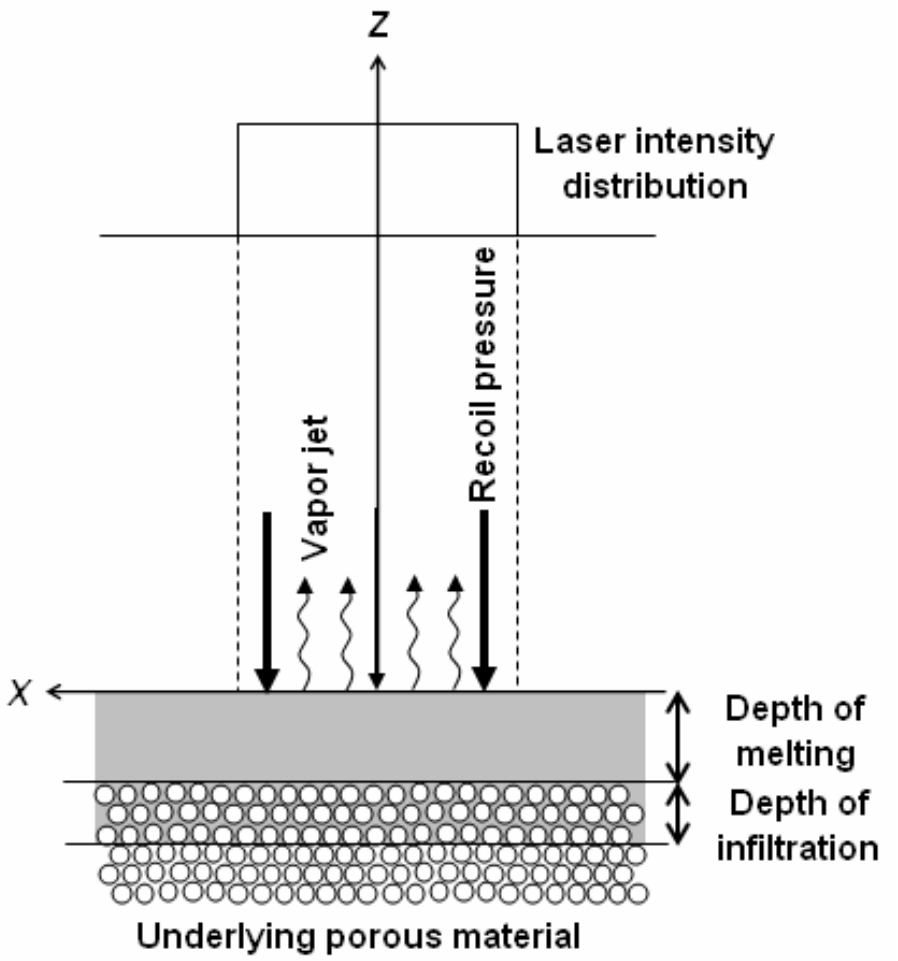


Fig. 4.2 Physical model showing the interaction of laser beam with porous ceramic substrate during the laser surface modification. Various effects such as surface melting, evaporation, generation of evaporation recoil pressure, and melt infiltration are shown.

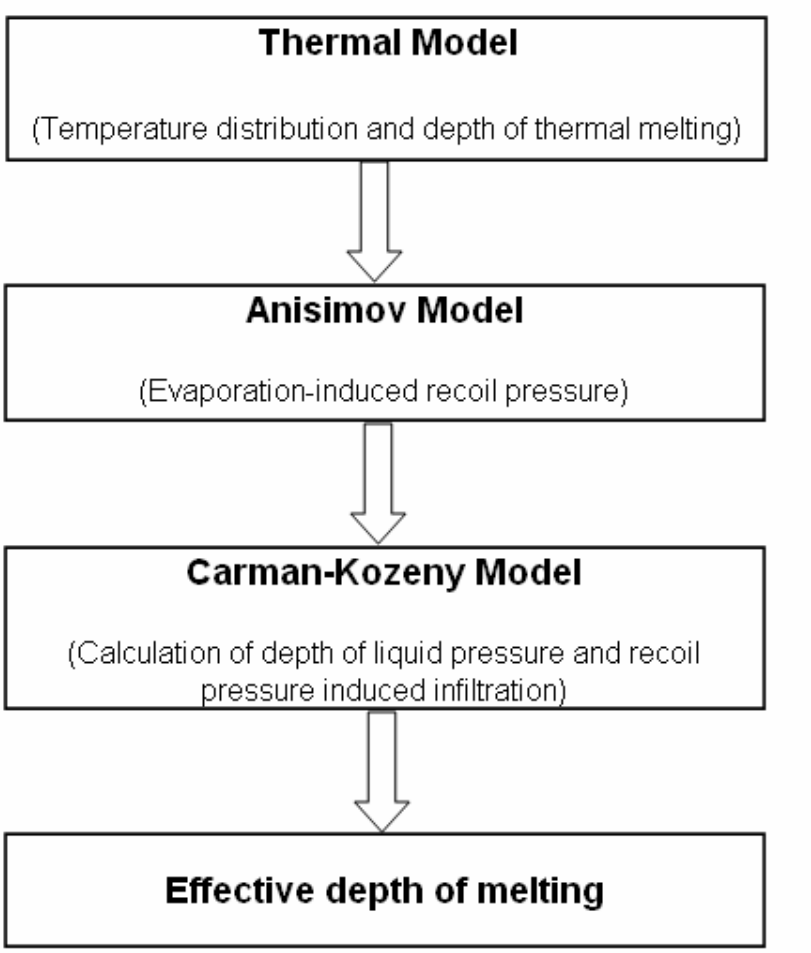


Fig. 4.3 Schematic of an integrative modeling method for predicting the overall depth of melting in laser surface modified alumina ceramic.

volume appeared to be large enough to include the entire depth of melting, the heat affected zone, and the depth of the substrate that did not reach the temperature high enough to cause any noticeable microstructural changes. The governing three-dimensional heat conduction equation is given by [13]

$$\frac{\partial T(x,\, y,\, z,\, t)}{\partial t} = \alpha\left(\frac{\partial^2 T(x,\, t)}{\partial x^2} + \frac{\partial^2 T(y,\, t)}{\partial y^2} + \frac{\partial^2 T(z,\, t)}{\partial z^2} \right), \tag{4.1}$$

where α is the thermal diffusivity of the material and is equal to $K/\rho c_p$; K is the thermal conductivity; and c_p is the specific heat of the material. The initial condition of $T = T_0 =$ 298 K was applied at time $t = 0$.

Boundary condition 1: At the surface of the sample, the heat transfer equation is given by the balance between the laser energy absorbed by the sample and the radiation losses:

$$-K\left(\frac{\partial T(x,t)}{\partial x} + \frac{\partial T(y,t)}{\partial y} + \frac{\partial T(0,t)}{\partial z} \right) = \delta AI - \varepsilon\sigma\left(T(x,\, y,\, 0,\, t)^4 - T_0{}^4 \right)$$

$$\delta = 1 \qquad for\ 0 \le t \le t_p$$

$$\delta = 0 \qquad for\ t > t_p\,, \tag{4.2}$$

where A is the absorptivity of alumina; I is the laser intensity; ε is the emissivity of alumina for thermal radiation; σ is the Stefan-Boltzman constant; and t_p is the irradiation time.

Boundary condition 2: Convective boundary condition at the bottom surface of sample:

$$-K\left(\frac{\partial T(x,\, t)}{\partial x} + \frac{\partial T(y,\, t)}{\partial y} + \frac{\partial T(L,\, t)}{\partial z} \right) = h\left(T(x,\, y,\, L,\, t) - T_0 \right), \tag{4.3}$$

where h is the convective heat transfer coefficient; and L is the thickness of the sample. Major assumptions in the thermal analysis are listed here:

- Thermo-physical properties of the alumina are taken as independent of the temperature in view of difficulties associated with getting actual data and scarcity of adequate published literature on temperature dependent properties of alumina.
- Ceramics are highly absorbing materials. Absorptivity of alumina ceramic is considered constant and equal to 0.8 [50]. Due to high initial porosity, such high absorption of radiation is expected. Absorptivity of a material is a complex function and depends on temperature, surface condition, and wavelength of radiation. Due to lack of data on variation of absorptivity of alumina with these parameters, only constant value of absorptivity is used in the calculations.
- Effect of initial porosity in the alumina ceramic is considered while selecting the density and thermal conductivity used in the calculations [50].
- Initial condition corresponded to temperature of 298 K.

The solutions of the above heat transfer equations were obtained using heat transfer module of COMSOL Multiphysics^{TM} modeling package, which is based on finite element approach. The results were post processed to obtain the temporal and spatial distribution of temperature for the experimental laser processing fluences used for surface modifications of alumina. The properties of porous alumina used in calculations are presented in Table 4.1.

Table 4.1 Properties of alumina used in mathematical calculations.

Density, ρ (kg/m^3)	2280
Thermal Conductivity, K (W/m K)	14.6 [50]
Mass of the vapor molecule, m_v (Kg/atom)	1.693×10^{-25} [50]
Latent heat of evaporation, L_v (J/g^1)	1066.5 [50]
Convective heat transfer Coefficient, h (W/m^2 K)	200 [65]
Emissivity, ε	0.7 [66]
Specific heat, C_p (J/kg K)	800 [67]
Kinematic viscosity, υ (cm^2/s)	0.15 [68]

In the present context of laser surface modification of alumina ceramic, the temperature history is important for prediction of overall depth of melting from the temperature distribution inside the material and the fluid flow in the porous substrate assisted by evaporation-induced recoil pressure. The variation of surface temperature as a function of time for various laser fluences calculated from a three-dimensional thermal model is presented in Fig. 4.4. The figure indicated that at each laser fluence, the surface temperature rapidly increased with time, and reached maximum at a time corresponding to the irradiation time of the laser (t = 90 ms). Beyond irradiation time, the temperature decays until the room temperature is reached. Also, the temporal dependence of temperature increased rapidly with increasing the laser fluence employed for surface

modification. This resulted in higher maximum surface temperature at higher laser processing fluence (Fig. 4.5).

One of the significant observations in the temporal distribution of temperature is that the calculated maximum surface temperatures (Fig.4.4) exceeded the boiling point of alumina, T_v (~3800 K). Contrary to this, the various models of laser cutting, drilling, and welding have assumed that the surface temperature can not exceed the boiling point of the material and it always remain either equal to or less than the boiling point [69, 70]. Most of these models assumed the volumetric evaporation during the laser-material interaction and the evaporating front was simulated in terms of traditional 'Stefan problem'. However, during laser surface modification, the surface temperature can

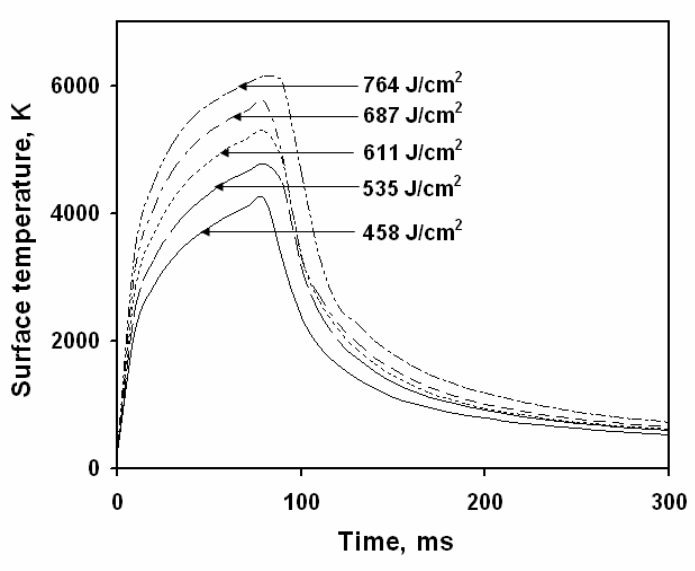


Fig. 4.4 Computed temporal evolution of surface temperature during laser surface modifications of alumina ceramic processed with a range of laser fluence from 458 J/cm^2 to 764 J /cm^2.

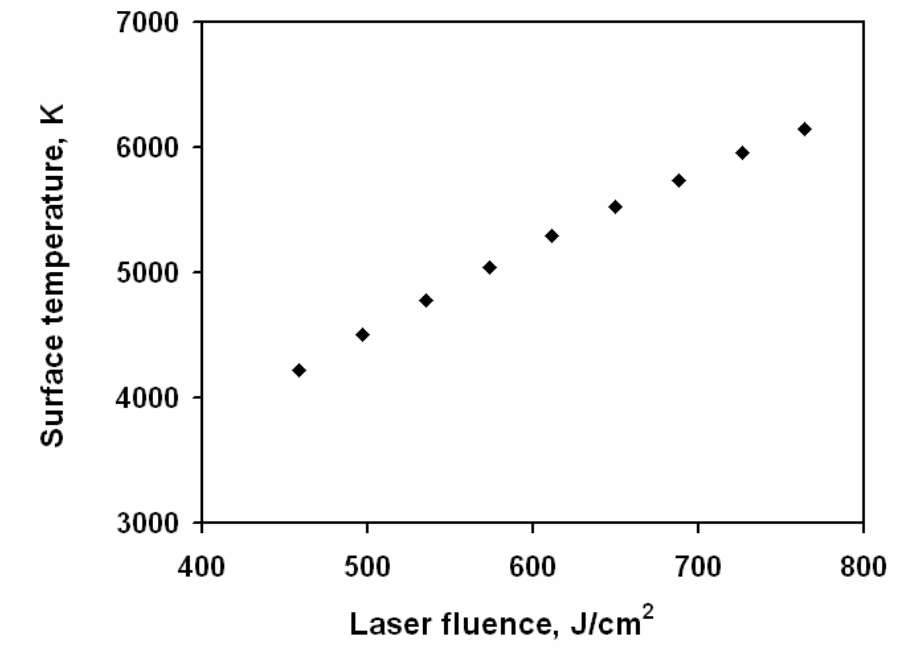


Fig. 4.5 Computed variation of maximum surface temperature with laser processing fluence during the surface modifications of alumina ceramic.

significantly exceed the boiling point provided the absorbed laser intensity is high and, therefore, only the evaporation at the surface is likely to occur. This is in agreement with the theoretical studies which indicated that volumetric evaporation can not take place during typical laser-material interactions observed in laser surface modifications [71]. Also, recently Semak et al. have suggested that evaporation front can not be simulated in terms of 'Stefan problem' and this approach can introduce significant errors in the prediction of temperatures [72]. Thus, the maximum surface temperatures in the range of 4000-6000 K, predicted from the thermal model employed in the present work are reasonable in view of laser surface processing with high power lasers.

The distribution of temperature below the surface of alumina material processed with various laser processing fluences is presented in Fig. 4.6. The figure indicated that the temperature gradually decreases below the surface of material and becomes uniform by reaching the initial temperature of the sample at about 2.5 mm below the surface. The depth of melting due to thermal effects corresponds to the distance from the surface to inside point of the material where temperature becomes equal to melting point. This can be easily obtained by tracing melting point the temperature distribution inside the material.

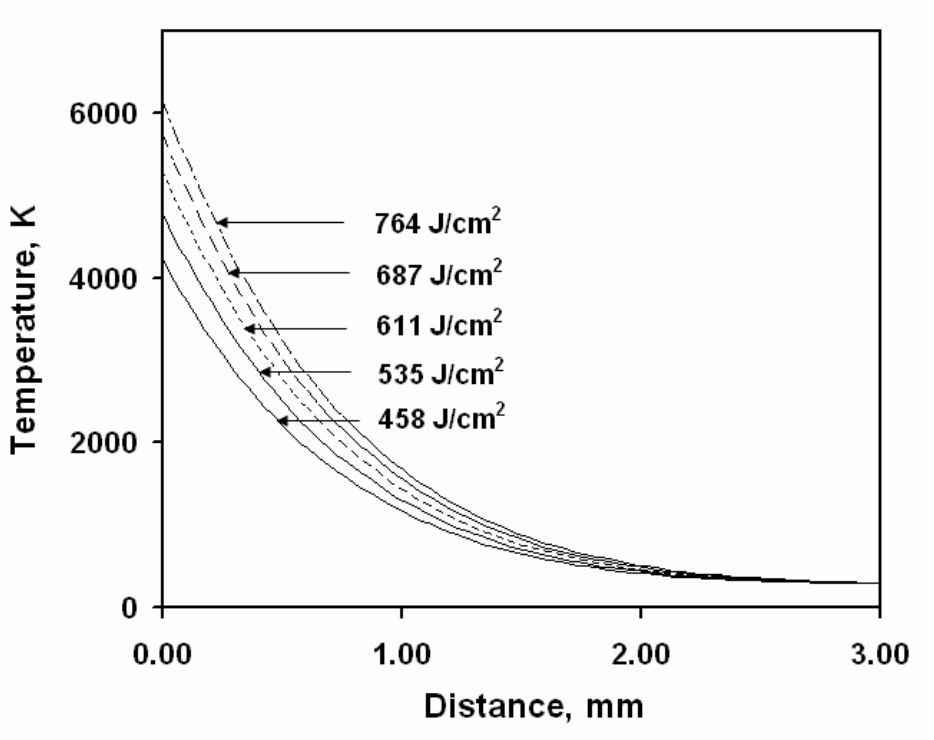


Fig. 4.6 Computed temperature distribution below the surface of alumina ceramic surface modified with a range of laser processing fluence from 458 J/cm^2 to 764 J /cm^2.

4.3 Temporal Evolution of Recoil Pressure

In addition to the thermal effects, the depth of melting is also influenced by hydro-dynamic effects during laser-material interactions. Particularly for the porous substrate, effects such as surface evaporation play important role in determining effective depth of melting. Early analysis of the evaporation process from the surface of material irradiated with laser radiation of intensity as high as 10^{13}-10^{14} W/m^2 was carried out by Anisimov [16, 17]. Based on the assumption that the absorption of laser radiation by the generated vapor plume as a result of surface evaporation is not appreciable, Anisimov proposed the velocity distribution functions for the vapor molecules [16]. For vapor molecules emitted from the evaporating surface, the velocity distribution function (f_1) is expressed as

$$f_1 = n_0\left(\frac{m_v}{2\pi kT_s}\right)^{3/2} \exp\left(-\frac{m_v\left(v_x{}^2 + v_y{}^2 + v_z{}^2\right)}{2kT_s}\right), \qquad \text{for } v_z > 0 \tag{4.4}$$

and, for vapor molecules returned to the evaporating surface, the velocity distribution function (f_2) is expressed as

$$f_2 = \beta\, n_1\left(\frac{m_v}{2\pi kT_1}\right)^{3/2} \exp\left(-\frac{m_v\left(v_x{}^2 + v_y{}^2 + (v_z - u_1)^2\right)}{2kT_1}\right), \quad \text{for } v_z < 0 \tag{4.5}$$

where k is the Boltzmann constant; m_v is the mass of the vapor molecule; T_s and n_0 are the surface temperature and the molecule number density at the evaporating surface respectively; and T_1 and n_1 are temperature and the molecule number density at the outer boundary of the kinetic layer formed near evaporating surface respectively. u_1 is the velocity at the outer boundary of the kinetic layer; β is the coefficient; and v_x, v_y, and v_z are the velocity components on the evaporating surface of the material. Based on these

relationships, an equation for calculation of evaporation-induced recoil pressure, p_s, at the evaporating surface from the surface temperature, which in turn depends on the incident laser energy density is given by [16]

$$\frac{p_s}{Q_0 / S} = \frac{1.69}{\sqrt{L_v}}\left(\frac{b}{1+2.2b^2}\right), \tag{4.6}$$

where Q_0 is the incident laser power; S is the area of laser spot; L_v is the latent heat of evaporation; and $b^2 = kT_s / m_v L_v$. Thus, the temperature fields determined from the three dimensional thermal analysis can facilitate the calculation of evaporation-induced recoil pressure at the evaporating surface during laser surface modifications of alumina ceramic using the experimentally verified physical model of melt hydrodynamics and laser-induced evaporation proposed by Anisimov.

The temporal evolution of the evaporation-induced recoil pressure during laser surface modification of alumina ceramic with laser processing fluences employed in the present effort is presented in Fig. 4.7. As indicated in the figure, during surface modification, the recoil pressure rapidly increases and reaches maximum value at the time corresponding to the laser irradiation time (t = 90 ms). The temporal evolution of recoil pressure showed the similar trend as obtained in the temporal evolution of surface temperature (Fig. 4.4) suggesting the strong dependence of evaporation-induced recoil pressure on the surface temperature. The observation is in agreement with the physical model of melt hydrodynamics and laser-induced evaporation proposed by Anisimov [16]. The variation of maximum evaporation-induced recoil pressure with the laser processing fluence during laser surface modification of alumina ceramic is presented in Fig. 4.8.

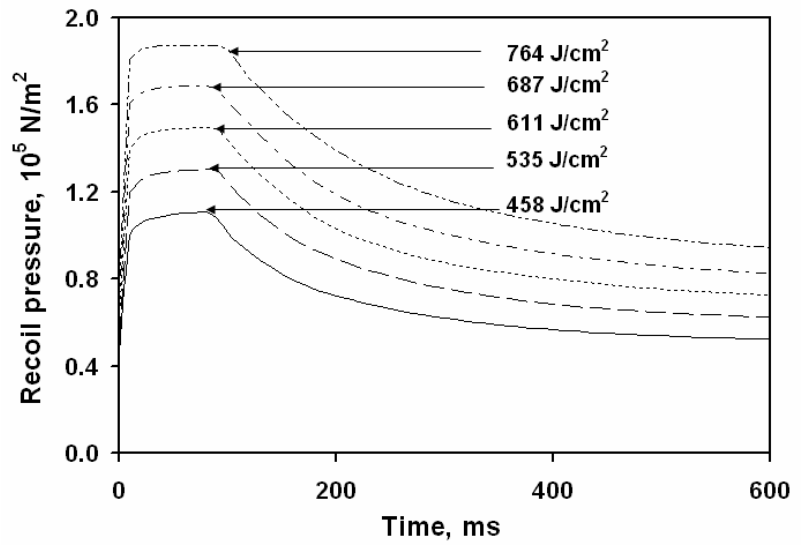


Fig. 4.7 Computed temporal evolution of evaporation-induced recoil pressure during the laser surface modification of alumina ceramic processed with a laser processing fluence of 458 J /cm^2.

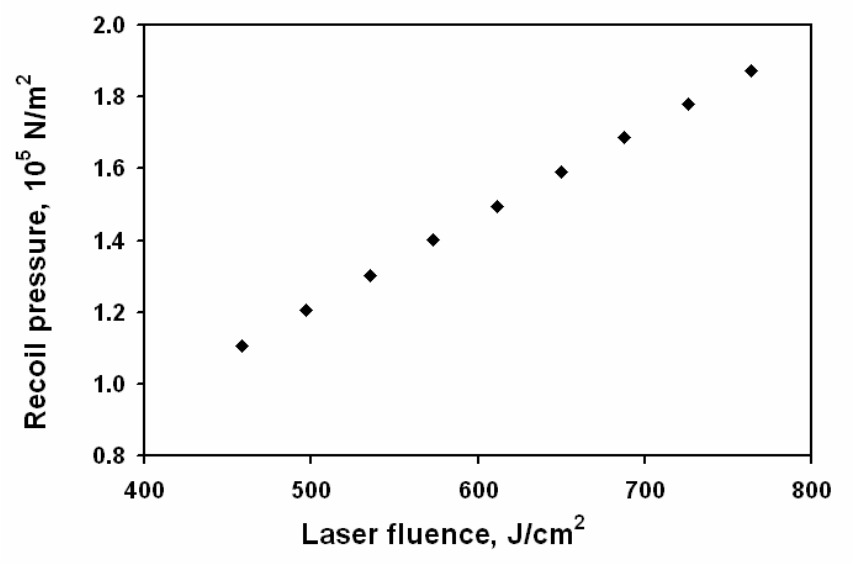


Fig. 4.8 Computed evaporation-induced maximum recoil pressure as a function of laser processing fluence employed during the laser surface modifications of alumina ceramic.

The recoil pressure generated due to surface evaporation during surface modifications is a strong function of laser fluence and increases almost linearly with laser fluence. The values of evaporation pressures are in strong agreement with the analysis of Anisimov, which suggested that the if surface temperature reached above the boiling point of material, the recoil pressure must be equal or higher than 0.55 p_s, where p_s is the saturated vapor pressure, which by definition, is 1 atm (~1.01325 × 10^5 N/m^2) at boiling temperature [16].

4.4 Melt Infiltration and Effective Depth of Melting

As explained in the previous section, the evaporation-induced recoil pressure generated at the surface during laser-material interaction is expected to drive the flow of the molten material into the porous substrate. This effect is clearly seen in Fig. 4.9, which presents a high magnification SEM micrograph in the interfacial region between the laser modified surface region and the underlying porous material. The figure also indicates the dendritic microstructure corresponding to the rapidly solidified molten alumina around the un-melted alumina particles. The dendritic microstructure of rapidly solidified alumina is characteristic of the laser surface processing which is associated with rapid cooling rates of the order of 10^2 K/s.

The influence of melt infiltration on the depth of melting requires the modeling of fluid flow effects under the regimes of evaporation induced recoil pressures. The calculation of depths of infiltration in the porous substrate based on fluid flow models. An analysis of viscous fluid flow through porous media is generally described in terms of

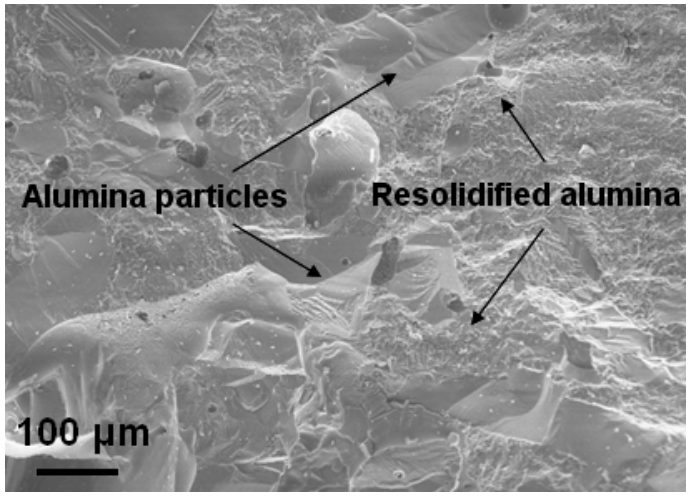


Fig. 4.9 High magnification SEM micrograph of the interfacial region of the laser surface modified alumina illustrating the infiltration of molten material into the underlying porous material assisted by evaporation-induced recoil pressures.

Darcy's law which states that average fluid velocity vector is proportional to the average pressure gradient, Δp. The fluid flow problem was modeled by Carman and Kozeny for calculation of flow rate by representing the porous media as an array of cylindrical tubes. The Carman-Kozeny equation which is derived from the Darcy's law can be expressed as [73]

$$\frac{dp}{dz} = -\frac{180\mu\, u\, (1-\omega)^2}{d_s{}^2\, \omega^3}, \tag{4.7}$$

where dp/dz is the pressure gradient across the melt depth; μ is the dynamic viscosity; u is the flow rate; ω is the porosity; and d_s is the average alumina particle diameter. The

pressure difference across the melt is given by the head of melt (corresponding to melt depth) and the evaporation induced recoil pressure:

$$\Delta p = -(\rho g h_1 + p_s) \tag{4.8}$$

where g is the acceleration due to gravity; and h_1 is the head of melt corresponding to the depth of melting. The above equations result in the calculation of linear flow rate, u (m/s) of molten alumina through the porous substrate. Actual depth of melting due to infiltration can then be obtained by multiplying the linear velocity with the time during which the material remains above the melting point determined from the temporal temperature distribution. Finally, the overall depth of melting can be calculated by integrating the depth of melting due to recoil pressure-induced infiltration with the depth of melting calculated from thermal analysis by tracing the melting temperature inside the material during surface modification. It has been reported that under certain thermal conditions shape of the melt pool is also affected by the surface tension effects in addition to the presence of recoil vapor pressure and thermocapillary forces. Surface tension and viscosity are determined by the same intermolecular forces [74]. Hence surface tension varies directly with the viscosity. A direct proportion between the two quantities has been established with a hard sphere model based on the fact that the surface tension and viscosity can be expressed as integrals over the product of interatomic forces and the pair distribution function [75]. The kinematic viscosity of alumina at the melting temperature (~2323 K) is approximately 0.15 cm^2/s which is very negligible. Hence by taking into account the direct variation of surface tension with viscosity, it was assumed that the corresponding effect of surface tension on the melt pool

geometry would also be negligible under the processing conditions employed in the present work. Hence the surface tension related effects were not considered in the calculation of melt infiltration.

Comparison of experimental values of depth of melting with the values calculated from the heat transfer and the fluid flow equations are presented in Fig. 4.10. The maximum depth of melting was calculated from the thermal model by tracing the melting point in the temperature distribution below the surface of molten alumina ceramic corresponding to the irradiation time (Fig. 4.6). As shown in the Fig. 4.10, the calculated depth of melting increases with laser processing fluence due to melting front advancing deeper into the material with increasing laser processing fluence. However, the thermal model underestimates the depths of melting compared to the experimental values. From the previous discussion, the laser-material interactions during the laser surface modification of porous alumina ceramics are associated with the evaporation-induced recoil pressures. These recoil pressures determined by the surface temperature, plays the vital role in driving the flow of fluid into the porous substrate. Such a recoil pressure assisted infiltration of fluid in the porous substrate tends to increase the observed values of depths of melting. Fig. 4.10, therefore, also presents a set of data points for the depths of melting calculated from the integrated approach involving the Carman-Kozeny equations (for the infiltration effects due liquid head and evaporation-induced recoil pressure) and the thermal analysis (for the effects of temperature distribution below the surface of alumina material). As indicated in the figure, such an integrated approach provides a better agreement between the experimental and predicted depths of melting. However, deviation of the predicted depths of melting from the experimental values

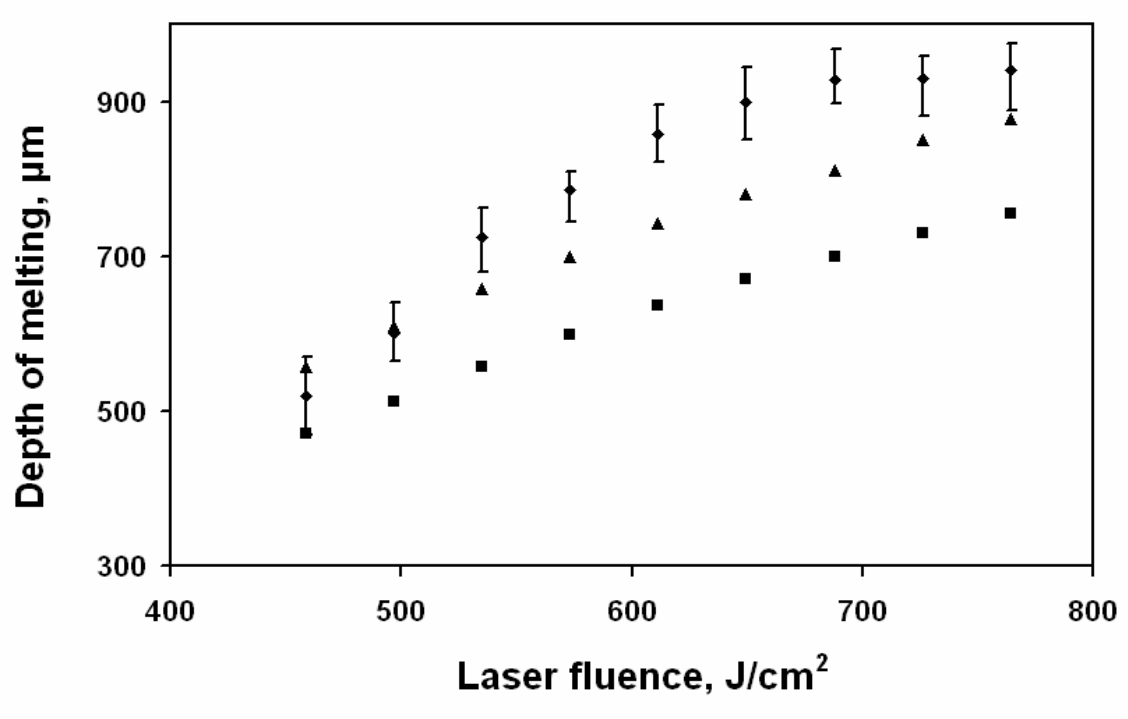


Fig. 4.10 Comparison of computed depth of melting from thermal and fluid flow model with experimental depth of melting (♦, Experimental; ■, thermal model; and ▲, integrative thermal and fluid flow model).

especially at the higher laser processing fluence may be due to the simplification of assumptions in the thermal model such as temperature independence of the thermo-physical properties and the idealized model of melt infiltration. Also, due to the dynamic nature of physical, chemical and microstructural phenomena associated with the laser interactions particularly with porous alumina, the accuracy of predictions is expected to be influenced by how well the complex interactions are defined in the mathematical calculations.

4.5 Influence of Thermal Effects on Evolution of Grain Structure

The thermal effects explained in the previous sections in the context of predicting the depth of melting also influences evolution of surface grain structure. The most important thermal parameter for such analysis is the cooling rate. The solution of the heat flow equation gives the temperature distribution within the material from which the temperature gradient (G) and the velocity of solid/liquid interface (R) can be calculated by the procedure outlined in reference [76]. Finally, cooling rate is given by the product of G and R. The well established relationship in the solidification theories exists between the secondary dendrite arms spacing ($SDAS$) and the cooling rates (T_c) and is given by [46]:

$$SDAS = A\,(T_c)^{-n}, \tag{4.9}$$

where A and n are material related constants. Grain size depends on the conditions of both nucleation and growth, of which, only the conditions of growth are explicitly dependent on the cooling rate. Hence under identical nucleation conditions during solidification, the similar equation can be written for the relationship between the grain size and the cooling rate with different values of constants [77]. The calculated values of cooling rate are presented in Table 4.2. The table clearly indicates that as the laser fluence increased the cooling rate decreased resulting in larger grain size of the faceted surface grains at higher laser fluences (Fig. 4.11). This is in general agreement with the solidification theories which indicate the decrease in grain size with increasing cooling rate. The cooling rates in the range of 2-6 $\times 10^2$ K/s corresponding to laser fluences 458-573 J/cm^2 appeared to be conducive to the growth of well defined multi-plane faceted

Table 4.2 Summary of the values of temperature gradient (G) at solid/liquid interface, solidification rate (R) and cooling rate calculated from thermal model for laser surface modified alumina at various laser fluences.

Laser Fluence (J/cm^2)	***G* (K/m)**	***R* (m/s)**	**Cooling Rate (K/s)**
458	9.79×10^4	6.07×10^{-3}	5.94×10^2
496	8.30×10^4	6.05×10^{-3}	5.02×10^2
535	6.81×10^4	5.42×10^{-3}	3.69×10^2
573	5.16×10^4	5.05×10^{-3}	2.60×10^2
611	4.04×10^4	4.88×10^{-3}	1.97×10^2
649	3.12×10^4	4.56×10^{-3}	1.42×10^2
687	2.57×10^4	4.21×10^{-3}	1.08×10^2
726	1.99×10^4	3.54×10^{-3}	0.70×10^2

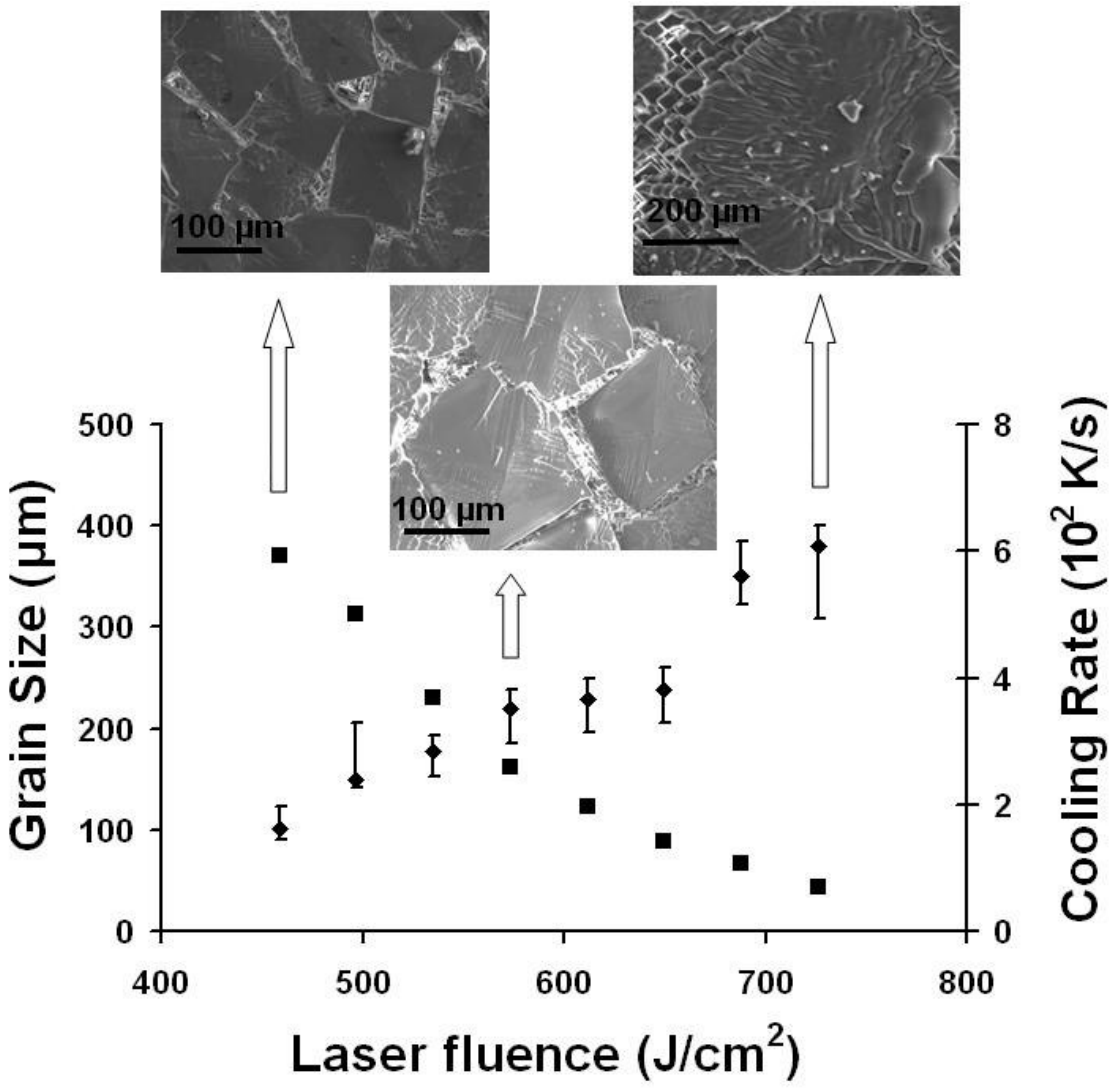


Fig. 4.11 Grain size, cooling rate, and corresponding SEM micrographs of the surface grains in laser surface modified alumina at various laser fluences [(♦) grain size and (■) curvature factor].

grains (Fig. 4.11); whereas, further drop in cooling rates to the range 0.7-2 × 10^2 K/s corresponding to laser fluences 611-726 J/cm^2 generated the near circular grains of ill-defined facets (Fig. 4.11). Such a transition from well defined to ill-defined facets in the grain may be due to simultaneous growth of multiple planes at intermediate ratio of growth velocities at lower cooling rates.

4.6 Summary

Analysis of thermal effects during laser interaction with porous alumina ceramic indicated that surface of the molten material undergoes surface evaporation. It was found that rapid surface evaporation generated high (> 10^5 Pa) recoil pressures during laser surface modification. Such high recoil pressures seemed to drive the flow of molten material into the underlying porous substrate, thus extending the depth of melting. An integrated modeling approach combining thermal and fluid flow analysis predicted the overall depth of melting. The integrated approach was found to yield better agreements between predicted and experimental values of depths of melting compared to thermal modeling approach alone. Such predictions of the depths of modification based on fundamental physical processes during laser-material interactions are important in tailoring the microstructure/properties during surface modification experiments. The mechanical property modification, especially the fracture toughness relevant to this type of material (ceramic) and intended application (machining), based on the type and extent of laser surface structuring are explained in detail in next chapter with focus on fracture toughness improvements.

Chapter 5

Fracture Properties of Laser Surface Modified Alumina

Previous chapters dealt with the analysis of the type and extent of physical effects during laser surface modification of alumina ceramics and its influence on microstructure evolution. These physical and microstructural effects are expected to influence a host of mechanical properties of laser surface modified alumina ceramic. One of such important properties relevant to alumina ceramic material and its intended application is the fracture toughness. Thus, the microstructure of the laser modified alumina ceramic is expected to influence fracture properties of the ceramic.

The fracture toughness of materials is generally determined using two methods: bending method and indentation method [78]. In bending method, a V-notch of finite dimensions is introduced in the beam of sample which is then tested in bending test arrangement. The fracture toughness is determined from maximum load, specimen dimension and notch dimensions. The method produces highly reproducible results for highly dense monolithic material. However, the simplest and most popular technique for measuring the fracture toughness of ceramic materials is based on indentation method. In this technique, no standard test samples have to be prepared saving time and costs. Only polished and flat surfaces (less than 1 mm^2) are required and fracture toughness measurements can be directly calculated from surface crack lengths, hardness and Young's Modulus of the sample. A voluminous literature is available on the evaluation of fracture toughness of ceramic material using indentation technique [79-84]. In case of the

laser surface modified alumina ceramic, indentation is most suitable for determining the fracture toughness of the modified alumina ceramic. As discussed earlier, the typical depths of modification is in the range of 500-800 μm, whereas, typical depths of Vickers indentation is in the range of 8-10 μm. Thus, the depth of surface modified alumina is significantly larger than the depth of indentation and hence Vickers indentation technique is expected to give representative fracture toughness of the surface modified region without interference from the underlying porous alumina. This chapter discusses the results on fracture toughness of laser surface modified alumina obtained using microindentation technique. Also, the influence of solidification microstructure on the fracture behavior of laser surface modified alumina ceramics is discussed.

5.1 Influence of Microstructure on Fracture Toughness

A typical Vickers hardness indentation in the polished laser surface modified alumina ceramic is presented in Fig. 5.1. Vickers hardness, H (GPa) was determined from the diagonal length measurements using the relationship:

$$H = 0.0018544\left(\frac{P}{d^2}\right), \tag{5.1}$$

where P is the applied load (N) and d is the mean indentation diagonal length (mm).[14] Fracture toughness can be obtained by measuring the length of the radial cracks emerging from the corners of the indentation. The fracture toughness, K_{IC} (MPa.m$^{-1/2}$), is given by:

$$K_{IC} = 0.016\left(\frac{E}{H}\right)^{1/2}\frac{P}{c^{3/2}}, \tag{5.2}$$

where E is the Young's Modulus (380 GPa) and c is the diagonal crack length (m) [45].

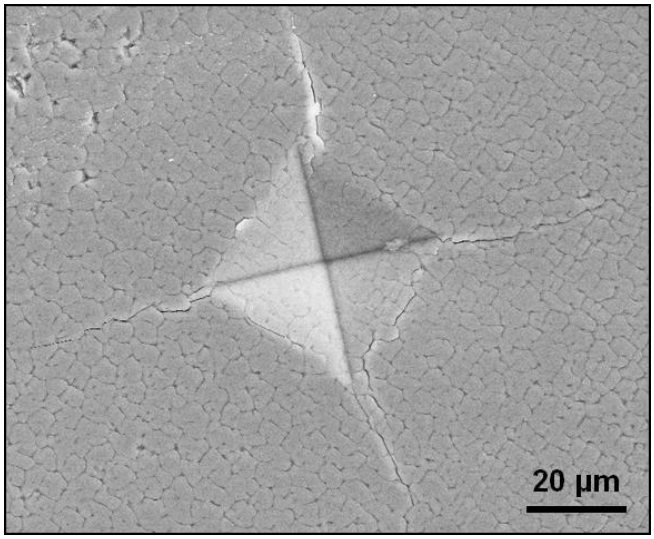


Fig. 5.1 Typical Vickers hardness indentation in laser surface modified alumina ceramic.

The variation of fracture toughness with laser processing fluence is presented in Fig. 5.2. The figure indicates that fracture toughness increases with laser fluence employed for surface modification of alumina ceramic. It seems that such improvements in fracture toughness with increasing laser fluence resulted from associated microstructural changes. One of the important microstructural parameters during rapid solidification of alumina ceramics is secondary dendrite arms spacing (SDAS). SDAS depends on the thermal effects during solidification and influences the mechanical properties of the solidified material. Fig. 5.3 indicates that SDAS increases with increasing laser fluence. Fig. 5.3 also presents variation of calculated cooling rates with laser fluence based on the thermal analysis presented in previous chapter. Increasing laser fluence corresponded to coarsening of the SDAS. Such coarser microstructure is expected to offer increased resistance to initiation and propagation of cracks resulting in better fracture toughness [85].

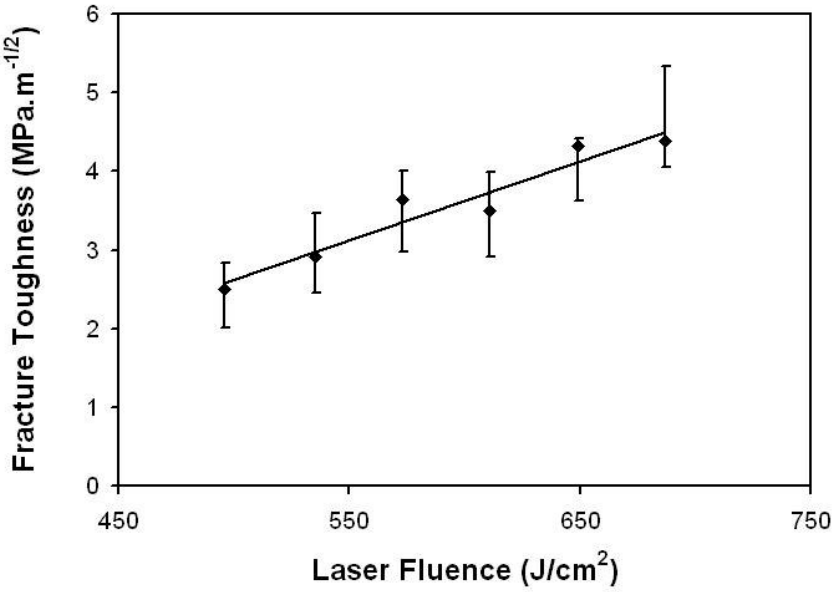


Fig. 5.2 Variation of fracture toughness (K_{IC}) of laser surface modified alumina ceramic with laser fluence.

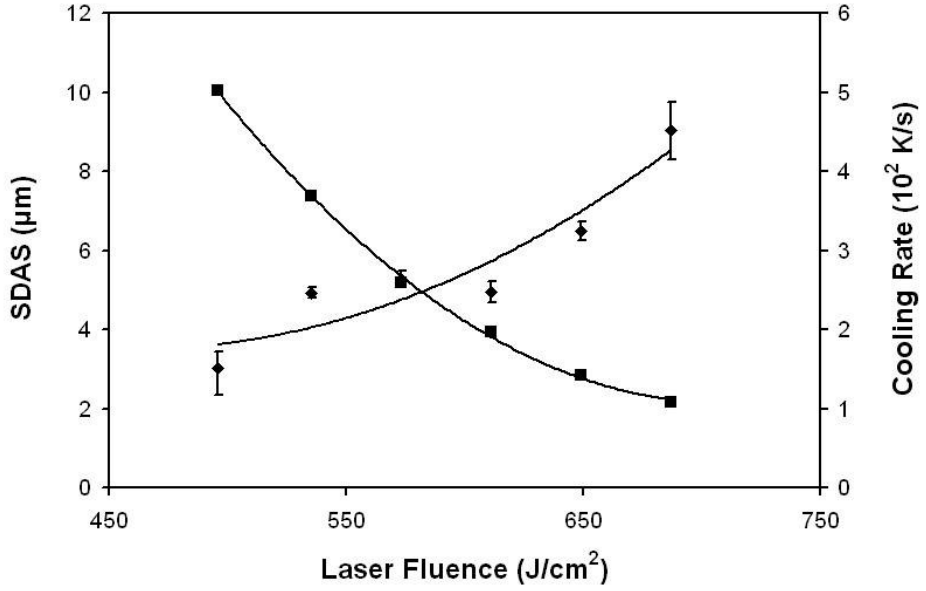


Fig. 5.3 Variation of secondary dendrite arms spacing, SDAS (♦) and calculated cooling rate (■) with laser fluence employed for surface modification of alumina ceramic.

High magnification micrographs near the indentation corners of the alumina samples surface modified with lower (535 J/cm^2) and higher (649 J/cm^2) laser fluence are presented in Fig. 5.4. The figure clearly indicates that at lower laser fluence, the fracture mode is predominantly mixed (transgranular and intergranular). However, the fracture modes changes to predominantly intergranular at higher laser fluence. Such transition of fracture mode from mixed (fast fracture) to intergranular (slow fracture) with increasing laser fluence seems to be due to coarsening of the microstructural features such as SDAS. Thus laser surface modification of alumina ceramic to produce faceted and crystallographically textured surface microstructure present a highly flexible technique for improving the fracture toughness by controlling the thermal effects and microstructural parameters.

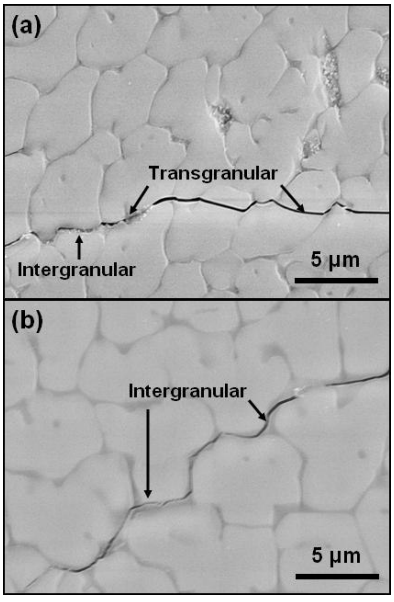


Fig. 5.4 High magnification scanning electron micrographs of laser surface modified alumina ceramic after indentation fracture: (a) 535 J/cm^2 and (b) 649 J/cm^2.

5.2 Summary

Laser surface modification of porous alumina ceramic resulted in the crack-free densification of surface while retaining the bulk porous structure. The densified surface was characterized by formation of faceted and crystallographically textured surface mocrostructure. It was found that fracture toughness of the laser structured alumina ceramic increased with increasing laser fluence. Improvement in the fracture toughness is primarily due to better surface densification of the ceramic. This may also due to coarsening of the microstructural feature (SDAS) at higher laser fluence. Coarser microstructural features in faceted and crystallographically textured surfaces were found to offer better resistance to the initiation and propagation of cracks as indicated by transition in fracture mode from predominantly mixed (fast) to predominantly intergranular (slow) at higher laser fluence. Laser surface modification thus established the feasibility of improving the properties of lightweight structural alumina ceramics by optimizing the laser processing parameters.

Chapter 6

Conclusions and Suggested Future Work

6.1 Conclusions

- Laser surface modification of porous alumina ceramics resulted in formation of highly dense and refined microstructure characterized by multifaceted pyramidal grains with well defined edges and vertices.
- In spite of rapid cooling rates (~10^2 K/s) encountered during laser surface modifications, stable α-alumina phase was observed primarily due to availability of catalytic nucleation sites provided by underlying material.
- The faceting of the surface grains was associated with the development of surface crystallographic texture corresponding to (1 1 0) planes. Laser processing parameters strongly influenced the surface crystallographic texture and the associated faceting of the grains. Intermediate laser fluence (573 J/cm^2) within a range 458 J/cm^2 to 726 J/cm^2 fluences resulted in most pronounced surface texture.
- Grain size of the faceted surface grains was found to be increased with increasing laser fluence. This was primarily due to slower cooling rates associated with higher laser fluences in accordance with the established solidification theories.
- Fractal analysis of series of digitized surface microstructures from the laser surface modified alumina indicated that useful correlations can be derived between the fractal dimensions and the surface microstructural features such as grain size, porosity and roughness.

- An integrative modeling approach combining the thermal and the fluid flow analysis resulted in better agreement between the predicted and experimental values of depths of melting.
- Within a range of laser processing parameters, the maximum depths of melting in laser surface modified ceramics was found to be increased with increasing laser fluence. This was due to deeper penetration of thermal energy at higher fluences.
- During surface modifications, the surface of the melt was subjected to very high recoil pressures (> 10^5 Pa) induced by rapid surface evaporation. The temporal evolution of recoil pressure indicated that recoil pressure reaches maximum value for irradiation time of laser beam. Such high recoil pressure seemed to drive the flow of molten material into the underlying porous substrate, thus extending the depth of melting.
- Laser surface modifications resulted in improvements in micro-indentation fracture toughness with increasing laser fluence primarily due coarsening of grain structure. The coarser grains seem to offer increased resistance to initiation and propagation of cracks indicated by transition in fracture mode from predominantly mixed (intergranular and transgranular) to predominantly intergranular resulting in better fracture toughness.

6.2 Suggested Future Work

Most of the present work dealt with the evolution of surface microstructure during laser surface modification of alumina ceramic grinding wheels for precision machining

applications. Also, attempts had been made to develop simplified models taking into consideration physical effects during laser interaction with porous alumina ceramic. Having established the feasibility of this technique and gained the understanding of microstructure development, implementation of this technique in actual manufacturing environment necessitate the detailed studies on other important aspects of the process. In view of this, following major directions for future research work are suggested:

- Advanced modeling of the physical processes taking place during laser interaction with porous alumina ceramic. Thermal modeling should take into account temperature dependent thermo-physical properties and effects such as capillary effects, shear stresses, etc.
- Detailed characterization of mechanical properties of the laser modified alumina ceramic to establish the integrity of the surface modified layer on the alumina grinding wheel during machining/grinding application.
- Detailed experimental studies on the effectiveness of the laser surface modified grinding wheel in the micro-scale removal of material. Within the laboratory setting, it is necessary to determine material removal rates, surface finish of the workpiece, life of the laser surface modified alumina grinding wheel, and processing speeds during precision grinding/machining of advanced materials.
- In view of the varying abrasive sizes, porosities and wheel thicknesses, it will be important to understand the microstructure evolution in laser modified grinding wheels with varying surface microstructures. This may facilitate the implementation of laser surface modification for wide range of commercial grinding wheels.

References

[1] C. Santos, K. Strecker, S. A. Baldacim, O. M. M. Silva, and C. R. M. da Silva, Mechanical properties improvement related to the isothermal holding time in Si_3N_4 ceramics sintered with an alternative additive. International Journal of Refractory Metals and Hard Materials 21:245-250 (2003).

[2] E. Medvedovski, Wear-resistant engineering ceramics. Wear 249:821-828 (2001).

[3] J. Dusza and M. Steen, Fractography and fracture mechanics property assessment of advanced structural Ceramics. International Materials Review 44:165-216 (1999).

[4] P. Reis, V. Filho, J. Davim, X. Xu, and J. Ferreira, Wear behavior on advanced structural ceramics: α-sialon matrix reinforced with β-sialon fibers. Materials & Design 26:417-423 (2005).

[5] E. Cappelli, S. Orlando, D. Sciti, M. Montozzi and L. Pandolfi, Ceramic surface modifications induced by pulsed laser treatment. Applied Surface Science 154-155:682-688 (2005).

[6] K. H. Gahr and J. Schneider, Surface modifications of ceramics for improved tribological properties. Ceramic International 26:363-370 (2000).

[7] L. Bradley, L. Li and F. H. Stott, Flame-assisted laser surface treatment of refractory materials for crack-free densification. Materials Science and Engineering A 278:204-212 (2000).

[8] S. P. Harimkar, A. N. Samant. A. A. Khangar and N. B. Dahotre, Prediction of solidification microstructures during laser dressing of alumina-based grinding wheel material. Journal of Physics D: Applied Physics 39:1642-1649 (2006).

[9] W. M. Steen, Laser materials processing. Springer-Verlag, London (1991).

[10] N. B. Dahotre and S. P. Harimkar, Laser Fabrication and Machining of Materials. Springer, New York (2007).

[11] A. J. Welch, C. Gardner, Optical and thermal response of tissue to laser radiation. CRC Press, Baca Raton (2002).

[12] W. W. Duley, Laser processing and analysis of materials. Plenum Press, New York (1983).

[13] H. S. Carslaw, J. C. Jaeger, Conduction of heat in solids. Oxford University Press, Oxford (1959).

[14] D. Rosenthal, The theory of moving sources of heat and its application to metal treatment. Transactions of the ASME 68:849-866 (1946).

[15] M. C. Flemings, Solidification processing. McGraw Hill, New York (1974).

[16] S. I. Anisimov, Vaporization of metal absorbing laser radiation. Soviet Physics JETP 27:182-183 (1968).

[17] S. I. Anisimov and V. A. Khokhlov, Instabilities in laser-matter interaction. CRC Press, Boca Raton (1995).

[18] D. Bäuerle, Laser processing and chemistry. Springer, Berlin (2000).

[19] M. Von Allmen, Laser-beam interactions with materials. Springer-Verlag, Berlin (1987).

[20] A. Vogel and V. Venugopalan, Mechanisms of pulsed laser ablation of biological tissues. Chemical Reviews 103:577-644 (2003).

[21] K. P. Thompson, Q. S. Ren, and J. M. Parel, Therapeutic and diagnostic application of lasers in ophthalmology. In: R. W. Waynant (Ed.) Lasers in medicine. CRC Press, Boca Raton (2002).

[22] A. I. Katsamas and G. N. Haidemenopoulos, Surface hardening of low-alloy 15CrNi6 steel by CO2 laser beam. Surface Coatings and Technology 115:249-255 (1999).

[23] J. Mazumder, Laser heat treatment: state of the art. Journal of Metals 35:18-26 (1983).

[24] Y.W. Kim, P. R. Strutt and H. Nowotny, Laser melting and heat treatment of M2 tool steel: A microstructural characterization. Metallurgical and Materials Transactions A 10:881-886 (1979).

[25] P. S. Mohanty and J. Mazumder, Solidification behavior and microstructural evolution during laser beam-material interaction. Metallurgical and Materials Transactions B 29:1269-1279 (1998).

[26] K.G. Watkins, M.A. McMahon, and W.M. Steen, Microstructure and corrosion properties of laser surface processed aluminium alloys: a review. Materials Science and Engineering A 231:55-61 (1997).

[27] A. Y. Fasasi, M. Pons, C. Tassin, A. Galerie, G. Sainfort and C. Polak, Laser surface melting of mild steel with submicronic titanium carbide powders. Journal of Materials Science 29:5121-5126 (1994).

[28] V. Oliveira, R. Vilar, and O. Conde, Excimer laser ablation of Al_2O_3-TiC ceramics: laser induced modifications of surface topography and structure. Applied Surface Science 127-129:831-836 (1998).

[29] C. J. Arcoria, M. G. Lippas, and B. A. Vitasek, Enamel surface roughness analysis after laser ablation and acid-etching. Journal of Oral Rehabilitation 20:213-224 (1993).

[30] T. Sumomogi, H. Sakai, M. Nakata, and T. Endo, Nanoscale evaluation of surface roughness of metal films prepared by laser ablation. Applied Physics A 66:S815-S818 (1998).

[31] C. G. Levi, V. Jayaram, J. J. Valencia and R. Mehrabian, Phase selection in electrohydrodynamic atomization of alumina. Journal of Materials Research 3:969-983 (1988).

[32] T. C. Buttery, A. Statham, J. B. Percival and M. S. Hamed, Some effects of dressing on grinding performance. Wear 55:195-219 (1979).

[33] N. R. Babu, V. Radhakrishnan and Y. V. G. S. Murti, Investigations on laser dressing of grinding wheels-Part I: a preliminary study. ASME Journal of Engineering for Industry 111:244-252 (1989).

[34] N. R. Babu and V. Radhakrishnan, Investigations on laser dressing of grinding wheels-Part II: Grinding performance of a laser dressed aluminum oxide wheel. ASME Journal of Engineering for Industry 111:253-261 (1989).

[35] C. Zhang C and Y. C. Shin, A novel laser-assisted truing and dressing technique for vitrified CBN wheels. International Journal of Machine Tools and Manufacture 42:825-835 (2002).

[36] A. A. Khangar, E. A. Kenik and N. B. Dahotre, Microstructure and microtexture in laser-dressed alumina grinding wheel material. Ceramic International 31:621-29 (2005).

[37] M. J. Jackson, G. M. Robinson, N. B. Dahotre, A. Khangar and R. Moss, Laser dressing of aluminium oxide grinding wheels. British Ceramic Transactions 102:237-245 (2003).

[38] A. Khangar A and N. B. Dahotre, Morphological modification in laser-dressed grinding wheel material for microscale grinding. Journal of Materials Processing Technology 170:1-10 (2005).

[39] S. Schreck and K. H. Z. Gahr, Laser-assisted structuring of ceramic and steel surfaces for improving tribological properties. Applied Surface Science 247:616-622 (2005).

[40] A. Kurella, N. B. Dahotre, Phase and morphological evolution in laser textured zirconia coating on Ti alloy. TMS Outstanding Student Paper (2005)

[41] L. Bradley, L. Li, and F. H. Stott, Flame-assisted laser surface treatment of refractory materials for crack-free densification. Materials Science and Engineering A 278:204-212 (2000)

[42] J. Heywood, Grinding wheels and their uses, The Penton Publishing Company, Cleveland, OH (1938).

[43] B. D. Cullity, Elements of X-ray diffraction, Addison-Wesley Publishing Co, Reading (1978).

[44] H. P. Klug and L. E. Alexander, X-ray diffraction procedures for polycrystalline and amorphous materials. John Wiley & Sons, New York (1954).

[45] K. A. Khalil and S. W. Kim, Effect of Processing Parameters on the mechanical and microstructural behavior of ultra-fine Al_2O_3-(ZrO_2 + 18%mol Y_2O_3) bioceramic, densified by high-frequency induction heat sintering. International Journal of Applied Ceramic Technology 3:322-330 (2006).

[46] W. Kurz and D. J. Fisher, Fundamentals of Solidification. Trans Tech, Zurich (1998).

[47] J. W. Cahn, Theory of crystal growth and interface motion in crystalline materials. Acta Metallurgica 8:554-562 (1960).

[48] J. A. Sekhar, A. Bharti, and R. Trivedi, Faceted-nonfaceted dendritic transitions during the laser processing of Al_2O_3-1.0 Wt Pct MgO. Metallurgical Transactions A 20: 2191-2194 (1989).

[49] K. A. Jackson, D. R. Ulhmann, and J. D. Hunt, On the nature of crystal growth from the melt. Journal of Crystal Growth 1:1-36 (1967).

[50] W. H. Gitzen, Alumina as a ceramic material. American Ceramic Society, Westerville (1970).

[51] M. Li, K. Nagashio, and K. Kuribayashi, Containerless solidification of undercooled oxide and metallic eutectic melts. Materials Science and Engineering A 375-377:528-533 (1990).

[52] R. Krishnan, S. Dash, R. Kesavamoorthy, C. B. Rao, A. K. Tyagi, and B. Raj, Laser surface modification and characterization of air plasma sprayed alumina coatings. Surface Coatings and Technology 200:2791-2799 (2006).

[53] S. Ruppi, Deposition, microstructure and properties of texture-controlled CVD α-Al_2O_3 coatings. International Journal of Refractory Metals and Hard Materials 23:306-316 (2005).

[54] A. van der Drift, Evolutionary selection, a principle governing growth orientation in vapour-deposited layers. Philips Research Report 22:267-288 (1967).

[55] F. Paritosh and D. J. Srolovitz, Modifying the microstructure and morphology of film surface layers by manipulating chemical vapor deposition reactor conditions. Journal of Applied Physics 89:4857-4865 (2001).

[56] B. B. Mandelbrot, D. E. Passoja, and A. J. Paullay, Fractal character of fractal surfaces of metal. Nature 320:429-431 (1986).

[57] M. Tanaka, Characterization of grain-boundary configuration and fracture surface roughness by fractal geometry and creep-rupture properties of metallic materials. Journal of Materials Science 27:4717-4725 (1992).

[58] R. H. Dauskardt, F. Haubensak, and R. O. Ritchie, On the interpretation of the fractal character of fracture surfaces. Acta Metallurgica et Materialia 38:143-59 (1990).

[59] E. Hornbogen, Fractals in microstructure of metals. International Materials Review 34:277-296 (1989).

[60] G. Laird and J. C. Rawers, Fractal analysis of carbide morphology in high-Cr white cast irons. Metallurgical Transactions A 23:2941-2945 (1992).

[61] Z. Huda and B. Ralph, Mechanism of grain growth and intergranular precipitation of gamma in nickel base alloy. Practical Methods 27:64-74 (1990).

[62] R. Jayaganthan, K. Mohankumar, V. N. Sekhar, A. A. Tay, and V. Kripesh, Fractal analysis of intermetallic compounds in Sn-Ag, Sn-Ag-Bi, and Sn-Ag-Cu diffusion couples. Thin Solid Films 60:1089-1094 (2006).

[63] Y. Wang and K. W. Xu, Characterization of surface morphology of copper tungsten thin film by surface fractal geometry and resistivity. Thin Solid Films 468:310-315 (2004).

[64] J. Li, H. Liao, X. Wang, and C. Coddet, Fractal perimeters of polishing-induced pull-outs present on polished cross sections of plasma-sprayed yttria stabilized zirconia coatings. Journal of American Ceramic Society 86:1906-1910 (2003).

[65] F. P. Incropera and D. P. DeWitt, Fundamentals of Heat and Mass Transfer. Wiley, New York (1990).

[66] Y. S. Touloukian, Thermophysical Properties of High Temperature Materials. IFI/Plenum, New York (1967).

[67] J. Wilson and F. B. Hawkes, Lasers: Principles and Applications. Prentice-Hall, New York (1987).

[68] V. P. Elyutin, B. S. Mitin, and Y. A. Nagibin, Properties of Liquid $A1_20_3$. Inorganic Materials 8:416-418 (1972).

[69] A. Kar and J. Mazumder, Mathematical Modeling of Key-Hole Laser Welding. Journal of Applied Physics 78:6353-6360 (1995).

[70] A. Kar and J. Mazumder, Two-dimensional model for material damage due to melting and vaporization during laser irradiation. Journal of Applied Physics 68:3884-3891 (1990).

[71] Y. V. Afanasiev and O. N. Krokhin, Soviet Physics JETP 25:639 (1967).

[72] V. V. Semak, B. Damkroger, and S. Kempka, Temporal evolution of the temperature field in the beam interaction zone during laser material processing. Journal of Physics D: Applied Physics 32:1819-1825 (1999).

[73] P. C. Carman, Fluid flow through granular bed. Transactions of the Institution of Chemical Engineers 15:150-166 (1937).

[74] L. Han, F. W. Liou, and S. Musti, Thermal behavior and geometry model of melt pool in laser material process, Journal of Heat Transfer 127:1005-1014 (2005).

[75] S. Mukherjee, W. L. Johnson, W. K. Rhim, Noncontact measurement of high-temperature surface tension and viscosity of bulk metallic glass-forming alloys using the drop oscillation technique, Applied Physics Letters 86:014104 (2005).

[76] M. Bass, Laser Materials Processing. North-Holland Publishing Company, Amsterdam (1983)

[77] D. Eskin, Q. Du, D. Ruvalcaba, and L. Katgerman, Experimental study of structure formation in binary Al–Cu alloys at different cooling rates. Materials Science and Engineering A 405:1-10 (2005).

[78] H. Fischer and R. Marx, Fracture toughness of dental ceramics: comparison of bending and indentation method, Dental Materials 18:12-19 (2002).

[79] A. G. Evans and E. A. Charles, Fracture toughness determination by indentation, Journal of American Ceramic Society 59:371-372 (1976).

[80] G. R. Anstis, P. Chantiklul, B. R. Lawn, and D. B. Marshall, A critical evaluation of indentation techniques for measuring fracture toughness: I. Direct crack measurements, Journal of American Ceramic Society 64:533-538 (1981).

[81] K. Niihara, R. Morena, and D. P. Hasselman, Evaluation of K_{Ic} of brittle solids by the indentation method with low crack-to-indent ratios, Journal of Materials Science Letters 1:13-16 (1982).

[82] M. T. Laugier, Palmquist indentation crack analyses for tough-ness determination in WC-Co composites, Key Enginering Materials 32:77-84 (1989).

[83] D. K. Shetty, I. G. Wright, P. N. Mincer, and A. H. Clauer, Indentation fracture of WC-Co cermets. Journal of Materials Science 20:1873-1882 (1985).

[84] Z. Li, A. Ghosh, A. S. Kobayashi, and R. C. Bradt, Indentation fracture toughness of sintered silicon carbide in the Palmqvist crack regime. Journal of American Ceramic Society 72:904-911 (1989).

[85] L. C. Lim and A. Muchtar, Micro- and macro-indentation fracture toughness of alumina. Journal of Materials Science Letters 21:1145-1147 (2002).

Appendices

Appendix A: List of Publications

■ **Book**

Narendra B. Dahotre and **Sandip P. Harimkar,** ***Laser Fabrication and Machining of Materials,*** Springer (Oct 2007; ISBN: 978-0-387-72343-3).

The book covers the theory behind the various laser machining and fabrication techniques as well as its applications. The broad topics covered are laser assisted machining (drilling, cutting, shaping, and micromachining) and fabrication (welding, forming, and rapid prototyping) processes. Also, a section on special topics such as laser machining in medical application, laser interference processing, and laser shock processing are included.

■ **Journal Publications**

1. **Sandip P. Harimkar**, Anoop N. Samant and Narendra B. Dahotre, Temporally evolved recoil pressure driven melt infiltration during laser surface modifications of porous alumina ceramic, *Journal of Applied Physics*, **101** 054911 (2007)
2. Anoop N. Samant, **Sandip P. Harimkar** and Narendra B. Dahotre, Laser surface modifications of advanced ceramics-A modeling approach, *JOM*, **59** 35-38 (2007).
3. **Sandip P. Harimkar** and Narendra B. Dahotre, Characterization of microstructure in laser surface modified alumina ceramic, *Materials Characterization* Published Online, Article in Press (2007).

4. **Sandip P. Harimkar**, C Daniel, C. Holzapfel, P. Leibenguth, F Mücklich and Narendra B. Dahotre, Validation of crystallographic correlation for faceted morphology in laser surface engineered alumina ceramic, *Scripta Materialia*, **57** 401-404 (2007).
5. Kantesh Balani, Yao Chen, **Sandip P. Harimkar**, Narendra B. Dahotre and Arvind Agarwal, Tribological Behavior of plasma sprayed carbon nanotube reinforced hydroxyapatite-coating in physiological solution, *Acta Biomaterialia*, **3** 944-951(2007).
6. A Basu, A. N. Samant, **S. P. Harimkar,** J. D. Majumdar, I. Manna, and N. B. Dahotre, Laser surface cladding of Fe-Cr-Mo-Y-B-C bulk metallic glass composition on AISI 4041 steel, *Surface Coatings and Technology*, Published Online, Article in Press (2007).
7. **Sandip P. Harimkar** and Narendra B. Dahotre, Crystallographic and morphological textures in laser surface modified alumina ceramic, *Journal of Applied Physics*, **100** 024901 (2006).
8. **Sandip P. Harimkar**, Anoop N. Samant, Abhijeet A. Khangar and Narendra B. Dahotre, Prediction of solidification microstructures during laser dressing of alumina-based grinding wheel material, *Journal of Physics D: Applied Physics*, **39** 1642-1649 (2006).
9. **Sandip P. Harimkar** and Narendra B. Dahotre, Evolution of surface morphology in laser dressed alumina grinding material, *International Journal of Applied Ceramic Technology*, **3** 375-381 (2006).

10. **Sandip P. Harimkar** and NB Dahotre, Effect of laser fluence on surface microstructure of alumina ceramic, *Advances in Applied Ceramics* **105** 304-308 (2006).
11. **S. Harimkar** and N. B. Dahotre, Laser assisted densification of surface porosity in structural alumina ceramic, *Physica Status Solidi a*, **204** 1105-1113 (2006).
12. Kishore, **S. P. Harimkar** and D. S. Desai, Impact response of epoxy systems containing short fibres and/or oxide particles as reinforcements, *Polymer International*, **53** 1274-1281 (2004).
13. **Sandip P. Harimkar** and Narendra B. Dahotre, Laser-assisted rapid surface microstructuring of porous alumina ceramic, *Applied Surface Science*, in review (2007).
14. **Sandip P. Harimkar** and Narendra B. Dahotre, Microindentation fracture behavior of laser surface modified alumina ceramic, *Scripta Materialia*, in review (2007).
15. Anoop Samant, **Sandip P. Harimkar**, and Narendra B. Dahotre, Laser beam operation mode dependent grain morphology of alumina, *Journal of Applied Physics*, in review (2007).

■ **Conference Publication**

1. **Sandip P. Harimkar** and Narendra B. Dahotre, A novel approach to laser surface dressing of alumina ceramic, *Proceedings of 1st International Congress on Ceramics: Global Roadmap*, Toronto, ISBN: 9780470104910 (2006).

2. **Sandip P. Harimkar** and NB Dahotre, Laser surface engineering of alumina ceramic compacts: an approach of laser dressing, *Proceedings of Materials Science and Technology-2006 (MS&T'06),* October 15-19, Cincinnati, USA. pp. 239-245 (2006).

■ **Posters/Presentations**

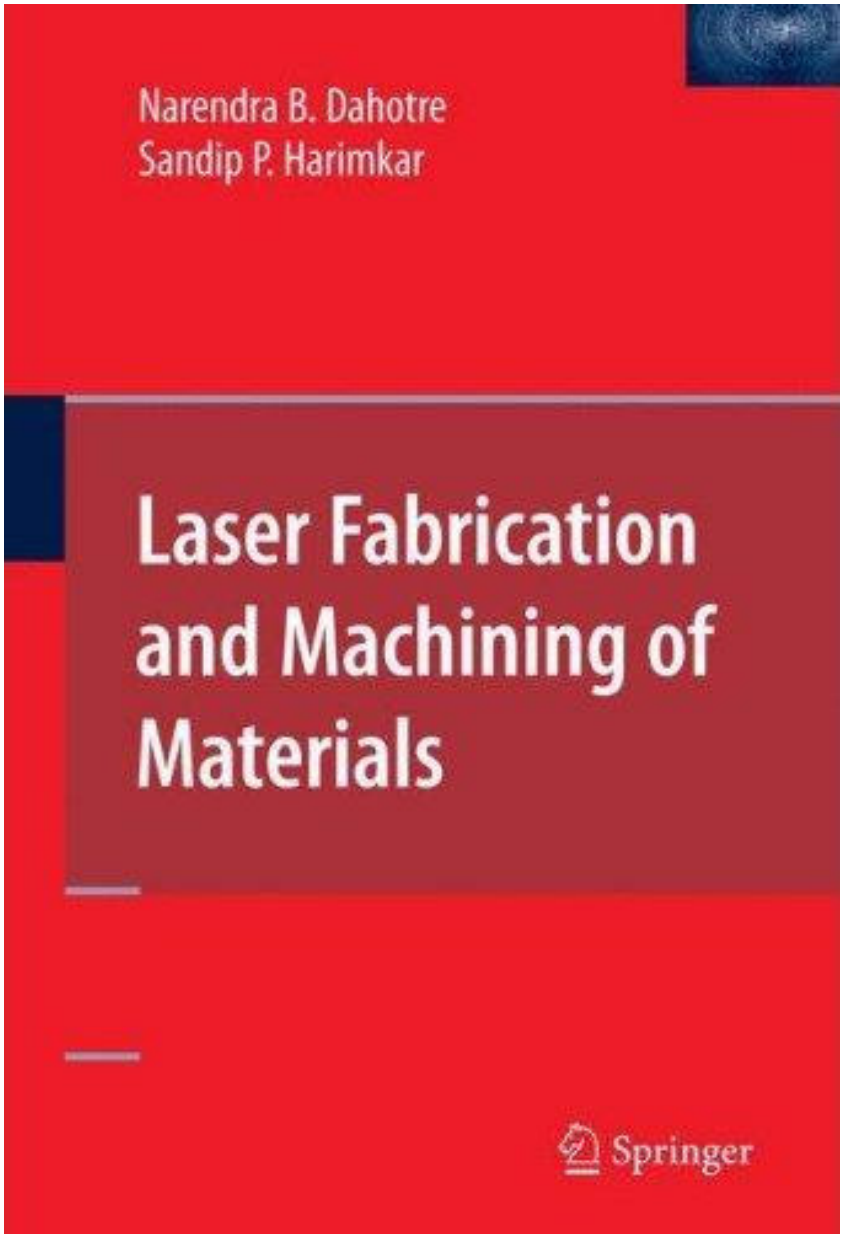
1. **Sandip P. Harimkar** and Narendra B. Dahotre, Laser surface modifications of alumina ceramic for applications in precision grinding of materials, *TMS-2007*, Orlando, Florida, February 25-March 1 (2007).
2. **Sandip P. Harimkar** and Narendra B. Dahotre, Laser surface engineering of alumina ceramics: a novel approach of laser dressing, *Materials Science and Technology-2006 (MS&T'06),* October 15-19, Cincinnati, USA. pp. 239-245 (2006).
3. **Sandip P. Harimkar** and Narendra B. Dahotre, A novel approach to laser surface dressing of alumina ceramic, *1st International Congress on Ceramics*, Toronto, Canada, June 25-29 (2006).
4. **Sandip P. Harimkar** and Narendra B. Dahotre, Faceted Al_2O_3 grains by laser surface modification, *Ceramographic Contest*, American Ceramic Society (2006).
5. **Sandip P. Harimkar** and Narendra B. Dahotre, Laser induced microstructuring and microtexturing of alumina ceramic surfaces, *ASM Meeting*, Oak Ridge Chapter, November (2006).
6. A. Basu, **S. Harimkar**, J. Majumdar, N. Dahotre, and I. Manna, Laser surface cladding of Fe-Cr-Mo-Y-B-C bulk metallic glass on plain carbon steel, TRIBO-

CORROSION 2006, An international symposium on tribo-corrosion held in NFTDC, Hyderabad, December 4-5 (2006).

7. **Sandip P. Harimkar**, Anoop N. Samant, Abhijeet A. Khangar and Narendra B. Dahotre, Transient thermal and microstructural evolutions in alumina during laser surface modification, *ASM Meeting*, Oak Ridge Chapter, November (2005).

Appendix B: Reprints of Published Works

Book: Narendra B. Dahotre and Sandip P. Harimkar, Laser Fabrication and Machining of Materials, Springer, 2007.



Contents

Part I Fundamentals of Laser Processing 1

1 Basics of Lasers 3
- 1.1 Introduction. 3
- 1.2 Nature of Electromagnetic Radiation 3
- 1.3 Laser Operation Mechanism. 6
  - 1.3.1 Population Inversion 6
  - 2.3.2 Stimulated Emission 8
  - 3.3.3 Amplification 9
- 1.4 Properties of Laser Radiation 13
  - 1.4.1 Monochromaticity. 13
  - 1.4.2 Collimation 15
  - 1.4.3 Beam Coherence 16
  - 1.4.4 Brightness or Radiance 17
  - 1.4.5 Focal Spot Size 17
  - 1.4.6 Transverse Modes 18
  - 1.4.7 Temporal Modes 20
  - 1.4.8 Frequency Multiplication 22
- 1.5 Types of Industrial Lasers 23
  - 1.5.1 Solid-State Lasers 24
  - 1.5.2 Gas Lasers. 25
  - 1.5.3 Semiconductor Lasers. 27
  - 1.5.4 Liquid Dye Lasers. 31

2 Laser Materials Interaction 34
- 2.1 Introduction. 34
- 2.2 Absorption of Laser Radiation 34
- 2.3 Thermal Effects 40
  - 2.3.1 Heating 40
  - 2.3.2 Melting 43
  - 2.3.3 Vaporization 45
  - 2.3.4 Important Considerations for Thermal Analysis 50

2.4 Vapor Expansion and Recoil Pressures 55
2.5 Plasma Formation 59
2.6 Ablation 61

Part II Laser Machining 67

3 Manufacturing Processes: An Overview 69
3.1 Introduction 69
3.2 Manufacturing Processes 69
3.2.1 Casting Processes 70
3.2.2 Forming Processes 71
3.2.3 Joining Processes 74
3.2.4 Machining Processes 75
3.3 Lasers in Manufacturing 79
3.3.1 Laser Casting 79
3.3.2 Laser Forming/Shaping 80
3.3.3 Laser Joining 83
3.3.4 Laser Machining 84
3.4 Selection of Manufacturing Processes 85
3.4.1 Properties of Materials 85
3.4.2 Geometrical Complexity of Product 88
3.4.3 Quality Parameters 90
3.4.4 Manufacturing Economics 92

4 Laser Drilling 97
4.1 Introduction 97
4.2 Laser Drilling Approaches 98
4.3 Melt Expulsion During Laser Drilling 99
4.4 Analysis of Laser Drilling Process 103
4.5 Quality Aspects 117
4.6 Practical Considerations 124
4.6.1 Effect of Laser Parameters 125
4.6.2 Effect of Focusing Conditions 128
4.6.3 Effect of Assist Gas Type, Gas Pressure, and Nozzle Design 129
4.7 Laser Drilling Applications 134
4.7.1 Drilling of Cool Holes 134
4.7.2 Drilling of Diamonds 136
4.7.3 Microdrilling 136
4.8 Advances in Laser Drilling 137

5 Laser Cutting 144
5.1 Introduction 144
5.2 Laser Cutting Approaches 145
5.2.1 Evaporative Laser Cutting 148

5.2.2 Laser Fusion Cutting. 152
5.2.3 Reactive or Oxygen-Assisted Laser Cutting. 158
5.2.4 Controlled Fracture Technique 167
5.3 Quality Aspects. 171
5.3.1 Striations 171
5.3.2 Dross 176
5.3.3 Heat-Affected Zone 179
5.4 Practical Considerations 183
5.4.1 Effect of Laser Type 183
5.4.2 Effect of Laser Power 183
5.4.3 Effect of Optical Systems 186
5.4.4 Effect of Nozzle Parameters 187
5.4.5 Effect of Assist Gas Type 190
5.5 Laser Cutting of Various Materials 193
5.5.1 Metallic Materials. 193
5.5.2 Polymers 197
5.5.3 Ceramics and Glasses 198
5.6 Laser Cutting Applications. 200
5.7 Advances in Laser Cutting 201
5.7.1 Laser Cutting Assisted by Additional Energy Sources 201
5.7.2 Underwater Cutting 202
5.7.3 Laser Cutting of Composites and Laminates 203

6 Three-dimensional Laser Machining 207
6.1 Introduction. 207
6.2 Laser-assisted Machining 207
6.2.1 LAM Process 208
6.2.2 Analysis of LAM Process. 209
6.2.3 LAM Process Results 215
6.3 Laser Machining 225
6.3.1 Machining Using Single Laser Beam. 225
6.3.2 Machining Using Intersecting Laser Beams. 233
6.4 Applications of Three-dimensional Laser Machining 243

7 Laser Micromachining 247
7.1 Introduction. 247
7.2 Laser Micromachining Mechanisms 247
7.2.1 Laser Ablation 248
7.2.2 Laser-Assisted Chemical Etching. 260
7.3 Laser Micromachining Techniques 265
7.3.1 Direct Writing Technique 265
7.3.2 Mask Projection Technique 267
7.3.3 Interference Technique 268
7.3.4 Combined Techniques. 270

7.4 Laser Micromachining Applications 271
7.4.1 Microvia Drilling 271
7.4.2 Drilling of Inkjet Nozzle Holes 272
7.4.3 Resistor Trimming 273
7.4.4 Laser Scribing and Dicing 276
7.4.5 Laser Marking and Engraving 277
7.4.6 Biomedical Applications 280
7.4.7 Thin Film Applications 282
7.4.8 Fuel Injector Drilling 283
7.4.9 Stripping of Wire Insulation 285

Part III Laser Fabrication 289

8 Laser Forming 291
8.1 Introduction 291
8.2 Laser Forming Processes 292
8.2.1 Bending or Temperature Gradient Mechanism 294
8.2.2 Buckling Mechanism 296
8.2.3 Upsetting Mechanism 299
8.3 Analysis of Laser Forming Processes 299
8.3.1 Temperature Gradient Mechanism 300
8.3.2 Buckling Mechanism 308
8.4 Practical Considerations 312
8.4.1 Processing Parameters 312
8.4.2 Bending rates and Edge Effects 323
8.4.3 Laser Forming Strategies and Control 329
8.4.4 Microstructure and Properties of Laser-Formed Components 337
8.5 Laser Forming Applications 341
8.5.1 Correction of Bending Angles 341
8.5.2 Laser Forming of Complex Shapes 341
8.5.3 Rapid Prototyping 343
8.5.4 Flexible Straightening of Car Body Shells 343
8.5.5 Microfabrication 344
8.5.6 Laser Forming in Space 344
8.6 Advances in Laser Forming 344
8.6.1 Laser Forming of Tubes 344
8.6.2 Laser Forming with Preload 347
8.6.3 Laser Forming with Two Beams 348
8.6.4 Laser Forming of Composite Materials 348

9 Laser-Based Rapid Prototyping Processes 353
9.1 Introduction 353
9.2 Basics of Rapid Prototyping Processes 353
9.3 Classification of Rapid Prototyping Processes 355

9.3.1 Liquid-Based RP Processes. 356
9.3.2 Powder-Based RP Processes 357
9.3.3 Solid-Based RP Processes. 358
9.3.4 Concept Modelers 359
9.4 Laser-Based Rapid Prototyping Processes 359
9.4.1 Stereolithography 359
9.4.2 Selective Laser Sintering. 379
9.4.3 Laminated Object Manufacturing 397
9.4.4 Laser Engineered Net Shaping (Lens) 402
9.5 Applications of Rapid Prototyping Processes. 405

10 Laser Welding. 412
10.1 Introduction. 412
10.2 Laser Welding Process 412
10.3 Analysis of Laser Welding Process 415
10.4 Quality Aspects. 427
10.4.1 Porosity 427
10.4.2 Cracking 429
10.4.3 Heat-Affected Zone. 431
10.4.4 Mechanical Properties of Laser Welds 432
10.5 Practical Considerations 433
10.5.1 Effect of Laser Parameters 433
10.5.2 Effect of Focusing Conditions. 435
10.5.3 Effect of Shielding Gas. 435
10.5.4 Effect of Welding Speed 437
10.5.5 Joint Configurations 437
10.6 Laser Welding of Various Materials 438
10.6.1 Metallic Materials. 438
10.6.2 Ceramics 439
10.6.3 Polymers 440
10.6.4 Composites 440
10.6.5 Dissimilar Materials 442
10.7 Advances in Laser Welding 443
10.7.1 Arc-Augmented Laser Welding 443
10.7.2 Multibeam/Dual-Beam Laser Welding. 443
10.7.3 Laser Welding of Tailor Welded Blanks 444

Part IV Special Topics in Laser Processing 450

11 Laser Interference Processing. 451
11.1 Introduction. 451
11.2 Theory of Interference 451
11.3 Interferometry for Materials Surface Processing 453
11.3.1 Laser and Materials Aspects 454
11.3.2 Interferometer Design Aspects 456

11.4 Applications of Laser Interference Processing 459
11.4.1 Crystallization and Structuring of Semiconductor Films 459
11.4.2 Structuring of Monolayer and Multilayer Films 464
11.4.3 Structuring of Biomaterials 472

12 Laser Shock Processing 477
12.1 Introduction 477
12.2 Fundamentals of Laser Shock Processing 477
12.3 Analysis of Laser Shock Processing Process 480
12.4 Processing Parameters 484
12.4.1 Effect of Laser Intensity 484
12.4.2 Effect of Pulse Duration 484
12.4.3 Effect of Temporal Pulse Shape 486
12.4.4 Effect of Laser Wavelength 486
12.4.5 Effect of Spatial Energy Distribution 488
12.4.6 Effect of Coating Material 489
12.5 Mechanical Effects During Laser Shock Processing 491
12.6 Microstructure Modification During Laser Shock Processing 493
12.7 Applications of Laser Shock Processing 496

13 Laser Dressing of Grinding Wheels 499
13.1 Introduction 499
13.2 Grinding Process and Need of Wheel Dressing 499
13.3 Laser-based Wheel Dressing Techniques 502
13.3.1 Laser-assisted Dressing 502
13.3.2 Laser Dressing 506
13.3.3 Recent Approaches of Laser Dressing 511

14 Lasers Processing in Medicine and Surgery 522
14.1 Introduction 522
14.2 Laser–Tissue Interactions 522
14.2.1 Photothermal Interactions 526
14.2.2 Photochemical Interactions (Photoablation) 529
14.2.3 Photodisruptive Interactions 532
14.3 Laser Applications in Medicine and Surgery 534
14.3.1 Lasers in Ophthalmology 534
14.3.2 Lasers in Dermatology 540
14.3.3 Lasers in Otolaryngology: Head and Neck Surgery 545
14.3.4 Lasers in Angioplasty 545
14.3.5 Lasers in Osteotomy 547
14.3.6 Lasers in Dentistry 547

Index 000

Journal Articles:

INSTITUTE OF PHYSICS PUBLISHING JOURNAL OF PHYSICS D: APPLIED PHYSICS
J. Phys. D: Appl. Phys. **39** (2006) 1642–1649 doi:10.1088/0022-3727/39/8/025

Prediction of solidification microstructures during laser dressing of alumina-based grinding wheel material

S P Harimkar[1], **A N Samant**[1], **A A Khangar**[1,3], **Narendra B Dahotre**[1,2,4]

[1] Department of Materials Science and Engineering, University of Tennessee, Knoxville, TN 37996, USA
[2] Metals and Ceramics Division, Oak Ridge National Laboratory, Oak Ridge, TN 37831, USA

E-mail: ndahotre@utk.edu

Received 1 November 2005, in final form 26 January 2006
Published 30 March 2006
Online at stacks.iop.org/JPhysD/39/1642

Abstract
Alumina-based grinding wheels are dressed by modifying the surface of the wheels through laser surface melting and solidification with laser powers of 500 W (343 J cm^{-2}), 750 W (514 J cm^{-2}) and 1000 W (686 J cm^{-2}) with an irradiation time of 14.4 ms. The rapid solidification rate associated with laser processing results in significant refinement of the surface grains characterized by well-defined regular facets and vertices. Such microstructures are helpful in finish/micro-scale grinding applications. In order to predict the microstructure from the laser processing parameters and the thermo-physical properties of materials, a one dimensional heat flow model is proposed. The effective thermal conductivity of the porous alumina ceramic, which is incorporated in the heat flow model, is calculated using fractal dimensions from analytical correlations. The proposed thermal model predicts the general trend of increasing melt depth with increasing laser power, which is in reasonable agreement with experimental observations. Also, the cooling rates are derived from the thermal model by calculating the values of the temperature gradient (G) at the solid/liquid interface and the velocity of the solid/liquid interface. The calculated values of the cooling rate decrease with increasing laser power in agreement with the established values in the literature. An attempt is made to correlate the observed secondary dendrite arm spacing with the calculated cooling rates.

1. Introduction

Various types of alumina-based abrasive materials such as regular alumina, semi-friable alumina, white alumina and pink alumina are traditionally used in grinding applications [1, 2]. Grinding is a complex thermo-mechanical process. The wheel surfaces are subjected to high material removal rates and frictional heat generation, leading to loss of dimensional stability and effective number of cutting edges in the wheel surface in addition to poor form tolerance and the appearance of surface and subsurface defects in the ground products. The most important step in the grinding process is the restoration of the cutting efficiency of the wheels by periodical re-sharpening of the wheels using a diamond dresser, which mechanically removes material from the surface of the wheel and thus exposes the new abrasive grains for cutting action [3]. Even though conventional diamond dressing is still used extensively in industrial grinding practice, the operation has its own demerits. This includes the uncontrolled fracture of the bond

[3] Currently with Milwaukee Electric Tool Corporation, Brookfield, WI 53005, USA.
[4] Author to whom any correspondence should be addressed.

0022-3727/06/081642+08$30.00 © 2006 IOP Publishing Ltd Printed in the UK

material and break-off of abrasive grains [4]. Also, it has been reported that 90% of the wheel material is removed in the dressing operation, thus increasing the consumable costs in addition to the costs of process down-time for the dressing operation [5].

The use of lasers was first proposed by Babu *et al* for the in-process dressing of grinding wheels. The advantages offered by this non-contact process include ease of automation, improved productivity and consistent quality of wheel surface topography [6–9]. These preliminary studies have suggested that laser dressing causes the generation of well-defined grooves by locally damaging the worn-out grits and/or dislodging the chips loaded during grinding operation. The performance of laser dressing has been compared with diamond dressing by studying the surface topography with varying dressing feed and laser intensity. Also, the grinding forces and the finish obtained with laser dressing and conventional diamond dressing have been compared at different laser intensities for different durations of grinding. The result showed that for finish machining lower laser intensities in the range of $4.0 \times 10^{10}\,\mathrm{W\,m^{-2}}$ gives better results [7, 8]. A thermal model has been proposed to predict the groove shape on the wheel surface during laser dressing in an attempt to arrive at the suitable laser parameters for dressing [9]. An alternate approach, commonly referred to as laser-assisted dressing, integrates the laser technology with conventional dressing [10]. The focused laser beam is used to locally heat the surface of the rotating grinding wheel ahead of the dressing tool (typically a single point diamond dresser). With a suitable laser energy density and heating time the vitrified bond of the wheel gets softened or even melted, facilitating the removal of bonding material. The main objectives behind such processes are to reduce the wear of the dressing tool and to improve the surface quality of the wheel by locally heating and thus changing the material removal mode at the ceramic wheel surface from brittle fracture to ductile flow. The wear rate of the diamond dresser and hence the life can be well controlled by controlling the temperature at the tip of the diamond by adequately selecting the laser dressing conditions. Extensive experiments have been carried out to investigate the feasibility of the laser-assisted dressing in terms of truing efficiency, truing accuracy, wear of the diamond dresser and truing force characteristics [11]. The results shown that the laser-assisted dressing and truing offers a number of advantages over the conventional diamond dressing.

While most of the previous studies have been concerned with the assessment of the grinding characteristics of the laser dressed grinding wheels, very little interest has been directed towards understanding the laser interaction with the grinding wheel material and the subsequent evolution of the surface topography. Recently, our research group has carried out a systematic and detailed characterization of the surface topography and the microstructural evolution of laser dressed grinding wheels. The most important findings are the refinement of grains and the formation of well-defined cutting edges and vertices on the wheel surface ideal for precision grinding [12–14]. The formation of such a desirable microstructure is correlated with the evolution of crystallographic texture during the rapid solidification process associated with the laser dressing operation. The present study aims at extending our understanding of the solidification characteristics of alumina grinding wheels based on the temperature history during laser processing and predicting the micro-structural features such as the re-solidified melt depth from the laser processing parameters. The calculated melt depths are compared with experimentally obtained values for various laser powers, taking into consideration the effect of porosity on the thermo-physical properties of an alumina-based grinding wheel material. A one dimensional unsteady state thermal model is presented from which the cooling rates, the temperature gradients and the melt interface velocities are calculated. The integration of computational modelling and experimental efforts is expected to provide a model that leads to better control over the outcome of the laser based dressing technique.

2. Experimental procedure

2.1. Materials

Commercially available alumina-based grinding wheels (purchased from MSC Industrial Supply Co., Melville, NY) doped with 0.25% chromia were used for the laser dressing studies. The chemical composition of the abrasive grain material was $99.52Al_2O_3$–$0.05Fe_2O_3$–$0.18Na_2$ O–$0.25Cr_2O_3$ (wt%) and the grain size was 220 μm. The bonding ingredients were compacted and sintered in a high temperature furnace such that the relative proportions of grains and porosity were about 60 and 40% by volume, respectively. Although the laser setup was configured for in-process dressing of the entire grinding wheel surface, the present study used flat coupons of area $5 \times 5\,\mathrm{cm^2}$ and thickness 2.54 cm cut from standard grinding wheels for subsequent laser surface processing.

2.2. Laser surface processing

The surface of the alumina grinding wheel coupon was dressed with a fibre optically delivered beam of 2.5 kW Hobart continuous wave Nd : YAG laser. The laser beam was radial to the grinding wheel surface, and details of the laser dressing setup are given in [14]. A rectangular beam of dimensions 3.5 mm $\times$600 μm and a scan velocity of $250\,\mathrm{cm\,min^{-1}}$ would dress the entire surface of the grinding wheel by parallel laser tracks. The dressing is carried out at three different laser powers of 500 W ($343\,\mathrm{J\,cm^{-2}}$), 750 W ($514\,\mathrm{J\,cm^{-2}}$) and 1000 W ($686\,\mathrm{J\,cm^{-2}}$).

2.3. Characterization

For microstructural characterization, specimens from the laser dressed samples were sectioned perpendicular to the laser processing direction. These cross sectional specimens were mounted in epoxy moulds and polished using 400, 600, 800 and 1200 grit SiC pads with final polishing in alumina slurry on a microcloth. Microstructural characterization of the polished samples was done on a Hitachi S3500 SEM. Low magnification pictures of the cross sections of the resolidified layer in the laser dressed samples were obtained. The maximum melt depth was measured at five locations in three different cross sectional areas, and the average value of the melt depth with scatter was reported for each laser power used (figure 6).

Also, high magnification pictures were obtained to calculate the secondary dendrite arm spacing (SDAS) using the linear intercept method.

3. Thermal model

Fourier's second law was used to model the heat transfer phenomena taking place during the laser processing of alumina-based grinding wheels. In previous work, the authors examined the solidification structure in a single track as a function of the distance from the centre of the track (in the direction orthogonal to the laser beam traverse) [12]. In the majority of the volume around the centre of the laser track, grains were multifaceted and equiaxed, having a dendritic structure on them. Further analysis of the cross section of the melt depth (laser treated volume) [12] showed a microstructure consisting of uniformly distributed multifaceted equiaxed grains. The same microstructure is observed in the present study. Therefore, a one-dimensional heat flow model was developed. The temperature distribution within the material and the melt depth within a track from the surface was predicted from this model. Although multiple tracks with nearly no overlap between them were laid down for coverage of the entire surface, the model considers the effects of heat flow only in a single track. Such an approach was considered reasonable because the low thermal conductivity of alumina limits thermal effects from the previously laid tracks. Assuming a laser processing speed of 250 cm min^{-1} and beam width of 600 μm, the laser beam irradiation time (residence time) is 14.4 ms in this study.

The governing equation is as follows [15]:

$$\frac{\partial T(x,t)}{\partial t} = \alpha \frac{\mathrm{d}^2 T(x,t)}{\mathrm{d}x^2}, \tag{1}$$

where α is the thermal diffusivity of the material and is equal to $k/\rho C_p$; k is the thermal conductivity of the material; ρ is the density of the material and C_p is the specific heat. The initial condition of $T = T_0 = 298$ K was applied at time $t = 0$.

The convection and radiation effects were also considered.

If L is the length of the sample, then the convection occurring at $x = L$ is given by

$$-k\frac{\partial T(L,t)}{\partial x} = h(T(L,t) - T_0), \tag{2}$$

where h is the convective heat transfer coefficient.

For radiation, the following equation holds true:

$$\begin{aligned} -k\frac{\partial T(0,t)}{\partial x} &= \delta A I - \varepsilon\sigma(T(0,t)^4 - T_0^4) \\ \delta &= 1 \quad 0 \leqslant t \leqslant t_\mathrm{p} \\ \delta &= 0 \quad t > t_\mathrm{p}, \end{aligned} \tag{3}$$

where t_p is the irradiation time; I is the laser power intensity (power per unit area) of the incident beam; A is the absorptivity of alumina; ε is the emissivity of alumina for thermal radiation and σ is the Stefan–Boltzmann constant = 5.67×10^{-8} W m^{-2} K^{-4}.

In this investigation, FEMLAB's heat transfer transient mode was employed to obtain the temperature distribution within the material using the finite element approach. Six vital modes were used to solve the problem. In the draw mode, the geometry of the sample was specified, whereas the boundary mode permitted specification of all the boundary conditions as discontinuous functions that were used to model the heating and the cooling processes. The different terms involved in the governing equation that defined the different material properties were presented by the subdomain mode. The different characteristics of the finite element mesh were specified in the mesh mode, and Lagrange elements were used to mesh the model. The parameters of the solver and the solver type were set in the solver mode. The 'time dependent' solver was used in FEMLAB. A time step of 1 ms was used in the present study. Finally, the post mode was used to analyse the results given by the solver. The temperature distribution and the temperature gradient were visualized in this mode.

As mentioned earlier, the commercially obtained alumina grinding wheels contained 40% porosity by volume. Such a large volume of porosity is expected to play a vital role in influencing both the temperature profiles and the melt depths obtained during laser processing. Hence, considering the effects of porosity was a crucial part of the work. The effects of porosity were considered by appropriately adjusting the material properties such as the density and thermal conductivity. A model proposed by Sabau *et al* which can be generalized for any porous media, was employed in the present study to determine the effective thermal conductivity [16]. The model considers a rectangular box representing a continuous matrix (porosity in the present case) and dispersed or solid phase (alumina particles in the present case) at the centre of the unit cell. In this model, the effective and solid thermal conductivities were nondimensionalized with the matrix thermal conductivity:

$$\overline{k_\mathrm{ex}} = \frac{k_\mathrm{ex}}{k_\mathrm{l}}, \tag{4}$$

$$\overline{k_\mathrm{s}} = \frac{k_\mathrm{s}}{k_\mathrm{l}}, \tag{5}$$

where k_ex is the effective thermal conductivity, k_s is the thermal conductivity of the dispersed phase and k_l is the thermal conductivity of the continuous matrix. The effective thermal conductivity is given by

$$\overline{k_\mathrm{ex}} = 1 - \frac{\pi b_x}{4}\left(1 + \frac{2}{c_x} + \frac{2}{c_x^2}\log(1 - c_x)\right), \tag{6}$$

where b_x and c_x are defined as follows:

$$b_x = \left(\frac{\phi_\mathrm{s}}{\psi_\mathrm{s}}\right)^{1-\delta_\mathrm{f}(1-1/d_x)}, \tag{7}$$

$$c_x = \left(1 - \frac{1}{\overline{k_\mathrm{s}}}\right)\left(\frac{\phi_\mathrm{s}}{\psi_\mathrm{s}}\right)^{\delta_\mathrm{f}(1-1/d_x)}, \tag{8}$$

where ϕ_s is the fraction of dispersed phase (0.6 considering 40% porosity by volume) and ψ_s is the shape factor ($\pi/6$ for the representative unit cell in which the dispersed phase is represented by a sphere) and

$$\delta_\mathrm{f} = \frac{1}{3 - (1/\mathrm{d}x) - (1/\mathrm{d}y) - (1/\mathrm{d}z)}, \tag{9}$$

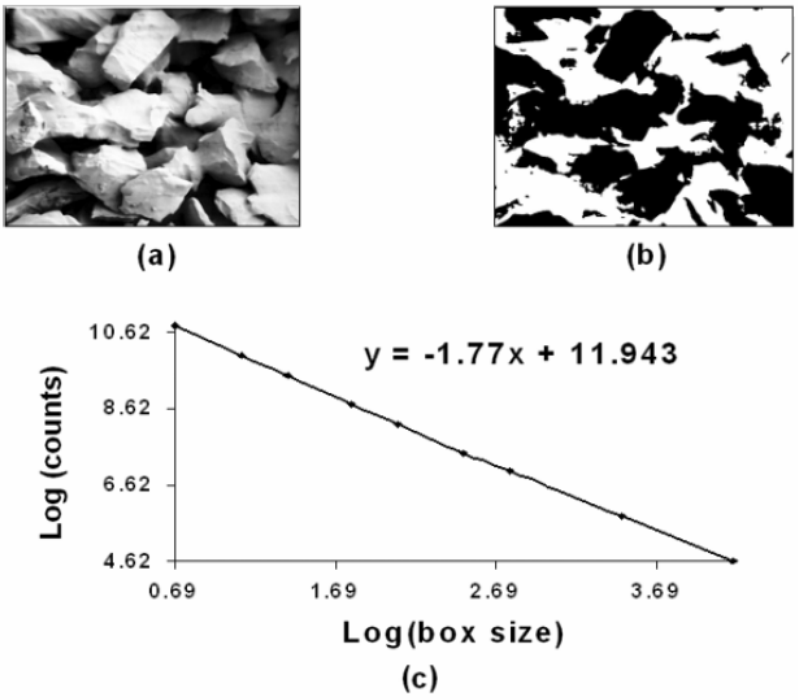


Figure 1. Determination of the fractal dimensions using the box counting technique. (*a*) SEM micrograph; (*b*) corresponding binary image and (*c*) log–log plot giving the fractal dimension from the slope of the line.

where dx, dy, dz are the local fractal dimensions. To determine the local fractal dimensions, the SEM image of the porous ceramic is converted from a spatial domain of brightness to a frequency domain using Fourier transforms. The image is then filtered to remove noise followed by thresholding to convert it to a binary digital image (figure 1) using a public domain software called Image J (available with National Institutes of Health, USA). The fractal dimension of 1.77 in figure 1 was determined by using the box counting method, which places a grid of N boxes of size r over the two-dimensional surface being examined. The number of boxes ($N(r)$) required to cover the feature of interest are counted. Using the Hausdroff measure, the basic fractal equation may be written as

$$N(r) = Cr^{D_b}, \tag{10}$$

$$\log N = \log C - D_b \log r. \tag{11}$$

D is the box dimension, while C is a constant. The process is repeated with different box sizes (r). The fractal dimension is then determined from the slope of the plot between $\log N(r)$ versus $\log r$ (figure 1(*c*)). Substitution of the above fractal dimension in the above equations gives a thermal conductivity of 12.1 $W m^{-1} K^{-1}$ for alumina ceramic with 40% porosity by volume. Furthermore, although the thermo-physical properties of binding material are also expected to affect the thermal conductivity of the wheel material, they are not taken into account in the present computations due to the following reasons: (1) the abrasive wheel material consists of 99.52 wt% alumina and a negligible amount of bonding material (explained in section 2.1); (2) the bonding material mainly consists of oxides and silicates having comparable thermal properties (the thermal conductivities of Cr_2O_3 and Al_2O_3 are 32.94 $W m^{-1} K^{-1}$ and 29 $W m^{-1} K^{-1}$, respectively) and (3) the thermal properties of complex compositions such as present in the bond materials are often difficult to find in the literature or they are simply not estimated. In light of this, the properties used in computational modelling are listed in table 1.

Table 1. Properties of alumina used in the mathematical calculations.

ρ ($kg m^{-3}$)	k ($W m^{-1} K^{-1}$)	h ($W m^{-2} K^{-1}$)	ε	C_p ($J kg^{-1} K^{-1}$)
2280[a]	12.1[b]	200[c]	0.7[d]	800[e]

[a] Computed using the weighted average method applied to fully dense alumina ($\rho = 3800 kg m^{-3}$) and 40% porosity by volume.
[b] Computed using the model presented in [16].
[c] Reference [17].
[d] Reference [18].
[e] Reference [19].

4. Results and discussion

Laser dressing causes localized melting and resolidication of the surface layer of the grinding wheel. The surface microstructures of alumina grinding wheels before and after laser dressing are shown in figure 2. Although the molten alumina does flow into the wheel pores, due to extremely rapid cooling rate ($>10^3 °C s^{-1}$) the molten material solidifies rapidly without filling in the entire pore. Therefore, the

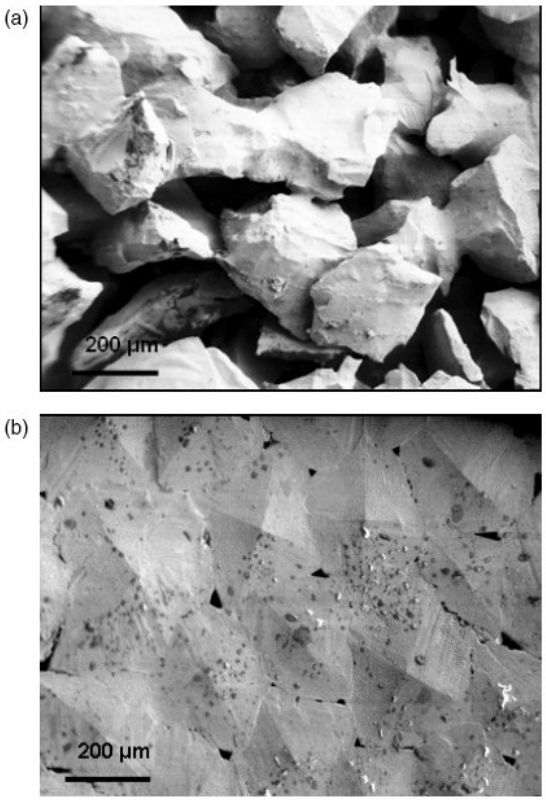


Figure 2. Scanning electron micrographs of the alumina samples (*a*) before dressing and (*b*) after dressing.

porosity drops down substantially from ~40 to <3% in the laser melted region (figure 2). Laser dressing results in substantial grain refinement at the surface in addition to the appearance of a characteristic morphology of the surface grains (figure 2(*b*)). The refinement of the surface grains is a result of the high cooling rates associated with rapid solidification. The surface grains have a wide range of size distributions; however, the shape of the surface grains is regular, with well-defined edges and vertices. The laser dressed grinding wheels are not completely free of porosity and exhibit distributed micro-pores between the multifaceted surface grains (figure 2(*b*)) which can be helpful for micro-scale precision machining by collecting the microparticles removed during machining and also the removed tips of faceted surface grains of a laser dressed grinding wheel. Such a faceted microstructure with reduced porosity can be beneficial for precision/micro-scale machining applications. Furthermore, the rapid quenching rate solidifies the molten surface layer into a faceted structure before coming into actual contact with the workpiece if a simultaneous dressing and grinding approach is adopted. X-ray diffraction studies have revealed the presence of the equilibrium α-alumina phase, the most stable phase of alumina, in the laser dressed samples. Detailed investigations of the evolution of the microstructure and the micro-texture in the laser dressed alumina-based grinding wheel material have already been carried out [12, 13].

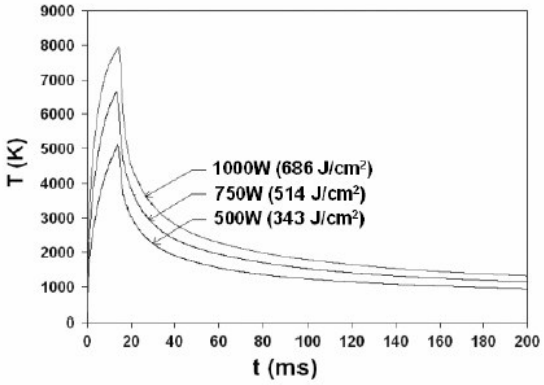


Figure 3. Calculated surface temperature profiles showing heating during laser irradiation ($t \leqslant 14.4$ ms) and cooling after irradiation ($t \geqslant 14.4$ ms).

The calculated surface temperature profiles for laser powers of 500 W (343 J cm^{-2}), 750 W (514 J cm^{-2}) and 1000 W (686 J cm^{-2}), assuming a 14.4 ms laser irradiation time, are plotted in figure 3. The absorptivity value of the surface strongly depends on the wavelength of the laser beam, initial surface roughness and temperature. Due to the high porosity, the grinding wheel surface has an open structure with a high roughness (figure 2); consequently, for the present laser source (1.06 μm wavelength) an absorptivity value of 0.8 is assumed for the temperature calculations [20]. The temperature profiles show that the surface temperature increases with time and reaches a maximum value at a time equal to the irradiation time. After the irradiation time the temperature decreases rapidly, which is typical of rapid solidification processes. The maximum temperature at the surface increases with increasing laser power. The variation of the melt depth was calculated as a function of time by tracing the melting point in the temperature versus the distance from the surface profiles for different times (figure 4). These profiles indicate that the melt interface penetrates inside the material, reaches a maximum and retreats during solidification. The maximum calculated melt depth increases with increasing power.

Figure 5 shows SEM microstructures of melt depth profiles for laser powers of 500 W (343 J cm^{-2}), 750 W (514 J cm^{-2}) and 1000 W (686 J cm^{-2}). The semi-spherical shape of the recast layer is due to the distribution of the laser beam energy such that the energy maximum corresponds to the maximum depth. The micrographs show the increasing melt depth with laser powers varying from 500 W (343 J cm^{-2}) to 750 W (514 J cm^{-2}) due to increased penetration of the laser energy inside the material. However, the change in the melt depth corresponding to a power variation from 750 W (514 J cm^{-2}) to 1000 W (686 J cm^{-2}) is not very significant. It seems that the melt depth reaches a maximum value for a certain laser energy, beyond which no significant increase in the melt depth occurs. This may be due to the higher temperatures associated with greater laser power and consequent decreased thermal conductivities at higher temperatures. The thermal conductivity is a strong function of the temperature and decreases rapidly with increasing temperature. Also, for

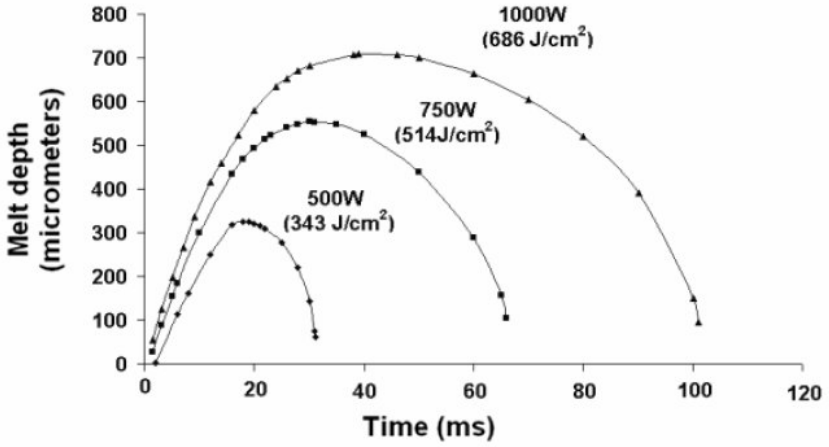


Figure 4. Calculated melt depth profiles as a function of time.

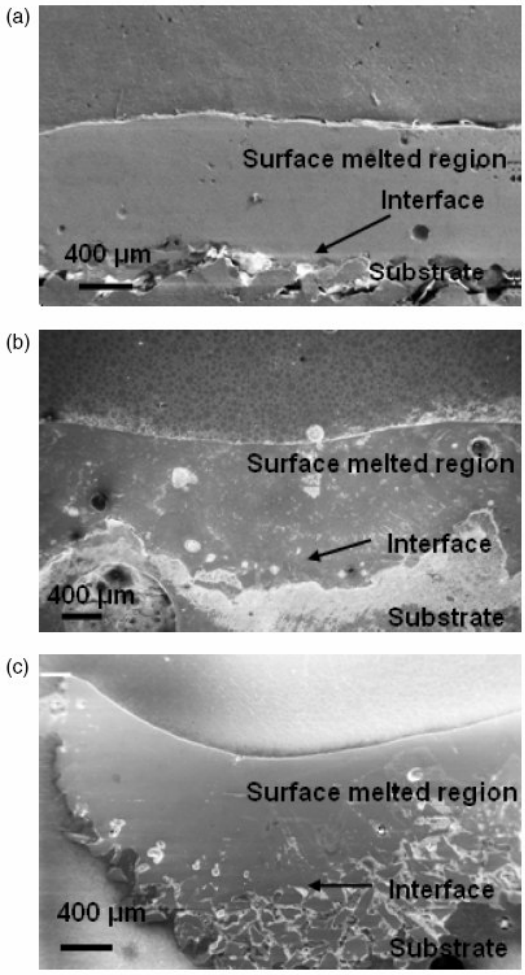


Figure 5. Polished cross sections of the laser dressed samples mounted in epoxy moulds for laser values power of (*a*) 500 W, (*b*) 750 W and (*c*) 1000 W.

alumina ceramics the thermal conductivity is proportional to the inverse temperature above the Debye temperature [21]. Hence, at higher laser fluences the decrease in thermal conductivity limits the increase in melt depth, and the melt depth is determined mainly by the contribution of the molten material flow in the porous substrate region during laser dressing. Such an observation provides the possibility of a tool for finding the laser energy that achieves the maximum melt depth.

The experimental and calculated values of the melt depth as a function of the laser fluence are compared in figure 6. The experimental values are factored out to consider the effect of the porosity. The calculated and experimental melt depth values have a similar increasing trend with increasing laser fluence. The difference in the values can be attributed to the simplifying assumptions in the computational model such as the temperature independence of the thermo-physical properties and the omission of the heat of fusion associated with the liquid–solid phase transformations. One of the effects of porosity is the flow of molten material through the pores, which will increase the effective melt depth in the laser dressed samples. The SEM micrograph in figure 7 illustrates this effect: the single large alumina particle is surrounded by highly dense molten material. The dendritic growth in the microstructure is also evident.

To obtain the thermal aspects of the solidification process that in turn has a bearing on the resulting grain size, the cooling rates were calculated from the thermal model for laser powers of 500 W (343 J cm^{-2}), 750 W (514 J cm^{-2}) and 1000 W (686 J cm^{-2}). The temperature gradient (G) within the solid at the solid/liquid interface and the velocity of the solid/liquid interface (R) were determined from the computed temperature distribution (figure 3) and melt pool depth (figure 4), respectively. The average cooling rate is then given by the product of G and R. Average SDAS (secondary dendrite arm spacing) values corresponding to each laser fluence were obtained using the linear intercept method. Figure 8 is a schematic of the SDAS measurement on a high magnification SEM image. The linear intercept method involves measuring the distances (spacings) between

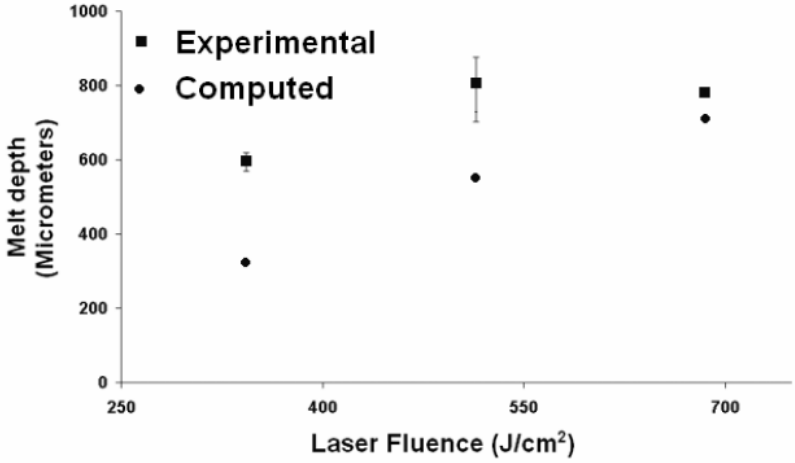


Figure 6. Comparison of experimental and calculated values of melt depths for three laser fluences.

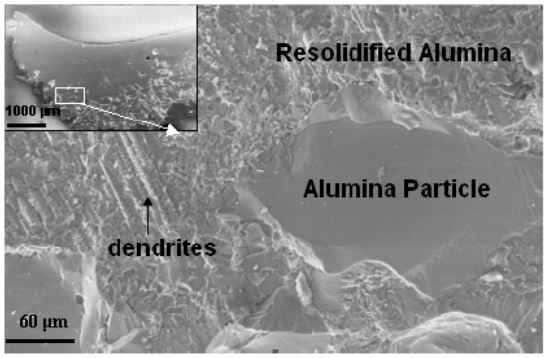


Figure 7. SEM micrograph showing the flow of molten material around alumina particles which would contribute to an increase in the effective melt depth.

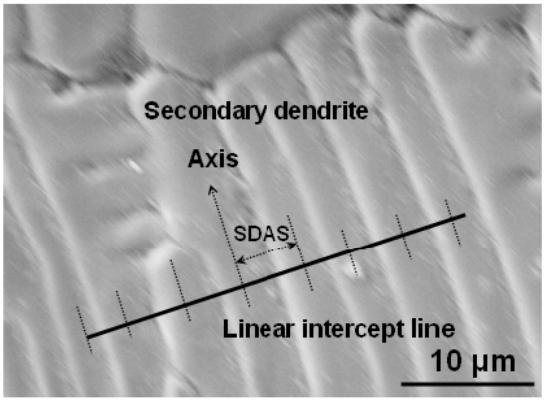


Figure 8. Secondary dendrite arm spacing (SDAS) measurement from a high magnification SEM image using the linear intercept method.

secondary dendrite arms along a line normal to the dendrite arms. This procedure is repeated for a number of image frames, and an average secondary dendrite arm SDAS is calculated. Table 2 summarizes the calculated values for the temperature gradient, melt velocity, and cooling rate and the experimental values for SDAS. The SDAS value for 500 W is the smallest due to the higher cooling rate for 500 W. This agrees with the solidification theory that relates SDAS and the cooling rate according to [22] SDAS $= B(\text{cooling rate})^{-1/3}$, where B is a proportionality constant. However, the SDAS values for 750 W (514 J cm^{-2}) and 1000 W (686 J cm^{-2}) do not differ significantly from each other as would be expected. Like the melt depth, the change in SDAS corresponding to the change in laser fluence from 750 W (514 J cm^{-2}) to 1000 W (685 J cm^{-2}) is also not very significant (table 2). This may be related to dynamic physical, chemical and microstructural changes that influence heat transfer and warrant further studies.

In general, a one-dimensional heat flow model can be used to successfully predict the solidification characteristics during laser dressing of alumina-based grinding wheels. The accuracy of the predictions depends on how well the complex interactions between the laser beam and the porous wheel structure are defined.

5. Conclusions

Dressing of porous alumina grinding wheels using lasers resulted in a highly dense and refined surface microstructure characterized by multifaceted surface grains with well defined cutting edges and vertices. In general, an increase in laser power results in an increase in the maximum melt depth (recast layer) of the laser dressed specimens; however, the increase in maximum melt depth is not significant above a laser power of 750 W (514 J cm^{-2}). This may be due to a decrease in thermal conductivity at high power due to an inverse temperature dependence of the thermal conductivity above the Debye temperature. The proposed one-dimensional thermal model predicts the temperature history during the laser processing. It takes into account the effects of porosity on thermal conductivity using analytical correlations between

Table 2. Summary of the calculated values of the temperature gradient (G) at the solid/liquid interface, solidification rate (R) and cooling rate; and experimental value of the SDAS for alumina grinding wheels dressed at three different laser powers.

Power (W)	Laser fluence ($J\,cm^{-2}$)	G ($K\,m^{-1}$)	R ($m\,s^{-1}$)	Cooling rate ($K\,s^{-1}$)	SDAS (μm)
500	343	1.24×10^5	22.95×10^{-3}	2.860×10^3	3.5
750	514	1.10×10^5	20.07×10^{-3}	2.225×10^3	4.7
1000	686	1.20×10^5	16.29×10^{-3}	1.961×10^3	4.4

the fractal dimensions of the porous material and thermal conductivity. The calculated values of the melt depths are in reasonable agreement with the experimentally determined values at each power. The rapid solidification microstructures were predicted in terms of SDAS from the cooling rate calculations derived from the heat flow model. The heat flow model indicates larger SDAS at lower cooling rates. However, not much change is observed in both the SDAS and the melt depth as a function of the laser fluence above 750 W ($514\,J\,cm^{-2}$).

References

[1] Jackson M J and Mills B 2000 Materials selection applied to vitrified alumina and CBN grinding wheels *J. Mater. Process. Technol.* **108** 114–24

[2] Haywood J 1938 *Grinding Wheels and their Uses: A Handbook and Textbook on Modern Grinding and Polishing, Practice and Theory* (Cleveland, OH: Penton Publishing Company)

[3] Torrance A A and Badger J A 2000 The relation between traverse dressing of vitrified grinding wheels and their performance *Int. J. Mach. Tools Manuf.* **40** 1787–811

[4] Lachance S, Bauer R and Warkentin A 2004 Applications of region growing method to evaluate the surface conditions of grinding wheels *Int. J. Mach. Tools Manuf.* **44** 823–9

[5] Buttery T C, Statham A, Percival J B and Hamed M S 1979 Some effects of dressing on grinding performance *Wear* **55** 195–219

[6] Babu N R, Radhakrishnan V and Murti Y V G S 1989 Investigations on laser dressing of grinding wheels—Part I: A preliminary study *ASME J. Eng. Ind.* **111** 244–52

[7] Babu N R and Radhakrishnan V 1989 Investigations on laser dressing of grinding wheels—Part II: Grinding performance of a laser dressed aluminum oxide wheel *ASME J. Eng. Ind.* **111** 253–61

[8] Babu N R and Radhakrishnan V 1995 Influence of dressing feed on the performance of laser dressed Al_2O_3 wheel in wet grinding *Int. J. Mach. Tools Manuf.* **35** 661–71

[9] Phanindranath V and Babu N R 1996 A theoretical model for prediction of groove geometry on laser dressed grinding wheel surface *Int. J. Mach. Tools Manuf.* **36** 1–16

[10] Zhang C and Shin Y C 2002 A novel laser-assisted truing and dressing technique for vitrified CBN wheels *Int. J. Mach. Tools Manuf.* **42** 825–35

[11] Zhang C and Shin Y C 2003 Wear of diamond dresser in laser assisted truing and dressing of vitrified CBN wheels *Int. J. Mach. Tools Manuf.* **43** 41–9

[12] Khangar A A, Kenik E A and Dahotre N B 2005 Microstructure and microtexture in laser-dressed alumina grinding wheel material *Ceram. Int.* **31** 621–29

[13] Jackson M J, Robinson G M, Dahotre N B, Khangar A and Moss R 2003 Laser dressing of aluminium oxide grinding wheels *Br. Ceram. Trans.* **102** 237–45

[14] Khangar A and Dahotre N B 2005 Morphological modification in laser-dressed grinding wheel material for microscale grinding *J. Mater. Process. Technol.* **170** 1–10

[15] Carslaw H S and Jaeger J C 1967 *Conduction of Heat in Solids* (Oxford: Oxford University Press)

[16] Sabau A S, Tao Y X, Liu G and Vidhuvalavan G 1997 Effective thermal conductivity for anisotropic, granular porous media using fractal concepts *National Heat Transfer ASME (Baltimore)*

[17] Modest M F 1996 Laser Machining of Ablating Materials-Through Cutting and Drilling Models *International Congress on Applications of Lasers and Electro-Optics (Detroit)* vol 81C, p 58

[18] Touloukian Y S 1967 *Thermophysical Properties of High Temperature Materials* vol 4 (New York: IFI/Plenum) p 28

[19] Wilson J and Hawkes F B 1987 *Lasers: Principles and Applications* (New York: Prentice Hall)

[20] Gitzen W H 1970 *Alumina as a Ceramic Material* (Westerville, OH: American Ceramic Society)

[21] Uhlmann D R and Kingery W D 1976 *Introduction to Ceramics* (New York: Wiley)

[22] Kurz W and Fisher D J 1998 *Fundamentals of solidification* (Zurich: Trans Tech Publications)

JOURNAL OF APPLIED PHYSICS 100, 024901 (2006)

Crystallographic and morphological textures in laser surface modified alumina ceramic

Sandip P. Harimkar
Department of Materials Science and Engineering, University of Tennessee, Knoxville, Tennessee 37996

Narendra B. Dahotre[a)]
Department of Materials Science and Engineering, University of Tennessee, Knoxville, Tennessee 37996 and Materials Science and Technology Division, Oak Ridge National Laboratory, Oak Ridge, Tennessee 37831

(Received 29 March 2006; accepted 9 May 2006; published online 17 July 2006)

Laser surface modification is an advanced technique for improving the surface performance of alumina ceramics in refractory and abrasive machining applications. Surface performance is expected to be greatly influenced by the crystallographic and morphological textures of surface grains generated during rapid solidification associated with laser processing. In this study, an investigation of the evolution of crystallographic and morphological textures during laser surface modifications of alumina ceramic was carried out using a 4 kW Nd:YAG laser with fluences in the range of 458–726 J/cm^2. In these regimes of laser surface processing, the formation of equilibrium α-alumina was found to be assisted by catalytic sites provided by the substrate. Microstructure evolution was explored in terms of the development of crystallographic and morphological (size and shape) textures of surface grains as a function of laser processing parameters. The interdependence of crystallographic and morphological textures of the surface grains is discussed within the framework of faceted growth model suggesting that the formation of crystal shapes is governed by the relative velocities of certain crystallographic facets. Also, the effect of thermal aspects of laser processing on the morphology of the surface grains is discussed from the viewpoint of existing solidification theories. © *2006 American Institute of Physics*. [DOI: 10.1063/1.2214365]

I. INTRODUCTION

Alumina ceramic is an important class of materials which encounters rapid solidifications during various processing such as plasma spraying[1,2] and laser surface treatment.[3–7] These rapid solidification techniques are the convenient means of developing unconventional phases and morphologies in the microstructure of materials.[8–10] These techniques have been extensively utilized in the nonequilibrium processing of metallic materials. Along with crystalline phases, the metastable or amorphous phases obtained by rapid solidification have been potentially useful in improving the mechanical, magnetic, electrical, and other properties of materials.[11] In the case of alumina, among several phases, the most important are the stable phase, α-alumina and a metastable phase, γ-alumina. The stable phase α-alumina has a corundum structure with aluminum atoms in octahedral sites surrounded by six oxygen neighbors at a mean distance of 1.91 Å, whereas the γ-alumina is described by a defect spinel structure in which the aluminum coordination varies from 3–5 with tetrahedrally coordinated Al^{3+} predominating.[12] Solidification characteristics of the alumina ceramics have been studied by electrohydrodynamic atomization which is a containerless solidification technique.[13,14] Detailed investigation of phase selection and microstructure evolution in the rapidly cooled alumina droplets of 10 nm to 300 μm diameter have shown that amorphous phase forms in droplets below 100 nm, γ phase between 100 nm and 2 μm, partially transformed δ between 2 and 10 μm, and stable corundum structure above 20 μm. Also, the surface of the coarse droplets exhibited three distinct morphologies: faceted, dendritic, and cellular.[14] Also, the formation of metastable γ-alumina is observed during the solidification of alumina particles in plasma sprayed coatings on copper.[15]

In spite of the wide applicability of the laser surface processing of alumina ceramics, the detailed studies on evolution of phase and morphology during laser surface processing are limited. Also, the rapid solidification of ceramics during laser surface melting is far from the containerless solidification in that the melt undercooling is very small because the substrate acts as a catalytic site that can lower the nucleation barrier. Hence, the present study was directed towards understanding microstructure evolution during rapid solidification associated with laser surface processing of alumina ceramic compacts. The microstructure evolution was studied in terms of the development of crystallographic texture and morphology of the surface grains. The microstructural results are correlated with the cooling rates derived from heat flow model.

II. EXPERIMENTAL PROCEDURE

A. Materials

The commercially available alumina-based grinding wheel compacts (purchased from MSC Industrial Supply Co., Melville, NY) made of alumina doped with 0.25% chro-

a)Author to whom correspondence should be addressed; electronic mail: ndahotre@utk.edu

 © 2006 American Institute of Physics

mia were used for the laser surface modification studies. The alumina grains consisted of 99.52% Al_2O_3 and the average grain size was around 220 μm. The alumina compacts were prepared by compacting and sintering the bonding ingredients in a high temperature furnace such that the relative proportions of alumina grains and porosity were about 60% and 40% by volume, respectively. Flat coupons of area of 5 $\times$5 cm^2 and thickness of 2.54 cm were used for laser surface processing.

B. Laser surface processing

The surface of the alumina compact was irradiated with a fiber optically delivered beam of 4 kW HAAS continuous wave Nd:YAG (yttrium aluminum garnet) laser. An elliptical beam with major and minor axis dimensions of 5.0 and 1.5 mm, respectively, and laser scan velocity of 100 cm/min would modify the entire surface of the compacts by parallel laser tracks. In subsequent trials, the surface modification was carried out by the laser powers in increments of 100 W above 1200 W (458 J/cm^2) up to 1900 W (726 J/cm^2).

C. Analysis

X-ray diffraction analysis of the laser surface modified alumina compacts was conducted using Norelco (Philips Electronic Instruments, Mount Vernon, NY) x-ray diffractometer with Cu K_α (λ=1.54 Å) radiation at 20 kV and 10 mA. Each specimen was scanned at a step size of 0.02° and for a count time of 1 s with diffraction angles varying between 20° and 100°. X-ray diffraction data were used for calculating the surface texture coefficients. Hitachi S3500 scanning electron microscope (SEM) was used to characterize the morphological features of the surface grains in laser surface modified alumina. A detailed investigation of the morphology of the surface grains formed during the laser surface modification of alumina was carried out in terms of curvature factor and size of grains. Public domain software IMAGEJ (National Institute of Health, USA) is used for image processing. The grain size of the surface grains is given as the diagonal distance of the polygonal grain. For both curvature factor and grain size, several (more than five) measurements were done and the average value along with the error bar is reported.

III. RESULTS AND DISCUSSION

X-ray diffraction spectra of alumina ceramic substrate surface and the laser melted surfaces at various powers are presented in Fig. 1. The x-ray analysis indicated the formation of stable α-alumina phase at all the laser fluences employed in the present study. During laser surface melting (rapid processing) of ceramics the solidification can proceed by direct growth of the crystalline phases from the solid liquid interface into the melt without nucleation within the melt pool. Hence the substrate below the melted region can act as catalytic sites for the growth of stable α-alumina. The observation of α-alumina in the present study is supported by the previous observations which indicated that the formation of metastable phases require the elimination of the catalytic sites for nucleation of α-alumina[16] which is not likely to

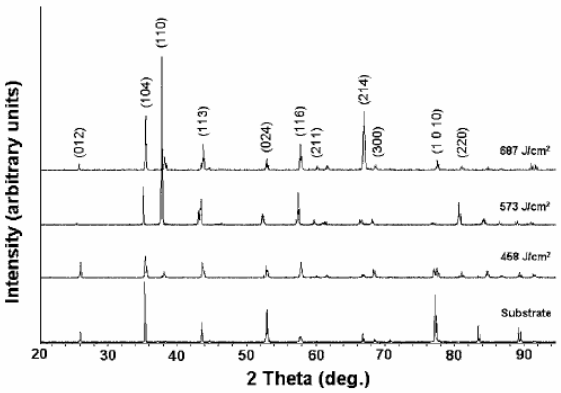


FIG. 1. X-ray diffraction patterns of alumina substrate and laser surface modified alumina at laser fluences of 458, 573, and 687 J/cm^2.

happen during the surface melting of alumina ceramic such as in the present case. Also, studies have indicated that laser surface processing can transform the metastable γ-alumina in plasma sprayed coatings into more stable α-alumina.[17] Hence the laser processing regimes employed in the present work for surface modification of alumina ceramic resulted in the formation of α-alumina due to the availability of the catalytic sites at the melt-substrate interface for growth of stable phases and consequent low undercoolings in the constrained solidification.

Careful analysis of the x-ray diffraction data also revealed the systematic variation of the intensities of some of the (h k l) peaks with laser fluence which can be related with the evolution of crystallographic texture during laser surface processing of alumina material. In this regard, a detailed calculation of texture coefficients have been done for predominant (h k l) peaks observed in the x-ray diffraction spectra. The texture coefficient (TC) for each (h k l) reflection is defined as[18]

$$\mathrm{TC}(h\ k\ l) = \frac{I(h\ k\ l)}{I_0(h\ k\ l)} \left\{ \frac{1}{n} \sum \frac{I(h\ k\ l)}{I_0(h\ k\ l)} \right\}^{-1}, \tag{1}$$

where $I(h\ k\ l)$ are measured intensities of (h k l) reflection, $I_0(h\ k\ l)$ are powder diffraction intensities of α-alumina according to the JCPDS (Card No. 46-1212), and n is the number of reflections used in the calculations. Following (h k l) reflections corresponding to α-alumina were used in the texture coefficient calculations: (0 1 2), (1 0 4), (1 1 0), (1 1 3), (0 2 4), (1 1 6), (2 1 1), (2 1 4), (1 0 10), (2 2 0), and (2 2 3). Table I summarizes the results of texture coefficient calculations for the observed (h k l) reflections in α-alumina at various laser fluences. In order to select the dominant reflections which show the strong texture in the laser surface modified alumina, an average texture coefficient is defined:

$$\mathrm{TC}_{\mathrm{av}}(h\ k\ l) = \frac{\sum \mathrm{TC}(h\ k\ l)}{N}, \tag{2}$$

where N is the number of laser fluences used in the study. The results of these calculations are also presented in Fig. 2, which indicate that the (1 1 0), (2 2 0), and (2 1 1) are the

TABLE I. Texture coefficients (TCs) of various (h k l) planes for alumina substrate and laser surface modified alumina at various laser fluences.

(h k l)	Substrate	496 J/cm^2	573 J/cm^2	649 J/cm^2	726 J/cm^2	TC_{avg}(h k l)
(012)	0.14	0.74	0.02	0.13	0.00	0.22
(104)	0.35	1.13	0.17	0.49	0.02	0.42
(110)	0.00	1.73	3.52	1.16	0.30	1.39
(113)	0.17	0.16	0.17	0.06	0.91	0.36
(024)	0.56	1.36	0.13	0.90	0.22	0.74
(116)	0.04	0.17	0.16	0.72	0.08	0.23
(211)	0.00	1.13	2.22	2.26	0.00	1.53
(214)	0.22	0.16	0.09	1.42	0.05	0.83
(1 0 10)	0.92	0.25	0.04	0.10	0.00	0.22
(220)	0.00	3.45	4.84	2.55	1.58	2.54
(223)	0.22	1.24	0.81	2.15	0.28	1.05

strongest reflections which corresponded to higher values of average texture coefficients. Hence these reflections were selected for further analysis of texture evolution during laser surface modification of alumina ceramic with various laser fluences. The variations of TC for (1 1 0), (2 2 0), and (2 1 1) reflections of α-alumina with laser fluence are presented in Fig. 3. The figure clearly indicates the systematic variation of the texture coefficients of these planes with laser fluence. The texture coefficient of the (1 1 0), (2 2 0), and (2 1 1) reflections increased with laser fluence, reached maximum around 573 J/cm^2, and then decreased at high laser fluences. This can also be observed from the x-ray diffraction spectra (Fig. 1) which show the absence of (1 1 0) and (2 2 0) reflections in the substrate [corresponding to TC(1 1 0) and TC(2 2 0)=0] and very low intensity at high laser fluence [corresponding to small values of TC(1 1 0) and TC(2 2 0)]. The intensities of (1 1 0) and (2 2 0) reflections reached maximum around the laser fluence of 573 J/cm^2 resulting in correspondingly maximum texture coefficient. The (2 1 1) reflection also exhibited the nearly similar trend of variation of texture coefficient with the laser fluence. The development of strong texture at 573 J/cm^2 can be related with the formation of highly faceted morphology of the surface grains (discussed in next sections).

The evolution of crystallographic texture during solidification or film growth has a strong effect on the evolution of resultant surface features such as faceted morphology of the surface grains. Early model of the faceted growth was proposed by van der Drift.[19] The model considers that each crystallite or grain grows with each crystallographic facet moving with a known normal velocity until a facet meets the surface of another growing crystallite. The grain boundaries are thus formed when the surfaces of different grains impinge upon each other. The evolution of the faceted morphology then depends on the relative growth velocities of the various facets. This is schematically illustrated for the three-dimensional case with (1 0 0) and (1 1 1) as growing facets (Fig. 4). The figure indicates that the surface morphology is determined by the ratio of velocities (α_{3D}) of (1 0 0) and (1 1 1) facets (v_{100} and v_{111}, respectively). The ratio is given by

$$\alpha_{3D} = \sqrt{3}\frac{v_{100}}{v_{111}}, \tag{3}$$

where $\sqrt{3}$ is the numerical prefactor chosen such that simple, highly symmetric morphologies occur at integer values of α_{3D}. Hence, if a crystal with facets (1 0 0) and (1 1 1) and velocity ratio described by α_{3D} is allowed to grow without impingement, it will asymptotically approach a characteristic, idiomorphic crystal shapes shown in Fig. 4.[20] For intermediate velocity ratios (α_{3D} between 1.0 and 3.0) multiple planes will grow dominantly until they impinge upon each other thereby providing a multiplane faceted grain. From this discussion, in the context of laser surface modification of alumina ceramic the evolution of (1 1 0) or (2 2 0) and (2 1 1) texture may be related with the relative growth of (1 1 0)

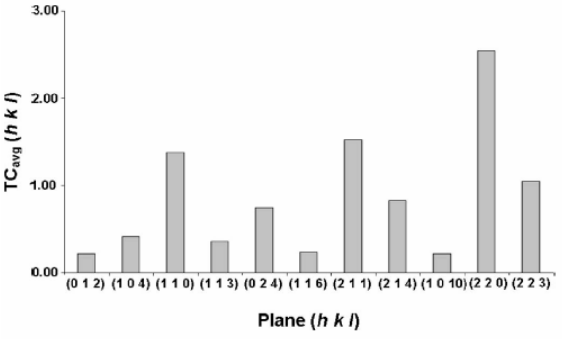


FIG. 2. Average texture coefficient for various (h k l) planes of α-alumina calculated over a range of laser fluences used for surface modifications.

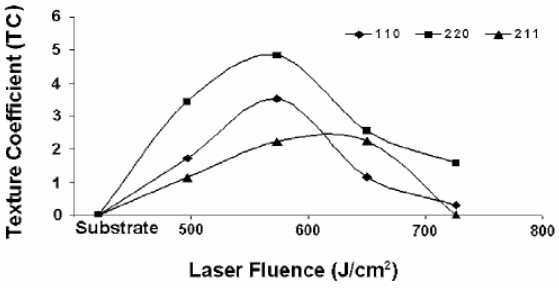


FIG. 3. Texture coefficients (TC) of (1 1 0), (2 2 0), and (2 1 1) planes of α-alumina as a function of laser fluence. (Note the data point corresponding to the texture coefficients of substrate.)

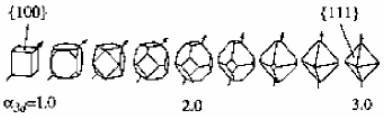


FIG. 4. van der Drift model illustrating the evolution of idiomorphic crystal shapes with the ratio of relative velocities (α_{3D}) of the {1 0 0} and {1 1 1} facets for the three-dimensional case (Ref. 20).

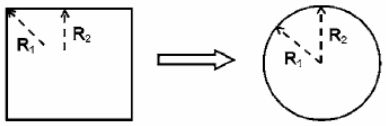


FIG. 6. Schematic representation of the polygonal surface grains used for curvature factor calculation. Curvature factor is given by ratio R_1/R_2.

or (2 2 0) and (2 1 1) planes in hexagonal lattice. A schematic of the formation of faceted crystal from the intersection of {1 1 0} and {2 1 1} planes in hexagonal lattice is presented in Fig. 5. The corresponding shape is compared with the SEM micrograph of the faceted morphology of the surface grains in laser surface modified alumina ceramic.

The surface of the laser surface modified alumina ceramics was characterized by the formation of faceted surface grains by the virtue of development of texture as discussed in the previous section. In addition to facets, these surface grains were also characterized for size and shape. The evolution of shape as function of laser fluence can be expressed in terms of a curvature factor. The curvature factor of the faceted surface grain is defined as

$$\text{curvature factor (CF)} = \frac{K_2}{K_1} = \frac{R_1}{R_2}, \tag{4}$$

where K and R are the curvature and radius of curvature, respectively, measured at the corner (subscript 1) and side (subscript 2) of the polygonal faceted surface grains (Fig. 6). For a nearly perfect polygon, with a very small value of R_1 (radius of curvature at the corner of the polygonal grain) and a very large value of R_2 (radius of curvature at the side of the polygonal grain), the curvature factor yields the value close to zero, whereas for a perfectly circular grain with equal R_1 and R_2, the curvature factor equals unity [Eq. (4)]. Hence evolution of shape of surface grains from polygonal to nearly circular grains can be characterized by considering the variation of curvature factor from zero to unity.

The effect of laser processing parameters on the evolution of morphology of the surface grains can be visualized in the relationship between the curvature factor and the grain size of the faceted surface grains presented in Fig. 7 along with the corresponding SEM micrographs of surface morphology of the laser surface modified alumina. Figure 7 indicates that the increase in laser fluence increased the grain size of the faceted surface grains. Also, the curvature factor showed a consistent low value (~0.1) up to the laser fluence of 611 J/cm^2 indicating polygonal faceted surface morphology of the surface grains. Above 611 J/cm^2, the curvature factor deviated towards larger values suggesting the initiation of the change in morphology of grains from polygonal towards nearly circular grains. The observation of the SEM micrographs in Fig. 7 indicates that well developed faceted surface grains form at the laser fluence of 573 J/cm^2. This may be due to the evolution of strong crystallographic texture related to {1 1 0} and {2 1 1} planes of α-alumina and correspondingly highest values of texture coefficients for these planes (Fig. 3). Above 573 J/cm^2, the degree of faceting progressively decreased and surface grains grew towards nearly circular shape with correspondingly higher values of curvature factor (>0.3) (Fig. 7). The progressive decrease in faceting follows the diminishing trend of texture coefficients of {1 1 0} and {2 1 1} planes above 573 J/cm^2 (Fig. 3). At laser fluences less than 573 J/cm^2, the shapes of the surface grains were polygonal as suggested by the low values of curvature factor. However, the small grain size indicated that the grains were still in the initial stage of faceting with correspondingly lower values of texture coefficients of {1 1 0} and {2 1 1} planes (Fig. 3). Although these sets of planes ({1 1 0} and {2 1 1}) appeared to produce multiplane faceted grains under laser fluences employed in the present work, it

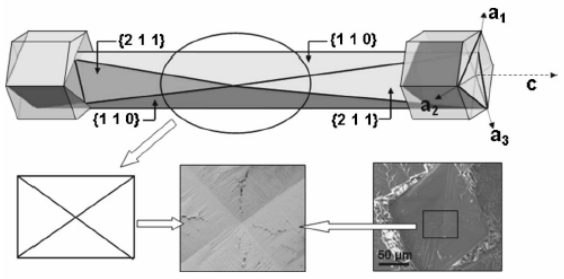


FIG. 5. Schematic of the development of faceted morphology from crystallographic texture in laser surface modified alumina.

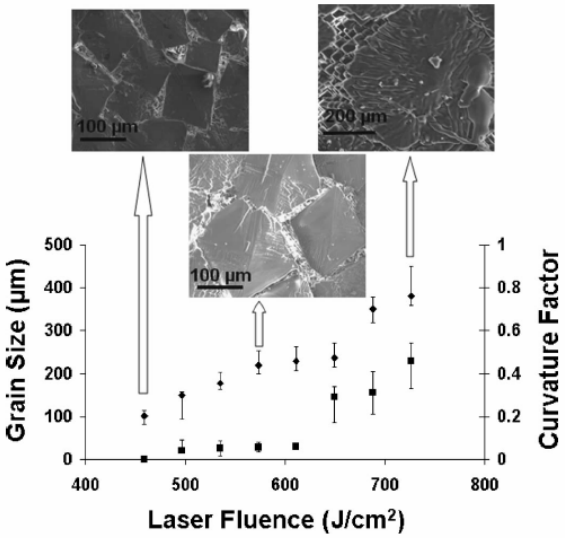


FIG. 7. Grain size, curvature factor, and corresponding SEM micrographs of the surface grains in laser surface modified alumina at various laser fluences[(♦) grain size and (■) curvature factor].

is still not completely understood as why these particular sets of planes grow predominantly. This remains a major focus of authors' ongoing research efforts. It is, however, understood that rapid quenching rates associated with laser surface processing can freeze the multiplanar growth process at any intermediate stage to provide idiomorphic crystal shapes such as observed in the present case.

In order to get insight into the evolution of surface morphology in the laser surface modified alumina, thermal aspects of the laser processing such as cooling rates need to be considered. Hence a simple one-dimensional thermal model was proposed to estimate the cooling rates associated with the laser processing. The consideration of one-dimensional model is reasonable from the viewpoint of uniformity of microstructure consisting of distributed multifaceted equiaxed grains in the majority of laser treated volume and low thermal conductivity of alumina. The governing equation is[21]

$$\frac{\partial T(x,t)}{\partial t} = \alpha \frac{d^2 T(x,t)}{dx^2}, \tag{5}$$

where α is the thermal diffusivity of the material and is equal to $k/\rho C_p$, k is the thermal conductivity of the material, ρ is the density of the material, and C_p is the specific heat. The effective thermal conductivity of the porous alumina is calculated based on the analytical correlations based on fractal dimensions. The details of assumptions and the properties of alumina used in the model are presented in the authors' work.[7] The solution of the heat flow equation gives the temperature distribution within the material from which the temperature gradient (G) and the velocity of solid/liquid interface (R) can be calculated by the procedure outlined in Ref. 7. Finally, cooling rate is given by the product of G and R. The well established relationship in the solidification theories exists between the secondary dendrite arm spacing (SDAS) and the cooling rates (T_c) and is given by[22]

$$\mathrm{SDAS} = A(T_c)^{-n}, \tag{6}$$

where A and n are material related constants. Grain size depends on the conditions of both nucleation and growth of which only the conditions of growth are explicitly dependent on the cooling rate. Hence under identical nucleation conditions during solidification, the similar equation can be written for the relationship between the grain size and the cooling rate with different values of constants.[23] The calculated values of cooling rate are presented in Table II. The table clearly indicates that as the laser fluence increased the cooling rate decreased resulting in larger grain size of the faceted surface grains at higher laser fluences (Fig. 7). This is in general agreement with the solidification theories which indicate the decrease in grain size with increasing cooling rate. The cooling rates in the range of $(2-6)\times 10^2$ K/s corresponding to laser fluences of 458–573 J/cm^2 appeared to be conducive to the growth of well defined multiplane faceted grains; whereas further drop in cooling rates in the range of $(0.7–2)\times 10^2$ K/s corresponding to laser fluences of 611–726 J/cm^2 generated the near circular grains of ill-defined facets (Fig. 7). Such a transition from well defined to ill-defined facets in the grain may be due to simultaneous growth of multiple planes at intermediate ratio of growth velocities (α_{3D}) at lower cooling rates.

TABLE II. Summary of the values of temperature gradient (G) at solid/liquid interface, solidification rate (R), and cooling rate calculated from one-dimensional thermal model for laser surface modified alumina at various laser fluences.

Laser fluence (J/cm^2)	G (K/m)	R (m/s)	Cooling Rate (K/s)
458	9.79×10^4	6.07×10^{-3}	5.94×10^2
496	8.30×10^4	6.05×10^{-3}	5.02×10^2
535	6.81×10^4	5.42×10^{-3}	3.69×10^2
573	5.16×10^4	5.05×10^{-3}	2.60×10^2
611	4.04×10^4	4.88×10^{-3}	1.97×10^2
649	3.12×10^4	4.56×10^{-3}	1.42×10^2
687	2.57×10^4	4.21×10^{-3}	1.08×10^2
726	1.99×10^4	3.54×10^{-3}	0.70×10^2

IV. CONCLUSIONS

Laser surface modifications of alumina ceramic with the 4 kW continuous wave Nd:YAG laser with fluences in the range of 458–726 J/cm^2 resulted in the formation of stable α-alumina phase. The growth of stable α-alumina was governed by the catalytic sites provided by the substrate which lowered the nucleation barrier for the nucleation of stable phase. The surface grains evolved into the highly faceted morphology at the laser fluence of 573 J/cm^2 and correspondingly highest values of texture coefficients for {1 1 0} and {2 1 1} planes. Evolution of such faceted surface morphology can be due to relative growth velocities of the {1 1 0} and {2 1 1} facet planes as suggested by the van der Drift model of faceted growth. This also explains the progressively decreasing degree of faceting above and below 573 J/cm^2 as indicated by SEM micrographs and corresponding progressively decreasing values of texture coefficients for {1 1 0} and {2 1 1} planes. The morphological evolution of the faceted surface grains in terms of the size and shape showed a strong dependence on the laser processing parameters. The grain size of the surface grains increased with increasing laser fluence. This is supported by the thermal analysis indicating the lower values of calculated cooling rates associated with higher laser fluence which is in agreement with the established solidification theories.

[1]Y. Gao, X. Xu, Z. Yan, and G. Xin, Surf. Coat. Technol. **154**, 189 (2002).
[2]X. Lin, Y. Zeng, X. Zhou, and C. Ding, Mater. Sci. Eng., A **357**, 228 (2003).
[3]D. Triantafyllidis, L. Li, and F. H. Stott, Thin Solid Films **453–454**, 76 (2004).
[4]D. Triantafyllidis, L. Li, and F. H. Stott, Appl. Surf. Sci. **186**, 140 (2002).
[5]A. Khangar and N. B. Dahotre, J. Mater. Process. Technol. **170**, 1 (2005).
[6]A. Khangar, E. A. Kenik, and N. B. Dahotre, Ceram. Int. **31**, 621 (2005).
[7]S. P. Harimkar, A. N. Samant, A. A. Khangar, and N. B. Dahotre, J. Phys. D **39**, 1642 (2006).
[8]Y. Liu, F. Lan, G. Yang, and Y. Zhou, J. Cryst. Growth **271**, 313 (2004).
[9]S. Bysakh, K. Chattopadhyay, T. Maiwald, R. Galun, and B. L. Mordike, Mater. Sci. Eng., A **375–377**, 661 (2004).
[10]R. Tewari, G. K. Dey, and N. Prabhu, Mater. Sci. Eng., A **304–306**, 548 (2001).
[11]O. Uzun, T. Karaaslan, M. Gogebakan, and M. Keskin, J. Alloys Compd. **376**, 149 (2004).

[12]S. Ansell, S. Krishnan, J. K. R. Weber, J. J. Felten, P. C. Nordine, M. A. Beno, D. L. Price, and M. L. Saboungi, Phys. Rev. Lett. **78**, 464 (1997).
[13]V. Jayaram, C. G. Levi, T. Whitney, and R. Mehrabian, Mater. Sci. Eng., A **124**, 65 (1990).
[14]C. G. Levi, V. Jayaram, J. J. Valencia, and R. Mehrabian, J. Mater. Res. **3**, 969 (1988).
[15]R. Krishnan, S. Dash, C. B. Rao, R. V. S. Rao, A. K. Tyagi, and B. Raj, Scr. Mater. **45**, 693 (2001).
[16]M. Li, K. Nagashio, and K. Kuribayashi, Mater. Sci. Eng., A **375–377**, 528 (1990).
[17]R. Krishnan, S. Dash, R. Kesavamoorthy, C. B. Rao, A. K. Tyagi, and B. Raj, Surf. Coat. Technol. **200**, 2791 (2006).
[18]S. Ruppi, Int. J. Refract. Met. Hard Mater. **23**, 306 (2005).
[19]A. van der Drift, Philips Res. Rep. **22**, 267 (1967).
[20]F. Paritosh and D. J. Srolovitz, J. Appl. Phys. **89**, 4857 (2001).
[21]H. S. Carslaw and J. C. Jaeger, *Conduction of Heat in Solids* (Oxford, New York, 1967).
[22]W. Kurz and D. J. Fisher, *Fundamentals of Solidification* (Trans Tech, Zurich, 1998).
[23]D. Eskin, Q. Du, D. Ruvalcaba, and L. Katgerman, Mater. Sci. Eng., A **405**, 1 (2005).

Int. J. Appl. Ceram. Technol., 3 [5] 375–381 (2006)

International Journal of Applied Ceramic Technology
Ceramic Product Development and Commercialization

Evolution of Surface Morphology in Laser-Dressed Alumina Grinding Wheel Material

Sandip P. Harimkar and Narendra B. Dahotre*

Department of Materials Science and Engineering, University of Tennessee, Knoxville, Tennessee 37996

An approach to laser dressing of alumina grinding wheels is proposed based on solidification microstructures associated with rapid cooling rates obtained in laser surface processing. Laser dressing of alumina grinding wheels forms surface microstructures characterized by multifaceted grains that are expected to facilitate the micro-scale material removal during precision machining. A detailed investigation of variation of grain size and melt depth with laser fluence is conducted. The results are correlated with calculated cooling rates derived from a thermal model. In addition, based on microscopic observations, the formation of surface grains by stacking of individual multifaceted grains formed during laser dressing is suggested.

Introduction

Lasers surface engineering (LSE) is a well-established technique for achieving improved surface properties of materials.[1–3] The high cooling rates associated with the laser surface processing result in the formation of various novel phases and morphology with improved properties.[4] Moreover, the advantages of laser surface processing stem from its amenability in controlling the surface properties by varying the laser processing parameters systematically. Lasers have been successfully used to improve the wear and corrosion resistance of metallic materials either by surface melting or cladding/coating high-performance materials on the metallic substrates.[5,6] Laser surface processing of metallic materials has been extensively reviewed in the literature in the context of various techniques such as laser heating,[7] alloying,[8] coatings,[6] cladding,[9] and so forth. Ceramic material is an important class of engineering materials where the improvement in the surface properties is of particular interest in specialized applications.[10] However, relatively less attention has been directed toward laser surface modifications of ceramics compared with metallic materials.

Alumina ceramic is an important conventional abrasive material used in machining (grinding) applications. Abrasive grinding wheels consist of irregular alumina particles (grains) compacted and bonded together with bonding ingredients (typically vitrified glassy compositions) and contain a certain level of controlled porosity. Each particle on the surface of the grinding wheel acts as a cutting tool and contributes to the total material removed during machining. Among various wheel

Materials Science and Technology Division, Oak Ridge National Laboratory, Oak Ridge, Tennessee 37831
*ndahotre@utk.edu
© 2006 The American Ceramic Society
No claim to original U.S. government works

and workpiece parameters, the performance of grinding wheels is highly influenced by the particle (grain) size and the sharpness of the abrasive grains. However, the properties of these surface grains progressively deteriorate as the number of grinding passes increases. During grinding, due to sliding forces, the surface grains become blunt and lose their ability to remove efficiently the material from the workpiece (Fig. 1a). The most common practice in industry is called diamond dressing (mechanical dressing), which uses a single point diamond tool to fracture and remove the blunt surface grains and expose new sharp grains, thus regenerating the new surface for efficient grinding (Fig. 1b). However, the process has many quality and economic disadvantages such as an increase in consumable cost due to wear of diamond tool and wheel and decrease of production rate due to frequent dressing. It has been reported that up to 90% of the wheel material is consumed in dressing operation compared to the actual grinding of the workpiece.[11] In addition, the diamond dressing imparts various surface and sub-surface defects such as cracks, which may lead to premature fracture of the grinding wheel during machining operation.

Attempts have been made to use lasers as dressing tools for grinding wheels due to the inherent advantages of the laser processing such as noncontact dressing and ease of automation. The primary motivation for such studies came from the ability of lasers to ablate selectively the low melting point bonding ingredients and/or blunt surface alumina grains of the grinding wheels so as to expose the new sharper grains on the surface of wheel for cutting action. Hence, to carry out such an ablation of material, the laser dressing at high laser intensities such as 4×10^{10} W/m^2 was suggested.[12,13] In one of the other studies, lasers are used in combination with the conventional diamond dressing.[14] Here, a laser selectively heats the grinding wheel surface, which is subsequently dressed by the diamond tool. The primary purpose in such studies is to reduce the wear of the diamond dressing tools by preheating the wheel surface by laser ahead of the diamond tool. Most of these approaches have had limited success in realizing the full potential of noncontact laser dressing such as in-process dressing, improved productivity, low cost of production, and consistency in workpiece finish.

Recently, considerable efforts have been made by our research group to develop the laser dressing method for alumina grinding wheels.[15–18] A novel approach is proposed for laser dressing technique using laser intensities lower than that required for ablation of grinding wheel surface ingredients. The approach is based on the surface melting and solidification rather than direct ablation of material. A laser beam is directed normal to the grinding surface of wheel with laser intensities high enough to cause melting of the blunt grains on the grinding wheel surface. In addition, under these regimes of laser intensities, the low melting point bonding ingredients evaporate, thus facilitating the melting and solidification of high melting point alumina (melting point $\sim$2300 K). The rapid solidification associated with laser melting of alumina results in a wheel surface morphology characterized by multifaceted grains with micropores between the faceted grains. Each multifaceted grain exhibits well-defined edges and vertex that can act as a single micro-cutting tool on the grinding wheel surface (Fig. 1c). Additionally, as these surface features are on the micron scale, such a laser-dressed grinding wheel with surface microstructural features is well suited

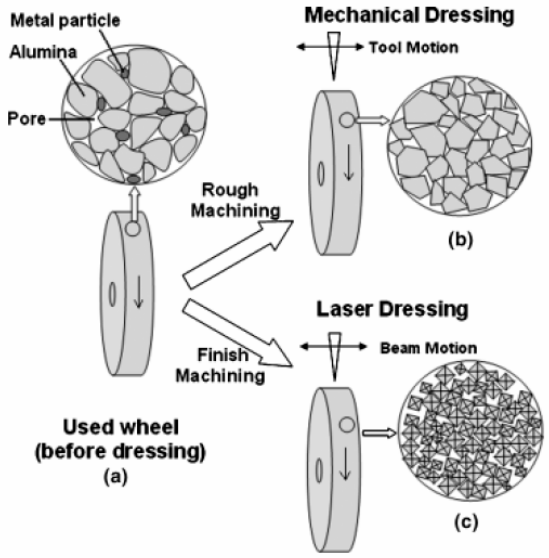


Fig. 1. Schematic of the dressing set up and surface morphology obtained in two different approaches of wheel dressing. (a) Used grinding wheel surface before dressing showing blunt surface grains with the metal particles loaded in the interconnected porosity; (b) surface features of diamond-dressed grinding wheel showing newly exposed irregular, sharp grains obtained by removing the blunt surface layer; and (c) surface features of laser-dressed grinding wheel obtained by rapid solidification of alumina grinding wheel surface showing highly refined multi-faceted grains with well defined edges and vertices.

for the microscale grinding application. The solidification microstructures on a surface of grinding wheel can be efficiently controlled by changing the laser dressing parameters, making the lasers reliable and efficient dressing tools for grinding wheels for precision machining applications. The present study is directed toward a detailed morphological characterization of the laser-dressed grinding wheel obtained using this novel dressing method.

Experimental Procedure

Materials

Commercially available alumina grinding wheels (of size $8 \times 1 \times 1\text{–}1/4''$ and grade 60I purchased from MSC Industrial Supply Co., Melville, NY) made of alumina-based material doped with chromia were used for the laser dressing studies. The abrasive grain material consists of 99.52% Al_2O_3, and the average grain size was around 220 μm. The relative proportions of grains and porosity were about 60% and 40% by volume, respectively. Although the laser setup was configured for in-process dressing of the entire grinding wheel surface, the present study used flat coupons of area 5cm × 5 cm and thickness 2.54 cm cut from new standard grinding wheels for subsequent laser surface processing. Here, the laser dressing is intended to refine the surface microstructure of the grinding wheel for applications in micro-scale material removal during grinding.

Laser Surface Processing

The surface of the alumina grinding wheel coupon was dressed with a fiber optically delivered beam of a 4 kW HAAS continuous wave Nd:YAG laser. The laser beam was directed normal to the grinding wheel surface. An elliptical beam with major and minor axes dimensions of 5.0 mm and 1.5 mm, respectively, and a laser scan velocity of 100 cm/min would dress the entire surface of the grinding wheel by parallel laser tracks. In subsequent trials, the dressing was carried out by increasing the laser powers in steps of 100 W above 1200 W (458 J/cm^2) up to 1900 W (726 J/cm^2).

Characterization

For microstructural characterization, specimens from the laser-dressed samples were sectioned perpendicular to the laser-processing direction. These cross-sectional specimens were mounted in epoxy molds and polished using 400, 600, 800, and 1200 grit SiC pads with final polishing in alumina slurry on a microcloth. Microstructural characterization of the polished samples was performed on a Hitachi S3500 SEM (Hitachi, Ibaraki, Japan). Low-magnification pictures of the cross sections of the resolidified layer in the laser-dressed samples were obtained. Maximum melt depth was measured at five locations in three different cross-sectional areas, and the average value of the melt depth with scatter was reported for each laser fluence used.

Results and Discussion

The effect of laser dressing on the microstructure of the alumina grinding wheel surface is illustrated in Fig. 2. The figure clearly shows that the surface morphology of the grinding wheel before laser dressing (left-hand side of Fig. 2a) consists of coarse irregular grains marked with high porosity. Such a highly irregular, coarse surface morphology is suitable for the rough machining of material where the main focus is the bulk removal of material. The high porosity of the surface helps in collecting the removed material particles (swarf). However, such a coarse microstructure results in a rough surface finish of the workpiece due to the large chip size generated and material removal by the ploughing action of the protruded grains. In contrast, laser dressing results in the formation of a highly dense and refined surface microstructure consisting of multifaceted grains with well-defined edges and vertices (Fig. 2b). Such a microstructure with multi-faceted grains and micro-porosity (marked in Fig. 2a) between the grains is expected to be helpful for finish/precision machining applications where the main goal is not the volume of material removed but the achievement of a fine surface finish by the cutting action of these microcutting edges and tips. Hence, in view of the characteristic surface microstructure of laser-dressed grinding wheels (multi-faceted surface grain morphology for micro-scale material removal and micro-porosity for collection of micro-particles during precision grinding), the present approach of laser dressing of grinding wheels offers tremendous potential for precision grinding applications. Preliminary grinding studies on steel with laser-dressed wheels produced a smooth workpiece finish with low cumulative material loss, thus, supporting the role of faceted grains on the wheel surface in the precision machining applications.[17]

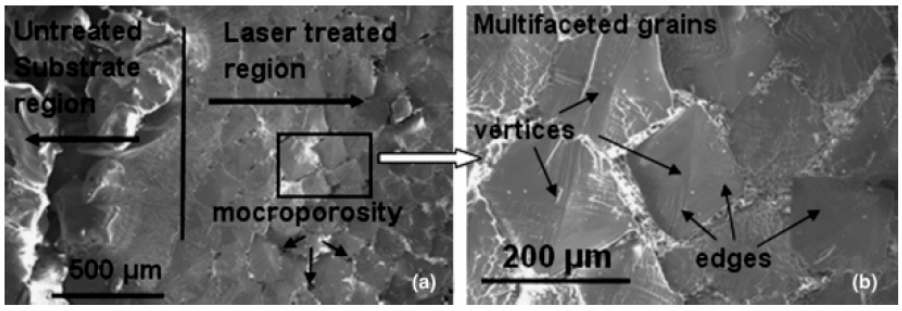


Fig. 2. Scanning electron microscopy micrographs of sample treated at laser fluence of 573 J/cm^2 (a) refined microstructure obtained by laser dressing along with the untreated area and (b) high magnification view of laser-dressed surface showing multifaceted grains with well defined edges and vertices.

The micro-scale material removal during grinding with a laser-dressed grinding wheel is likely to occur by chip formation. Initial understanding of the material removal mechanisms during grinding can be formulated using indentation fracture mechanics, which considers each abrasive grain as a square pyramidal indentor with tangential motion along the surface of the workpiece.[18] In the context of these models based on indentation fracture mechanics, the present laser dressing approach offers tremendous potential due to regular pyramidal multifaceted shapes of the grains formed during solidification of alumina during laser dressing. The detailed evaluation of grinding performance of these faceted grain structures is ongoing and will be reported in due course of time.

Furthermore, as mentioned earlier in section 'Materials', the abrasive grain material consists of 99.52% Al_2O_3 and the rest consists of the low melting bonding material. In the present laser-processing regimes, the high melting point ingredient such as α-alumina particles (Melting point $\sim$2300 K) melted and re-solidified and most of the low melting bonding ingredients appeared to have evaporated. Thus, the re-solidified layer consisted of mainly α-alumina. In the present study, as well as in earlier efforts,[16] this was confirmed by the observation of only peaks corresponding to α-aluminum during X-ray diffraction (XRD) analysis of the surface of laser-dressed alumina. The absence of any peaks in the XRD spectrum corresponding to any bonding material species in wheels prior to and after laser surface processing may be due to the very small volume of the material that was outside of the detection limits of these analysis techniques. Detection of a miniscule amount of bond material is possible by techniques such as transmission electron microscopy (TEM), which will be considered during future efforts.

The performance of the grinding wheel is highly determined by the grain size and grain morphology of the surface grains. The grain size of the surface of wheel is directly related to the achievable surface finish of the workpiece in surface grinding applications. Hence, in order to arrive at the optimum laser dressing parameters, a detailed investigation of the effect of laser parameters on the morphology of the surface grains of the laser-dressed grinding wheel needs to be conducted. In this study, the grain size of the laser-dressed wheel is represented as the average diagonal distance of the polygonal grains. Several measurements are performed and the average value of the grain size with error bars is reported. Increasing laser fluence progressively increases the grain size of the multifaceted grains (Fig. 3). Laser surface processing is a thermal process and such a behavior of increasing grain size with laser fluence can be the result of thermal aspects of the process. To gain more insight into such a behavior, cooling rate calculations have been performed based on a one-dimensional thermal model. The consideration of a one-dimensional model is reasonable from the viewpoint of the uniformity of the microstructure consisting of distributed multifaceted equiaxed grains within the laser-treated surface volume. Although multiple tracks with nearly no overlap between them were laid down for coverage of the entire surface, the model considers the effects of heat flow only in a single track. The low thermal conductivity of alumina limits the thermal effects from the previously laid tracks. The governing equation is[19]

$$\frac{\partial T(x,t)}{\partial t} = \alpha \frac{\mathrm{d}^2 T(x,t)}{\mathrm{d}x^2} \qquad (1)$$

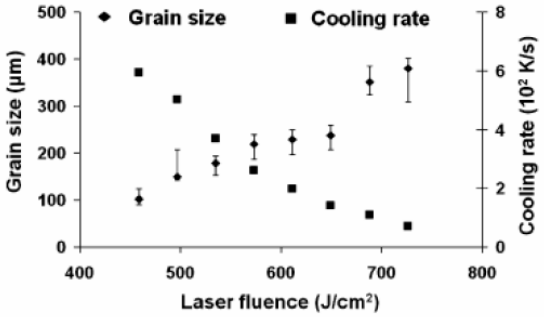


Fig. 3. Variation of calculated cooling rate and experimental grain size with laser fluence.

where α is the thermal diffusivity of the material and is equal to $k/\rho C_p$; k is the thermal conductivity of the material; ρ is the density of the material; and C_p is the specific heat. The effective thermal conductivity of the porous alumina is calculated based on the analytical correlations based on fractal dimensions. The details of assumptions and the properties of alumina used in the model are presented in the authors' work.[20] The model gives the temperature distribution within the material from which the temperature gradient (G) and the velocity of solid/liquid interface (R) can be calculated by the procedure outlined in reference.[20] Finally, the cooling rate is given by the product of G and R. A well-established relationship in the solidification theories exists between the secondary dendrite arms spacing (SDAS) and the cooling rates (T_c) and is given by[21]

$$\text{SDAS} = A\,(T_c)^{-n} \tag{2}$$

where A and n are material-related constants. The grain size depends on the conditions of both nucleation and growth, of which, only the conditions of growth are explicitly dependent on the cooling rate. Hence, under identical nucleation conditions during solidification, a similar equation can be written for the relationship between the grain size and the cooling rate with different values of the constants. The calculated values of cooling rate are plotted on the same plot (Fig. 3) to indicate the correlation between the faceted surface grain size and the cooling rates obtained at different laser fluences. The figure clearly indicates that as the laser fluence increases, the cooling rate decreases, resulting in a higher grain size of the faceted surface grains at higher laser fluences. This is in general agreement with the solidification theories that indicate the decrease in grain size with increasing cooling rate.[22]

One of the important parameters in the laser surface processing is the interaction depth of laser energy with the grinding wheel. In the context of laser dressing, this can be given by the depth of melting (thickness of resolidified layer) on the alumina wheel surface. The performance of laser-dressed grinding wheels may also be affected by the thickness of the resolidified layer at the wheel surface in terms of the life of the laser-dressed wheel with consistent performance. A typical cross section of the laser dressed grinding wheel consists of a resolified layer above highly porous alumina material with a well-defined interface (Fig. 4). The variation of depth of melting during laser dressing with laser fluence is given in Fig. 5. As the laser fluence increases, the melting depth increases and reaches a maximum value around a laser fluence of 700 J/cm^2, above which the change in depth of melting is marginal. The reason for such an observation is the limit of maximum temperature that the surface can reach during laser processing. The maximum temperature at the surface defines the location of the melting temperature in the temperature distribution within the material. As the maximum temperature reached at the surface is limited by the evaporation, further increase in the laser fluence would start evaporating material from the surface grinding wheel and the surface will still be at its evaporation temperature. Hence, once the surface evaporation is initiated,

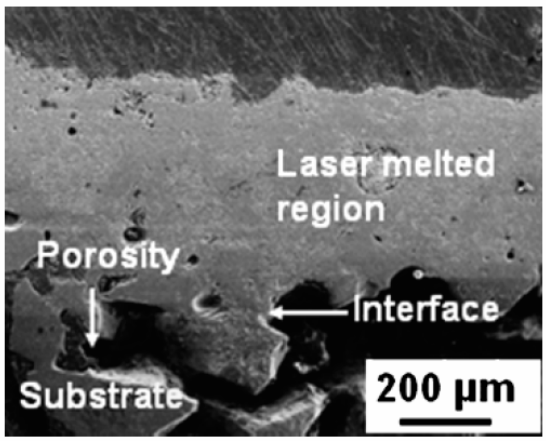


Fig. 4. Typical cross-section of laser-dressed alumina grinding wheel showing dense resolidified layer above highly porous alumina (laser fluence of 573 J/cm^2).

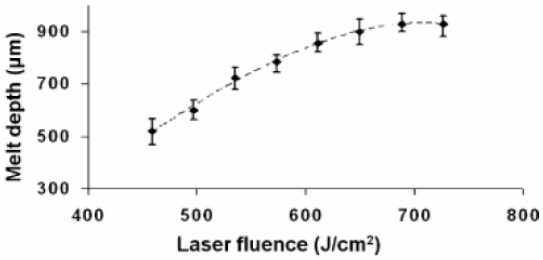


Fig. 5. Variation of depth of melting in laser-dressed alumina grinding wheel specimens with laser fluence.

the melt depth would remain constant with a further increase in laser fluence because the surface would always be at its maximum temperature (evaporation temperature). In addition, the thermal conductivity of alumina ceramics decreases rapidly with increasing temperature.[23] Hence, at high laser fluences ($>700\,J/cm^2$), the decrease in thermal conductivity limits the further increase in melt depth.

An attempt is made to understand the evolution of the morphology of the surface grains during laser processing. Figure 6(a) presents a microstructure showing the early stages in the arrangement/assembly of faceted grains. The microstructure obtained at a laser fluence of $382\,J/cm^2$ is marked with uniformly distributed fine grains. A careful examination of the surface microstructure shows a systematic arrangement/assembly of small cuboidal crystallites from under the grains on the top surface layer (Fig. 6). Surface grains thus seem to be assembled from the systematic stacking of the cuboidal crystallites, which come together to form the surface layer (Fig. 6c). The formation of such distributed assemblies of crystallites may be due to the porosity of the alumina substrate and the rapid solidification rates associated with laser processing such that the solidification is governed by the hydrodynamics of melt flow in the pores, whereas the faceting of the surface grains can be due to the competitive growth of various crystallographic planes that determine the energetically favorable shape of the crystals during solidification. Based on this observation, a schematic of the formation of surface grains is suggested (Fig. 6b). Solidification during laser processing proceeds by the dendritic growth due to the rapid solidification rates associated with the process. The cuboidal crystallites are the parts of these dendrites growing toward the

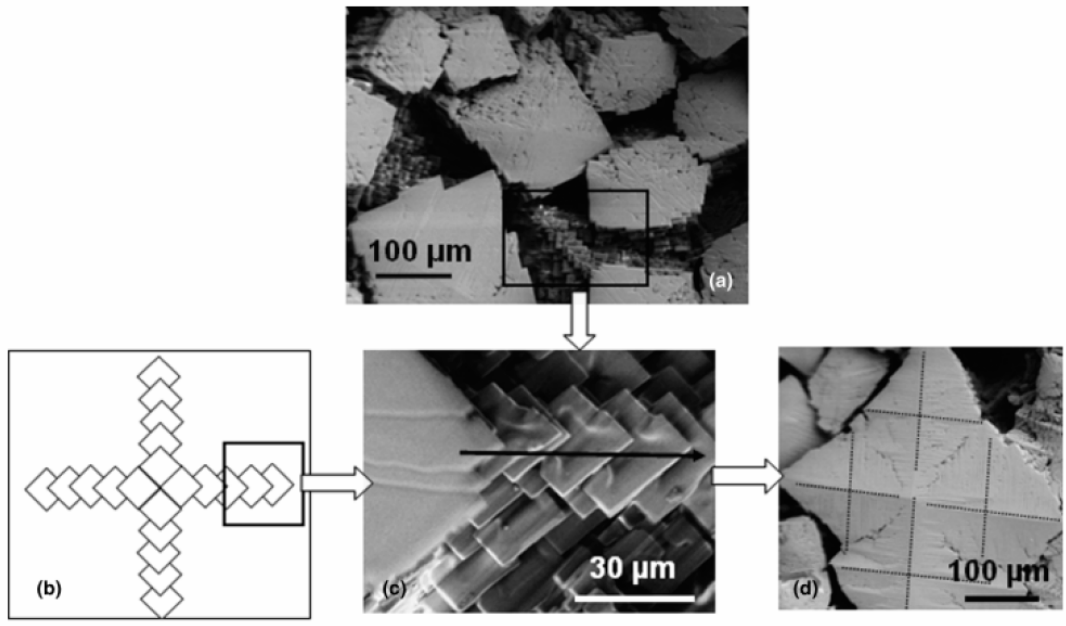


Fig. 6. Formation of faceted surface grain by systematic assembly of cuboidal crystallites (laser fluence 382 J/cm2). (a) Individual small grains (cuboids), (b) and (c) schematic and corresponding photograph of the assembly of small individual cuboids respectively, and (d) fully developed surface grain.

surface of the sample in the direction opposite to the heat flow. At the end of the solidification, such an assembly of stacked grain forms at the surface of laser-dressed alumina (Fig. 6d). As the laser fluence increases, the cooling rate decreases (Fig. 3), resulting in the spatially efficient (densely packed) assembly of stacked crystallites (Fig. 2b). Such dense assemblies of grains are likely to be energetically (thermodynamically) efficient arrangements. In contrast, at the lower laser fluence (382 J/cm^2), the assembly of grains leads to a more open surface structure with less efficient spatial stacking that in turn is likely to be energetically less efficient arrangements (Fig. 6a).

Conclusion

A novel approach of laser dressing is suggested based on the characteristic solidification microstructures formed on the surface of an alumina grinding wheel surface. Rapid solidification rates associated with laser dressing result in the formation of highly refined multifaceted grains, which facilitate the micro-scale material removal during precision machining of materials. A detailed investigation of the effect of laser dressing parameters on the microstructural features indicated an increase in faceted surface grain size with laser fluence from 458 to 726 J/cm^2. This increase in grain size with fluence is attributed to the slower cooling rates associated with higher laser fluences. Increase in laser fluence increases the spatially efficient assembly of faceted grains in the surface layer. The melting depth in laser-dressed wheels is found to increase with laser fluence up to 700 J/cm^2; thereafter, the change in melt depth is insignificant because of the maximum limit of the surface temperature associated with laser processing. Hence, the surface characteristics of the laser-dressed grinding wheel (faceted grain size and the depth of melting) can be well controlled by the laser processing parameters, rendering lasers as convenient and flexible tools for process dressing.

References

1. A. Agarwal and N. B. Dahotre, "Laser Surface Engineering of Steel for Hard Refractory Ceramic Composite Coating," *Int. J. Refract. Met. Hard Mater.*, 17 [4] 283–293 (1999).
2. P. Kadolkar and N. B. Dahotre, "Variation of Structure with Input Energy During Laser Surface Engineering of Ceramic Coatings on Aluminum Alloys," *Appl. Surf. Sci.*, 199 [1–4] 222–233 (2002).
3. J. D. Majumdar, B. R. Chandra, B. L. Mordike, R. Galun, and I. Manna, "Laser Surface Engineering of a Magnesium Alloy with Al+Al_2O_3," *Surf. Coat. Technol.*, 179 [2–3] 297–305 (2004).
4. B. J. Kooi, Y. T. Pei, J. Th, and M. De Hosson, "The Evolution of Microstructure in a Laser Clad TiB–Ti Composite Coating," *Acta Mater.*, 51 [3] 831–845 (2003).
5. I. Manna, J. D. Majumdar, U. K. Chatterjee, and A. K. Nath, "Laser Surface Engineering of Copper with Chromium for Enhanced Wear Resistance," *Scr. Mater.*, 35 [3] 405–410 (1996).
6. G. Abbas, Z. Liu, and P. Skeldon, "Corrosion Behaviour of Laser-Melted Magnesium Alloys," *Appl. Surf. Sci.*, 247 [1–4] 347–353 (2005).
7. P. A. Molian and M. Baldwin, "Effects of Single-Pass Laser Heat Treatment on Erosion Behavior of Cast Irons," *Wear*, 118 [3] 319–327 (1987).
8. Y. S. Tian, C. Z. Chen, L. X. Chen, and Q. H. Huo, "Microstructures and Wear Properties of Composite Coatings Produced by Laser Alloying of Ti–6Al–4V with Graphite and Silicon Mixed Powders," *Mater. Lett.*, 60 [1] 109–113 (2006).
9. J. Xu and W. Liu, "Wear Characteristic of In Situ Synthetic TiB_2 Particulate-Reinforced Al Matrix Composite Formed by Laser Cladding," *Wear*, 260 [4–5] 486–492 (2006).
10. G. Nicolas, M. Autric, W. Marine, and G. A. Shafeev, "Laser Induced Surface Modifications on ZrO_2 Ceramics," *Appl. Surf. Sci.*, 109–110 289–292 (1997).
11. T. C. Buttery, A. Statham, J. B. Percival, and M. S. Hamed, "Some Effects of Dressing on Grinding Performance," *Wear*, 55 [2] 195–219 (1979).
12. N. R. Babu, V. Radhakrishnan, and Y. V. G. S. Murti, "Investigations on Laser Dressing of Grinding Wheels—Part I: a Preliminary Study," *ASME J. Eng. Ind.*, 111 244–252 (1989).
13. N. R. Babu and V. Radhakrishnan, "Investigations on Laser Dressing of Grinding Wheels—Part II: Grinding Performance of a Laser Dressed Aluminum Oxide Wheel," *ASME J. Eng. Ind.*, 111 253–261 (1989).
14. C. Zhang and Y. C. Shin, "A Novel Laser-Assisted Truing and Dressing Technique for Vitrified CBN Wheels," *Int. J. Mach. Tools Manu.*, 42 825–835 (2002).
15. A. A. Khangar, E. A. Kenik, and N. B. Dahotre, "Microstructure and Microtexture in Laser-Dressed Alumina Grinding Wheel Material," *Ceram. Int.*, 31 621–629 (2005).
16. M. J. Jackson, G. M. Robinson, N. B. Dahotre, A. Khangar, and R. Moss, "Laser Dressing of Aluminium Oxide Grinding Wheels," *Br. Ceram. Trans.*, 102 237–245 (2003).
17. A. A. Khangar and N. B. Dahotre, "Morphological Modification in Laser-Dressed Grinding Wheel Material for Microscale Grinding," *J. Mater. Process. Technol.*, 170 1–10 (2005).
18. S. Malkin and J. E. Ritter, "Grinding Mechanisms and Strength Degradation in Ceramics," *J. Eng. Ind.*, 111 167–174 (1989).
19. H. S. Carslaw and J. C. Jaeger, *Conduction of Heat in Solids*, Oxford Press, New York, 1967.
20. S. P. Harimkar, A. N. Samant, A. A. Khangar, and N. B. Dahotre, "Prediction of Solidification Microstructures During Laser Dressing of Alumina-Based Grinding Wheel Material," *J. Phys. D: Appl. Phys.*, 39 1642–1649 (2006).
21. W. Kurz and D. J. Fisher, *Fundamentals of Solidification*, Trans Tech Publications, Zurich, (1998).
22. D. Eskin, Q. Du, D. Ruvalcaba, and L. Katgerman, "Experimental Study of Structure Formation in Binary Al-Cu Alloys at Different Cooling Rates," *Mater. Sci. Eng.*, 405 1–10 (2005).
23. W. H. Gitzen, *Alumina as a Ceramic Material*, American Ceramic Society, Ohio, 1970.

Effect of laser fluence on surface microstructure of alumina ceramic

S. P. Harimkar[1] and N. B. Dahotre*[1,2]

The present study discusses the microstructure development during surface modifications of alumina ceramic using high power continuous wave Nd:YAG laser. Laser fluence influenced the microstructure in terms of changes in morphology and (1 1 0) crystallographic texture of the surface grains. The microstructural observations can be used to establish the guidelines for optimising the laser fluence to achieve the desired morphology of the surface grains and extent of texture in the surface modified alumina ceramic.

Keywords: Laser surface modification, Ceramic, Alumina, Texture, Microstructure

Introduction

Ceramic is an important class of material which is finding increased applications as biomaterials and advanced structural and engineering materials where surface modifications becomes important.[1,2] The surface properties of these engineered ceramics are greatly influenced by the surface microstructure defined by the morphology and crystallographic texture of the surface grains. Such surface microstructural features are primarily inherited from the surface modification processes. Laser surface modifications (LSM) has emerged as a flexible and convenient technique for improving the surface properties of ceramics.[3,4] Laser surface modifications of porous alumina ceramic have recently attracted significant research interest for improving the surface properties for various applications. For example, LSM of alumina ceramic linings (used in furnaces, incinerators, heat exchangers, etc.) are expected to extend the life of the linings by minimising the localised thermal and environmental attack owing to sealing of the surface pores during surface modification.[5] Also, LSM of alumina abrasives wheels have the potential to regenerate the surface topography suitable for precision machining of materials.[6] Thus, LSM of porous alumina ceramic exhibit a great potential in a wide range of applications, with each application requiring the characteristic microstructure at the surface. Hence optimising the laser processing parameters to control the microstructural features evolved during surface modifications plays a key role in tailoring the surface properties for various applications. Despite great potential of laser surface modified ceramics in various advanced applications, detailed investigations of microstructure development during LSM are limited. Keeping this in view, the present study is directed towards understanding the laser interaction with an industrially important alumina ceramic during LSM. To the authors' knowledge, this is the first study which handles the LSM of alumina ceramics in a systematic manner taking into account the influence of laser fluence on the morphology and texture of alumina surface.

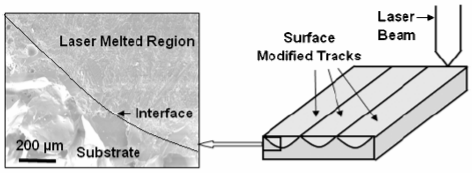
Experimental methods

In the present study, alumina compacts used were obtained from commercial source (MSC Industrial Supply Co.). These alumina compacts were cut from the industrial grinding wheels of grade 60 I. The maximum grain size in this grade is determined by sieve number 60, whereas, the minimum grain size is determined by the sieve number 70. This corresponds to the grain size 211–255 μm and the porosity of ~40 vol.-% in the initial ceramic compacts. The chemical composition of the compacts consisted of 99·52 wt-%Al_2O_3, 0·25 wt-% chromia and other proprietary trace components as binding agents. A 4 kW HAAS continuous wave Nd:YAG (1·06 μm wavelength) laser with fibre optically delivered beam was used to irradiate the surface of alumina ceramic compacts. In general, alumina has higher absorptivity (~0·68) at 1·06 μm wavelength of Nd:YAG laser[7,8] and it is expected even more for porous alumina used in the present study. The laser surface processing is carried out with an elliptical laser beam (major and minor axes dimensions of 5·0 and 1·5 mm respectively) and laser scan velocity of 0·0166 m s^{-1} (100 cm min) such that entire surface of the ceramic compact would be modified by parallel laser tracks (Fig. 1). The laser fluence in the increment of around 38 above 458 up to 687 J cm^{-2} was used in the present investigation to modify the surface of 2·5 cm thick and flat ceramic compact of area 5×5 cm^2. X-ray diffraction analysis of the laser surface modified alumina compacts was conducted using Norelco (Philips electronic instruments, NY) X-ray diffractometer with Cu K_α (λ=1·54 Å) radiation at 20 kV and 10 mA and diffraction angles varying between 20 and 100°. Hitachi S3500 SEM was used to characterise the morphological

[1]Department of Materials Science and Engineering, University of Tennessee, Knoxville, TN 37996, USA
[2]Materials Science and Technology Division, Oak Ridge National Laboratory, Oak Ridge, TN 37831, USA

*Corresponding author, email ndahotre@utk.edu

© 2006 Institute of Materials, Minerals and Mining
Published by Maney on behalf of the Institute
Received 7 July 2006; accepted 2 September 2006
DOI 10.1179/174367606X152688



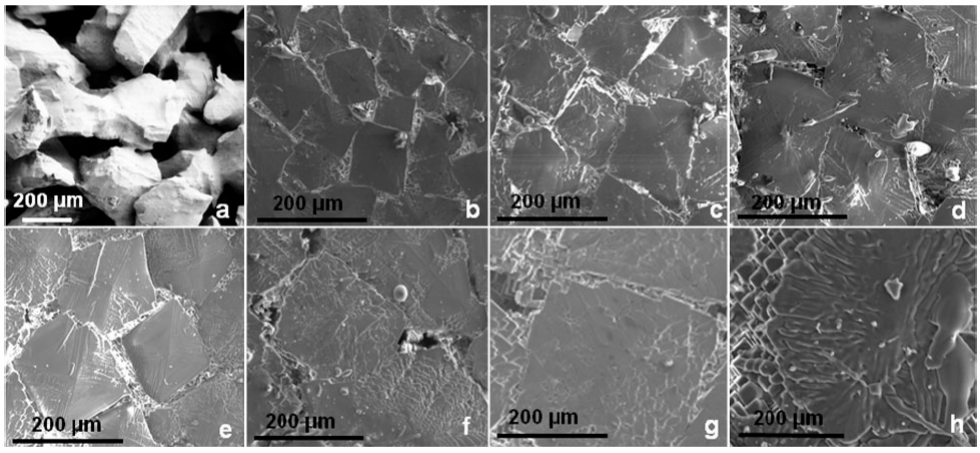
1 Schematic of laser surface modification process for alumina ceramic and corresponding SEM image of cross-sectional view indicating distinct interface between laser melted region and substrate

features of the surface grains in laser surface modified alumina. A public domain image processing software, image J (available from National Institute of Health) was employed for the determination of surface porosity and the surface grain size in the laser surface modified alumina. The measurements were carried out on five specimens and an average value was reported along with positive and negative error bars.

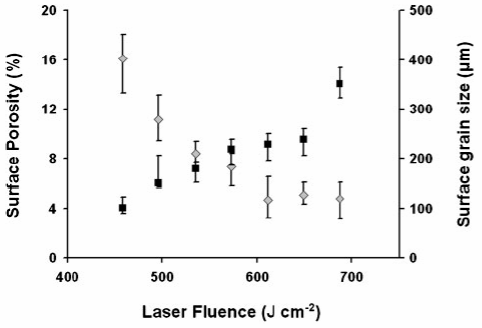
Results and discussion

Laser surface modification of porous alumina ceramics with the range of laser fluence (458–687 J cm^{-2}) employed in the present study results in the melting followed by formation of thin resolidified layer at the surface. Figure 1 presents the typical microstructure in the cross-section of the laser surface modified alumina ceramic (with laser fluence of 535 J cm^{-2}) in half laser track as indicated in the corresponding schematic of the surface modification process. The figure clearly shows the highly dense semi-elliptical resolidified area and a highly porous underlying substrate separated by a well defined interface between them. The semi-elliptical shape of the resolidified layer is a direct consequence of near Gaussian energy distribution of energy in the laser beam. The maximum melting depth corresponded to the energy maxima at the centre of laser beam. Also, the maximum depth of melting (~600 μm) in case of porous ceramics is expected to be greater than that in highly dense alumina for the similar laser fluence due to complex interaction of the laser beam with the porous materials. Also, the previous investigations have shown that the depth of melting increased with the increasing laser processing parameters until the evaporation threshold is reached. At the laser processing parameters corresponding to the evaporation threshold, the melt depth reaches the maximum value.[6,8] High conductivity (~0·8), high surface roughness and high porosity (~40 vol.-%) of the porous alumina used in the present study are expected to facilitate the higher laser energy absorption and flow of material through the porous structure resulting in higher effective melt depth.[8] Also, even though the present experiments are carried out with no overlap between the adjacent tracks, the uniformity of the thickness of laser surface modified layer can be controlled by controlling the degree of overlap between the adjacent laser tracks.

The effects of laser irradiation on the surface microstructure of the alumina ceramic are illustrated in Fig. 2. The figure presents a set of SEM surface images corresponding to the untreated alumina substrate (Fig. 2*a*) and laser surface modified alumina at laser fluence of 458–687 J cm^{-2} (Fig. 2*b*–*h*). The untreated substrate consisted of irregular alumina grains with a high degree of interconnected porosity. The surface modification of such highly porous alumina substrate with high power laser resulted in highly dense surface microstructure marked by systematic development of surface morphologies as a function of laser fluence. It is evident that the surface microstructure of laser modified alumina ceramic is characterised by faceted polygonal surface grains with varying sizes and extent of surface faceting depending on laser fluence. Based on these microscopic observations, two distinct regimes of explored laser processing conditions can be identified: one corresponding to the laser fluence <573 J cm^{-2} and the other corresponding to laser fluence >573 J cm^{-2}. Below 573 J cm^{-2} (Fig. 2*b*–*c*), the laser surface modified alumina underwent progressive development of faceting on polygonal surface grains. The surface grain morphology corresponding to laser fluence of 573 J cm^{-2} is



2 Images (SEM) of surface of *a* untreated alumina substrate and laser surface modified alumina at laser fluence of *b* 458, *c* 496, *d* 535, *e* 573, *f* 611, *g* 649 and *h* 687 J cm^{-2}

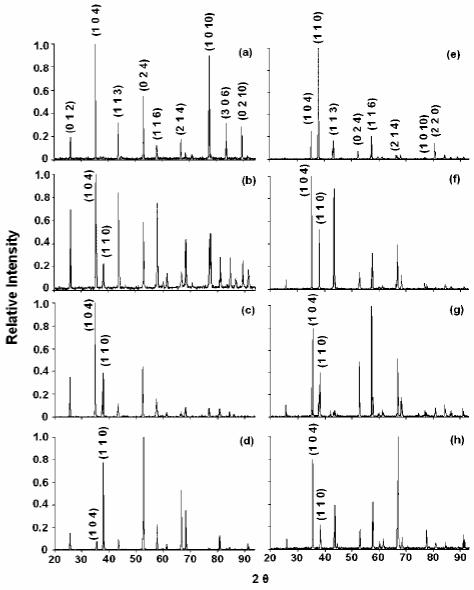


■: grain size; ◇: porosity

3 Variation of surface porosity and surface grain size of laser surface modified alumina with laser fluence

characterised by highest extent of faceting with well defined multifaceted microstructure of each polygonal surface grain. Interestingly, >573 J cm^{-2}, the surface grains tend to deviate from polygonal shapes transitioning from irregular to near circular shapes. Such an analysis is particularly useful for applications where alumina ceramics are used as abrasives for machining of materials. The intermediate laser powers are expected to provide the better surface topography for the microscale material removal owing to highly well defined faceted morphology of the surface grains. The laser processing of ceramics, by the virtue of rapid solidification rates is expected to facilitate the formation of unconventional phases and morphologies of the grains. Previous investigations of the authors have shown that laser surface processing of alumina ceramic is associated with the surface cooling rates of the order of 10^2 K s^{-1} calculated from the heat transfer model.[6] Also, the cooling rates decreased with increasing laser processing fluence.[9]

The variation of surface porosity and the grain size of the faceted grains with laser processing fluence is presented in Fig. 3. In general, the polygonal surface grain size (average of diagonal dimensions) increased with increasing laser fluence. This is a direct consequence of decreasing cooling rate with increase in laser fluence. This general trend of increase in grain size with increasing laser fluence (i.e. decreasing cooling rate) is in agreement with the established solidification theories.[10] The surface porosity showed the decreasing trend with increasing fluence. This also seems to be the consequence of increasing the surface grain size resulting in enhanced space filling on the surface of alumina processed with higher laser fluence. Thus, for the applications requiring sealing of surface porosity, selection of higher laser powers, which results in minimum surface porosity, are desirable. In addition to the development of surface microstructural features desired for a specific application, important considerations needs to be given to the inherent tendency of brittle ceramics to cracking owing to thermal stresses associated with laser processing. The present experimental investigations did not show severe cracking in substrate surface. This may be due to accommodation of thermal stresses due to porous nature of the substrate. Also, nearly crack free surface modification were obtained at higher laser processing

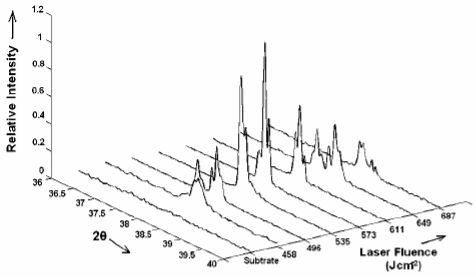


4 X-ray diffraction patterns of *a* untreated alumina substrate and laser surface modified alumina at laser fluence of *b* 458, *c* 496, *d* 535, *e* 573, *f* 611, *g* 649 and *h* 687 J cm^{-2}

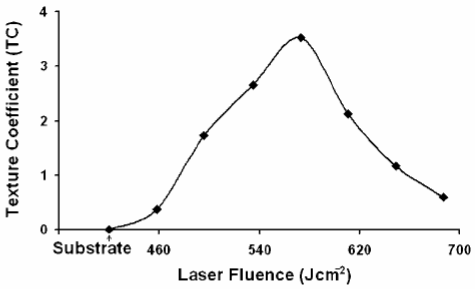
fluence seems to be the consequence of slower cooling rates associated with higher processing fluence.[6] Thus, tendency to cracking of the ceramics can be minimised by optimising the laser processing parameters and also by employing additional methods such as preheating of the specimens before the laser processing.

The development of characteristic surface microstructures (Fig. 2) can be explained on the basis of development of crystallographic texture in the laser surface modified alumina ceramic. The X-ray diffraction spectra of the surface of alumina substrate (Fig. 4*a*) and the laser surface modified alumina at laser fluence varying from 458 to 687 J cm^{-2} (Fig. 4*b–h*) can assist in evaluation of crystallographic texture. In order for the relative comparison among X-ray spectra of surface modified alumina using various laser fluences, the raw intensity counts data was normalised to obtain relative intensities of peaks in each spectrum. Both the substrate and laser surface modified specimens indicated the presence of highly stable α-Al_2O_3 phase (ICDD PDF#: 46-1212). The reformation of such a stable phase under the rapid solidification rates prevailing during laser surface processing was due to the presence of underlying substrate that provided heterogeneous nucleation sites for the formation of stable α-Al_2O_3 phase.[11–13]

Further analysis of the X-ray spectra revealed a systematic variation of relative intensities of (1 1 0) and (1 0 4) planes with laser fluence. The substrate showed a strongest peak corresponding to (1 0 4) reflection in agreement with the standard randomly oriented reference pattern (ICDD PDF#: 46-1212) and the absence of peak corresponding to (1 1 0) reflection. Earlier described two regimes of laser fluence (less and greater



5 Relative intensity of (1 1 0) reflection (2θ=37·785°) of α-Al_2O_3 substrate and laser surface modified alumina with various laser fluences



6 Variation of (1 1 0) TC of laser surface modified alumina ceramic with laser fluence (arrow indicates (1 1 0) TC of untreated substrate).

than 573 J cm^{-2}) also indicated the systematic variation of relative intensity of (1 1 0) plane. The relative intensity of (1 1 0) reflection increased progressively with laser fluence up to 573 J cm^{-2} followed by a gradual decrease above the fluence of 573 J cm^{-2} (Fig. 5). This is accompanied by the general reverse trend of variation of the relative intensity of (1 0 4) plane compared with the trend of variation of the relative intensity of (1 1 0) plane with laser fluence (Fig. 4). Intensities corresponding to other planes did not indicate any specific trend in variation of peak intensity as a function of laser fluence. Thus, there existed an intermediate value of laser fluence (573 J cm^{-2}) which showed strongest (1 1 0) peak and weak (1 0 4) peak (This (1 0 4) peak is the strongest peak in pattern of substrate and also in the reference pattern of randomly oriented sample corresponding to ICDD PDF#: 46-1212). The development of texture with the laser fluence can be quantified in terms of the texture coefficient (TC) given by

$$\mathrm{TC}(hkl) = \frac{I(hkl)}{I_0(hkl)} \left\{ \frac{1}{n} \sum \frac{I(hkl)}{I_0(hkl)} \right\}^{-1} \quad (1)$$

where $I(h\ k\ l)$ are measured intensities of $(h\ k\ l)$ reflection; $I_0(h\ k\ l)$ are powder diffraction intensities of α-alumina according to the ICDD PDF#: 46-1212; and n is the number of reflections used in the calculations. Following $(h\ k\ l)$ reflections corresponding to α-alumina were used in the TC calculations: (0 1 2), (1 0 4), (1 1 0), (1 1 3), (0 2 4), (1 1 6), (2 1 1), (2 1 4), (1 0 10), (2 2 0) and (2 2 3). The results of TC calculations for (1 1 0) reflection are presented in Fig. 6. The figure indicates that the TC increased gradually with increasing laser fluence up to 573 J cm^{-2}; reached maximum at 573 J cm^{-2} and then decreased progressively >573 J cm^{-2}, thus substantiating the formation of strong (1 1 0) texture at the intermediate laser fluence (573 J cm^{-2}). These two regimes of explored laser fluences (less and greater than 573 J cm^{-2}) for the variation of TCs and the relative intensity of (1 1 0) plane corresponded closely with the regimes of laser fluences which showed a distinct variations in the morphology of surface grains in laser surface modified alumina ceramic (discussed in the previous section). Thus the formation of highly ordered microstructure with well defined multifaceted grains in laser surface modified alumina at laser fluence of 573 J cm^{-2} seemed to be due to development of strong texture corresponding to (1 1 0) plane. Below and above 573 J cm^{-2}, the microstructure is relatively less well defined with a less extent of faceting of surface grains that corresponded to the diminishing (1 1 0) texture as indicated in Fig. 6.

The evolution of texture and its effect on the morphology of surface grains have been extensively studied in case of chemical vapour deposition of thin films.[14] The effect of vapor deposition reactor conditions on the texture and morphology of the films have been discussed within the framework of van der Drift model of evolutionary selection.[15] The model predicts the evolution of faceted surface microstructure based on the ratio of velocities of fast growing facets determined by the deposition reactor conditions. The principle of this model has been verified earlier by the authors for evolution of faceted grain structure in laser surface modifies alumina[16] and for the first time systematic study of variation of texture and morphology with the laser fluence is presented here. However, such a variation of texture and morphology in laser surface modified alumina from the thermal aspect of laser processing are very complex and forms the basis of authors' continuing research work along with the development of relevant model for selection of laser processing conditions for controlling the surface microstructure. The control of surface microstructure plays a key role in determining the surface properties for various applications.

Conclusions

Laser surface modifications of alumina ceramic with continuous Nd:YAG laser results in the formation of surface microstructure consisting of faceted surface grains. Laser powers employed for the laser surface modification strongly influence the microstructure in terms of texture and morphology of the surface grains. Highly ordered and well defined faceted microstructure at the intermediate laser power (573 J cm^{-2}) corresponds to the formation of strong (1 1 0) texture as indicated by strongest relative intensity of peak corresponding to (1 1 0) reflection and the highest value of (1 1 0) TC. Above and below this laser processing power, the order and degree of faceting of the surface grains decreases progressively accompanied with progressively diminishing value of relative intensity of peak corresponding to (1 1 0) plane and the (1 1 0) TC thus reinforcing the role of texture in determining the surface microstructure in laser surface modified alumina ceramic.

References

1. A. C. Queiroz, J. D. Santos, R. Vilar, S. Eugénio and F. J. Monteiro: *Biomaterials*, 2004, **25**, 4607–4614.
2. G. Nicolas, M. Autric, W. Marine and G. A. Shafeev: *Appl. Surf. Sci.*, 1997, **109**, 289–292.
3. E. Cappelli, S. Orlando, D. Sciti, M. Montozzi and L. Pandolfi: *Appl. Surf. Sci.*, 2000, **154**, 682–688.
4. K. H. Gahr and J. Schneider: *Ceram. Int.*, 2000, **26**, 363–370.
5. L. Bradley, L. Li and F. H. Stott: *Mater. Sci. Eng. A*, 2000, **278A**, 204–212.
6. S. P. Harimkar, A. N. Samant. A. A. Khangar and N. B. Dahotre: *J. Phys. D*, 2006, **39D**, 1642–1649.
7. J. Lawrence: *Optics Lasers Eng.*, 2004, **41**, 505–514.
8. W. H. Gitzen: 'Alumina as a ceramic material', 89–96; 1970, Wasterville, OH, American Ceramic Society.
9. S. P. Harimkar and N. B. Dahotre: *Int. J. Appl. Ceram. Technol.*, 2006, **3**, 375–381.
10. W. Kurz and D. J. Fisher: 'Fundamentals of solidification', 133–150; 1998, Zurich, Trans. Tech. Publications.
11. S. C. Kuiry, S. Wannaparhun, N. B. Dahotre and S. Seal: *Scrip. Mater.*, 2004, **50**, 1237–1240.
12. M. Li, K. Nagashio and K. Kuribayashi: *Mater. Sci. Eng. A*, 2004, **375A**, 528–533.
13. R. Krishnan, S. Dash, R. Kesavamoorthy, C. B. Rao, A. K. Tyagi and B. Raj: *Surf. Coat. Technol.*, 2006, **200**, 2791–2799.
14. F. Paritosh and D. J. Srolovitz: *J. Appl. Phys.*, 2001, **89**, 4857–4865.
15. A. V. Drift: *Philips Res. Reports*, 1967, **22**, 267–288.
16. S. P. Harimkar and N. B. Dahotre: *J. Appl. Phys.*, 2006, **100**, 1–6.

Available online at www.sciencedirect.com
ScienceDirect
Scripta Materialia 57 (2007) 401–404
Scripta MATERIALIA
www.elsevier.com/locate/scriptamat

Validation of crystallographic correlation for faceted morphology in laser surface engineered alumina ceramic

S.P. Harimkar,[a] C. Daniel,[a,b] C. Holzapfel,[c,1] P. Leibenguth,[c] F. Mücklich[c] and Narendra B. Dahotre[a,b,*]

[a] *Department of Materials Science and Engineering, University of Tennessee, Knoxville, TN 37996, USA*
[b] *Materials Science and Technology Division, Oak Ridge National Laboratory, Oak Ridge, TN 37831-6083, USA*
[c] *Materials Science Department, Saarland University, D-66141 Saarbrücken, Germany*

Received 2 April 2007; accepted 2 May 2007
Available online 8 June 2007

Surface modification of alumina ceramics using high energy-density lasers is associated with the formation of highly faceted pyramidal surface grains. Recently, we have developed a phenomenological crystallographic correlation that explains the faceted morphology by a $(1\bar{2}10)$ texture. Based on high-resolution electron back-scattered diffraction, the present work proposes a precise correlation showing that faceting of surface grains is closely linked with the evolution of a texture with $(2\bar{3}10)$ parallel to the surface and the (0001) normal to the direction of laser treatment trace.
Published by Elsevier Ltd. on behalf of Acta Materialia Inc.

Keywords: Ceramics; Laser surface engineering; Rapid solidification; Microstructure; Texture

Rapid solidification of materials during laser surface engineering (LSE) has long been recognized as a convenient means for developing unconventional (metastable and non-equilibrium) phases and morphologies in the microstructure of materials. Such microstructures in rapidly solidified materials are potentially useful for improving the mechanical and magnetic properties of materials [1,2]. Rapid solidification of metallic systems has been extensively reviewed in the literature from the viewpoint of the evolution of characteristic microstructures [3,4]. Most of such unconventional microstructures are derived from the high undercooling prior to nucleation and high cooling rates during subsequent rapid solidification. Recently, the utilization of laser surface engineered ceramic materials is steadily increasing in structural, electronic, engineering and biomedical applications where rapid solidification microstructures are expected to influence the properties of functional surfaces [5,6]. However, studies on rapid solidification of ceramics are limited, primarily due to the proposition that the low thermal conductivity of most ceramics inhibits rapid solidification. In contrast, the structural complexity of advanced ceramics is expected to facilitate the comparatively sluggish kinetics and consequently enhance the ability for undercooling, and hence suppress the nucleation of equilibrium phases [7].

Among the various ceramic materials, alumina ceramics constitute an interesting system for rapid solidification experiments due to the abundance of metastable crystalline phases. Furthermore, some of these phases are of significant commercial importance as catalysts or catalyst supports. A prior study of rapid solidification of alumina ceramic was conducted using electro-hydrodynamic atomization of alumina particles. It was observed that, depending upon the particle size of the atomized powders, these particles solidify into three distinct surface morphologies: faceted, dendritic and cellular [7]. However, the development of such characteristic morphological features has not been discussed in terms of the characteristic crystallographic information associated with them. Recently, significant research efforts have been directed by our group towards understanding the rapid solidification characteristics of alumina ceramic subjected to laser surface modifications. One of the most important microstructural

* Corresponding author. Address: Department of Materials Science and Engineering, University of Tennessee, Knoxville, TN 37996, USA. Tel.: +1 865 974 3609; e-mail: ndahotre@utk.edu
[1] Present address: Schleifring und Apparatebau GmbH, Am Hardtanger 10, D-82256 Fürstenfeldbruck, Germany.

1359-6462/$ - see front matter Published by Elsevier Ltd. on behalf of Acta Materialia Inc.
doi:10.1016/j.scriptamat.2007.05.008

changes observed in rapidly solidified alumina is the formation of polygonal surface grains with well-defined facets [8]. These surface microstructures have the potential to provide unique functional surfaces desirable in various manufacturing processes. For example, the faceted microstructure of a laser-modified alumina grinding wheel has demonstrated the ability to facilitate the microscale material removal during precision machining applications [9–11]. However, in order to reliably utilize these faceted surface microstructures, it is necessary to achieve a complete understanding of their crystallographic nature. In previous investigations, it was proposed that the faceted morphology of the surface grains is associated with the evolution of higher texture coefficients corresponding to $\{11\bar{2}0\}$ and $\{21\bar{3}1\}$ planes [8], based on preliminary analysis of X-ray diffraction (XRD) patterns. However, based on high-resolution electron back-scattered diffraction (EBSD), the present work proposes the existence of a more pronounced fiber texture that corresponds to calculation of the crystallographic correlations.

Alumina ceramic compacts were obtained from MSC Industrial Supply Co. The material consisted of about 40 vol.% porosity with an average particle size of around 220 μm. The chemical composition of the compacts primarily consisted of α-Al_2O_3 (>99.5%) and other trace components as binding agents. Flat specimens with a thickness of 2.5 cm and a surface area of 5×5 cm^2 were surface modified using a 4 kW continuous wave Nd:YAG laser (HAAS Laser Technologies Inc.) with a beam delivered via fiber optics. An elliptical laser beam spot shape (with major and minor axes dimensions of 5.0 mm and 1.5 mm, respectively) was scanned over the surface of ceramic compacts at a linear velocity of 100 cm min^{-1}. Based on earlier observations, faceted surface morphology is predominantly formed at a laser fluence of ~573 J cm^{-2} [8]. A Hitachi S3500 scanning electron microscope (SEM) was used to characterize the morphological features of the surface grains. XRD analysis of the laser surface modified alumina compacts was conducted using a Norelco (Philips Electronic Instruments, NY) X-ray diffractometer with Cu K_α ($\lambda = 1.54$ Å) radiation at 20 kV and 10 mA, and diffraction angles varying between 20° and 100°. EBSD patterns were obtained using a field emission electron microscope in a dual beam workstation (FEI Strata DB235) equipped with an orientation imaging microscopy system (TSL). During EBSD, the sample was tilted by 70° to the horizontal plane, and the electron beam was scanned over a selected surface area. The crystallographic data obtained using EBSD were indexed according to hexagonal α-Al_20_3 and presented as calculated pole figures.

When alumina ceramics are irradiated with a high-power laser, the absorption of laser energy causes the melting and subsequent rapid solidification of alumina. Figure 1 presents the microstructure of rapidly solidified alumina ceramic after irradiation with the laser beam. As indicated in the figure, the surface microstructure is characterized by dendritic polygonal grains with well-defined facets. The faceted surface grains are also characterized by the presence of underlying cuboidal crystallites, which seem to be the basic building blocks for the formation of faceted polygonal surface grains.

There are various theories of faceted crystal growth during solidification [12–14]. The first model is related to the formation of metastable phases at large undercooling. This is based on a theory of faceted growth during solidification proposed by Cahn [12], which takes into account the undercooling as a driving force. It was proposed that there exists a critical undercooling, ΔT_{crit}, below which the driving force is not sufficient to move the interface normal to itself, resulting in non-faceted grain morphology. In the context of our specimens, it seems at first that the faceted morphology of polygonal surface grains with underlying cuboidal crystallites is the direct consequence of the phase transformation of α-Al_2O_3 to γ-Al_2O_3 at large undercooling rates. However, during laser surface modifications, the underlying substrate is expected to provide the catalytic nucleation sites for the growth of stable α-Al_2O_3 and accompanying low undercooling in constrained solidification. This is confirmed by the observation of stable α-Al_2O_3 phase in the laser surface modified alumina ceramic [8]. The above discussion rules out the faceted growth model based on metastable phase formation at large undercooling [12,13] for the present experimental conditions. However, faceting behavior of the α-Al_2O_3 phase in the present investigations is in accordance with the solid–liquid interface model of Jackson [14]. According to this model, a faceted interface is formed when the dimensionless parameter, J, is greater than 2. This dimensionless parameter is given by:

$$J = \left(\frac{\Delta S}{R}\right)\xi = \left(\frac{\Delta H}{T_m R}\right)\xi, \quad (1)$$

where ΔS, ΔH, T_m and R are the entropy of fusion, the heat of fusion, the melting point and the gas constant, respectively; ξ is a parameter close to unity [13,14].

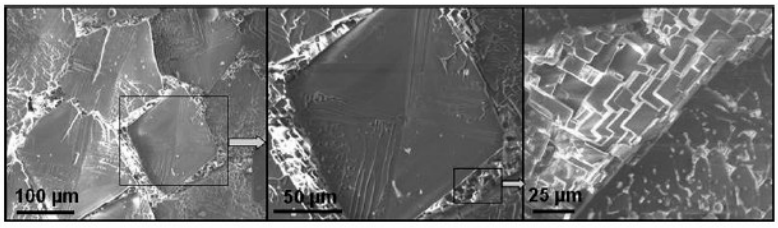


Figure 1. Faceted morphology of polygonal surface grains associated with laser surface modification of an alumina ceramic.

For α-Al_2O_3, the heat of fusion (ΔH) is 26 kcal mol^{-1} and the melting point (T_m) is 2323 K such that $\Delta S/R$ and hence J are equal to 5.63, suggesting faceted growth in alumina [15].

Previous investigations by the authors based on XRD studies have indicated that faceted surface grains in laser surface modified alumina ceramic can be closely linked to the evolution of the crystallographic texture [8]. The crystallographic texture was indicated by the highest values of texture coefficients corresponding to {11$\bar{2}$0} and {21$\bar{3}$1} planes in regular XRD patterns. Based on this observation, it was proposed that the formation of regular polygonal surface grains with well-defined facets is associated with the multiplanar growth of alumina grains during rapid solidification at cooling rates in the range of 10^2 K s^{-1} [16]. Figure 2 presents the schematic of a multiplanar faceted surface grain constructed by the intersection of $(2\bar{3}1\bar{1})$, $(2\bar{3}11)$, $(\bar{2}110)$ and $(2\bar{1}\bar{1}0)$ planes ({21$\bar{3}$1} and {11$\bar{2}$0} type planes, respectively) corresponding to the hexagonal representation of the crystal structure of α-Al_2O_3 phase. The base of the pyramidal construction corresponds to the $(2\bar{3}10)$ plane. The actual shape of the surface grains as seen in an SEM micrograph (Fig. 1) closely follows this scheme. Therefore, a $(2\bar{3}10)$ fiber texture should be obtained according to this correlation.

One representative example of a Kikuchi pattern obtained from the surface of laser surface modified alumina is presented in Figure 3. The Kikuchi patterns

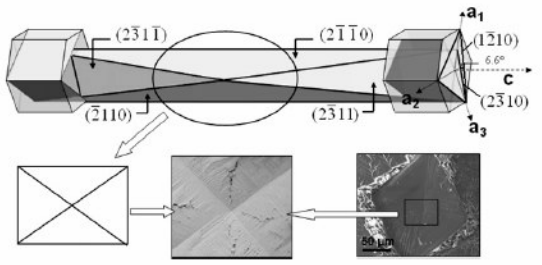


Figure 2. Schematic showing the development of faceted morphology of a surface grain from the evolution of crystallographic texture. The indices are represented in a hexagonal crystal system corresponding to α-alumina [8].

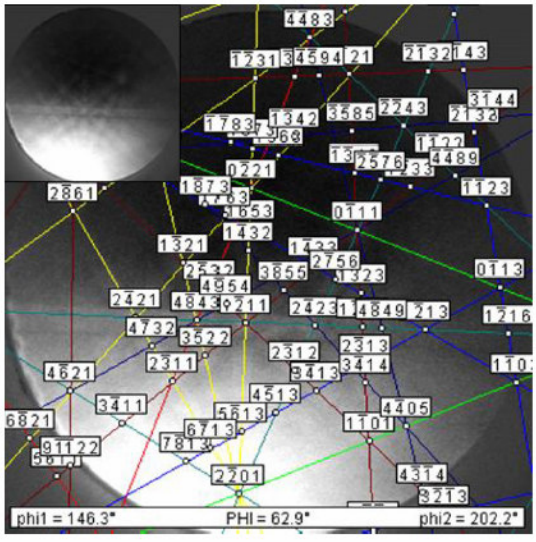


Figure 3. Example of Kikuchi pattern used for the calculation of the EBSD orientation map from the surface of laser surface modified alumina ceramic. Inset shows the unindexed Kikuchi pattern. The ceramic samples were coated with about 10 nm carbon and unpolished because important surface features and morphology contribute to lower-quality patterns which had to be manually checked for accuracy.

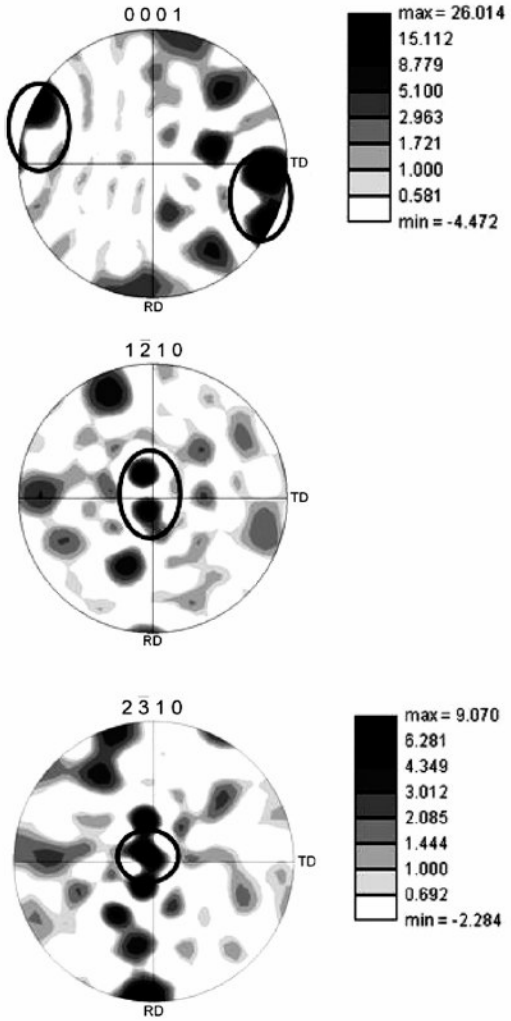


Figure 4. Calculated pole figures showing the distribution of {0001}, {1$\bar{2}$10}, {2$\bar{3}$10} poles with respect to surface normal. Maximum intensities are circled and show the (2$\bar{3}$10) texture as discussed in the text.

obtained at different positions on the sample confirmed the presence of α-Al_2O_3 and were indexed according to the corresponding hexagonal crystal structure. The EBSD orientation maps based on a number of such Kikuchi patterns from the surface revealed the crystallographic orientations of the large surface grains formed during laser surface modification of alumina ceramic.

Figure 4 presents the $\{0001\}$, $\{1\bar{2}10\}$ and $\{2\bar{3}10\}$ pole figures calculated from EBSD orientation maps. The figure indicates a high density of $\{0001\}$ poles perpendicular to the surface normal; these poles are concentrated in two opposite directions following the hexagonal representation of the unit cell. It also shows 6°–7° tilt between the surface normal and the $(1\bar{2}10)$ pole and a non-tilted $(2\bar{3}10)$ pole. Based on the calculations from the crystallographic model (Fig. 2), the tilt angle between $\{1\bar{2}10\}$ and $\{2\bar{3}10\}$ is found to be 6.6°. Thus, all these observations are in close agreement with the proposed correlations for faceting based on the evolution of crystallographic texture.

In summary, we report that rapid solidification encountered during the laser surface modification of alumina ceramic facilitates the development of microstructure characterized by well-defined faceted polygonal surface grains. The morphology of the faceted grains is closely linked with the evolution of a texture with $(2\bar{3}10)$ parallel to the surface and the (0001) normal in the direction of the laser treatment trace. A combination of theoretical structure correlations and experimental orientation data allows a complete description of the faceted morphology of the surface grains in laser surface engineered alumina ceramic. In addition, such an understanding might lead to improved tailoring of alumina ceramic surfaces in applications where surface texture plays an important role in determining functional properties.

This research was sponsored in part by the Laboratory Directed Research and Development Program of Oak Ridge National Laboratory (ORNL), managed by UT-Battelle, LLC for the US Department of Energy under Contract No. DE-AC05-00OR22725. Claus Daniel's work was performed under ORNL's Eugene P. Wigner Fellowship Program.

[1] H. Jones, Mater. Sci. Eng. A 304–306 (2001) 11.
[2] Y. Liu, F. Lan, G. Yang, Y. Zhou, J. Cryst. Growth 271 (2004) 313.
[3] J. Cai, G.C. Ma, Z. Liu, H.F. Zhang, Z.Q. Hu, J. Alloys Compd. 422 (2006) 92.
[4] Z.M. Zhou, Y.P. Wang, J. Gao, M. Kolbe, Mater. Sci. Eng. A 398 (2005) 318.
[5] E. Cappelli, S. Orlando, D. Sciti, M. Montozzi, L. Pandolfi, Appl. Surf. Sci. 154 (2000) 682.
[6] K.H. Gahr, J. Schneider, Ceram. Int. 26 (2000) 363.
[7] C.G. Levi, V. Jayaram, J.J. Valencia, R. Mehrabian, J. Mater. Res. 3 (1988) 969.
[8] S.P. Harimkar, N.B. Dahotre, J. Appl. Phys. 100 (2006) 024901.
[9] S.P. Harimkar, A.N. Samant, A.A. Khangar, N.B. Dahotre, J. Phys. D: Appl. Phys. 39 (2006) 1642.
[10] S.P. Harimkar, N.B. Dahotre, Int. J. Appl. Ceram. Technol. 3 (2006) 375–381.
[11] S.P. Harimkar, N.B. Dahotre, Adv. Appl. Ceram. 105 (2006) 304–308.
[12] J.W. Cahn, Acta Metall. 8 (1960) 554.
[13] J.A. Sekhar, A. Bharti, R. Trivedi, Metall. Trans. A 20 (1989) 2191.
[14] K.A. Jackson, in: R.H. Doremus, B.W. Roberts, D. Turnbull (Eds.), Growth and Perfection of Crystals, John Wiley, New York, 1958, pp. 319–324.
[15] W.H. Gitzen, Alumina as a Ceramic Material, American Ceramic Society, Westerville, 1970.
[16] A. Khangar, E.A. Kenik, N.B. Dahotre, Ceram. Int. 31 (2005) 621–629.

ELSEVIER

Materials Characterization xx (2007) xxx – xxx

MATERIALS CHARACTERIZATION

Characterization of microstructure in laser surface modified alumina ceramic

Sandip P. Harimkar [a], Narendra B. Dahotre [a,b,*]

[a] Department of Materials Science and Engineering, University of Tennessee, Knoxville, TN 37996, USA
[b] Materials Science and Technology Division, Oak Ridge National Laboratory, Oak Ridge, TN 37831, USA

Received 16 June 2006; received in revised form 27 October 2006; accepted 3 June 2007

Abstract

Surfaces of alumina ceramic compacts were modified by irradiating with a high-power continuous wave laser to form a rapidly solidified continuous surface layer. A detailed characterization of the laser surface modified alumina using X-ray diffraction (XRD) and scanning electron microscopy (SEM) revealed a development of (110) crystallographic texture and a systematic evolution of surface microstructure in terms of surface grain size, porosity and roughness with laser processing fluence. Also, due to complexity of surface microstructures, a fractal based approach is suggested to completely describe the surface state of laser surface modified alumina. The results indicated that fractal dimensions of the surface microstructures can be effectively correlated with the surface features of laser surface modified alumina.
© 2007 Elsevier Inc. All rights reserved.

Keywords: Alumina; Laser surface modification; Microstructure; Texture; Fractal dimension

1. Introduction

Surface modification of alumina ceramics is rapidly gaining importance due to increased utilization of alumina ceramics in structural, electronic and biomedical applications where performance is determined primarily by the surface properties [1–3]. Lasers have emerged as effective tools for the surface modifications of alumina ceramics for improving the surface properties through structural, microstructural and chemical transformations [4–8]. In this context, laser surface modifications of alumina ceramic are utilized for transformation of metastable γ-phase into equilibrium α-phase in ceramic coatings [5], sealing of surface porosity and surface cracks in refractory ceramics [6], reconditioning of the ceramic grinding wheel surface for micro-cutting action during laser dressing [7,8]. Laser processing parameters during such surface modifications are expected to influence the surface microstructure of laser modified alumina which in turn influences the surface properties. Hence in order to augment our understanding on the influence of laser processing parameters on the surface properties, the first step and challenge is to characterize the microstructure of the surface modified alumina.

Recently, a concept of fractal geometry which was originally developed for the analysis of irregular features in nature is finding increased applications in

* Corresponding author. Department of Materials Science and Engineering, University of Tennessee, Knoxville, TN 37996, USA. Tel.: +1 865 975 3609; fax: +1 865 975 4115.
E-mail address: ndahotre@utk.edu (N.B. Dahotre).

1044-5803/$ - see front matter © 2007 Elsevier Inc. All rights reserved.
doi:10.1016/j.matchar.2007.06.002

the fields of materials science for the characterization of microstructures [9–13]. Fractal dimensions effectively describe the complex and geometrically irregular microstructure and have been successfully applied in the characterization of grain boundaries [10], fracture surfaces [11], dendritic microstructures [12], and precipitates, [13] etc. The effectiveness of this approach for the characterization of microstructures is derived from the ability to establish the useful numerical correlations between the fractal dimensions and the various properties of the material such as fracture toughness, creep strength, etc. [14].

The present study is intended to completely characterize the surface microstructure of the laser modified alumina in terms of the surface morphology and crystallographic texture. Also, detailed analysis on the evolution of surface microstructural features (porosity, grain size and roughness) with laser processing fluence used for surface modification is conducted. Finally, concept of fractal geometry is applied to characterize the surface microstructure and derive the useful correlations between fractal dimensions and the surface microstructural features.

2. Materials and methods

2.1. Materials

Alumina-based ceramic compacts (5 cm × 5 cm × 2.5 cm) used for the laser surface modification experiments were cut from commercially available vitrified grinding wheels (supplied by MSC Industrial Supply Co.) using a carbide grit rod saw (Make: STANLEY™) in dry condition. The cuts were made only in the cross sections of the grinding wheel and the as-compacted surfaces were subjected to laser surface modification. The grinding wheels are commercially made from artificial aluminum oxide produced by melting bauxite at high temperature in an arc type electric furnace [15]. The compacts consisted of irregular abrasive grains of average size around 220 μm with average porosity of around 40% by volume. The abrasive grains were primarily composed of Al_2O_3 (>99.52 wt.%) with traces of Cr_2O_3.

2.2. Laser surface modification

A 4-kW HASS continuous wave (cw) Nd:YAG laser with optically delivered beam was used for surface modification of alumina compacts. Flat surfaces of alumina ceramic compacts were irradiated with an elliptical laser beam and the scan velocity of 100 cm/min such that the entire surface of specimen would be modified by laying subsequent parallel laser tracks with minimal overlap (<10%). The laser processing was carried out with laser fluence in the increment of around 38 J/cm^2 above 458 J/cm^2 up to 649 J/cm^2. Below 458 J/cm^2, there is no significant coupling of laser energy with the ceramic substrate resulting in no observable surface melting. Hence laser fluence is selected above 458 J/cm^2 up to 649 J/cm^2 such that effective surface modification of the alumina ceramic surface is achieved by surface melting. The selection of experimental laser fluences for surface modification of alumina in the present study is based on the previously published results which suggested the initiation of surface melting of alumina ceramic around 458 J/cm^2 indicated by minimum observable depth of melting [8].

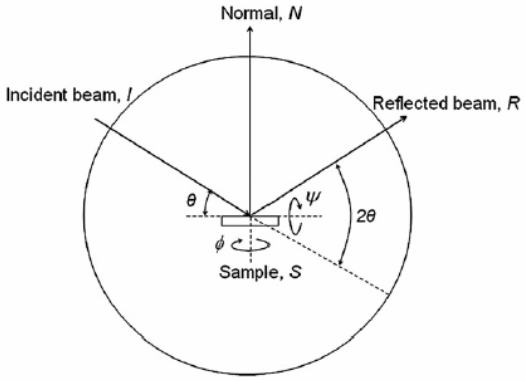


Fig. 1. Schematic of the diffractometer geometry for texture analysis.

2.3. Characterization

Detailed characterization of the microstructure before and after laser surface modifications of alumina ceramic compacts was conducted using scanning electron microscopy (SEM) and X-ray diffraction techniques. For microstructural analysis, the specimens were prepared by cutting small coupons (1.5 cm × 1.5 cm × 1.0 cm) from laser surface modified specimens with a ISOMET™ low speed saw (Make: BUEHLER™) using a diamond blade (Make: BUEHLER™) in dry condition. The surfaces before and after laser surface modifications were preserved during specimen cutting to ensure that microstructure, surface condition, roughness is unaffected by the sample preparation methods. The dry condition during cutting is used to prevent the impregnation of cutting media into porous alumina samples and eliminate the possibility of undesirable affects during subsequent microstructural characterization.

The characterization of surface morphology of the alumina compacts before and after laser surface

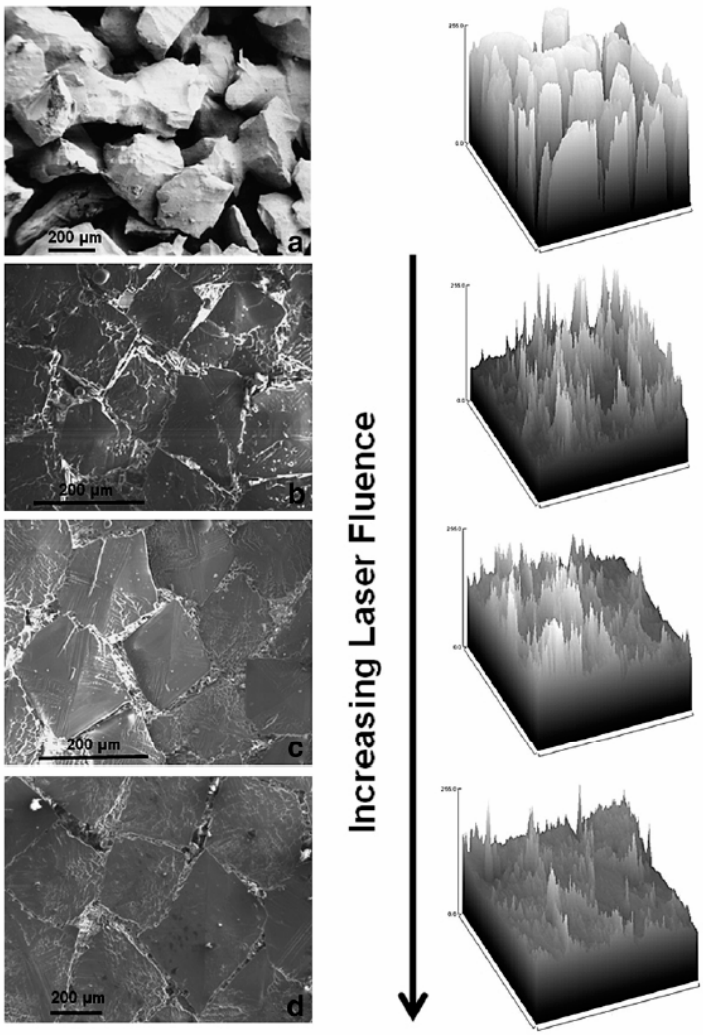


Fig. 2. SEM micrographs and corresponding 3D topographical maps showing the evolution of surface morphology in laser surface modified alumina ceramics. (a) Alumina ceramic substrate before surface modification and (b–d) after surface modification with laser fluence of 496, 573 and 649 J/cm^2 respectively.

modifications is conducted using a HITACHI™ S3500 SEM. The SEM was operated in high vacuum mode at an accelerating voltage of 15 kV and filament current of 78 μA. Also, the qualitative elemental analysis of laser modified alumina was conducted using Energy Dispersive Spectrometer (EDS) system attached to the SEM. Due to low conductivity of the alumina ceramic, sample preparation for SEM included an additional step of coating the specimen with gold to minimize the build up of electric charge. The gold coatings on the samples of alumina ceramic were deposited using SPI MODULE™ sputter coater operated at pressure of 10^{-1} Torr and sputtering current of 20 mA for deposition time of 20 s

X-ray diffraction analysis of the laser surface modified alumina coupons was carried out using Philips Norelco X-ray diffractometer operating with Cu Kα (λ=1.54178 Å) radiation at 20 kV and 10 mA. The diffraction angle was varied between 20 and 100° 2-theta at a step increment of 0.02° 2-theta with a count time of 1 s. The surfaces of alumina ceramic before and after laser surface modification (without any pulverizing into powder) were directly examined by X-ray

Table 1
Average values of porosity, grain size and surface roughness of laser surface modified alumina ceramic with a range of laser processing fluence

Laser fluence (J/cm^2)	Porosity (vol.%)	Grain size (μm)	Surface roughness, Ra (μm)
458	16.12	102	3.49
496	11.17	150	2.76
535	8.40	178	1.95
573	7.30	219	1.66
611	4.66	229	1.18
649	5.10	238	1.93

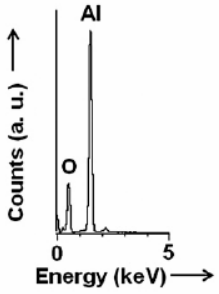


Fig. 3. EDS spectrum from laser surface modified alumina ceramic illustrating the presence of Al and O elements.

diffraction to facilitate the study of development of preferred orientation.

For detailed texture analysis, Philips X'Pert Analytical Diffractometer with Cu Kα radiation as a point source operating at 45 kV and 40 mA was used. Reflection method was used to obtain the pole figures by varying rotation angle, φ, between 0° and 360° and varying tilt angle, ψ, between 0° and 85°. Schematic of the typical diffraction geometry along with various rotation and tilt axes for texture analysis is presented in Fig. 1 [16,17]. For texture measurement, each coupon of un-modified and laser surface modified alumina ceramic was mounted directly on the specimen holder using adhesive binder such that surface of the sample is as flat as possible. During texture analysis, the counter is fixed in the 2-theta position corresponding to the planes which are expected to exhibit the preferred orientation. In the present study, texture analysis is conducted for determining preferred orientation of (110) plane corresponding to diffraction angle of 37.785° 2-theta. Once the counter is fixed at diffraction angle (2-theta), the sample holder is slowly rotated about the diffraction axis such that surface of the sample is equally inclined to the incident and diffracted beam directions. This corresponds to initial position of the sample (Fig. 1). The sample is then slowly rotated about the rotation and tilt axes to obtain a series of φ-scans at different tilt angles. The step size for the rotation and tilt axes was 5° and the time per step was 1 s. The diffraction data obtained from these experiments were used to generate the pole figures of (110) planes presented as contour plots with zero angle at the center using the method described in reference [16].

A stylus-based Mahr Federal Perthometer M1 with stylus tip radius of 2 μm was used for the measurement of surface roughness parameter, R_a (arithmetic mean deviation of the roughness profile). The measurement was conducted for a tracing length of 1.75 mm on the surface of five laser surface modified specimens and the average value along with positive and negative error bars is reported. During the measurements, the sample was firmly mounted on the horizontal stage with adhesive binder to prevent the movement of specimen during traversing of stylus tip. The grain size of the surface grains is given as the diagonal distance of the polygonal grain. The surface grain size and the porosity were determined by the image analysis of several (more than five) SEM micrographs and the average value along with the positive and negative error bars is reported.

For fractal analysis, the SEM images were converted from spatial domain of brightness to frequency domain components using Fourier transforms and then filtered from noises followed by thresholding to convert them into binary digital images using a public domain software, ImageJ (available from the National Institute of Health, USA). Fractal dimensions were calculated using image processing of SEM micrographs in combination with the implementation of box counting algorithm using the software, ImageJ. In box counting

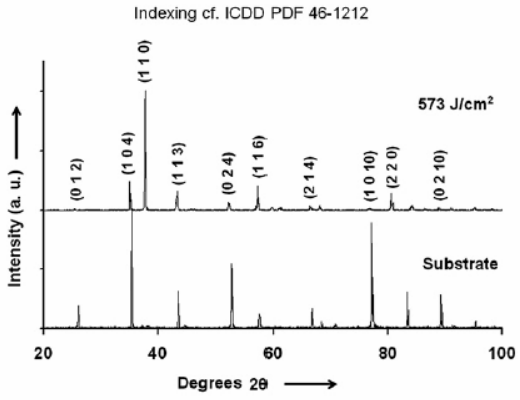


Fig. 4. XRD spectra from untreated (substrate) and laser-treated alumina ceramic surface (with laser fluence of 573 J/cm^2) showing the emergence of strong (110) peak in laser surface modified alumina.

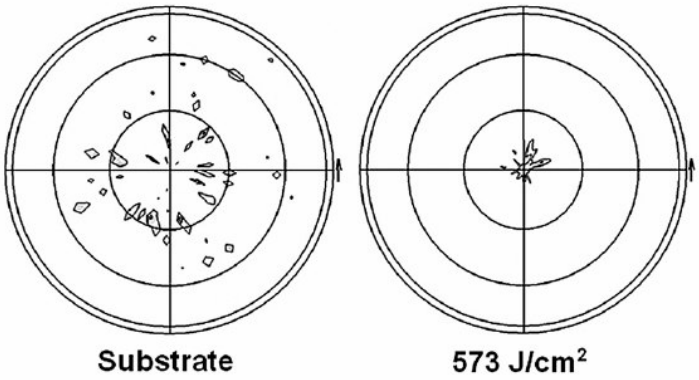


Fig. 5. Pole figures corresponding to (110) reflection in the untreated (substrate) and laser-treated alumina ceramic surface (with laser fluence of 573 J/cm^2) showing the development of strong (110) texture in laser surface modified alumina.

technique, the fractal dimension (D_b) is measured from the number of square boxes, $N(r)$ required to completely cover the surface profile and size of the boxes, r [18]. The basic fractal equations using Hausdorff measure can be written as:

$$N(r) = Cr^{D_b}, \quad (1)$$

$$\log N = \log C - D_b \log r, \quad (2)$$

where, C is constant. The process is repeated for calculating the number of boxes $N(r)$ required to cover the surface features with different sizes of the boxes (r). The slope of the straight line obtained by plotting the number of boxes ($N(r)$) against its size (r) for various box sizes on a double logarithmic scale yields the fractal dimension of the surface features in the microstructure.

3. Results

3.1. Microstructural characterization

SEM micrographs of alumina ceramic before and after laser surface modifications are presented in Fig. 2. The surface of alumina substrate consisted of irregular abrasive grains with a high degree of interconnected porosity (Fig. 2a). Fig. 2 also indicates the morphological changes at the surface of the alumina ceramic associated with the laser surface modifications (Fig. 2b–d). Upon surface modifications, the surfaces of alumina ceramic undergo significant refinement in the microstructure with a considerable reduction in the surface porosity. Also, the laser modified surface is characterized by the formation of the multi-faceted surface grains with polygonal shapes [7].

Furthermore, the SEM micrographs and the corresponding 3D topographical maps presented in Fig. 2 also indicate that the surface morphology of the laser modified surfaces is greatly influenced by the laser processing fluence. As the laser fluence increases, the size of the polygonal surface grain increases as indicated by the progressive increase in the flat crater-like areas in the topographical maps. Also, the surface porosity in the laser-treated alumina decreases with laser fluence as indicated by the progressive flattening of the topographical map and

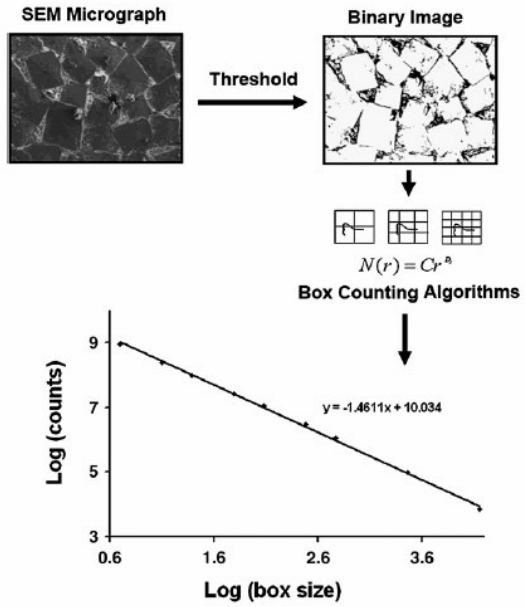


Fig. 6. Calculation of fractal dimension from SEM micrograph using image processing and box counting algorithm. The slope of the log–log plot shown in the figure corresponds to the fractal dimension.

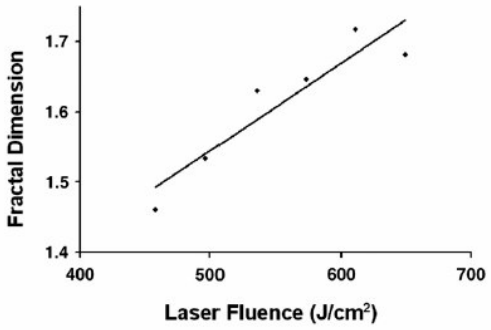


Fig. 7. Variation of fractal dimension with laser processing fluence used for surface modification of alumina ceramic.

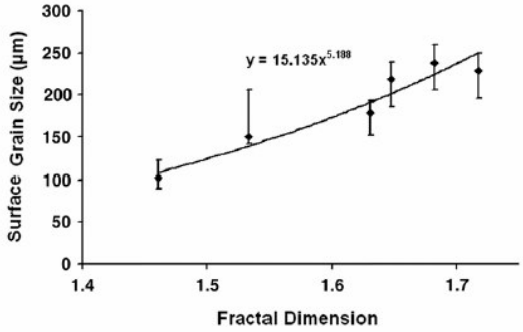


Fig. 9. Variation of polygonal surface grain size of the laser surface modified alumina with fractal dimensions (correlation parameter of data fitting, R^2=0.9385).

the disappearance of contrast peaks corresponding to the surface porosity. Table 1 summarizes the results of microstructural characterization such as surface porosity, polygonal grain size and surface roughness of the laser surface modified alumina with a range of laser processing fluence employed in present work. As indicated in the table, the surface porosity and the surface roughness show a general decreasing trend with increasing laser processing fluence. The only exception to this trend is the values of surface porosity and roughness of laser surface modified alumina at the highest laser fluence (649 J/cm^2). A typical EDS spectrum of the laser surface modified alumina presented in Fig. 3 illustrates the presence of primarily Al and O elements corresponding to alumina.

Fig. 4 presents the X-ray diffraction spectra obtained from the surface of alumina substrate and the surface of laser-treated alumina. The XRD spectra show the presence of equilibrium α-alumina indexed according to ICDD PDF card no. 46-1212. It is evident that the intensity of (104) reflection is strongest in the XRD spectrum of the substrate in accordance with the reference pattern from randomly oriented sample (ICDD PDF card no. 46-1212). However, the strongest peak in the laser surface modified sample corresponds to the (110) reflection. Furthermore, the X-ray pole figure analysis of the substrate shows widely distributed (110) poles corresponding to the (110) reflections, whereas laser surface modified alumina exhibits highly concentrated (110) poles suggesting the development of (110) texture in the laser-treated alumina sample (Fig. 5).

3.2. Fractal characterization

The important steps in the calculation of fractal dimension using image processing of SEM micrograph in combination with implementation of box counting algorithm (using public-domain software, ImageJ, available from the National Institute of Health, USA) are presented in Fig. 6 for laser surface modified alumina ceramic with a laser fluence of 458 J/cm^2. Fractal dimension of 1.4611 was determined for this case.

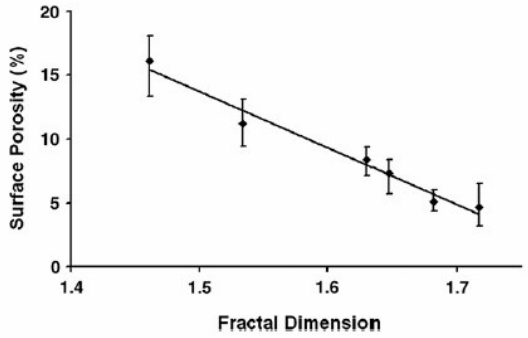


Fig. 8. Variation of surface porosity of the laser surface modified alumina with fractal dimensions (correlation parameter of data fitting, R^2=0.9735).

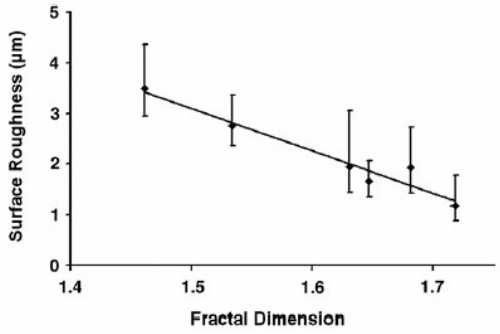


Fig. 10. Variation of surface roughness of the laser surface modified alumina with fractal dimensions (correlation parameter of data fitting, R^2=0.9456).

Fig. 7 presents the variation of fractal dimension with the laser processing fluence used for surface modification of alumina. For each laser processing fluence, corresponding SEM images with same magnification were given as input to avoid any magnification related errors. Fractal dimensions of the surface microstructures of the laser surface modified alumina range between 1.46 and 1.71. The figure indicates that the fractal dimensions increased with laser processing fluence.

Various correlations between the fractal dimension and the microstructural features such as porosity, polygonal grain size and surface roughness are presented in Figs. 8–10. As indicated in the Fig. 8, the fractal dimension of the laser surface modified alumina is negatively and linearly related to the amount of porosity with a correlation parameter of data fitting (R^2) of 0.9735. Fig. 9 shows the variation of polygonal surface grain size with the fractal dimension. The following power relationship with a correlation parameter of data fitting (R^2) of 0.9385 can be drawn from Fig. 9:

$$d = kD^{5.188}, \tag{3}$$

where d is the size of polygonal surface grains and D is fractal dimension. The relationship between the fractal dimension and the surface roughness of the laser surface modified alumina followed the negative and linear relationship with correlation parameter of data fitting (R^2) of 0.9456 (Fig. 10).

4. Discussions

4.1. Microstructure evolution

When the surface of highly porous alumina ceramics are irradiated with a high-power laser, the absorption of energy at the surface results in heating and subsequent melting of material at the surface. In addition to the high absorptivity (~0.8 for 1.06 μm wavelength) [19] of the alumina ceramics, the energy absorption is further enhanced by the high surface roughness and high porosity (~40%) of the material (Fig. 2a). The porosity facilitates the energy absorption due to multiple reflections of the laser radiation from the surface of the alumina particles. The solidification of the molten material at the surface proceeds from the interface between the porous substrate and the molten material without homogeneous nucleation within the molten material. This interface provides the catalytic nucleation sites for the heterogeneous nucleation and growth of the crystals. The molten material at the surface thus results in the formation of resolidified layer at the surface. The solidification during the laser processing is often characterized by the rapid cooling rates of the order of 10^2 K/s. Such rapid cooling rates are known to result in the formation of novel phases and morphologies in the microstructure of materials. Thus, the refinement of microstructure and the formation of multifaceted polygonal surface grains in the laser surface modified alumina seem to be the direct consequence of rapid cooling rates associated with laser surface modification and associated effects on microstructure development.

The thermal conditions during laser surface modifications are expected to be greatly influenced by the laser processing fluence. These thermal conditions, in turn, determine the evolution of surface microstructures during the solidification associated with laser surface modifications. As presented in Fig. 2, increasing grain size with increasing laser fluence is in direct agreement with the established relationships between the grain size and the cooling rates [20]. As the laser fluence increases for the same traverse speed, the cooling rate decreases resulting in larger grains at higher laser fluences. Also, as the laser fluence increases, the energy input during the laser surface modification increases resulting in the melting of larger volume of surface alumina material. Subsequent dynamic melt flow and rapid solidification of the melt result in the reduced porosity and surface roughness in the surface modified alumina ceramic at higher laser fluence (Table 1). The only exception, to the reasoning of reduced surface porosity and surface roughness at higher laser processing fluence, observed at highest laser fluence (649 J/cm^2) may be due to the initiation of the surface vaporization causing turbulence at the molten surface layer and consequent increase in the surface porosity and surface roughness. Also, observation of strong peaks corresponding to Al and O elements in the EDS spectrum suggests that composition of the laser surface modified alumina ceramic consisted of alumina as a primary phase (Fig. 3). At the thermal conditions during surface modifications where the alumina (melting point ~2323 K) melts, the low melting point bonding ingredient such as Na_2O in the initial alumina compacts evaporate away and hence does not show any corresponding elemental peaks in EDS spectrum.

The observation of equilibrium alpha alumina phase in the X-ray spectrum from the laser surface modified alumina ceramic (Fig. 4) indicates that the thermal conditions during laser surface modification preclude the formation of metastable alumina phases. This is expected from the viewpoint that during laser surface modifications the underlying substrate provides the nucleation sites for the growth of equilibrium alumina phase and decreases the undercooling in constrained solidification. It is well established that formation of

metastable phases during solidification is facilitated by high undercoolings obtained by eliminating the potential nucleation sites. The XRD spectrum from the substrate (Fig. 4) showing strongest (104) peak has the relative intensities close to that of standard randomly oriented polycrystalline sample (ICDD PDF card no. 46-1212) indicating the random crystallographic orientations or absence of texture in the initial substrate. Also, XRD spectra and pole figure results (Figs. 4 and 5) indicate the development of strong crystallographic texture corresponding to (110) plane in the laser surface modified alumina. During laser surface modification, the solidification proceeds from the melt–substrate interface towards the surface of the melt as governed by the directional heat flow processes. Even though the underlying substrate (which provides random nucleation sites) shows the random orientation, the passive solidification mechanism of the laser melted surface alumina develops the (110) texture due to geometric selection of the orientation of crystals during growth resulting from differences in the growth rates along the different crystallographic directions in the crystal [21]. Such competitive growth of crystallites and eventual evolution of the fastest growing planes at the surface of rapidly solidified alumina melt is facilitated by the rapid cooling rates ($\sim 10^2$ K/s) characteristic of the laser surface processing. Furthermore, the morphological changes in the surface microstructure of alumina ceramic indicated by the development of multifaceted polygonal faceted surface grains after laser processing seems to be derived from the development of (110) crystallographic texture in the resolidified surface layer.

4.2. Fractal analysis

The surface microstructures of laser surface modified alumina are complex and this complexity of microstructure arises from a combination of surface microstructural features such as grain size, grain shape, grain shape factor, pore volume, pore distribution, pore morphology, surface roughness, grain and subgrain dendritic structures, etc. As indicated in Fig. 7, the fractal dimensions of the surface microstructures associated with laser surface modifications increased with increasing the laser processing fluence suggesting the increased complexity of the surface microstructural features at higher laser fluences. At higher laser processing fluence, increased complexity of the surface microstructure may arise from increased complexity of the physical phenomena during laser–material interaction. Thus, fractal geometry approach provides a practical tool for the complete characterization of complex surface microstructures developed during laser surface modifications of alumina ceramic. Similar studies on the characterization of surface morphologies of thin films have demonstrated that the complexity of thin film morphology was fractal in nature and can be better characterized quantitatively using fractal dimensions than the conventional approaches [22].

The fractal analysis presented in Fig. 8 indicated that the fractal dimension of the microstructure is greatly influenced by the percentage of surface porosity. The fractal dimension increases with decreasing surface porosity suggesting the increased microstructural complexity of the smaller pores. Such a relationship between the fractal dimension and the porosity is in agreement with the previous studies on the fractal analysis of porosity in polished samples of plasma-sprayed yttria-stabilized zirconia coatings [23]. The approach of fractal dimension for the surface porosities can be further extended to the characterization of internal structure of porous material for predicting the permeability [24]. As observed in the Figs. 8–10, the fractal dimensions of the surface microstructures of the laser surface modified alumina can be effectively correlated with the surface microstructural properties such as surface porosity, polygonal grain size, and surface roughness indicated by the high correlation parameter of data fitting ($R^2 > 0.9$). Such relationships can be effectively utilized in predicting the porosity, surface roughness, and grain sizes of the surface microstructure from the fractal dimension obtained by direct image analysis of the SEM micrographs. Thus fractal geometry based approach for the characterization of complex irregular microstructures serves as an assessment tool for establishing the structure–property correlations in the various materials processing techniques.

5. Conclusions

1. Laser surface modification of alumina ceramics result in the development of (110) crystallographic texture and the systematic evolution of the microstructure (grain size, surface porosity, etc.) with the laser processing fluence.
2. The fractal analysis of a series of digitized surface microstructures from the laser surface modified alumina indicated that useful correlations can be derived between the fractal dimensions and the surface microstructural features such as porosity, grain size and the roughness.
3. The fractal approach is more appropriate in the characterization of complex and irregular surface microstructures observed in the surface modified

alumina and can be effectively utilized for predicting the properties of material from fractal dimensions of the microstructure.

References

[1] Bradley L, Li L, Stott FH. Characteristics of the microstructures of alumina-based refractory materials treated with CO_2 and diode lasers. Appl Surf Sci 1999;138–139:233–9.

[2] Okutomi M, Nomura H, Tsukamoto T, Dahotre NB, Shen H. Surface modification and characterization of functional oxide ceramic using CO_2 laser. Nucl Instrum Methods Phys Res B Beam Interact Mater Atoms 2000;169:6–11.

[3] Queiroz AC, Santos JD, Vilar R, Eugénio S, Monteiro FJ. Laser surface modification of hydroxyapatite and glass reinforced hydroxyapatite. Biomaterials 2004;25:4607–14.

[4] Harimkar SP, Dahotre NB. Crystallographic and morphological textures in laser surface modified alumina ceramic. J Appl Phys 2006;100:1–6.

[5] Krishnan R, Dash S, Kesavamoorthy R, Rao CB, Tyagi AK, Raj B. Laser surface modification and characterization of air plasma sprayed alumina coatings. Surf Coat Technol 2006;200:2791–9.

[6] Liu Z. Crack-free surface sealing of plasma sprayed ceramic coatings using an excimer laser. Appl Surf Sci 2002;186:135–9.

[7] Harimkar SP, Samant AN, Khangar AA, Dahotre NB. Prediction of solidification microstructures during laser dressing of alumina-based grinding wheel material. J Phys D Appl Phys 2006;39: 1642–9.

[8] Harimkar SP, Dahotre NB. Evolution of surface morphology in laser dressed alumina grinding wheel material. Int J Appl Cer Technol 2006;3:375–81.

[9] Mandelbrot BB, Passoja DE, Paullay AJ. Fractal character of fractal surfaces of metal. Nature 1986;320:429–31.

[10] Tanaka M. Characterization of grain-boundary configuration and fracture surface roughness by fractal geometry and creep-rupture properties of metallic materials. J Mater Sci 1992;27:4717–25.

[11] Dauskardt RH, Haubensak F, Ritchie RO. On the interpretation of the fractal character of fracture surfaces. Acta Metall Mater 1990;38:143–59.

[12] Hornbogen E. Fractals in microstructure of metals. Int Mater Rev 1989;34:277–96.

[13] Laird G, Rawers JC. Fractal analysis of carbide morphology in high-Cr white cast irons. Metall Trans A Phys Metall Mater Sci 1992;23:2941–5.

[14] Huda Z, Ralph B. Mechanism of grain growth and intergranular precipitation of gamma in nickel base alloy. Pract Methods 1990;27:64–74.

[15] Heywood J. Grinding wheels and their uses. Cleveland, OH: The Penton Publishing Co.; 1938. p. 8–15.

[16] Cullity BD. Elements of X-ray diffraction. Reading, MA: Addison-Wesley Publishing Co, Inc.; 1978. p. 250–6.

[17] Klug HP, Alexander LE. X-ray diffraction procedures for polycrystalline and amorphous materials. New York, NY: John Wiley & Sons, Inc.; 1954. p. 555–85.

[18] Jayaganthan R, Mohankumar K, Sekhar VN, Tay AA, Kripesh V. Fractal analysis of intermetallic compounds in Sn-Ag, Sn-Ag-Bi, and Sn-Ag-Cu diffusion couples. Thin Solid Films 2006;60: 1089–94.

[19] Gitzen WH. Alumina as a ceramic material. Westerville, OH: American Ceramic Society; 1970. p. 89–92.

[20] Eskin D, Du Q, Ruvalcaba D, Katgerman L. Experimental study of structure formation in binary Al-Cu alloys at different cooling rates. Mater Sci Eng A Struct Mater Prop Microstruct Process 2005;405:1–10.

[21] Rodriguez-Navarro A. Model of texture development in polycrystalline films growing on amorphous substrates with different topographies. Thin Solid Films 2001;389:288–95.

[22] Wang Y, Xu KW. Characterization of surface morphology of copper tungsten thin film by surface fractal geometry and resistivity. Thin Solid Films 2004;468:310–5.

[23] Li J, Liao H, Wang X, Coddet C. Fractal perimeters of polishing-induced pull-outs present on polished cross sections of plasma-sprayed yttria stabilized zirconia coatings. J Am Ceram Soc 2003;86:1906–10.

[24] Pape H, Clauser C, Iffland J. Permeability prediction based on fractal pore-space geometry. Geophysics 1999;64:1447–60.

phys. stat. sol. (a) **204**, No. 4, 1105–1113 (2007) / **DOI** 10.1002/pssa.200622379

Laser assisted densification of surface porosity in structural alumina ceramic

S. Harimkar[1] and **N. B. Dahotre**[*, 1, 2]

[1] Department of Materials Science and Engineering, University of Tennessee, Knoxville, TN 37996, USA
[2] Materials Science and Technology Division, Oak Ridge National Laboratory, Oak Ridge, TN 37831, USA

Received 4 August 2006, revised 8 November 2006, accepted 21 December 2006
Published online 15 February 2007

PACS 61.80.Ba, 68.37.Hk, 81.05.Je, 81.05.Rm, 81.40.Wx, 81.65.–b

Alumina ceramics are extensively used in structural components due to excellent thermal and mechanical properties. The effective utilization of alumina ceramic in these applications necessitates the minimization of inherent processing defects such as porosity. Laser processing can be effectively used for densification of the surface porosity of these ceramics especially desirable for the applications where ceramics are exposed to high temperatures and aggressive environments. The present study discusses the influence of laser processing fluence on the surface porosity of the alumina ceramic irradiated with a continuous wave Nd:YAG laser beam. A detailed scanning electron microscopy characterization was carried out to indicate the mechanism of densification of porosity during laser irradiation based on development of solidification microstructures. Finally, a fractal geometry based approach was introduced to characterize the surface microstructures such that useful correlation can be developed for the prediction of surface porosity directly from the fractal dimensions.

© 2007 WILEY-VCH Verlag GmbH & Co. KGaA, Weinheim

1 Introduction

Structural ceramics are the advanced materials, which are increasingly used for manufacturing of components under various load combinations at elevated temperatures and aggressive environments. Various properties exhibited by these materials include high hardness and wear resistance, oxidation resistance, chemical stability, creep resistance, and thermal shock resistance [1, 2]. Industrially important structural ceramics include various oxides, carbides, nitrides, and borides [3, 4]. In spite of the attractive properties, the actual utilization of structural ceramics in applications where high fracture strength is desirable is still limited primarily due to their inherent brittleness, low flaw tolerance and low reliability. These limiting properties of the structural ceramics are partly derived from the bonding characteristics of ceramics and from limited number of independent operating slip systems. In addition, fracture strength is also influenced by the defects such as pores introduced during processing of ceramics [1].

In general, porosity in the structural ceramics is detrimental in many applications. For example in applications where ceramics are exposed to fluid environment, ceramic tends to absorb fluid or water due to capillary action of the pores. When such soaked ceramics are exposed to freezing temperatures, the build up pressures due to expansion associated with liquid to ice transformation may cause the cracking and ultimate fracture of ceramics [5]. Also, the porosity and defects at the surface can cause the accelerated corrosion due to preferential chemical attack at these inhomogeneities [6]. Hence, considerable

[*] Corresponding author: e-mail: ndahotre@utk.edu, Phone: +1 865 974 3609, Fax: +1 865 974 4115

© 2007 WILEY-VCH Verlag GmbH & Co. KGaA, Weinheim

research has been directed towards improvements in the processing of ceramics such that the formation of defects such as porosity are prevented and/or minimized. Such a flaw diminution approach is based on reduction in defects by using improved powder properties and powder processing, clean room manufacturing, etc. [7]. Recently, secondary processing approaches for selective minimization of the defects introduced in primary ceramic processing are attracting increased research interest particularly for specialized applications [8–10]. One of such approaches is the laser surface engineering of ceramics where the surface properties of the structural ceramics are modified by localized surface melting [10–12]. Laser assisted surface melting of the ceramics causes the sealing of surface inhomogeneities such as pores, cracks and pits resulting in consequent reduction in localized chemical degradation and elevated temperature cracking. Applications of such laser surface engineering approach for crack free sealing of the refractory ceramics used as lining in furnaces and waste incinerators can be cited [11, 12]. The sealing of surface porosity in ceramics causes the reduction in the penetration of molten slag and chemical degradation. Such an approach can also be used for improving the corrosion behavior of ceramics used as heat exchanger components under severe environment [12].

In spite of the great potential of the laser surface engineering approach for sealing surface porosity of structural ceramics and consequent improvement in the surface properties for variety of applications, detailed studies on the effect of laser processing parameters on the surface densification of the ceramics are limited. Hence, the present work is directed towards systematic study of effects of laser processing parameters on the surface porosity of industrially important alumina ceramic so as to arrive at optimized laser parameters. This is also intended to provide the insight into mechanism of surface densification. Finally, a fractal geometry based approach is introduced for microstructural characterization of laser surface modified alumina ceramic such that direct correlations between the surface porosity and laser processing parameters can be derived.

2 Experimental

Alumina-based ceramic compacts with initial porosity of 40% by volume were used for the laser surface densification studies. The ceramic compacts were the part of commercially available vitrified grinding wheels of grade 60 I supplied by MSC Industrial Supply Co. Maximum and minimum grain size in this grade is determined by sieve numbers 60 and 70 respectively corresponding to the grain size between 211–255 μm. The compacts were made of irregular alumina grains (average grain size around 220 μm) and were primarily composed of alpha alumina with traces of chromium which imparts characteristic pink color to it. The chemical composition of the ceramic compacts consisted of 99.52% Al_2O_3, 0.25% Cr_2O_3 and other trace binding ingredients.

The schematic of an experimental set up for laser surface processing is shown in Fig. 1. The flat surfaces of the porous alumina compacts were sealed by scanning the surface with a fiber optically delivered continuous wave Nd:YAG laser beam (HAAS Laser Technologies Inc). The laser beam is scanned on the surface with a linear speed of 100 cm/min such that entire surface of the specimen would be sealed by laying adjacent parallel tracks. The laser processing was carried out with laser fluence in the increment of around 38 J/cm^2 above 420 J/cm^2 up to 649 J/cm^2.

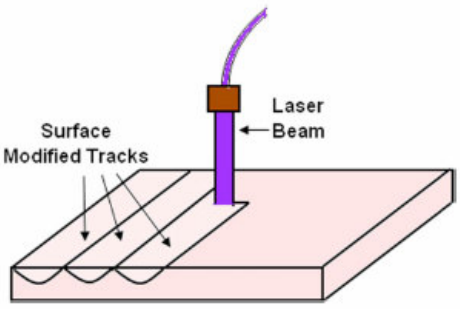


Fig. 1 (online colour at: www.pss-a.com) Schematic of the set up for the laser-assisted surface sealing of alumina ceramic.

© 2007 WILEY-VCH Verlag GmbH & Co. KGaA, Weinheim

Morphological characterization of alumina ceramic surface before and after laser processing was carried out using Hitachi S3500 scanning electron microscope (SEM). The surface porosity of the laser processed specimens was determined by the image analysis of several SEM micrographs and the average value along with the error bars is reported. For fractal analysis, the SEM images were converted from spatial domain of brightness to frequency domain components using Fourier transforms and then filtered from noises followed by thresholding to convert them into binary digital images using a public domain software, ImageJ (available from National Institute of Health, USA).

3 Results and discussion

3.1 Microstructural analysis

When the porous alumina ceramics are irradiated with a high power laser beam, the energy is absorbed into the material. The interaction of the laser beam with porous ceramic is a complex phenomenon due to effects of surface porosity. The surface porosity can cause the multiple reflection of the incident beam from the pore walls resulting in enhanced overall absorption of the laser energy. Depending on the incident laser fluence, the absorbed energy causes the heating, melting and vaporization at the surface of ceramic. For densification of surface porosity of the alumina ceramic, the regimes of laser processing which cause the surface melting are desirable. The molten material formed at the surface flows in the surface pores and subsequently undergoes rapid solidification forming a dense resolidified surface layer. Figure 2 presents a low magnification photograph of alumina ceramic before and after laser processing. The figure indicated the parallel tracks of resolidified material over a large area of alumina specimen resulting in crack free sealing of porosity on the surface of alumina.

Figure 3 presents the high magnification SEM micrographs of the surface of alumina substrate and the ceramic surfaces irradiated with a range of laser processing fluence. The figure indicated that, upon laser irradiation, the alumina ceramic substrate with a high surface porosity undergoes an interesting morphological change with a formation of refined polygonal surface grains on the surface accompanied with a marked decrease in surface porosity. The micrographs also indicated a systematic development of surface microstructure with progressive disappearance of surface porosity as the laser processing fluence was increased. The effect of laser fluence on the calculated surface porosity is presented in Fig. 4. In general, the surface porosity of alumina ceramic decreased with increasing laser fluence. The decrease is more progressive from lower to the intermediate values of laser fluence (420–535 J/cm^2). Above 535 J/cm^2, the surface porosity did not show substantial variation with laser fluence and it seems that very high increase in laser fluence is required to achieve the perfectly sealed surfaces with no apparent porosity.

Based on these observations, a schematic of the suggested mechanism of porosity densification at various laser processing fluences is presented in Fig. 5. The lower laser fluences melted less volume of the material and also provided higher cooling rates that generated fine polygonal grains [13] with densely solidified surface layer of less porosity (<40%) compared to that in the untreated material. This effect is

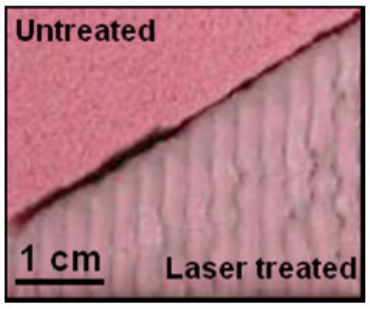


Fig. 2 (online colour at: www.pss-a.com) Low magnification picture showing alumina ceramic before (upper portion) and after (lower portion) surface modification.

© 2007 WILEY-VCH Verlag GmbH & Co. KGaA, Weinheim

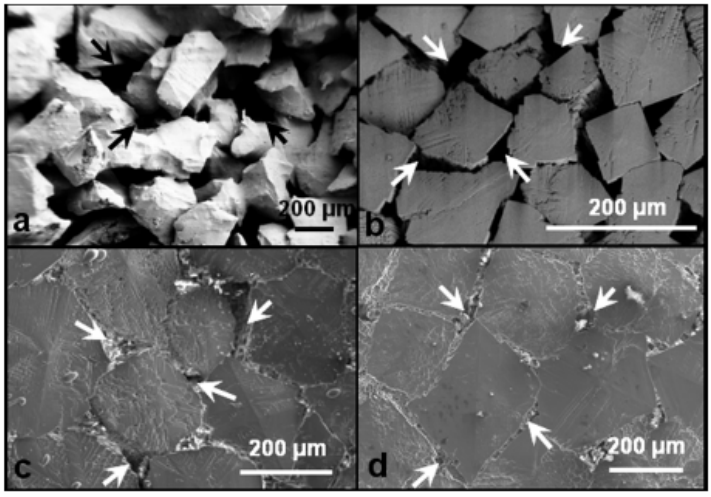


Fig. 3 Surface microstructures of the alumina ceramic substrate (a) before laser treatment; and after laser treatment with laser processing fluence of (b) 420 J/cm^2, (c) 535 J/cm^2 and (d) 649 J/cm^2 (arrows indicate the porosity).

consistent with the observation of surface microstructures of alumina ceramic irradiated with low values of laser processing fluence (420 J/cm^2) indicated in Fig. 3(b). As the laser processing fluence increased, more volume of the substrate material was melted and lesser cooling rate was associated with it [13]. This resulted in further growth of the polygonal grains that covered or filled the larger area of the surface thus reducing the interconnected surface porosity. Eventually, at higher fluences and associated slow cooling rates the grains grew larger [13] to impinge upon each other resulting in the final minimum value for surface porosity located between the edges of impinging grains. Also, as the laser fluence increases, the surface grains deviate from the polygonal shapes resulting in the enhanced ability to arrange in more compact manner to cover the surface area. This suggests that for efficient surface densification of the

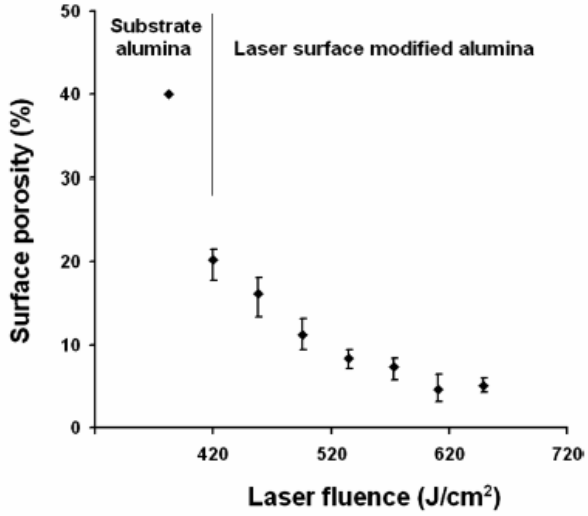


Fig. 4 Effect of laser processing fluence on the surface porosity of laser surface modified alumina ceramic.

© 2007 WILEY-VCH Verlag GmbH & Co. KGaA, Weinheim

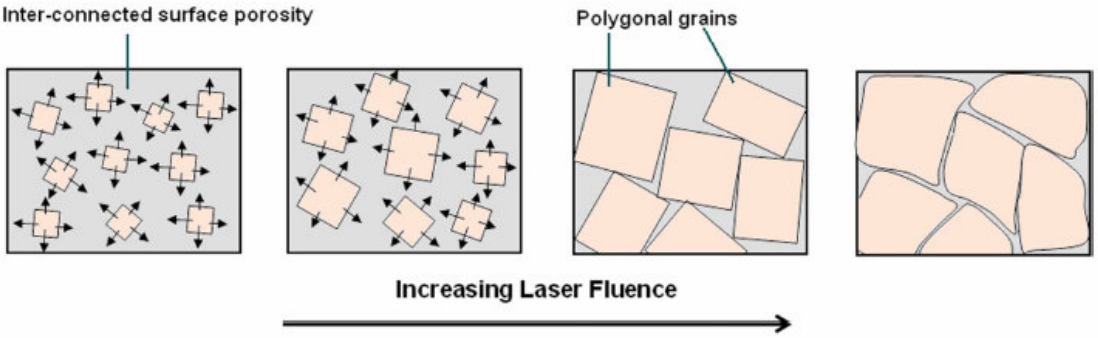


Fig. 5 (online colour at: www.pss-a.com) Schematic of mechanism of surface sealing of alumina ceramic as function of laser fluence.

porous ceramics, the laser processing fluence should be sufficiently high to fill in the complete surface area with resolidified grains. The mathematical formulations of such grain growth model for efficient densification of ceramics can be derived from the established solidification theories. It has been observed that the increasing laser processing fluence corresponds to the decreasing values of cooling rates calculated from thermal model [14]. This, in turn, can be directly correlated with the grain sizes of the resolidified alumina through a relationship of the type:

$$\text{Grain size} = k\,(\text{Cooling rate})^{-n}\,, \tag{1}$$

where k and n are material related constants. This relationship is directly evident from the SEM micrographs which indicate the increasing size of surface polygonal grains with increasing laser processing fluence i.e. decreasing cooling rates.

The cross section of the alumina ceramic surface sealed by laser assisted surface melting is presented in Fig. 6. The figure indicated the formation of highly dense surface layer of resolidified alumina (processed at 649 J/cm^2 of laser fluence) above a highly porous alumina substrate. Similarly, the cross sections of the samples processed at other laser fluences showed the same trend for variation of porosity (or density) in the solidified layer as that in the observations made for surface porosity. A careful observa-

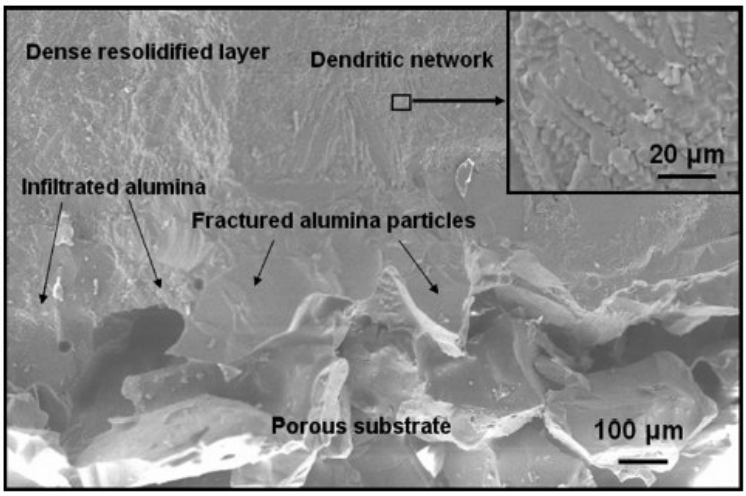


Fig. 6 Cross section of the alumina ceramic surface irradiated with laser fluence of 649 J/cm^2 for sealing the surface porosity.

© 2007 WILEY-VCH Verlag GmbH & Co. KGaA, Weinheim

tion of the micrograph in Fig. 6 indicated that the interface between the substrate and the solidified material is not distinct as observed in the laser surface melting of homogeneous material. The interface is diffused due to flow of molten material into the pores during laser surface treatment. Hence, the overall depth of melting in the material should be given by the sum of depth of melting due to absorption of energy and the increase in melting depth due to flow of molten material into the pores in the substrate material below the melt-solid interface prior to its complete solidification. Thus the overall depth of the laser modified surface region is observed to increase with increase in laser fluence [14]. Previous investigations of the authors have indicated that the observed depth of melting (and hence the depth of densified surface layer) in the alumina ceramic ranges around 520–930 μm depending on the laser fluence used for surface modification experiments. Also, the depth of melting was found to be increased with increasing laser fluence before reaching the maximum value (~930 μm) beyond which no significant change in depth of melting was observed. Such an observation may be due to initiation of surface evaporation such that the depth of melting bound by solid-liquid and liquid-vapor interface remain essentially constant and travel into the material with further increase in laser processing fluence [15].

An important practical consideration while designing laser-assisted surface porosity densification of ceramics is the in-service fracture failure of the ceramics. This consideration becomes even more serious in view of brittle nature of the ceramics and the rapid solidification associated with laser processing. Figure 6 also indicates the fracture failure modes across the cross section of the alumina ceramic surface sealed by laser irradiation. The substrate portion of the figure indicated the fast fracture features such as virgin surfaces of alumina particles suggesting the intergranular fracture. Near the interface, the fracture mode changes to the transgranular as indicated by the partially fractured alumina particles surrounded by resolidified material. In the resolidified portion of the figure, fracture features revealed the dendritic network characteristic of rapid solidification associated with laser surface melting. The inset of Fig. 6 presents a high magnification micrograph of dendritic network in fracture features of a resolidified layer. The dendrites in the microstructure are known to act as obstacles to the propagating cracks resulting in eventual bypassing or the stopping of the cracks [16]. Hence, transgranular fracture features in the interface area and the dendritic fracture features in the resolidified surface layer are expected to improve the fracture resistance of the ceramics irradiated with laser for sealing the surface porosity.

3.2 Fractal analysis

The performance of the surface sealed ceramics is expected to be influenced by the geometric aspects of the surface porosity. As discussed in the previous section, alumina ceramic irradiated with various laser fluences exhibited porosity over a range of dimensions and shape. Fractal dimension has successfully evolved as a useful parameter for the characterization of geometrically complex microstructures in porous material [17, 18]. In the present study, the fractal dimensions were calculated using image processing of SEM micrographs in combination with the implementation of box counting algorithm using a public-domain software, ImageJ (available from National Institute of Health, USA). In box counting technique, the fractal dimension (D_b) is measured from the number of square boxes, $N(r)$ required to completely cover the surface profile and size of the boxes, r [19]. The basic fractal equations can be written as:

$$N(r) = Cr^{-D_b}, \tag{2}$$

$$\log N = \log C - D_b \log r, \tag{3}$$

where C is constant. The process is repeated for calculating the number of boxes $N(r)$ required to cover the surface features with different sizes of the boxes (r). The slope of the straight line obtained by plotting the number of boxes ($N(r)$) against its size (r) for various box sizes on a double logarithmic scale yields the fractal dimension of the surface features in the microstructure. Figure 7 represents the important steps in the calculation of fractal dimension using a SEM micrograph from laser surface modified

© 2007 WILEY-VCH Verlag GmbH & Co. KGaA, Weinheim

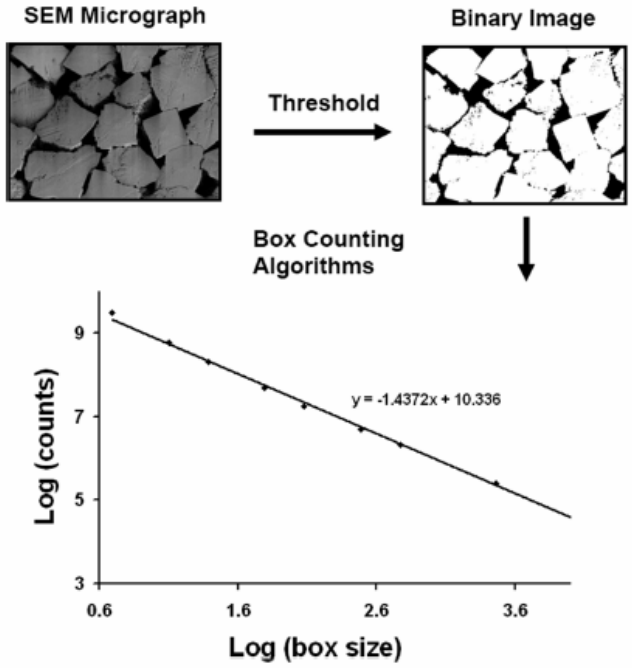


Fig. 7 Calculation of fractal dimension from SEM micrograph using image processing and box counting algorithm. The slope of the log–log plot shown in the figure corresponds to the fractal dimension.

alumina ceramic with a laser fluence of 420 J/cm^2. Fractal dimension of 1.4372 was determined for this case.

The variation of calculated fractal dimension of the surface microstructure with the surface porosity of the alumina ceramic irradiated with a range of laser fluence for sealing the surface porosity is presented in Fig. 8. The fractal dimension of the laser surface modified alumina is negatively and linearly related to the amount of porosity with a correlation parameter of data fitting (R^2) of 0.9504. Such a relationship between the fractal dimension and the porosity is in agreement with the previous studies on the fractal

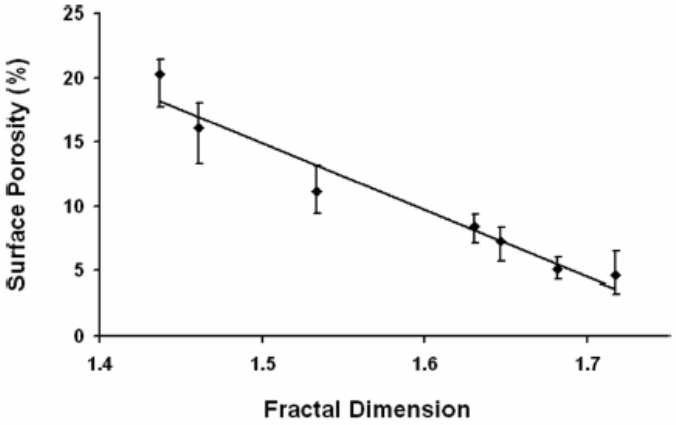


Fig. 8 Variation of surface porosity of the laser surface modified alumina with fractal dimensions (correlation parameter of data fitting, $R^2 = 0.9504$).

© 2007 WILEY-VCH Verlag GmbH & Co. KGaA, Weinheim

analysis of porosity in plasma-sprayed yttria-stabilized zirconia coatings [20]. Thus fractal geometry based approach can be helpful in establishing the useful correlations for predicting the surface porosity directly from the digital image based characterization of the surfaces.

The properties of the surface densified alumina are expected to be influenced by the surface microstructure resulted from laser-material interactions. Due to complexity of the laser-material interactions and resultant complexity of surface microstructure, the prediction of surface properties necessitates the complete description of the microstructure in terms of a convenient parameter representative of the given microstructure. The stereological analysis of such irregular microstructural features is often difficult because it assumes the repetitive pattern in the microstructure. Fractal analysis provides a precise way of quantitatively describing such complex, irregular microstructures in terms of single parameter (fractal dimension). Also, determination of fractal dimension is relatively easy and precise. Fractal dimension can be directly measured from the digital images using standard image processing based techniques. The fractal dimensions of the surface microstructure are found to have direct correlation with surface porosity characteristic of the microstructures.

Correlation between laser fluence and porosity can be further extended to prediction of fracture toughness of these laser surface modified ceramics. The follow-up efforts are on going to evaluate the fracture toughness of laser surface processed alumina materials and will be characterized in light of existing porosity. Such approach will allow prediction of fracture toughness as function of laser fluence based on porosity (measured by fractal analysis) without the need for direct measurement of fracture toughness. Results of these efforts will be presented in future publications.

4 Conclusions

Lasers can be efficiently used for densification of the surface porosities of the structural ceramics. The surface porosity of the laser treated alumina ceramics is found to decrease with increasing the laser fluence. The densification of the surface porosity is exhibited by the surface melting and subsequent rapid solidification. The effect is further assisted by the infiltration of the molten material into the porous structure. The concept of fractal dimension is introduced for the characterization of surface microstructures of laser densified alumina ceramic surfaces. The fractal dimension is found to increase with decreasing porosity in the microstructure suggesting the increased complexity of microstructures associated with denser surfaces. The proposed concept of fractal geometry can be effectively used to characterize the surface porosity in terms of fractal dimension so that useful correlations can be derived for direct prediction of the surface porosity from the laser processing parameters.

References

[1] J. Dusza and M. Steen, Int. Mater. Rev. **44**, 165 (1999).
[2] P. Reis, V. Filho, J. Davim, X. Xu, and J. Ferreira, Mater. Des. **26**, 417 (2005).
[3] C. Santos, K. Strecker, S. A. Baldacim, O. M. M. Silva, and C. R. M. da Silva, Int. J. Refract. Met. Hard Mater. **21**, 245 (2003).
[4] E. Medvedovski, Wear **249**, 821 (2001).
[5] K. Ikeda, H. S. Kim, K. Kaizu, and A. Higashi, J. Eur. Ceram. Soc. **24**, 3671 (2004).
[6] L. Bradley, L. Li, and F. H. Stott, Mater. Sci. Eng. A **278**, 204 (2000).
[7] D. Richter, G. Haour, and D. Richon, Mater. Des. **6**, 303 (1985).
[8] M. P. Albano and A. N. Scian, J. Am. Ceram. Soc. **80**, 117 (1997).
[9] M. D. Drory and A. G. Evans, J. Am. Ceram. Soc. **68**, 342 (1985).
[10] K. M. Jasim, R. D. Rawlings, and D. R. F. West, J. Mater. Sci. **27**, 3903 (1992).
[11] L. Bradley, L. Li, and F. H. Stott, Appl. Surf. Sci. **138**, 233 (1999).
[12] J. F. Li, L. Li, and F. H. Stott, J. Eur. Ceram. Soc. **24**, 3509 (2004).
[13] S. P. Harimkar and N. B. Dahotre, J. Appl. Phys. **100**, 024901 (2006).
[14] S. P. Harimkar, A. N. Samant, A. A. Khangar, and N. B. Dahotre, J. Phys. D, Appl. Phys. **39**, 1642 (2006).
[15] S. P. Harimkar and N. B. Dahotre, Int. J. Appl. Ceram. Technol. **3**, 375 (2006).

© 2007 WILEY-VCH Verlag GmbH & Co. KGaA, Weinheim

[16] G. He, J. Eckert, W. Loser, and L. Schultz, Nature Mater. **2**, 33 (2003).
[17] S. J. Huang, Y. C. Yu, T. Y. Lee, and T. S. Lu, Physica A **274**, 419 (1999).
[18] Q. Wei and D. Wang, Mater. Lett. **57**, 2015 (2003).
[19] R. Jayaganthan, K. Mohankumar, V. N. Sekhar, A. A. Tay, and V. Kripesh, Mater. Lett. **60**, 1089 (2006).
[20] J. Li, H. Liao, X. Wang, and C. Coddet, J. Am. Ceram. Soc. **86**, 1906 (2003).

© 2007 WILEY-VCH Verlag GmbH & Co. KGaA, Weinheim

Temporally evolved recoil pressure driven melt infiltration during laser surface modifications of porous alumina ceramic

Sandip P. Harimkar, Anoop N. Samant, and Narendra B. Dahotre[a)]
Department of Materials Science and Engineering, University of Tennessee, Knoxville, Tennessee 37996

(Received 23 October 2006; accepted 9 January 2007; published online 15 March 2007)

Laser surface modification of porous alumina ceramic with a high power laser is associated with a series of physical processes such as heating, melting, and evaporation of material. Above certain threshold laser intensity ($\sim 10^{10}$ W/m^2), rapid evaporation at melt surface generates strong recoil pressures. These laser-induced evaporation recoil pressures tend to drive the flow of molten material into the porous substrate thus contributing to the overall observed depth of melting. This paper presents a three-dimensional thermal model to calculate the temporal evolution of temperature during laser surface modifications of alumina ceramic. This is followed by the determination of recoil pressures at the evaporating surface based on experimentally verified physical model of melt hydrodynamics and laser-induced evaporation proposed by Anisimov [Sov. Phys. JETP **27**, 182 (1968)]. Finally, Carman-Kozeny equations were employed to analyze the effect of recoil pressure on the depth of infiltration which is subsequently integrated with the calculated depth of melting from thermal model. Such an integrative approach results in better agreement of the predicted values of depths of melting with the experimental values. © *2007 American Institute of Physics*.
[DOI: 10.1063/1.2710288]

I. INTRODUCTION

When a laser beam interacts with the solid, the primary effect is the heating of the solid surface. At sufficiently high laser intensities, generally in the neighborhood of 10^{10} W/m^2, surface material melts and the rapid evaporation takes place at the surface of the melt. The evaporation at the melt surface is associated with the emission of neutral atoms or molecules into the gas or vacuum around the solid by Langmuir vaporization.[1] The escaping vapor at the surface exerts recoil pressures exceeding $0.55p_s$, where p_s is the saturated vapor pressure on the melt surface which exceeds the highest value surface tension pressure.[2] This evaporation recoil pressure induces the hydrodynamic melt motion which plays an important role during the material removal processes such as laser cutting and drilling.[3–5]

During interaction of laser beam with highly porous substrates, the melt pool formed on the surface of the material also experiences the evaporation recoil pressure exerted due to rapid evaporation at the surface of the melt. Due to highly porous substrate below the solid-liquid interface, the evaporation recoil pressure is expected to drive the fluid flow into the porosity resulting in overall increase in the depth of molten material into the substrate.[6] The phenomenon is of particular importance during the laser surface modifications of porous material where the accurate prediction of the depth of modified layer by melting is desired. Porous alumina ceramics are extensively used in the structural and engineering application. Laser surface modifications of these alumina ceramics offer a great potential to improve the performance of the ceramic components. For example, laser surface modification of the alumina ceramic linings used in furnaces and incinerators minimizes the localized thermal attack at the surface pores and also prevents the penetration of corrosive liquid media thus extending the life of the linings.[7] Also, laser surface modifications of alumina ceramic grinding wheels recondition the surface for microscale material removal during precision surface grinding of material.[6,8] The depth of laser modified surface layer in these applications is expected to influence the performance of the ceramic by controlling surface morphology and topography of the rapidly solidified surface grains, thermal stresses in the resolidified layer, and tendency to surface and subsurface cracking.[9,10] Hence accurate prediction of the depth of laser modified layer during laser interaction with porous substrates plays an important role in intelligent manufacturing.

The present paper is directed towards understanding the interaction of laser beam with highly porous alumina substrates during laser surface modifications. A three-dimensional thermal model is presented to predict the temporal evolution of temperature and evaporation-induced recoil pressure resulting from the rapid surface evaporation. This paper presents the account of the influence of evaporation-induced recoil pressure on the hydrodynamic melt motion into porous substrate during laser surface modification. It is surprising to note that, even though laser interaction with porous ceramics is encountered in various practical applications, the effect of recoil pressure-assisted infiltration is long been ignored in the traditional models of laser processing. Finally, the paper presents an integrative approach based on heat transfer equations and the Carman-Kozeny fluid flow equations to predict the depths of melting in the laser surface modified alumina taking into account the evaporation-induced recoil pressures acting on the melt surface.

[a)]Author to whom correspondence should be addressed; electronic mail: ndahotre@utk.edu

 © 2007 American Institute of Physics

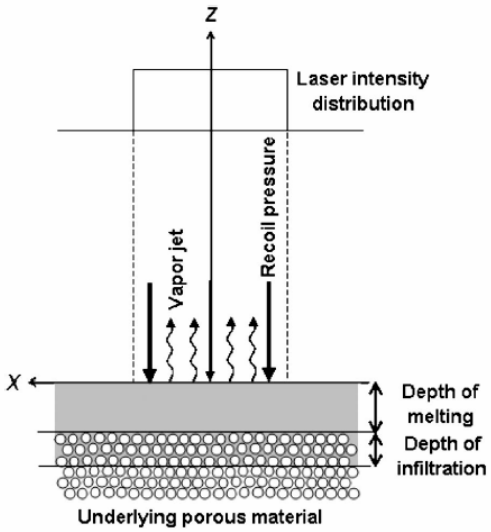


FIG. 1. Physical model showing the interaction of laser beam with porous ceramic substrate during the laser surface modification. Various effects such as surface melting, evaporation, generation of evaporation recoil pressure, and melt infiltration are shown.

II. EXPERIMENTAL PROCEDURE

The experimental investigations were carried out on the commercially available alumina ceramic compacts (purchased from MSC Industrial Supply Co., Melville, NY). The composition of the alumina grains consisted of primarily α-alumina with an average alumina grain size around 220 μm. The alumina grains were compacted and sintered such that relative proportions of grains and porosity were about 60 and 40 vol %, respectively, in the compacts. The surface of the flat coupons of the area 5×5 cm^2 and thickness 2.54 cm was modified by scanning a rectangular beam (of dimensions 5.0×1.5 mm^2) of uniform intensity with a linear scan speed of 100 cm/min. The surface modifications were carried out using 4 kW continuous wave neodymium-doped yttrium aluminum garnet (Nd:YAG) laser at laser processing fluences in increments of around 38 J/cm^2 above 458 J/cm^2 up to 764 J/cm^2 corresponding to the irradiation time of 90 ms. Following the surface modifications, the characterization of cross sections of the specimens was conducted under Hitachi S3500 scanning electron microscope (SEM). Image analysis of the SEM micrographs was conducted to determine the maximum depth of melting. For each laser processing fluence, the depth of melting was measured at five locations and average value of the melt depth was reported with positive and negative error bars.

III. MODEL DESCRIPTION

Schematic of the physical processes taking place during laser interaction with the porous alumina substrates is illustrated in Fig. 1. The processes are operative for the laser fluences above the threshold value of laser fluence required for evaporation to be initiated at the melt surface. The depth of melting is determined by the location of melting point in the temperature distribution within the material. Since the temperature distribution into the material evolves as a function of time, maximum depth of melting corresponds to the irradiation time (in the present case, the time of 90 ms). Also, the rapid evaporation at the surface of the melt generates the recoil pressure which drives the flow of molten material into the porous substrate, thus further extending the depth of melting. The overall depth of melting is then given by the sum of maximum depth of melting calculated from temperature distribution within the material and the depth of melt infiltration in the porous substrate induced by recoil pressure due to rapid evaporation at the melt surface. Thus, an integrative modeling approach is proposed to calculate the overall depth of melting from heat transfer equations given by Fourier's law and fluid flow equations derived from Darcy's law.

A three-dimensional thermal analysis presented in this paper is the extension of the one-dimensional heat flow model proposed earlier by Harimkar *et al.*[6] A control volume of $1\times1\times1$ cm^3 was considered for thermal analysis with the laser being irradiated on the top surface for irradiation time of 90 ms. Based on the experimental observations, selected control volume appeared to be large enough to include the entire depth of melting, the heat affected zone, and the depth of the substrate that did not reach the temperature high enough to cause any noticeable microstructural changes. The governing three-dimensional heat conduction equation is given by[11]

$$\frac{\partial T(x,y,z,t)}{\partial t}=\alpha\left[\frac{\partial^2 T(x,t)}{\partial x^2}+\frac{\partial^2 T(y,t)}{\partial y^2}+\frac{\partial^2 T(z,t)}{\partial z^2}\right], \quad (1)$$

where α is the thermal diffusivity of the material and is equal to $K/\rho c_p$, K is the thermal conductivity, and c_p is the specific heat of the material. The initial condition of $T=T_0=298$ K was applied at time $t=0$.

At the surface of the sample, the heat transfer equation is given by the balance between the laser energy absorbed by the sample and the radiation losses:

$$-K\left[\frac{\partial T(x,t)}{\partial x}+\frac{\partial T(y,t)}{\partial y}+\frac{\partial T(0,t)}{\partial z}\right]=\delta AI - \varepsilon\sigma[T(x,y,0,t)^4-T_0^4],$$

$$\delta=1 \quad \text{for } 0\leqslant t\leqslant t_p,$$

$$\delta=0 \quad \text{for } t>t_p, \quad (2)$$

where A is the absorptivity of alumina, I is the laser intensity, ε is the emissivity of alumina for thermal radiation, σ is the Stefan-Boltzmann constant, and t_p is the irradiation time.

Convective boundary condition at the bottom surface of the sample is given by

$$-K\left[\frac{\partial T(x,t)}{\partial x}+\frac{\partial T(y,t)}{\partial y}+\frac{\partial T(L,t)}{\partial z}\right]=h[T(x,y,L,t)-T_0], \quad (3)$$

where h is the convective heat transfer coefficient and L is the thickness of the sample.

TABLE I. Properties of alumina used in mathematical calculations.

Density ρ (kg/m^3)	2280[a]
Thermal conductivity K (W/m K)	14.6[b]
Mass of the vapor molecule m_v (kg/at.)	1.693×10^{-25}[b]
Latent heat of evaporation L_v (J/g)	1066.5[b]
Convective heat transfer coefficient h (W/m^2 K)	200[c]
Emissivity ε	0.7[d]
Specific heat C_p (J/kg K)	800[e]
Kinematic viscosity υ (cm^2/s)	0.15[f]

[a]Calculated using weighted average method applied to fully dense alumina (ρ=3800 kg m^{-3}) and porosity of 40% by volume.
[b]Reference 12.
[c]Reference 13.
[d]Reference 14.
[e]Reference 15.
[f]Reference 16.

The solutions of the above heat transfer equations were obtained using the heat transfer module of COMSOL Multiphysics™ modeling package, which is based on finite element approach. The results were postprocessed to obtain the temporal and spatial distribution of temperature for the experimental laser processing fluences used for surface modifications of alumina. The porosity in the alumina specimens that influence the properties of alumina, which in turn, is expected to influence both the temperature profiles and the depth of melting obtained during laser processing. Hence, the properties of the alumina such as conductivity and density have been appropriately selected to consider the effect of porosity. The properties of the porous alumina used in the calculations are presented in Table I.

Early analysis of the evaporation process from the surface of material irradiated with laser radiation of intensity as high as 10^{13}–10^{14} W/m^2 was carried out by Anisimov.[1] Based on the assumption that the absorption of laser radiation by the generated vapor plume as a result of surface evaporation is not appreciable, Anisimov proposed the velocity distribution functions for the vapor molecules.[1] For vapor molecules emitted from the evaporating surface, the velocity distribution function (f_1) is expressed as

$$f_1 = n_0\left(\frac{m_v}{2\pi kT_s}\right)^{3/2}\exp\left[-\frac{m_v(v_x^2+v_y^2+v_z^2)}{2kT_s}\right] \quad \text{for } v_z>0 \tag{4}$$

and, for vapor molecules returned to the evaporating surface, the velocity distribution function (f_2) is expressed as

$$f_2 = \beta n_1\left(\frac{m_v}{2\pi kT_1}\right)^{3/2}\exp\left\{-\frac{m_v[v_x^2+v_y^2+(v_z-u_1)^2]}{2kT_1}\right\} \quad \text{for } v_z<0 \tag{5}$$

where k is the Boltzmann constant, m_v is the mass of the vapor molecule, T_s and n_0 are the surface temperature and the molecule number density at the evaporating surface, respectively, and T_1 and n_1 are temperature and the molecule number density at the outer boundary of the kinetic layer formed near evaporating surface, respectively. u_1 is the velocity at the outer boundary of the kinetic layer, β is the coefficient, and v_x, v_y, and v_z are the velocity components on the evaporating surface of the material. Based on these relationships, an equation for calculation of evaporation-induced recoil pressure p_s at the evaporating surface from the surface temperature, which in turn depends on the incident laser energy density, is given by[1]

$$\frac{p_s}{Q_0/S} = \frac{1.69}{\sqrt{L_v}}\left(\frac{b}{1+2.2b^2}\right), \tag{6}$$

where Q_0 is the incident laser power, S is the area of laser spot, L_v is the latent heat of evaporation, and $b^2=kT_s/m_vL_v$. Thus, the temperature fields determined from the three-dimensional thermal analysis can facilitate the calculation of evaporation-induced recoil pressure at the evaporating surface during laser surface modifications of alumina ceramic using the experimentally verified physical model of melt hydrodynamics and laser-induced evaporation proposed by Anisimov.

The above analysis can be further extended to calculation of depths of infiltration in the porous substrate based on fluid flow models. An analysis of viscous fluid flow through porous media is generally described in terms of Darcy's law which states that average fluid velocity vector is proportional to the average pressure gradient Δp. The fluid flow problem was modeled by Carman and Kozeny for calculation of flow rate by representing the porous media as an array of cylindrical tubes. The Carman-Kozeny equation which is derived from Darcy's law can be expressed as[17]

$$\frac{dp}{dz} = -\frac{180\mu u(1-\omega)^2}{d_s^2\omega^3}, \tag{7}$$

where dp/dz is the pressure gradient across the melt depth, μ is the dynamic viscosity, u is the flow rate, ω is the porosity, and d_s is the average alumina particle diameter. The pressure difference across the melt is given by the head of melt (corresponding to melt depth) and the evaporation induced recoil pressure,

$$\Delta p = -(\rho g h_1 + p_s), \tag{8}$$

where g is the acceleration due to gravity, and h_1 is the head of melt corresponding to the depth of melting. The above equations result in the calculation of linear flow rate, u (m/s), of molten alumina through the porous substrate. Actual depth of melting due to infiltration can then be obtained by multiplying the linear velocity with the time during which the material remains above the melting point determined from the temporal temperature distribution. Finally, the overall depth of melting can be calculated by integrating the depth of melting due to recoil pressure-induced infiltration with the depth of melting calculated from thermal analysis by tracing the melting temperature inside the material during surface modification. Schematic of this integrative approach is presented in Fig. 2.

IV. RESULTS AND DISCUSSION

During the laser surface modification of alumina ceramic, a part of the laser energy is absorbed into the material. The amount of absorbed energy depends on several factors

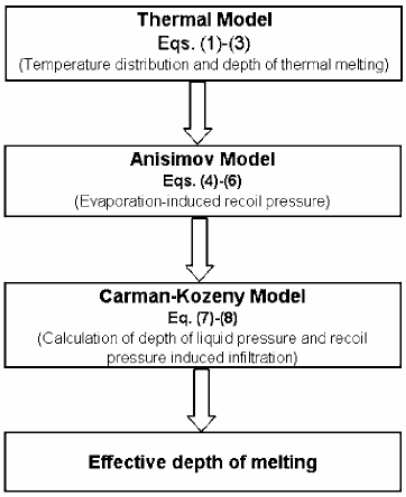


FIG. 2. Schematic of an integrative modeling method for predicting the overall depth of melting in laser surface modified alumina ceramic.

such as laser wavelength, temperature, surface roughness, and surface chemistry. In the case of highly porous substrates such as alumina ceramics, absorptivity of the surface at 1.06 μm wavelength is expected to be as high as 0.8 due to multiple reflections from the walls of pores.[12] The absorption of the laser radiation causes the rapid heating, melting, and evaporation of the material depending on the incident laser energy. The molten material formed during laser-material interaction subsequently solidifies resulting into the formation of recast layer. A typical cross sectional microstructure of the laser surface modified alumina at a laser fluence of 535 J/cm^2 is presented in Fig. 3. The semielliptical shape of the recast layer is a consequence of distribution of energy in the laser beam such that the maximum depth of melting at the center of melt pool corresponds to the energy maxima along the axis of the laser beam. Previous investigations have shown that the experimentally observed maximum depth of melting increases with increasing laser processing fluence due to increased penetration of laser energy into the material.[18]

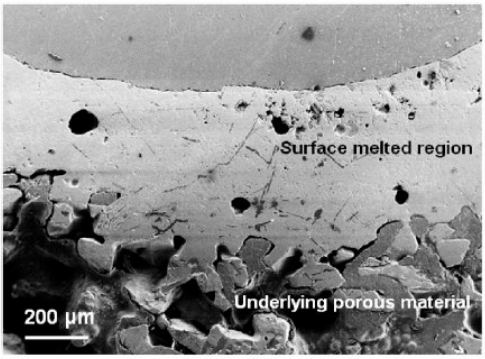


FIG. 3. Typical polished cross section of laser surface modified alumina ceramic mounted in epoxy mould. Surface modification was carried out at a laser fluence of 535 J/cm^2.

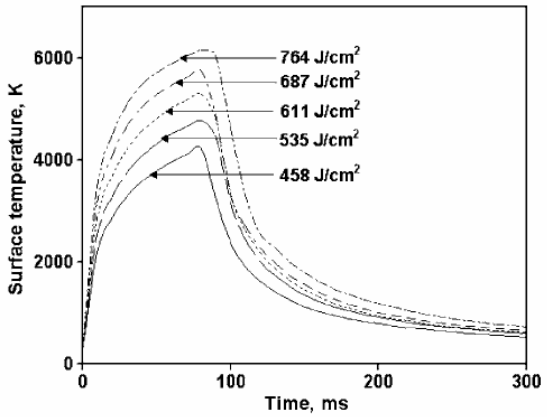


FIG. 4. Computed temporal evolution of surface temperature during laser surface modifications of alumina ceramic processed with a range of laser fluence from 458 to 764 J/cm^2.

An important consideration during the laser surface modifications of materials is the prediction of temporal evolution of the temperature. The temperature history during laser surface modification determines the phase transformations, dimensional changes, distribution of stresses, and microstructure. In the present context of laser surface modification of alumina ceramic, the temperature history is important for prediction of overall depth of melting from the temperature distribution inside the material and the fluid flow in the porous substrate assisted by evaporation-induced recoil pressure. The variation of surface temperature calculated from a three-dimensional thermal model is presented in Fig. 4 as a function of time for various laser fluences. The figure indicated that at each laser fluence, the surface temperature rapidly increased with time and reached maximum at a time corresponding to the irradiation time of the laser (t=90 ms). Beyond irradiation time, the temperature decays until the room temperature is reached. Also, the temporal dependence of temperature increased rapidly with increasing laser fluence employed for surface modification. This resulted in higher maximum surface temperature at higher laser processing fluence (Fig. 5). Figure 6 presents the distribution of temperature below the surface of alumina material processed with various laser processing fluences. The figure indicated that the temperature gradually decreases below the surface of material and becomes uniform by reaching the initial temperature of the sample at about 2.5 mm below the surface.

One of the significant observations in the temporal distribution of temperature is that the calculated maximum surface temperatures (Fig. 4) exceeded the boiling point of alumina, T_v (~3800 K). Contrary to this, the various models of laser cutting, drilling, and welding have assumed that the surface temperature cannot exceed the boiling point of the material and it always remains either equal to or less than the boiling point.[19,20] Most of these models assumed the volumetric evaporation during the laser-material interaction and the evaporating front was simulated in terms of traditional "Stefan problem." However, during laser surface modification, the surface temperature can significantly exceed the

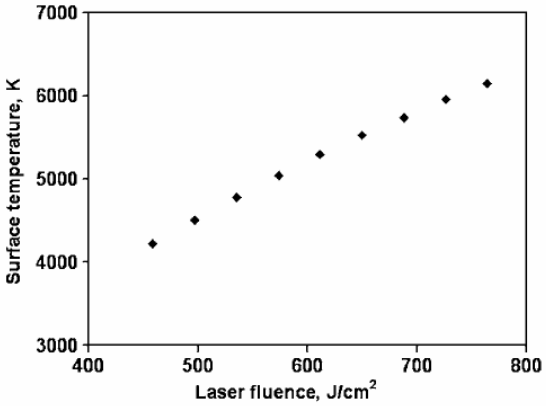


FIG. 5. Computed variation of maximum surface temperature with laser processing fluence during the surface modifications of alumina ceramic.

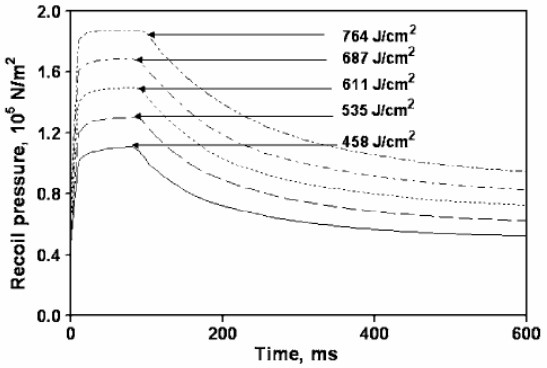


FIG. 7. Computed temporal evolution of evaporation-induced recoil pressure during the laser surface modification of alumina ceramic processed with a laser processing fluence of 458 J/cm^2.

boiling point provided that the absorbed laser intensity is high and, therefore, only the evaporation at the surface is likely to occur. This is in agreement with the theoretical studies which indicated that volumetric evaporation cannot take place during typical laser-material interactions observed in laser surface modifications.[21] Also, recently Semak *et al.* have suggested that evaporation front cannot be simulated in terms of Stefan problem and this approach can introduce significant errors in the prediction of temperatures.[22] Thus, the maximum surface temperatures in the range of 4000–6000 K, predicted from the thermal model employed in the present work, are reasonable in view of laser surface processing with high power lasers.

The temporal evolution of the evaporation-induced recoil pressure during the laser surface modification of alumina ceramic with laser processing fluences employed in the present effort is presented in Fig. 7. As indicated in the figure, during surface modification, the recoil pressure rapidly increases and reaches maximum value at the time corresponding to the laser irradiation time (t=90 ms). The temporal evolution of recoil pressure showed the similar trend as obtained in the temporal evolution of surface temperature (Fig. 4), suggesting the strong dependence of evaporation-induced recoil pressure on the surface temperature. The observation is in agreement with the physical model of melt hydrodynamics and laser-induced evaporation proposed by Anisimov.[1] The variation of maximum evaporation-induced recoil pressure with the laser processing fluence during laser surface modification of alumina ceramic is presented in Fig. 8. The recoil pressure generated due to surface evaporation during surface modifications is a strong function of laser fluence and increases almost linearly with laser fluence. The values of evaporation pressures are in strong agreement with the analysis of Anisimov, which suggested that if surface temperature reached above the boiling point of material, the recoil pressure must be equal or higher than $0.55p_s$, where p_s is the saturated vapor pressure, which by definition is 1 atm ($\sim 1.013\,25 \times 10^5$ N/m^2) at boiling temperature.[1]

In the case of highly porous alumina substrate, the evaporation-induced recoil pressure is expected to drive the flow of the molten material into the substrate. This effect is clearly seen in Fig. 9, which presents a high magnification SEM micrograph in the interfacial region between the laser modified surface region and the underlying porous material.

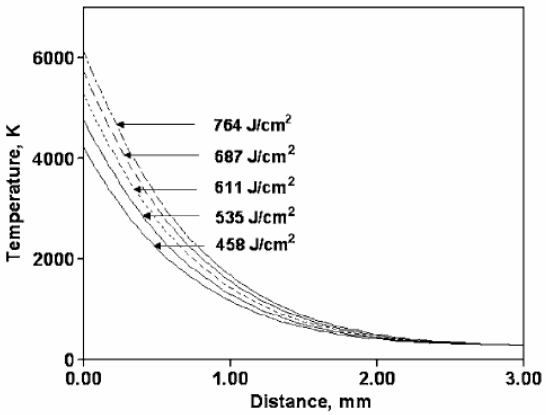


FIG. 6. Computed temperature distribution below the surface of alumina ceramic surface modified with a range of laser processing fluence from 458 to 764 J/cm^2.

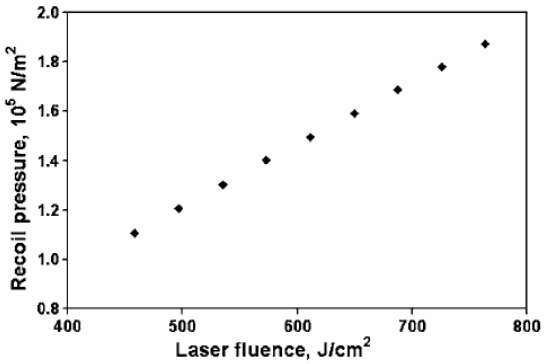


FIG. 8. Computed evaporation-induced recoil pressure as a function of laser processing fluence employed during the laser surface modifications of alumina ceramic.

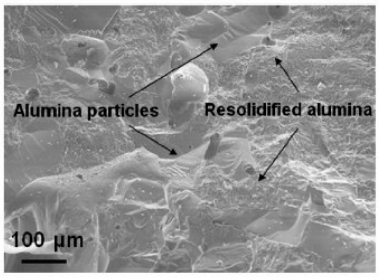


FIG. 9. High magnification SEM micrograph of the interfacial region of the laser surface modified alumina illustrating the infiltration of molten material into the underlying porous material assisted by evaporation-induced recoil pressures.

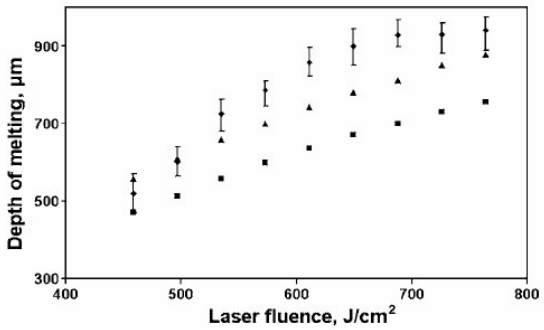


FIG. 10. Comparison of computed depth of melting from thermal and fluid flow model with experimental depth of melting (♦, Experimental; ■, thermal model; and ▲, integrative thermal and fluid flow model).

The figure indicates the dendritic microstructure corresponding to the rapidly solidified molten alumina around the unmelted alumina particles. The dendritic microstructure of rapidly solidified alumina is characteristic of the laser surface processing which is associated with rapid cooling rates of the order of 10^2 K/s.[10] In the case of metallic materials significantly higher cooling rates ($\sim 10^5$–10^7 K/s) are reported during laser surface processing.[23] The relatively lower cooling rates in the alumina ceramics are primarily due to low thermal conductivity (14.6 W/m K) of the porous ceramic material.

It has been reported that under certain thermal conditions shape of the melt pool is also affected by the surface tension effects in addition to the presence of recoil vapor pressure and thermocapillary forces.[24] Surface tension and viscosity are determined by the same intermolecular forces. Hence surface tension varies directly with the viscosity. A direct proportion between the two quantities has been established with a hard sphere model based on the fact that the surface tension and viscosity can be expressed as integrals over the product of interatomic forces and the pair distribution function.[25] The kinematic viscosity of alumina at the melting temperature ($\sim$2323 K) is approximately 0.15 cm^2/s which is very negligible. Hence by taking into account the direct variation of surface tension with viscosity, it was assumed that the corresponding effect of surface tension on the melt pool geometry would also be negligible under the processing conditions employed in the present work. Hence the surface tension related effects were not considered in the calculation of melt infiltration.

Comparison of experimental values of depth of melting with the values calculated from the heat transfer and the fluid flow equations is presented in Fig. 10. The maximum depth of melting was calculated from the thermal model by tracing the melting point in the temperature distribution below the surface of molten alumina ceramic corresponding to the irradiation time (Fig. 6). As shown in Fig. 10, the calculated depth of melting increases with laser processing fluence due to melting front advancing deeper into the material with increasing laser processing fluence. However, the thermal model underestimates the depths of melting compared to the experimental values. From the previous discussion, the laser-material interactions during the laser surface modification of porous alumina ceramics are associated with the evaporation-induced recoil pressures. These recoil pressures determined by the surface temperature play the vital role in driving the flow of fluid into the porous substrate. Such a recoil pressure assisted infiltration of fluid in the porous substrate tends to increase the observed values of depths of melting. Figure 10, therefore, also presents a set of data points for the depths of melting calculated from the integrated approach involving the Carman-Kozeny equations (for the infiltration effects due to liquid head and evaporation-induced recoil pressure) and the thermal analysis (for the effects of temperature distribution below the surface of alumina material). As indicated in the figure, such an integrated approach provides a better agreement between the experimental and predicted depths of melting. However, deviation of the predicted depths of melting from the experimental values especially at the higher laser processing fluence may be due to the simplification of assumptions in the thermal model such as temperature independence of the thermophysical properties and the idealized model of melt infiltration. Also, due to the dynamic nature of physical, chemical, and microstructural phenomena associated with the laser interactions particularly with porous alumina, the accuracy of predictions is expected to be influenced by how well the complex interactions are defined in the mathematical calculations.

V. CONCLUSIONS

During the laser surface modification of porous alumina ceramic with high power laser (delivering incident laser fluence of 458–764 J/cm^2), the surface of the material melts and subsequently solidifies into a highly dense recast layer. During surface modification, the surface of the melt is subjected to very high recoil pressures ($>10^5$ Pa) induced by rapid surface evaporation. The magnitudes of such evaporation-induced recoil pressures were estimated from temperature history derived from a three-dimensional thermal model. The temporal evolution of the evaporation-induced recoil pressures indicated that the recoil pressure reaches maximum value for irradiation time of the laser beam. Such high recoil pressures tend to drive the flow of molten material into the porous substrate, thus extending the depth of melting estimated from the temperature fields alone.

An integrative modeling approach combining the thermal analysis (three dimensional heat transfer model) and the fluid flow (Carman-Kozeny equations) results in better agreement between the predicted values of depths of melting with that obtained from experimental investigations.

[1]S. I. Anisimov, Sov. Phys. JETP **27**, 182 (1968).
[2]V. Semak and A. Matsunawa, J. Phys. D **30**, 2541 (1997).
[3]F. Quintero, F. Varas, J. Pou, F. Lusquiños, M. Boutinguiza, R. Soto, and M. Pérez-Amor, J. Phys. D **38**, 655 (2005).
[4]V. V. Semak, J. G. Thomas, and B. R. Campbell, J. Phys. D **37**, 2925 (2004).
[5]D. J. Lim, H. Ki, and J. Mazumder, J. Phys. D **39**, 2624 (2006).
[6]S. P. Harimkar, A. N. Samant, A. A. Khangar, and N. B. Dahotre, J. Phys. D **39**, 1642 (2006).
[7]L. Bradley, L. Li, and F. H. Stott, Appl. Surf. Sci. **138–139**, 233 (1999).
[8]A. A. Khangar, E. A. Kenik, and N. B. Dahotre, Ceram. Int. **31**, 621 (2005).
[9]J. F. Li, L. Li, and F. H. Stott, Acta Mater. **52**, 4385 (2004).
[10]S. P. Harimkar and N. B. Dahotre, J. Appl. Phys. **100**, 024901 (2006).
[11]H. S. Carslaw and J. C. Jaeger, *Conduction of Heat in Solids* (Oxford, New York, 1967).
[12]W. H. Gitzen, *Alumina as Ceramic Material* (American Ceramic Society, Westerville, OH, 1970).
[13]F. P. Incropera and D. P. DeWitt, *Fundamentals of Heat and Mass Transfer* (Wiley, New York, 1990).
[14]Y. S. Touloukian, *Thermophysical Properties of High Temperature Materials* (IFI/Plenum, New York, 1967).
[15]J. Wilson and F. B. Hawkes, *Lasers: Principles and Applications* (Prentice-Hall, New York, 1987).
[16]V. P. Elyutin, B. S. Mitin, and Y. A. Nagibin, Inorg. Mater. **8**, 416 (1972).
[17]P. C. Carman, Chem. Eng. Res. Des. **16**, 168 (1938).
[18]S. P. Harimkar and N. B. Dahotre, Int. J. Appl. Ceram. Technol. **3**, 375 (2006).
[19]A. Kar and J. Mazumder, J. Appl. Phys. **78**, 6353 (1995).
[20]A. Kar and J. Mazumder, J. Appl. Phys. **68**, 3884 (1990).
[21]Y. V. Afanasiev and O. N. Krokhin, Sov. Phys. JETP **25**, 639 (1967).
[22]V. V. Semak, B. Damkroger, and S. Kempka, J. Phys. D **32**, 1819 (1999).
[23]E. M. Breinan and B. H. Kear, in *Laser Materials Processing*, edited by M. Bass (North-Holland, Amsterdam, 1983), p. 235.
[24]L. Han, F. W. Liou, and S. Musti, J. Heat Transfer **127**, 1005 (2005).
[25]S. Mukherjee, W. L. Johnson, and W. K. Rhim, Appl. Phys. Lett. **86**, 014104 (2005).

Vita

Sandip P. Harimkar was born on June 2, 1977 in Achalpur, India. He completed his Bachelor of Engineering Degree in Metallurgical Engineering from Visvesvaraya National Institute of Technology, Nagpur, India in 1999. He then worked for two years in Bajaj Auto Limited, Aurangabad, India as a Section Manager of heat treatment facilities. He always wanted to pursue higher education in the areas of Materials Science and secured admission in prestigious Indian Institute of Science, Bangalore for a Masters program through a highly competitive national entrance examination. Subsequently, he obtained his Masters Degree in Metallurgical Engineering in year 2003. Sandip obtained his both Bachelors and Masters Degrees with highest academic achievements. After his Masters Degree, he worked for over one year in TVS Motor Company as an engineer in Research and Development department. His urge for higher education motivated him to pursue doctoral studies at the University of Tennessee, Knoxville. He currently works in the areas of laser processing of materials for advanced applications. He has authored one technical book with a leading publisher and also authored over 15 scientific papers published in high impact factor journals. He also serves as reviewer for leading scientific journals.